Demonstration of a Novel Modular Neutrino Detector

Inauguraldissertation
der Philosophisch-naturwissenschaftlichen Fakultät
der Universität Bern

vorgelegt von

Livio Jonas Calivers

von Ilanz/Glion GR

2025

Leiter der Arbeit:
Prof. Dr. Michele Weber

Co-Leiter der Arbeit:
Prof. Dr. Igor Kreslo

Albert Einstein Center for Fundamental Physics
Laboratorium für Hochenergiephysik
Physikalisches Institut

Demonstration of a Novel Modular Neutrino Detector

Inauguraldissertation
der Philosophisch-naturwissenschaftlichen Fakultät
der Universität Bern

vorgelegt von

Livio Jonas Calivers

von Ilanz/Glion GR

2025

Leiter der Arbeit:
Prof. Dr. Michele Weber

Co-Leiter der Arbeit:
Prof. Dr. Igor Kreslo

Albert Einstein Center for Fundamental Physics
Laboratorium für Hochenergiephysik
Physikalisches Institut

Bern, 06.06.2025

Der Dekan
Prof. Dr. Jean-Louis Reymond

Abstract

The Deep Underground Neutrino Experiment (DUNE) is designed to perform precision measurements of neutrino oscillations by combining a high-intensity, broad-spectrum neutrino beam with large-mass, highly granular detectors. A critical requirement for achieving this goal is the accurate characterisation of the unoscillated neutrino beam at a near detector site, located close to the beam source, before the neutrinos propagate over a distance of 1500 m to a far detector complex, where the oscillated beam is measured. The near site will be instrumented with a modular detector based on liquid argon time projection chamber (LArTPC) technology. The modular design of this detector has proven advantageous for operation in the high-rate environment of the intense neutrino flux at the DUNE near detector. In this thesis, it is shown how the optical segmentation imposed by the detector modularity enhances the ability to localise scintillation light and facilitates efficient matching between the light and charge signals produced by neutrino interactions, an essential capability for disentangling overlapping events within a single beam spill. To demonstrate and validate the modular approach, the 2x2 Demonstrator, which consists of four fully instrumented LArTPC modules, was developed as part of this thesis. The detector was operated in the Neutrinos at the Main Injector (NuMI) beam at the Fermi National Accelerator Laboratory and successfully integrated light and charge detection, cryogenic infrastructure, timing systems, and data acquisition under realistic beam conditions. As part of this work, a comprehensive light readout system was developed and implemented as a core component of the $2{\times}2$ Demonstrator, including the design and production of light detectors, the establishment of quality control procedures, the integration of an in-situ calibration system, and the implementation of a fully integrated run control. Performance measurements of the 2x2 Demonstrator show a photon detection efficiency of $(0.19 \pm 0.02)\,\%$ and $(0.63 \pm 0.13)\,\%$ for the deployed ArCLight and LCM light detection modules, respectively. Using timing information extracted from scintillation light data, the substructure of the NuMI beam spills was resolved and an interaction timing resolution of less than 4 ns was demonstrated.

Contents

List of Figures 8

List of Tables 11

List of Acronyms 15

1 Introduction 15

2 Experimental Neutrino Physics 19

2.1 History of neutrino experiments 19
2.2 Neutrino oscillation 24
2.3 The future of neutrino oscillation experiments 27
2.4 The Deep Underground Neutrino Experiment 29
2.4.1 Far Detector Complex 32
2.4.2 Near Detector Complex 33

3 A Modular Liquid Argon Near Detector for DUNE 38

3.1 Final state particles in matter 38
3.1.1 Interaction of charged particles 38
3.1.2 Interaction of photons 41
3.1.3 Electromagnetic Showers 42
3.1.4 Hadronic showers 43
3.2 LArTPC Detection principle 44
3.3 General requirements on charge and light detectors for LArTPCs 48
3.4 Review of former LArTPC experiments 49
3.5 Modular Near Detector for DUNE 53
3.5.1 Dimensional requirements 53
3.5.2 The ArgonCube concept at ND-LAr 55
3.5.3 Prototyping campaign 58

4 Light Readout for a Modular LArTPC 60

4.1 Requirements for the light readout in high-intensity environments 60
4.2 Overview 64
4.3 ArClight 65
4.3.1 Concept and Design 65
4.3.2 Evaporation Coating 67
4.3.3 Quality control scanning 70
4.4 Readout electronics 73

4.5 DAQ and detector configuration 76
4.6 In-situ SiPM calibration 78
4.6.1 LED setup 79
4.7 Light Simulation 82
4.7.1 Photon creation 82
4.7.2 Photon propagation 83
4.7.3 Electronics response 86
4.8 Light Reconstruction 86

5 The 2x2 Demonstrator - Motivation and Design 92
5.1 Overview and Motivation 92
5.2 NuMI beam and backgrounds 97
5.3 Cryogenics 102
5.4 MINERνA trackers in the 2x2 (Mx2) 105
5.5 Light readout 107
5.6 Charge readout 109
5.7 Trigger and Timing System 112

6 The 2x2 Demonstrator - Operation and First Results 116
6.1 Single module assembly and testing 116
6.2 Installation at MINOS 122
6.3 Light readout commissioning 125
6.4 Operation in the NuMI beamline 127
6.5 Extraction of the T_0 resolution using the NuMI beam structure 135

7 Conclusion and Outlook 147

Acknowledgements 150

General Remarks 152

Bibliography 152

List of Figures

2.1 Cowan and Reines detection principle 20
2.2 $\sin\theta_{23}$ vs. δ_{CP} in T2K and NOvA 27
2.3 Schematic of the upgraded ND280 29
2.4 DUNE beam characteristics 30
2.5 DUNE significance on mass ordering and CP violation 31
2.6 DUNE Phase I Far Detector 33
2.7 DUNE Near Detector Complex 34
2.8 ND-LAr + TMS principle 35
2.9 DUNE TMS 35
2.10 DUNE ND PRISM energy spectra 36

3.1 Bethe-Bloch for μ on argon 40
3.2 Bremsstrahlung 40
3.3 Attenuation coefficient for high-energetic photons in gaseous argon 42
3.4 TPC detection principle 44
3.5 Field dependence of ionisation and scintillation yield 47
3.6 Impact of the LArTPC size on hadron containment 54
3.7 DUNE ND-LAr detector design 56
3.8 Impact of detector segmentation on light pile-up 56
3.9 Overview ND-LAr Module 57

4.1 Illustration of the charge-light matching 61
4.2 Temporal and spatial resolution of the light readout 62
4.3 Light readout overview 64
4.4 Schematic diagram of the ArCLight 65
4.5 TPB emission and EJ280 absorption spectra 66
4.7 TPB layer structure for different coating techniques 68
4.8 TPB Evaporation chamber setup 69
4.9 TPB coating process 70
4.10 LED scanning setup 71
4.11 ArCLight LED scanning single SiPM response 72
4.12 ArCLight LED scanning total light yield 73
4.13 Schematic of a SiPM microcell structure 74
4.14 Pre-amp board with and without shield 75
4.15 Overview of the light readout control software 77
4.16 Example ADC integral spectrum with fitted “single” p.e. peaks 79
4.17 Calibration LED setup 80

4.18 LED pulser schematic . . . 81
4.19 16-channel LED Pulser . . . 82
4.20 Simulated visibility for a full-size ND-LAr TPC . . . 85
4.21 LRS detector coverage . . . 86
4.22 Waveform deconvolution . . . 88
4.23 Coherent noise filter . . . 89
4.24 Light hit time reconstruction methods . . . 90
4.25 Light hit time reconstruction truth studies . . . 90
4.26 Light hit and flash finder . . . 91

5.1 Overview of the main components of the 2x2 . . . 94
5.2 CAD drawing of the 2x2 including the access platforms and electronics racks 95
5.3 Technical drawing of a single 2x2 module . . . 96
5.4 Picture of the inside of a 2x2 module . . . 96
5.5 Situation plan of the 2x2 location . . . 98
5.6 Overview of the FNAL accelerator complex . . . 99
5.7 Beam flux and event rate for 2x2 . . . 100
5.8 2x2 track multiplicity . . . 100
5.9 2x2 expected particle production rates . . . 101
5.10 Effect of cross-section model on δ_{CP} sensitivity . . . 101
5.11 2x2 and ND-LAr expected CC pion multiplicity . . . 102
5.12 2x2 Cryogenics Overview . . . 103
5.13 Picture of the Mx2 . . . 106
5.14 Schematic of the LCM detection principle . . . 107
5.15 Picture of the 2x2 Light traps . . . 108
5.16 2x2 Light readout channel map . . . 109
5.17 Picture of a 2x2 charge readout pixel tile . . . 110
5.18 LArPix block diagram . . . 111
5.19 2x2 trigger and timing system overview . . . 113

6.1 Single module assembly structure . . . 117
6.2 Single module testing facility at Bern . . . 118
6.3 Gallery of cosmic ray-induced events in Module-0 . . . 120
6.4 PDE results for Module-0 and Module-1 . . . 121
6.5 Muon decay event with charge and light data . . . 122
6.6 2x2 module insertion . . . 123
6.7 Assembled 2x2 detector top flange . . . 124
6.8 SiPM breakdown voltage extraction . . . 126
6.9 Optimal SiPM overvoltage extraction . . . 127
6.10 SiPM gain distribution . . . 127
6.11 2x2 cooldown overview . . . 128
6.12 First HV ramp . . . 129
6.13 Electron lifetime in 2x2 . . . 130
6.14 Cumulative Protons On Target (POT) data for the July 2024 2x2 run . . 131
6.15 Neutrino candidate event display 1 . . . 132
6.16 Neutrino candidate event display 2 . . . 133
6.17 Neutrino candidate event display 3 . . . 134

6.18 NuMI beam spill structure 135
6.19 RWM time correction 137
6.20 Reconstructed T_0 Full Spill 138
6.21 Reconstructed T_0 Bunch Structure 139
6.22 Bunch spacing using FFT 140
6.23 Fitted bunch spacing 140
6.24 T0 ADC offset correction 141
6.25 ADC offset corrected T_0 distribution 142
6.26 Triple bunch overlay with fitted Gaussian 143
6.27 Triple bunch overlay with fitted Gaussian and background 143
6.28 Single bunch overlay with fitted Gaussian 144
6.29 T0 resolution vs. amplitude 144
6.30 Bunch resolution amplitude scan ArCLight 145
6.31 Bunch resolution amplitude scan LCM 146

List of Tables

2.1 Oscillation parameters global fit 26

3.1 Liquid argon properties 46

4.1 ND-LAr LRS requirements 64

6.1 Overview single module runs 119
6.2 T0 cable delay corrections 137

Acronyms

ADC Analogue-to-Digital Converter

APA Anode Plane Assemblie

API Application Programming Interface

ArCLight ArgonCube Light detector

ArCubeOptSim ArgonCube Optical Simulation

ArgoNeuT Argon Neutrino Teststand

ASIC Application-Specific Integrated Circuits

BJT Bipolar Junction Transistor

BNB Booster Neutrino Beam

BSM Beyond-the-Standard-Model

C Charge-symmetry

CAD Computer-Aided Design

CC Charged Current

CERN Conseil Européen pour la Recherche Nucléaire

CMOS Complementary Metal-Oxide-Semiconductor

CNC Computer Numerical Control

CORSIKA COsmic Ray SImulations for KAscade

CP Charge-Parity-symmetry

CPT Charge-Parity-Time-symmetry

CRP Charge Readout Planes

CRS Charge Readout System

CTE Coefficient of Thermal Expansion

DAC Digital-to-Analogue converter

DAQ Data Aquisition

DBSCAN Density-Based Spatial Clustering of Applications with Noise

DIS Deep Inelastic Scattering

DONUT Direct Observation of the Nu Tau

DQM Data Quality Monitoring

DUNE Deep Underground Neutrino Experiment

ECAL Electro-magnetic Calorimeter

edep-sim energy deposition simulation

ENC Equivalent-Noise-Charge

FD Far Detector

Fermilab Fermi National Accelerator Laboratory

FFT Fast Fourier Transform

FNAL Fermi National Accelerator Laboratory

FSD Full Size Demonstrator

FSI Final State Interaction

FWHM Full Width at Half Maximum

GDML Geometry Description Markup Language

GEANT4	GEometry ANd Tracking 4
HCAL	Hadronic Calorimeter
HPC	High-Performance Computing
HPgTPC	High-Pressure gaseous argon TPC
HV	High Voltage
ICARUS	Imaging Cosmic And Rare Underground Signals
IMB	Irvine–Michigan –Brookhaven
JINR	Joint Institute for Nuclear Research
KamiokaNDE	Kamioka Nucleon Decay Experiment
LAr	Liquid Argon
LArPix	Liquid Argon Pixelate charge readout
LArTPC	Liquid Argon Time Projection Chamber
LBNF	Long Baseline Neutrino Facility
LCM	Light Collection Module
LED	Light-Emitting Diode
LEP	Large Electron-Positron Collider
Linac	Linear Accelorator
LN	Liquid Nitrogen
LRS	Light Readout System
LUT	Look-Up-Table
MAWP	Maximum Allowable Working Pressure
m.w.e.	meters water equivalent
MC	Monte Carlo
MicroBooNE	Micro Booster Neutrino Experiment
MINOS	Main Injector Neutrino Oscillation Search
MIP	Minimum Ionising Particle
MOSFET	Metal Oxide Semiconductor Field Effect Transistor
MSW	Mikheyev-Smirnov-Wolfenstein
Mx2	Minerva trackers in 2x2
NC	Neutral Current
ND-GAr	Gasous Argon Near Detector
ND-LAr	Liquid Argon Near Detector
ND	Near Detector
NOvA	NuMI Off-Axis ν_e Appearance
NTP	Network Time Protocol
NuMI	Neutrinos from the Main Injector
p.e.	photoelectron
P	Parity-symmetry
PACMAN	Pixel Array Controller and Network
PCB	Printed Circuit Board
PDE	Photon Detection Efficiency
PID	Proportional–Integral –Derivative
P&ID	Piping and Instrumentation Diagram
PMNS	Pontecorvo-Maki-Nakagawa-Sakata
PMT	Photo Multiplier Tube
POT	Protons On Target
PPS	Pulse-per-Second

PRISM	Precision Reaction-Independent Spectrum Measurement
PS	Power Supply
PTFE	Polytetrafluoroethylene
QE	Quasi-Elastic
RFQ	Radio-Frequency Quadrupole
RTD	Resistance Temperature Detector
RWM	Resistive Wall Monitor
SAND	System for on-Axis Neutrino Detection
SBN	Short Baseline Neutrino
SiPM	Silicon Photo Multiplier
SNO	Sudbury Neutrino Observatory
SURF	Sanford Underground Research Facility
T2HK	Tokai-to-Hyper-Kamiokande
T2K	Tokai-to-Kamioka
TCP	Transmission Control Protocol
TMS	Temporary Muon Spectrometer
TPB	Tetraphenyl Butadiene
TPC	Time Projection Chamber
VGA	Variable Gain Amplifier
VME	Versa Module Eurocard
VUV	Vacuum Ultra Violet
WLS	Wavelength Shifting
WR	White Rabbit

Chapter 1

Introduction

Neutrino physics has emerged as a key area in particle physics, with groundbreaking discoveries such as neutrino oscillations [1], which provided direct evidence for non-zero neutrino masses. Despite significant advances, several fundamental questions remain open in neutrino physics. Key unresolved questions include the precise ordering of neutrino mass states, the detailed mechanisms underpinning neutrino mass generation, and the potential existence and magnitude of Charge-Parity-symmetry (CP) violation within the neutrino sector. Experimentally addressing these open questions is exceptionally challenging due to the inherently weak interactions of neutrinos. The extremely low neutrino interaction cross-section, on the order of $1 \times 10^{-38}\,\mathrm{cm}^2$ for neutrino energies relevant in current accelerator-based experiments [2], requires experimental setups with detectors of large masses and high granularity, as well as intense neutrino sources. Over the past decades, numerous experiments have contributed to our understanding of neutrino properties, with significant efforts dedicated to measuring oscillation parameters and searching for new physics beyond the Standard Model of particle physics. Addressing these fundamental questions motivates the design and implementation of advanced long-baseline neutrino experiments, which leverage powerful neutrino beams to investigate fundamental neutrino properties.

In long-baseline neutrino oscillation experiments, a neutrino beam is first produced and then characterised at a Near Detector (ND) before travelling hundreds to thousands of kilometres to a Far Detector (FD), where any changes in the beam composition due to oscillations are analysed. This allows for precise measurements of neutrino oscillation parameters and the study of fundamental neutrino properties. A key parameter to probe is the CP-violating phase in the neutrino mixing, which, if it is non-trivial, could have profound implications for the observed matter-antimatter asymmetry in the universe [3]. The long-baseline Deep Underground Neutrino Experiment (DUNE) experiment is designed as a next-generation neutrino precision measurement facility, aiming to study a wide range of neutrino interactions and properties [4–7]. It will explore key open questions such as determining the neutrino mass ordering, measuring the CP-violating phase, improving neutrino interaction cross-section measurements, and searches for new physics beyond the Standard Model. To achieve these objectives, DUNE will utilise a neutrino beam of unprecedented power and an advanced near and far detector system. The FD complex, located 1.5 km underground at the Sanford Underground Research

Facility (SURF), will use massive Liquid Argon Time Projection Chamber (LArTPC) modules as an observatory for neutrinos, including those of the oscillated beam. Complementary to this, the ND complex at Fermi National Accelerator Laboratory (FNAL) will characterise the unoscillated beam to perform oscillation measurements [8]. Besides accelerator neutrinos, the experiment is designed to be capable of observing neutrinos originating from solar processes and supernovae.

LArTPCs, as used in DUNE, have emerged as a powerful detector technology for neutrino physics, owing to their excellent spatial resolution, calorimetric capabilities, and ability to provide detailed event reconstruction. A LArTPC detects charged particles by collecting ionisation electrons produced in liquid argon and drifting them under a uniform electric field toward a readout system. Additionally, measuring the scintillation light emitted during the particles' passage allows for a precise three-dimensional reconstruction of their trajectory. Since their early development and conceptualisation in the 1970s, initially proposed by H. H. Chen [9], LArTPCs have evolved through various design iterations and technological advancements, leading to their application in modern neutrino experiments.

Driven by the extensive ongoing R&D efforts and lessons learned from previous LArTPC experiments, the development of a novel detector concept, called ArgonCube [10], was initiated at the University of Bern. The key idea of the ArgonCube concept is a modular rather than a monolithic approach for large-scale detectors. This modular design reduces the requirements of the detector in multiple aspects significantly, in particular for the High Voltage (HV) system, allowing for a much more robust and stable operation. This modular approach further brings advantages for operation in high-pileup environments due to improved charge-light matching capabilities within the optically isolated modules. As the unprecedented intensity of the neutrino beam in DUNE creates exactly such a high-pileup environment for its near detector location, ArgonCube was selected as the suitable detector concept for building a Liquid Argon Near Detector (ND-LAr) for DUNE. Realising this concept constitutes the primary objective of this thesis.

The ND-LAr forms an essential part of the DUNE ND by providing detailed characterisation of neutrino interactions, crucial for reducing systematic uncertainties. By closely matching the technology used in the far detector, ND-LAr ensures accurate extrapolation of near-detector measurements, thus improving sensitivity to neutrino oscillation parameters and enabling more precise exploration of fundamental physics questions. While its proximity to the source of the high-intensity neutrino beam presents significant challenges due to interaction pile-up, it simultaneously provides high statistics, enabling precision measurements.

The modular design of ND-LAr introduces many new challenges for the design of the various detector components. For the charge readout, the ND-LAr will be the first large-scale detector applying a pixelated readout based on the Liquid Argon Pixelate charge readout (LArPix) technology [11]. To avoid inactive areas in the detector, the modular approach also required the development of new compact solutions for the light readout. Initial designs and early prototypes for these systems have been developed in the course of the ArgonCube R&D program but were not yet applicable for deployment in a mature detector design [12, 13].

To progress towards implementing the ArgonCube in ND-LAr, substantial efforts are required in validating and advancing the existing conceptual prototypes. This involves not only enhancing and scaling up these prototypes but also creating a comprehensive, end-to-end readout system, encompassing all necessary readout electronics and data acquisition tools. Additionally, infrastructure and supporting systems for large-scale production, quality control, commissioning, and calibration of detector systems must be established. Requirements have been defined for each detector system that need to be met in order to fulfil the physics goals of the ND-LAr. Beyond validating each individual system, large-scale prototypes and demonstrators are essential to verify the physics performance of the fully integrated detector. Building such a demonstrator forms the central aim of this thesis.

The light readout system in ND-LAr is essential for precisely determining event timing, which is crucial in disentangling neutrino interactions and reducing background noise. Accurate detection of scintillation light improves the reconstruction of neutrino events, enhancing both spatial and energy resolution. Consequently, this system significantly contributes to the overall physics performance of ND-LAr, enabling clearer identification of neutrino interactions and calorimetric measurements.

A key goal of this work is to develop and validate the light readout system for a modular liquid argon time projection chamber, an essential component of the ND-LAr detector. Starting from an early prototype for a light detector design, a full system is developed to enable successful production, integration, commissioning, and operation of the light readout system. This includes the establishment of a production and quality control infrastructure for the light detectors, as well as the implementation of data acquisition and control software and a fully automatic calibration system.

To validate these developments in a realistic experimental environment, a large-scale demonstrator experiment, the 2x2 Demonstrator, is designed and built. The 2x2 Demonstrator consists of four downsized prototype TPC modules and is operated within the Neutrinos from the Main Injector (NuMI) beamline at Fermilab. By studying the performance of the detector components under real beam conditions, the demonstrator provides critical insights that will inform the final design and optimisation of ND-LAr, ensuring its capability to function effectively in a high-intensity neutrino flux. Beyond technical validation, the 2x2 Demonstrator enables physics analyses of neutrino interactions, contributing to reducing systematic uncertainties in interaction models and improving event reconstruction techniques.

To provide context for this work, Chapter 2 explores the historical development of experimental neutrino physics, with a focus on neutrino oscillations and emphasises the requirements for future experiments. Chapter 3 explores the fundamental principles of neutrino detection in liquid argon detectors, describes the operational mechanisms of LArTPCs, and introduces the ND-LAr detector concept, highlighting its design motivations, technological requirements, and the specific challenges posed by high-intensity neutrino beams.

Motivated by the requirements for ND-LAr, Chapter 4 presents a generalised approach to light detection systems in high-intensity environments, detailing the design, operation, and calibration of light readout components applicable to a range of experimental setups. The discussion extends to simulation techniques used to model photon propagation and detector response, as well as methods for event reconstruction. Chapter 5 presents the 2x2 Demonstrator, describing its design, the implementation in the NuMI beamline and the potential physics outcome of the experiment. The demonstrator integrates several key subsystems, including charge readout, light readout, cryogenic systems, high-voltage infrastructure, and triggering and timing frameworks. Each of these elements must function cohesively in a high-intensity environment to ensure robust performance and reliable data collection. Chapter 6 discusses the operational performance of the 2x2 Demonstrator, including its assembly, commissioning, data collection, and calibration results, with a particular focus on the light data. Finally, Chapter 7 summarises the key findings of this work and provides an outlook on the transition from the 2x2 Demonstrator to the full ND-LAr system.

Chapter 2

Experimental Neutrino Physics

In this chapter, the history of experimental neutrino physics, in particular neutrino oscillation physics, is outlined. The first section covers the major breakthroughs in neutrino physics in chronological order. To highlight the importance of future neutrino experiments focusing on neutrino oscillations, the oscillation theory and its main consequences are summarised in Section 2.2. In the last section of this chapter, the DUNE experiment and its physics scope are elaborated.

2.1 History of neutrino experiments

In the early 20th century, the physics world was puzzled by multiple experiments measuring the continuous energy spectrum of electrons emitted by β-decays. As β-decay was considered to be a two-body decay (electron and daughter nucleus), one would expect a discrete energy of the emitted electron. This, however, was proven not to be the case in 1914 by James Chadwick [14].

To address this, in his famous letter in 1930, Wolfgang Pauli proposed a charge-neutral, spin 1/2 particle with a mass "lower than 0.01 proton masses" [15], which Pauli called "neutron". By redefining the β-decay to the emission of an electron and a "neutron", the measured continuous spectrum could be explained. The particle that is today called the neutron was discovered in 1932 by Chadwick [16]. However, Francis Perrin deduced that the mass of the particle emitted in the β-decay has to be of mass significantly lower than the electron mass and thus could not be the particle discovered by Chadwick [17]. Pauli's particle was renamed the "neutrino" by Enrico Fermi, who developed a theory explaining β-decay [18]. Using the theory of Fermi, Hans Bethe and Rudolph Peierls showed that the neutrino-nucleus cross section must be $< 10^{-44}\,\mathrm{cm}^2$, and concluded "that there is no practically possible way of observing the neutrino" [19].

It took 26 years between the proposal and the first detection of the neutrino. In 1956, Clyde Cowan and Frederick Reines published results from their inverse β-decay experiment where they detected the first electron antineutrinos [20]. In an inverse β-decay, an electron antineutrino interacts via

$$\overline{\nu}_\mathrm{e} + \mathrm{p} \rightarrow \mathrm{n} + \mathrm{e}^+. \tag{2.1}$$

Cowan and Reines placed a water target next to the Savannah River nuclear reactor in South Carolina (USA), providing a high antineutrino flux. The positron emitted in the inverse β-decay interacts with shell electrons, producing two prompt back-to-back photons. To measure them, two liquid scintillator tanks coupled to Photo Multiplier Tubes (PMTs) with an overall timing resolution of 0.2 µs were placed above and below the water targets. The emitted neutron takes a few microseconds to thermalise and eventually gets captured by cadmium, which is added as a dopant to the water target. The neutron capture results again in the emission of gamma rays. Measuring two coincident gamma-rays in opposite directions, followed by a photon emission with a defined-range time delay, is a distinct signal for a $\overline{\nu}_e$ with a very low background. The detection principle and a schematic of the setup are illustrated in Figure 2.1.

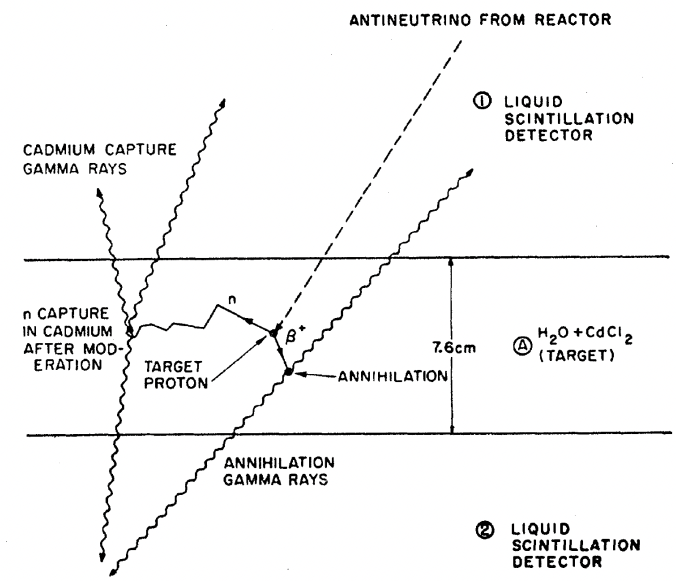

Figure 2.1 – Detection principle used by Cowan and Reines for the discovery of the (anti)neutrino. The incoming antineutrino interacts via inverse β-decay and produces a positron and a neutron. The positron annihilates with a shell electron, producing two fast back-to-back photons. The neutron eventually gets captured by a cadmium nucleus, resulting in a delayed second light pulse. Two liquid scintillator detectors are placed above and below the target to detect the gamma rays. Reprinted with permission from Physical Review [21]. Copyright 2025 by the American Physical Society.

In the mid-1950s, groundbreaking experiments significantly advanced the understanding of weak interactions and their fundamental symmetries. Notably, in 1957, Chien-Shiung Wu conducted an experiment demonstrating for the first time that parity (Parity-symmetry (P)) symmetry is violated in weak interactions [22]. Shortly thereafter, Maurice Goldhaber's experiment further clarified the nature of weakly interacting neutrinos [23]. Over these two pivotal years, it became clear that only left-handed neutrinos and right-handed antineutrinos participate in weak interactions. These findings were crucial in shaping the modern theoretical framework of neutrino physics.

In 1962, a group led by Leon M. Ledermann discovered the ν_μ [24]. This experiment was the first to use neutrinos produced by an accelerator beam. By shooting protons on a beryllium target, pions are produced, and these pions decay by emitting a ν_μ (or a $\overline{\nu}_\mu$). By applying a magnetic field right after the target, μ^+ can be focused and μ^- defocused, or vice versa. After blocking the π and μ with a large steel shield, one gets a relatively pure ν_μ (or $\overline{\nu}_\mu$) beam. (A detailed description of how a neutrino beam can be created is described in Sec. 5.2 with the example of the NuMI beam.) In the Ledermann experiment, a spark chamber was used to detect charged particles from interacting neutrinos. In a spark chamber, charged particles ionise a gas. By applying a high-voltage field between several metal plates placed in the chamber, an avalanche reaction is triggered, causing a temporary breakdown path along the original particle track visible as a series of "sparks". This setup allows the differentiation between muon and electron tracks since the latter would cause electromagnetic showers. It could be concluded that the observed interactions could not originate from the same type of neutrinos previously observed by Cowan and Reines, thereby indicating the discovery of a new neutrino flavour: the muon neutrino.

The first neutrinos (and not anti-neutrinos) were measured in 1968 by Raymond Davis, Don S. Harmer, and Kenneth C. Hoffman in the Homestake Mine, South Dakota (USA) [25]. The Homestake experiment was based on the interaction of ν_e originating from the sun with ^{37}Cl dissolved in water via

$$\nu_\mathrm{e} + {}^{37}\mathrm{Cl} \rightarrow \mathrm{e}^- + {}^{37}\mathrm{Ar}. \tag{2.2}$$

The number of neutrino interactions in this experiment could be determined offline by measuring the activity of the produced radioactive ^{37}Ar content. This method provides a sub-MeV energy threshold for incoming neutrinos needed to measure the relatively low energetic solar neutrinos. The experiment was located at SURF 1500 m below surface to prevent cosmic radiation background (where also the DUNE FD is located). Solar neutrinos are produced by fusion reactions taking place in the sun. However, the measured neutrino flux was only two-thirds of the expected flux calculated by solar models [26]. This discrepancy became known as the solar neutrino problem [27, 28].
The solar neutrino problem can be explained by neutrino oscillations. The theory was proposed by Bruno Pontecorvo in 1968 [29]. It proposes that neutrinos can transform into different neutrino species during their propagation through time and space.

A similar result as the solar neutrino problem was found for atmospheric neutrinos by the Kamioka Nucleon Decay Experiment (KamiokaNDE)-II experiment in 1988 [30] and later in 1991 in the Irvine–Michigan–Brookhaven (IMB) experiment [31]. Atmospheric neutrinos are predominantly produced via decaying pions and muons occurring in the Earth's atmosphere. The pions themself are produced by cosmic protons interacting with nuclei in the atmosphere. The KamiokaNDE experiments (KamiokaNDE I and II, Super-KamiokaNDE) are a series of experiments with water Cherenkov detectors located in the Mozumi Mine in Kamioka (Japan), which were initially designed to detect proton decays. IMB was also a water Cherenkov detector, which was located in a mine in Fairport Harbor, Ohio (USA). If a particle passes through the ultra-pure water of these detectors and has a speed that exceeds the speed of light in water, this produces an observable cone-shaped light emission along the particle's trajectory; the so-called Cherenkov light [32].

In a Cherenkov detector, an array of PMTs are installed on the walls of the water tanks to detect the Cherenkov light. By reconstructing the opening angle of the Cherenkov cone, the momentum and direction of the particle can be deduced. This, combined with the fact that ν_e and ν_μ interactions could be distinguished, represents a significant improvement compared to the radiochemical detectors used in earlier experiments. Cherenkov detectors are sensitive to both ν_e and ν_μ, as-well-as $\overline{\nu}_\mathrm{e}$ and $\overline{\nu}_\mu$, via the Charged Current (CC) interactions, including the Quasi-Elastic (QE) interaction

$$\nu_\ell + \mathrm{n} \to \ell^- + \mathrm{p}, \tag{2.3}$$

$$\bar{\nu}_\ell + \mathrm{p} \to \ell^+ + \mathrm{n}, \tag{2.4}$$

and the electron scattering

$$\nu_\ell + \mathrm{e}^- \to \nu_\ell + \mathrm{e}^-, \tag{2.5}$$

where $\ell = \mathrm{e}, \mu, \tau$. Due to the low energy of solar and atmospheric neutrinos, ν_τ and $\overline{\nu}_\tau$ interactions are not observable via CC interactions as the energy required to produce a $\tau^\mp$ is too high. The neutrino detection via electron scattering is mainly sensitive to ν_ℓ due to the additional CC contribution. Both IMB and the KamiokaNDE experiments were not sensitive to Neutral Current (NC) interactions.

The atmospheric neutrino problem was further studied in the latest version of the KamiokaNDE experiments using the 50 kt Super-KamiokaNDE detector. In 1998, it was measured that the ν_μ flux is $\approx 50\,\%$ lower for upwards directed atmospheric neutrinos which pass through the earth before hitting the detector than neutrinos originated in the atmosphere directly above the detector [33]. However, since the total neutrino flux could not be measured, it could not be proven if the neutrinos were disappearing due to neutrino oscillations.

With the discovery of the τ lepton [34], also the proposal for a third neutrino flavour, the ν_τ emerged. Precise measurements of the Z^0 boson cross-section at the Large Electron-Positron Collider (LEP) in Geneva (Switzerland) in 1990 concluded the number of light neutrinos coupling by weak interaction to be exactly three [35], thus making the ν_τ the last weakly interacting neutrino to be discovered.

The postulated ν_τ was discovered in 2001 at the Direct Observation of the Nu Tau (DONUT) experiment at Fermilab [36]. A 800 GeV proton beam was used to produce the charmed meson $\mathrm{D_s}$, similar to the Ledermann experiment, which decays to a $\overline{\nu}_\tau$ and a τ^-. In an emulsion-based detector, the τ could be detected, which was produced by a charged current ν_τ interaction. Emulsion detectors provide high-resolution tracking of particles, which is particularly needed to detect short-lived particles such as τ leptons. These detectors consist of multiple layers of photographic emulsions placed between layers of high-density target plates. After exposure to a neutrino beam, the emulsion layers are developed and later scanned using automated microscopes. This technique allows the reconstruction of tracks with a micrometre-level resolution. The experiment measured a total of 9 ν_τ events with an estimated background of 1.5 events [37].

The existence of neutrino oscillation was finally experimentally confirmed in 2002 by the Sudbury Neutrino Observatory (SNO) experiment located 2100 m underground in the Creighton Mine in Ontario (Canada) [1]. The 1 kt water Cherenkov detector was filled with heavy water (D_2O), which lowered the energy thresholds and enabled the direct detection of Neutral Current (NC) interactions in addition to CC interactions via

$$\nu_\ell + \mathrm{d} \rightarrow \nu_\ell + \mathrm{n} + \mathrm{p}, \tag{2.6}$$

$$\bar{\nu}_\ell + \mathrm{d} \rightarrow \bar{\nu}_\ell + \mathrm{n} + \mathrm{p}, \tag{2.7}$$

where $\ell =$e,μ,τ. For the NC interactions, the detector had equal sensitivities for all three lepton types. The deuterium captures the neutrons emitted in NC interactions, resulting in the emission of a ∼6 MeV photon, which can be detected by the PMTs. The spherical acrylic structure containing the D_2O was submerged in a bath of ultra-pure H_2O, adding additional shielding from background radiation. The total solar neutrino flux was measured to be consistent with the solar model expectations, and only the ν_e was suppressed, which was a direct proof of the existence of neutrino oscillations.

Since its discovery, the properties of neutrino oscillations have been studied by numerous experiments on solar, reactor, atmospheric and accelerator neutrinos. A particular impact had the discovery of a non-zero θ_{13} mixing angle. A non-zero θ_{13} allows for CP violation in neutrino oscillation, as will be shown in the next section. The discovery of CP violating process in the leptonic sector could help to explain the matter-antimatter asymmetry in the universe. As pointed out by Andrei Sakharov in 1967, in order to explain the asymmetry, baryon-generating interactions need to be found that fulfil the so-called “Sakharov conditions”. They state that for a given interaction

- baryon number violation
- Charge-symmetry (C) and CP violation
- interactions out of thermal equilibrium

must be fulfilled in order to produce matter and antimatter at different rates. The first two conditions ensure that more baryons than anti-baryons are produced. The third condition is needed since else Charge-Parity-Time-symmetry (CPT) symmetry would allow the inverse process annihilating the net baryon - anti-baryon difference. Processes fulfilling these conditions have been observed i.a. in the quark sector but the CP violation has been too low to explain the observed matter-antimatter asymmetry [38]. Thus, further CP violating processes have to be discovered to explain the full asymmetry.

First hints for a non-zero θ_{13} angle were found by Tokai-to-Kamioka (T2K) [39] and Main Injector Neutrino Oscillation Search (MINOS) [40]. Both T2K and MINOS are long-baseline neutrino oscillation experiments that use accelerator-generated neutrinos, as Lederman did, to study their transformation over large distances. T2K sends a neutrino beam from the J-PARC accelerator to the Super-KamiokaNDE detector, 295 km away. Its near detector, ND280, measures the unoscillated neutrino flux, ensuring a well-characterised beam before oscillations occur. MINOS used a neutrino beam produced at

Fermilab and directed toward a far detector in Minnesota, 735 km away. Both experiments measured an excess of ν_e in their far detector.

The discovery of a non-zero θ_{13} came from the Daya Bay Reactor Neutrino Experiment in 2012. Daya Bay measured the disappearance of reactor-produced MeV-scale $\overline{\nu}_\mathrm{e}$ over short distances. By deploying multiple detectors near and far from nuclear reactors in southern China, the experiment detected a deficit of $\overline{\nu}_\mathrm{e}$ at the far detectors, providing a direct measurement of a non-zero θ_{13} at the five sigma confidence level [41]. The combined findings on the full set of oscillation parameters are elucidated in the next section.

2.2 Neutrino oscillation

In this section, the theory and the current state of research in neutrino oscillation physics are summarised following Bettini [42] if not otherwise specified. The theory of neutrino oscillation is based on the non-equality of neutrino flavour eigenstates (ν_e,ν_μ,ν_τ) and neutrino mass eigenstates (ν_1,ν_2,ν_3). Note that there is no theoretical argument restricting the number of mass eigenstates to three. However, any further flavour state would not be active in weak interactions (see previous Section) and, therefore, is not further discussed in the following. The connection between the two sets of eigenstates can be described with a unitary mixing matrix, called the Pontecorvo-Maki-Nakagawa-Sakata (PMNS) matrix [43], as

$$\begin{pmatrix} \nu_e \\ \nu_\mu \\ \nu_\tau \end{pmatrix} = U_{\mathrm{PMNS}} \cdot \begin{pmatrix} \nu_1 \\ \nu_2 \\ \nu_3 \end{pmatrix} . \tag{2.8}$$

Consequently, a neutrino flavour eigenstate can be written as a mix of mass eigenstates

$$|\nu_\alpha\rangle = \sum_{i=1,2,3} U_{\alpha i} |\nu_i\rangle , \tag{2.9}$$

and vice versa

$$|\nu_i\rangle = \sum_{\alpha=e,\mu,\tau} U^\dagger_{\alpha i} |\nu_\alpha\rangle . \tag{2.10}$$

As a unitary matrix, the PMNS matrix can be parametrised by three rotations angles θ_{23},θ_{13} and θ_{12} and a set of additional phases. In particular, one can introduce a CP-violating phase δ_{CP} without breaking the unitarity of the matrix. A non-zero (and non-π) value for δ_{CP} (and $\theta_{13} \neq 0$) implies a CP violation due to the neutrino oscillation mechanism. Motivated by the suppression of the neutrino mass, if one allows the neutrino to be a Majorana fermion ($\nu =\bar{\nu}$), two additional phases Φ_1 and Φ_2 have to be added. As a result, the PMNS matrix can be split up into three different rotation matrices (plus one diagonal matrix for the Majorana phases), and one gets

$$U_{\mathrm{PMNS}} = \begin{pmatrix} 1 & 0 & 0 \\ 0 & c_{23} & s_{23} \\ 0 & -s_{23} & c_{23} \end{pmatrix} \begin{pmatrix} c_{13} & 0 & s_{13}e^{-i\delta_{\mathrm{CP}}} \\ 0 & 1 & 0 \\ -s_{13}e^{-i\delta_{\mathrm{CP}}} & 0 & c_{13} \end{pmatrix} \begin{pmatrix} c_{12} & s_{12} & 0 \\ -s_{12} & c_{12} & 0 \\ 0 & 0 & 1 \end{pmatrix} \begin{pmatrix} 1 & 0 & 0 \\ 0 & e^{i\Phi_1} & 0 \\ 0 & 0 & e^{i\Phi_2} \end{pmatrix} , \tag{2.11}$$

where $c_{ij} = \cos\theta_{ij}$ and $s_{ij} = \sin\theta_{ij}$.

This splitting has a historical background as the single matrices represent the mixing observable in either solar, reactor, or atmospheric neutrino experiments, respectively. For the discussion of oscillation probabilities, the Majorana phases cancel and can, therefore, have no effect.

Considering the momentum of neutrinos originating from the same source to be p, one can use the ultra-relativistic approximation of the energy of a neutrino in mass eigenstate i as

$$E_\mathrm{i} = \sqrt{p^2 + m_\mathrm{i}^2} \approx p + \frac{m_\mathrm{i}^2}{2p} \approx p + \frac{m_\mathrm{i}^2}{2E}, \tag{2.12}$$

where E is the average energy of the different states. By using the plane wave approximation, the evolution of a single mass eigenstate in time can be described by

$$|\nu_\mathrm{i}(t)\rangle = e^{-iE_\mathrm{i}t} |\nu_\mathrm{i}(0)\rangle \, . \tag{2.13}$$

As the different mass eigenstates have different E_i, their evolution in time differs, which leads to differences in the observable flavour state compared to $t = 0$.

When propagating in a vacuum, the probability that a neutrino of flavour state α is transferred to state β after a time t is

$$\begin{aligned} P(\nu_\alpha \to \nu_\beta) =& \left|\left\langle \nu_\beta \middle| \nu_\alpha(t) \right\rangle\right|^2 \\ =& \left| \sum_j \sum_i U_{\beta j} U^*_{\alpha i} e^{-iE_i t} \left\langle \nu_j \middle| \nu_j \right\rangle \right|^2 \\ =& \delta_{\alpha\beta} - 4 \sum_{i<j} \mathrm{Re}\left[U_{\alpha i} U^*_{\beta i} U^*_{\alpha j} U_{\beta j}\right] \sin^2\left(\Delta m^2_{ij} \frac{L}{4E}\right) \\ &+ 2 \sum_{i<j} \mathrm{Im}\left[U_{\alpha i} U^*_{\beta i} U^*_{\alpha j} U_{\beta j}\right] \sin\left(\Delta m^2_{ij} \frac{L}{2E}\right), \end{aligned} \tag{2.14}$$

where $L \approx ct$ is the distance travelled by the neutrino and Δm_{ij} is the absolute mass squared difference between the mass states i and j [44]. Neutrino oscillation can only occur when $\Delta m^2_{ij} \neq 0$. Therefore, measuring neutrino oscillations intrinsically proved that (at least two) neutrinos must have non-zero mass. By tuning the $\frac{L}{E}$ ratio for an experiment, the appearance or disappearance effect of single neutrino flavours can be optimised to measure the mixing parameters in a range with a high sensitivity.

Eq. 2.14 is only applicable for oscillations in vacuum; for neutrinos travelling through matter, interactions with shell electrons have to be considered. This so-called Mikheyev-Smirnov-Wolfenstein (MSW) effect primarily affects ν_e and $\overline{\nu}_\mathrm{e}$ and thus differs for the various mass eigenstates [45]. The MSW effect provides a crucial mechanism for probing the masses of different eigenstates in long-baseline experiments with appropriate experimental conditions. However, up until today, no experiment has had a high enough sensitivity to determine the ordering of their masses. There are two potential scenarios, the normal ($m_1 < m_2 < m_3$) and the inverted ($m_3 < m_1 < m_2$) ordering. As neutrinos travel through Earth's crust or mantle, the MSW effect amplifies the asymmetry between neutrinos and antineutrinos due to the presence of electrons, which interact differently with these particles. A longer baseline increases the sensitivity to the neutrino mass hierarchy because the matter effects accumulate over extended distances, enhancing the differences in oscillation probabilities between the normal and inverted mass orderings.

Similarly, the presence of a non-zero and nontrivial δ_{CP} introduces an asymmetry between neutrino and antineutrino oscillations, manifesting in the probability difference between $\nu_\mu \to \nu_\mathrm{e}$ and $\overline{\nu}_\mu \to \overline{\nu}_\mathrm{e}$ transitions, which can be measured in accelerator experiments. Calculating this asymmetry ΔP with Eq. 2.14 one gets:

$$\Delta P = P(\nu_\mu \to \nu_e) - P(\bar{\nu}_\mu \to \bar{\nu}_e) = -2J^* \sin(\delta_{\mathrm{CP}}) \prod_{i<j} \sin\left(\frac{\Delta m_{ij}^2 L}{4E}\right), \tag{2.15}$$

where $J^* = \cos(\theta_{13})\sin(2\theta_{12})\sin(2\theta_{23})\sin(2\theta_{13})$.
The magnitude of CP violation in neutrino oscillations depends on the $\sin\delta_{\mathrm{CP}}$ and the mixing angles, particularly θ_{13}, which enables the sensitivity to this effect. The equation also shows that by tuning the $\frac{L}{E}$ term, the sensitivity to CP violation can be optimised. Since also the MSW effect contributes to the same asymmetry, distinguishing genuine CP violation from matter-induced asymmetry requires long-baseline measurements.

The results of the latest global fit on all oscillation parameters (NuFit 6.0) are shown in Tab. 2.1.

Table 2.1 – Global fit on the three-flavour neutrino oscillation parameter (NuFit 6.0). All data was obtained from various experiments until September 2024. In the last row, $l = 1$ for normal ordering and $l = 2$ for inverted ordering. [46]

Parameter	Normal ordering ($\pm 1\sigma$)	Inverted ordering ($\pm 1\sigma$)
θ_{12} [°]	$33.68^{+0.73}_{-0.70}$	$33.44^{+0.73}_{-0.70}$
θ_{13} [°]	$8.56^{+0.11}_{-0.11}$	$8.59^{+0.11}_{-0.11}$
θ_{23} [°]	$43.3^{+1.0}_{-0.8}$	$47.9^{+0.7}_{-0.9}$
δ_{CP} [°]	212^{+26}_{-41}	274^{+22}_{-25}
Δm^2_{21} [eV^2]	$7.49^{+0.19}_{-0.19} \cdot 10^{-5}$	$7.49^{+0.19}_{-0.19} \cdot 10^{-5}$
Δm^2_{3l} [eV^2]	$+2.513^{+0.021}_{-0.019} \cdot 10^{-3}$	$-2.484^{+0.020}_{-0.020} \cdot 10^{-3}$

Based on the latest preliminary results from a T2K and NuMI Off-Axis ν_e Appearance (NOvA) joint fit, the inverted ordering is modestly favoured but not confirmed [47]. The same analysis shows that for normal mass ordering, no clear range of possible δ_{CP} values can be excluded. For the inverted mass ordering, CP conservation ($\delta_{\mathrm{CP}} = 0, \pi$ can be excluded at a three sigma level. The reason why for inverted ordering CP conservation can be excluded at a relatively high confidence level, while for normal ordering no clear statement can be made, is due to the level of agreement (respectively disagreement) between the two individual measurements of the two experiments, as shown in Figure 2.2.

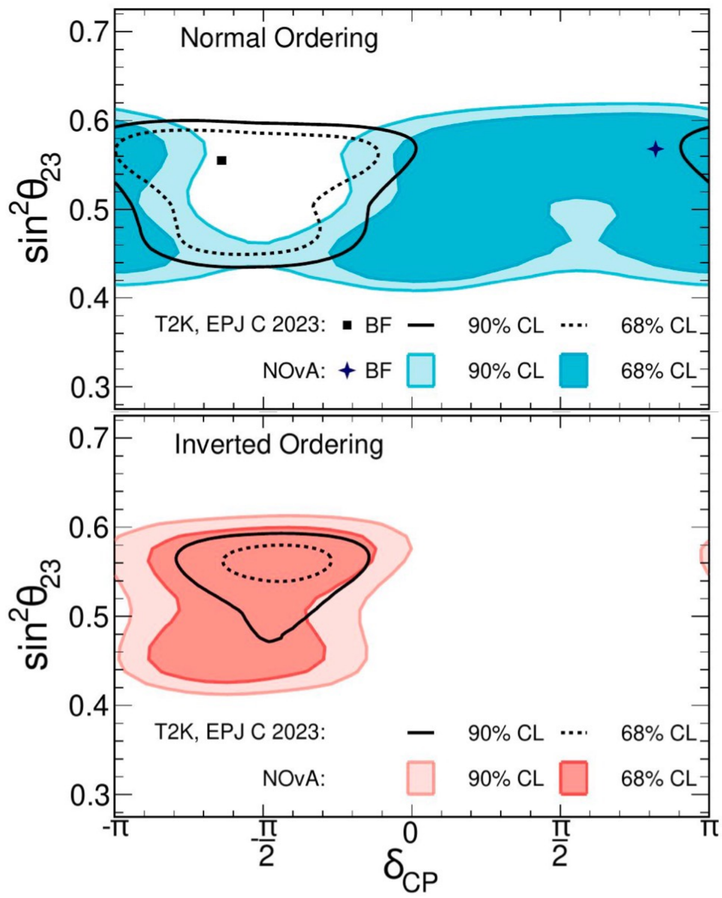

Figure 2.2 – The 68% and 90% confidence level contours in $\sin\theta_{23}$ vs. δ_{CP} in the normal mass ordering (upper plot) and inverted mass ordering (lower plot) for NOvA and T2K. [47]

2.3 The future of neutrino oscillation experiments

As shown in the previous section, the uncertainties on some of the neutrino oscillation parameters are still large. In particular, the questions of whether there is a CP violation in neutrino oscillations and how the mass eigenstates are ordered are so far unsolved. Currently operating experiments, such as NOvA and T2K, are not expected to achieve the sensitivity required to address these questions at the 5σ significance level. Thus, developing a next generation of experiments with increased sensitivity is vital for answering those questions.

Long-baseline experiments using accelerator neutrinos have excellent properties to study exactly these open questions, as the $\frac{L}{E}$ factor in Eq. 2.14 can be tuned for maximum sensitivity. Two noteworthy experiments introduced in the following are currently in development and production and aim to answer the remaining open questions: Hyper-KamiokaNDE and DUNE. Both these experiments will provide independent measurements of, in particular, the δ_{CP} value and the mass hierarchy.

Hyper-KamiokaNDE [48] is part of the ongoing KamiokaNDE experiment series in Japan. It follows the successful design of its predecessor, Super-KamiokaNDE, but features an approximately five times larger detector mass, increasing the number of expected neutrino interactions. The design includes an inner and outer vessel, where the inner will be equipped with over 20 k state-of-the-art PMTs. The outer vessel will also be equipped with light detectors, which will allow the tagging of incoming and outgoing particles from the inner vessel.

The corresponding Tokai-to-Hyper-Kamiokande (T2HK) is an upgrade of the existing T2K long-baseline experiment. Like T2K, T2HK will utilise an accelerator-driven neutrino beam produced at the Japan Proton Accelerator Research Complex (J-PARC) in Tokai and have both the near and far detectors placed off-axis. The beam infrastructure will be upgraded and operate in its final configuration at a power of approximately 1.3 MW, significantly higher than the current 750 kW used in T2K [49], increasing the neutrino event rate at the far detector. The neutrino energy spectrum will be around 600 MeV to tune the $\frac{L}{E}$ factor for maximising sensitivity to oscillation effects.

The ND280 near detector, currently used in T2K, is undergoing major upgrades, including upgraded Time Projection Chambers (TPCs) and scintillator-based tracking detectors to improve momentum and angular resolution [50]. An overview of the upgraded ND280 is shown in Figure 2.3. Additionally, an on-axis detector, INGRID, continuously monitors the beam profile and direction.
The off-axis placement of the near and far detectors is advantageous because it results in a narrower neutrino energy spectrum, reducing high-energy tails that contribute to background events. This off-axis configuration enhances sensitivity to oscillation parameters by providing a well-defined peak energy, closely matching the oscillation maximum. Furthermore, minimising contamination from high-energy neutrinos improves the accuracy of cross-section measurements, which are crucial for reducing systematic uncertainties in the experiment. [51]
With a total mass of $\sim$4 t and the off-axis positioning, the expected number of beam-related interactions in the ND280 per beam spill is low ($\mathcal{O}(1)$), and no specific design choices needed to be taken to mitigate pile-up.
The second experiment is the DUNE. Since the developments of the detector technology in this thesis were particularly motivated by this experiment, it will be elaborated in more detail in the next section.

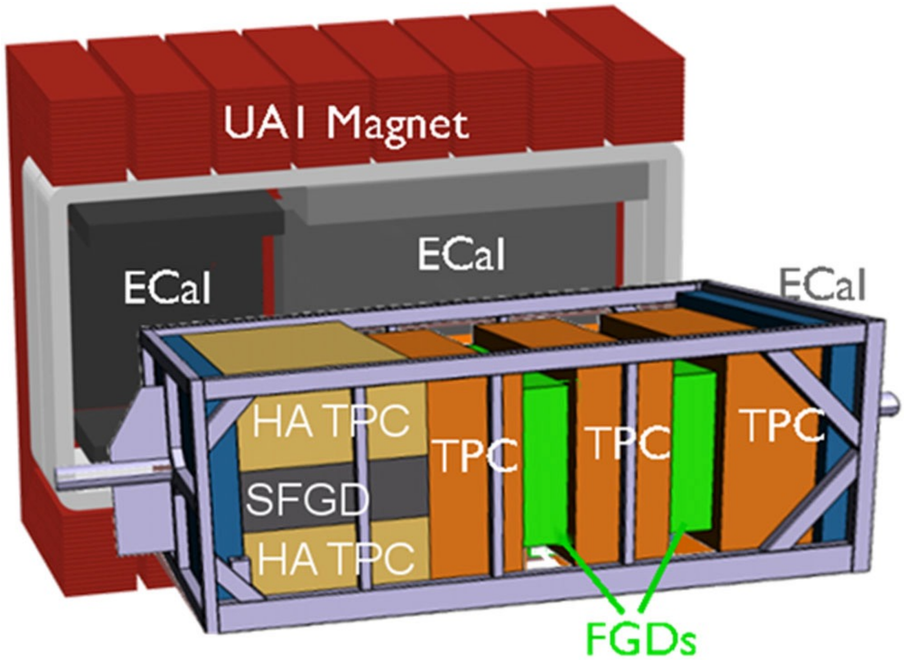

Figure 2.3 – Schematic overview of the upgraded ND280 detector used in T2K and T2HK. The detector is housed within the UA1 magnet, which provides a uniform magnetic field for momentum measurements. The upgraded part is closest to the incoming beam and consists of the Super-Fine-Grained-Detector (SFGD), which is the main tracking detector for vertex reconstruction, and the High-Angle gasTPCs (HA TPC), which can track particles at large angles. The downstream part of the detector will not be upgraded and consists of three gas TPCs interleaved with two Fine-Grained tracking Detectors (FGD). The entire detector is surrounded by Electromagnetic CALorimeters (ECALs) to track incoming and outgoing particles.

2.4 The Deep Underground Neutrino Experiment

The Deep Underground Neutrino Experiment (DUNE) is a long-baseline experiment and a general neutrino observatory currently in construction [4, 6, 7]. The experiment is hosted by Fermi National Accelerator Laboratory (Fermilab) and incorporates a Near Detector (ND) complex situated at the Fermilab main site in Batavia, Illinois (USA) and a FD complex at the Sanford Underground Research Facility (SURF) in Lead, South Dakota (USA). The DUNE collaboration plans to upgrade the existing accelerator facilities at Fermilab to produce a $\nu_\mu/\overline{\nu}_\mu$ beam with a power of 1.2 MW (with plans to upgrade to 2.1 MW in a later phase). The beam infrastructure is provided by the Long Baseline Neutrino Facility (LBNF) program. Figure 2.4a shows the comparison of the LBNF beam with other existing beam lines.

DUNE has chosen to use the LArTPC technology since it provides good reconstruction capabilities across a wide range of neutrino energies. The LArTPC technology will be discussed in detail in Chapter 3. LArTPCs can be instrumented with mm-scale readouts to provide high tracking resolution, allowing the study of complex interaction topologies. Despite certain limitations, such as undetected energy carried away by neutrons, LArT-

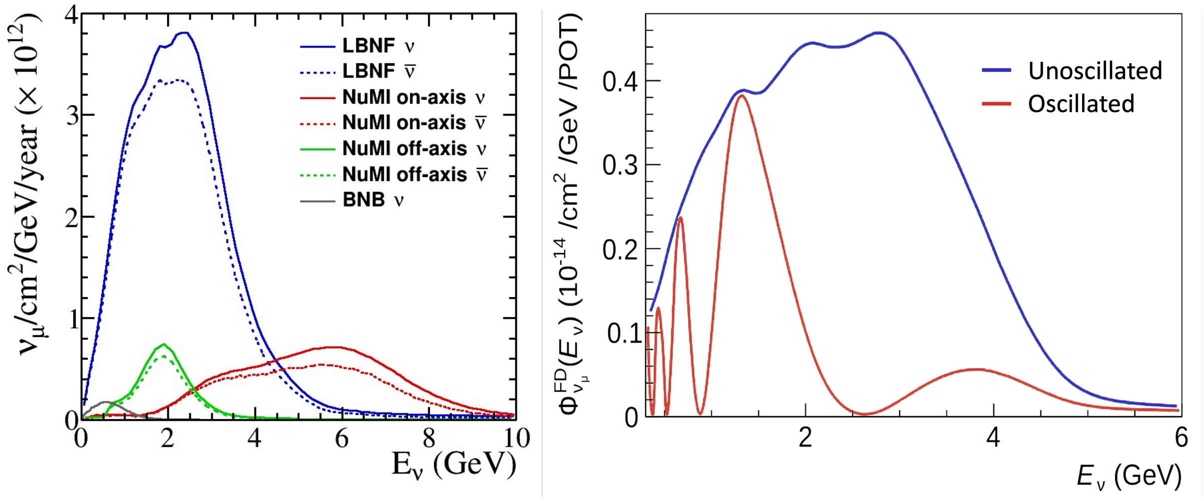

(a) **(b)**

Figure 2.4 – (a) Comparison of absolutely normalised (anti)neutrino fluxes from various Fermilab neutrino beams. LBNF denotes the beam facility built for DUNE. NuMI off-axis is the beam flux seen by the NOvA experiment [52] and BNB is the beamline used by the SBN program [53]. Figure taken from [54]. (b) Comparison of the oscillated and unoscillated beam simulated at the FD.

PCs generally achieve good energy resolution due to their capability to directly measure the deposited energy of charged particles, enabling precise calorimetric reconstruction of neutrino interactions when energy losses are properly accounted for. Together with the broadband-energy beam, this ensures sensitivity to multiple oscillation maxima as shown in Figure 2.4b, allowing for precise measurements of oscillation parameters. The sensitivity to a large energy range and a large variety of interaction modes also enables DUNE to study neutrino interactions, including those relevant for supernova neutrinos, solar neutrinos, and potential new physics signatures.

With a baseline of 1300 km and the broadband energy beam that provides access to multiple oscillation maxima, the experiment is capable of improving the precision of current oscillation parameter measurements. The high beam power and the massive FD lead to significantly improved statistical uncertainties compared to current experiments. In Figure 2.5, the expected significances for both mass ordering and non-zero CP-violation ($\delta_{\mathrm{CP}} \neq 0, \pi$) are depicted. The mass ordering is expected to be deduced at the 5σ level for any δ_{CP} value after two years of exposure. After a ten years exposure, for 50 % of possible δ_{CP} values a non-zero CP violation ($\delta_{\mathrm{CP}} \sim \pm\frac{\pi}{2}$) could be confirmed at the 5σ level.

Furthermore, positioning the FD at 1500 m below the surface significantly reduces background from cosmic radiation. This low background environment is needed for the detection of not only interactions from beam neutrinos but even more for potential supernova and solar neutrinos, broadening the scope of scientific exploration.

While the exceptionally high flux of the neutrino beam crossing the ND complex poses a major challenge for the detector technology to resolve event-pile-ups within single beam

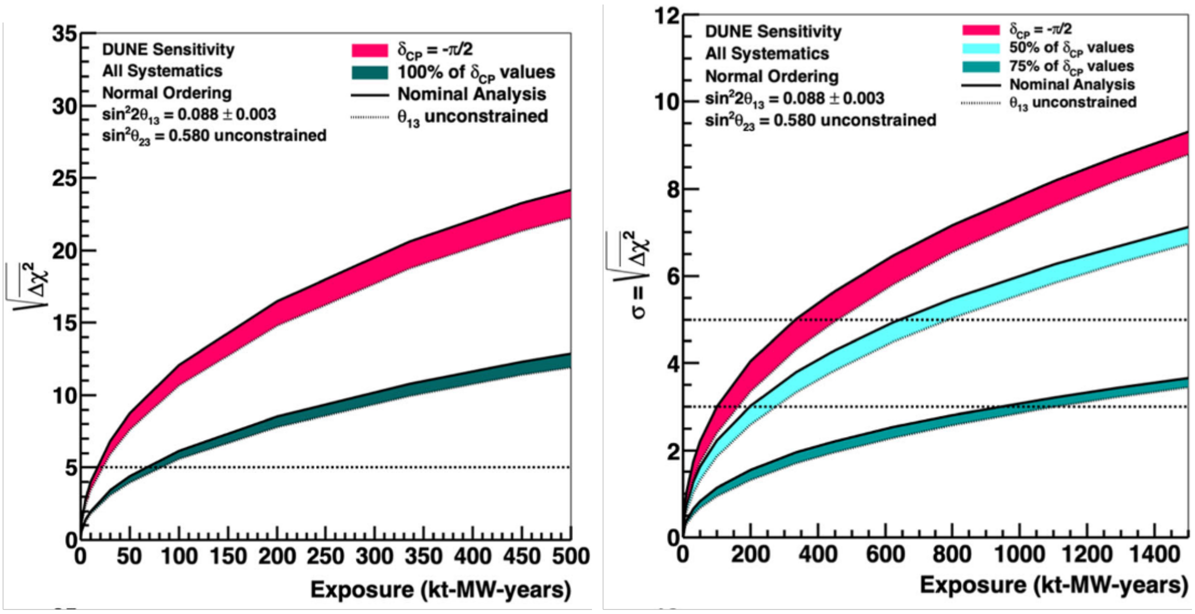

(a) (b)

Figure 2.5 – Expected significance of the DUNE experiment on (a) non-zero CP violation ($\delta_{\text{CP}} \neq 0, \pi$) and (b) mass ordering as a function of total exposure assuming normal mass ordering. The exposure is given in kt-MW-years to account for total detector mass, beam power, and exposure years. The equivalent plots assuming inverted mass ordering show similar results and are, therefore, not depicted. [55]

spills, it facilitates an unprecedented number of neutrino interaction measurements. This not only enhances the precision of neutrino cross-section measurements and thereby reduces uncertainties of the oscillation parameter measurements, but also provides a unique opportunity to explore rare Beyond-the-Standard-Model (BSM) processes in the weak sector.

In the initial phase, the DUNE FD will consist of two LArTPC detectors with a total mass of 34 kt. The expected interaction rate at the far detector can be simplified as

$$\left.\frac{\mathrm{d}N(\nu_\alpha)}{\mathrm{d}t}\right|_{\mathrm{FD}} = \int dE_\nu \; \Phi_{\mathrm{FD}}(E_\nu) \; \sigma_{\mathrm{FD}}(E_\nu) \; \epsilon_{\mathrm{FD}} \; P(E_\nu; \nu_\mu \to \nu_\alpha), \tag{2.16}$$

where Φ is the ν_α flux, σ_{FD} the neutrino cross section in the FD and ϵ_{FD} the efficiency of the FD.
A key challenge in order to make precision measurements of oscillation parameters in DUNE is to minimise systematic uncertainties. In detail, as shown in the above equation, this means reducing the uncertainties of the flux, cross-section and detector efficiency models for the FD.
To achieve this, the measurements at the ND are essential. Analogous to the FD, the ND placed close to the beam origin measures (neglecting oscillation behaviour on the short distance) the interaction rate

$$\left.\frac{\mathrm{d}N(\nu_\beta)}{\mathrm{d}t}\right|_{\mathrm{ND}} = \int dE_\nu \; \Phi_{\mathrm{ND}}(E_\nu) \; \sigma_{\mathrm{ND}}(E_\nu) \; \epsilon_{\mathrm{ND}}. \tag{2.17}$$

Although the neutrino flux at the ND differs from that at the FD, using measurements at the ND to constrain the flux model at the FD is essential. In an idealised scenario with perfect neutrino energy reconstruction and identical target materials in both detectors, the cross-section σ cancels out, eliminating its contribution to the uncertainty in the oscillation probability measurement. However, in practice, energy reconstruction is subject to smearing, meaning that the cancellation is incomplete. Nevertheless, precise cross-section measurements across the full energy spectrum at the ND enable reliable extrapolation to the oscillated flux at the FD. This approach is further enhanced by the PRISM method (explained in detail below), which involves moving the ND-LAr/TMS detector off-axis to sample narrower energy spectra. Given the high neutrino flux at the ND, the measurements are predominantly limited by systematic, rather than statistical, uncertainties.

2.4.1 Far Detector Complex

The far detector complex located in underground caverns at SURF is designed to host first two, and in a later phase four LArTPC detectors. The detectors are housed in cryostats, each with an outer dimension of approximately $66\,\mathrm{m} \times 19\,\mathrm{m} \times 18\,\mathrm{m}$ capable of holding approximately 17 kt of Liquid Argon (LAr).

The two detectors deployed in the first phase of the experiment use different design approaches. A short technical description of the two is added in the following. A detailed description of the functional principle of LArTPCs, needed to understand the technical details given here, can be found in Chapter 3.

One of the two detectors employs a single-phase horizontal-drift configuration [7] similar to the existing ICARUS [56] or MicroBooNE [57] detectors. The full volume is split into four individual drift regions, with the two cathode planes located parallel to the direction of the incoming beam. Wire-based Anode Plane Assemblies (APAs) are used to collect the charge at the end of each drift region. The 6 m high and 2.3 m wide APAs can be pre-assembled and tested before they are installed in the final cryostat structure. They are instrumented with three wire planes, oriented at 0°, $\pm 35.7^\circ$, enabling fine spatial reconstruction of neutrino interactions with millimetre-scale precision. While the first two layers only detect the drifted charge by induction, the last layer collects it. A schematic drawing of the detector is shown in Figure 2.6a.
To also collect the scintillation light created by final state particles, light collection modules are placed behind the APAs. To maximise the active LAr volume, traditional PMTs are not applicable. Hence, a total of approximately 1500 so-called X-ARAPUCA light traps are implemented. The X-ARAPUCA is an assembly of different wavelength shifting and dichroic materials, which uses a Silicon Photo Multiplier (SiPM) based readout. Due to its non-dielectric design, it could not be placed within the drift field (compared to the ArgonCube Light detector (ArCLight) detectors that will be discussed in Chapter 4).

The other detector uses a single-phase vertical-drift configuration [58]. In this design, charges will drift vertically to be read on Charge Readout Planess (CRPs) (explained in Ch. 1). Unlike the horizontal-drift detector, the vertical-drift detector has only two

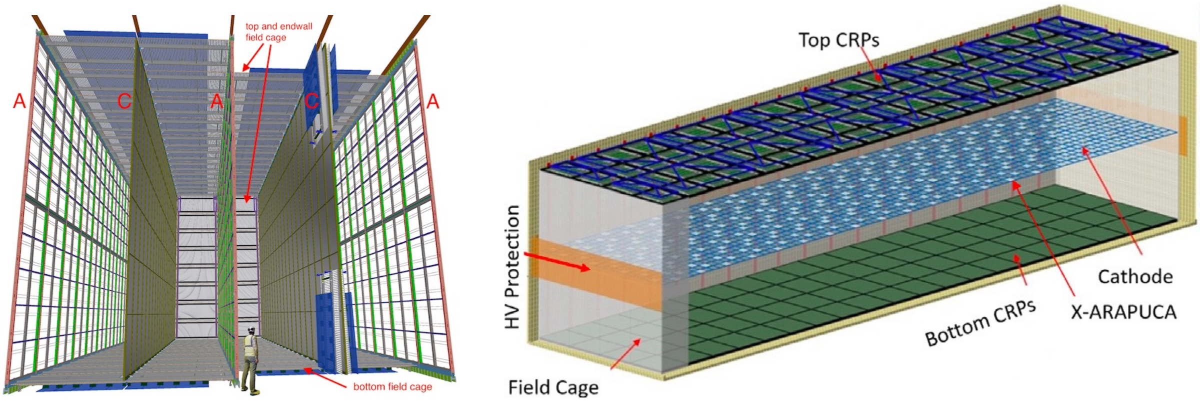

(a) **(b)**

Figure 2.6 – Schematic drawings of the (a) horizontal-drift and (b) vertical-drift detectors deployed in the first phase of DUNE. In the left drawing, the cathode and anode planes are denoted with C and A, respectively. [7, 58]

drift regions, with a cathode plane placed horizontally in the centre of the cryostat. A schematic drawing of the detector is shown in Figure 2.6b.
Due to the large opacity of the CRPs, no light collection modules could be placed behind it. Therefore, the light readout, using the same X-ARAPUCA light traps as the horizontal-drift, has to be installed on the cathode plane. Due to the large voltage present at the cathode plane, a power-over-fibre system was developed to enable the powering of the SiPMs.

Both configurations are undergoing extensive testing in the so-called ProtoDUNE program at Conseil Européen pour la Recherche Nucléaire (CERN). The horizontal-drift prototype, with a one-third scale of the full far detector, was successfully operated in 2018 [59]. Besides measuring cosmic radiation interactions, a CERN beamline was used to test the capabilities of the detector. The second prototype for the vertical-drift configuration will be tested in the same facility in early 2025.

2.4.2 Near Detector Complex

The ND complex is located 574 m downstream from the beam target in a cavern ~ 60 m underground. The complex consists of three complementary sub-detectors, the ND-LAr, Temporary Muon Spectrometer (TMS) and the System for on-Axis Neutrino Detection (SAND), each fulfilling a specific part of the requirements for the ND introduced above. The Precision Reaction-Independent Spectrum Measurement (PRISM) system allows the first two sub-detectors to be moved off-axis. An overview of the ND complex including the PRISM functionality is shown in Figure 2.7.

ND-LAr/TMS The ND-LAr has the same target material as the FD and enables direct comparisons of neutrino-argon interaction cross-sections. Thus, its key role is to reduce cross-section and detector systematic uncertainties. The LArTPC detector with a fiducial mass of 67 t is primarily optimised for hadronic containment and requires a

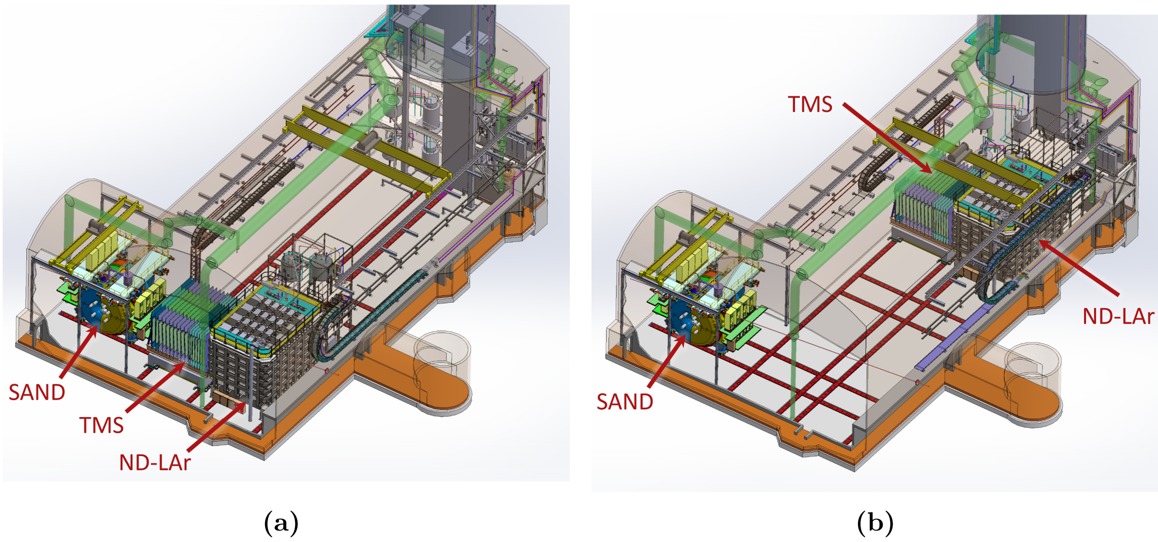

Figure 2.7 – Schematic of the Near Detector complex with all three sub-detectors - ND-LAr,TMS, and SAND - on-axis (a) and the first two moved off-axis by the PRISM system (b). [8]

secondary downstream detector to detect exiting particles. Its dimensions are chosen to have a 95% containment of hadronic showers and muons travelling laterally (but not muons exiting in the downstream direction). The intense neutrino flux present at the ND combined with the relatively high target density (compared to, e.g. the ND-280 in T2K) leads to an unprecedented neutrino pile-up environment requiring significant design changes compared to existing LArTPCs. Since this thesis specifically focuses on the development towards the ND-LAr, Chapter 3 will be dedicated to discussing its requirements and design.

The TMS installed directly downstream of ND-LAr has the primary purpose of measuring the momentum and charge of high-energy muons escaping in the downstream direction from the relatively compact ND-LAr volume. This concept is illustrated in Figure 2.8. By employing alternating layers of magnetised steel and scintillator, the TMS provides downstream tracking and energy measurement, using the muon's range through the material to determine its kinetic energy with a resolution of around 5 %, and exploiting the magnetic field to identify the muon's charge via its curvature. This functionality is crucial for correctly reconstructing neutrino events, particularly in the 0.5 GeV to 5 GeV energy range relevant for oscillation physics. Figure 2.9b shows the individual acceptance of ND-LAr and TMS, illustrating the importance of TMS for higher energetic interactions with a kinetic energy of the exiting muon above 1 GeV. Additionally, TMS ensures that ND-LAr can remain small and cost-effective by providing the necessary downstream measurement capabilities while also enabling the separation of neutrino and antineutrino interactions, vital for reducing wrong-sign background and constraining CP-violation effects.

The TMS, shown in Figure 2.9a, comprises 92 layers of magnetised steel interleaved with scintillator planes. These layers vary in thickness, increasing from 15 mm at the

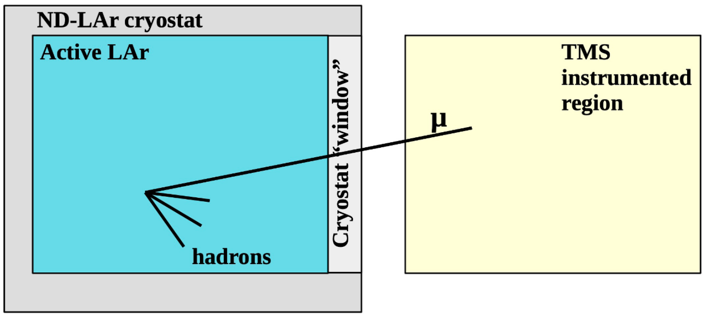

Figure 2.8 – Schematic illustrating the combined operation principle of ND-LAr and TMS. [60]

front to 80 mm at the back, ensuring adequate stopping power for muons up to 5 GeV/c while maintaining tracking precision for lower-energy muons. The magnetic field, approximately 1 T and oriented vertically, causes charged muons to bend in the horizontal plane, allowing for effective charge identification. Scintillator strips are read out via wavelength-shifting fibres coupled to SiPMs, providing precise spatial and timing resolution. The use of alternating stereo angles, along with occasional horizontal strip planes, enables accurate three-dimensional reconstruction. This design is informed by successful implementations in previous experiments, such as MINOS, and has been optimised to meet the high-rate environment and physics goals of DUNE. Together, ND-LAr and TMS form a robust near detector system capable of delivering the precision needed for long-baseline oscillation measurements.

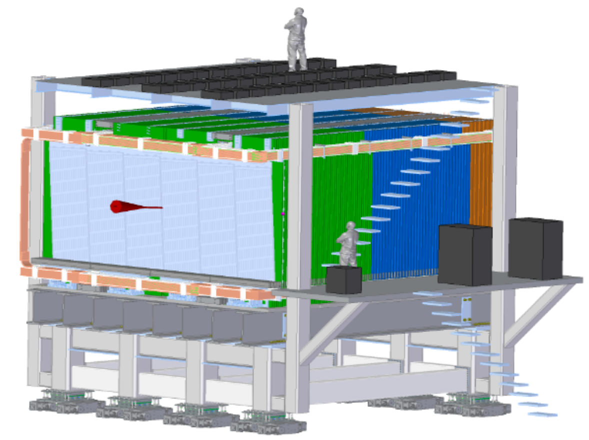

(a)

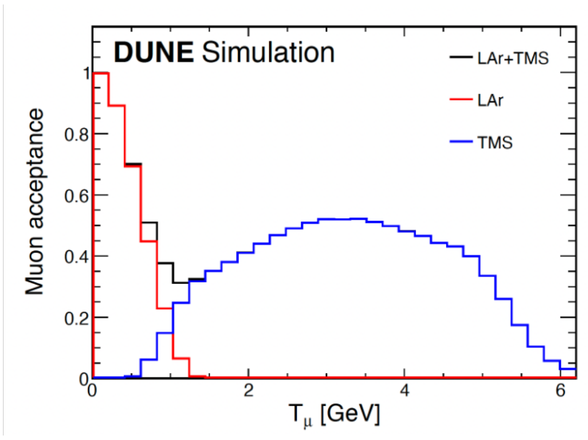

(b)

Figure 2.9 – (a) Drawing of the TMS detector design. (b) Simulation-based acceptance in ND-LAr and TMS (and together) as a function of true muon kinetic energy T_μ. [60]

For the second phase of DUNE, the TMS is planned to be replaced by the Gasous Argon Near Detector (ND-GAr) [8]. The ND-GAr detector not only consists of a High-Pressure gaseous argon TPC (HPgTPC) but also an Electro-magnetic Calorimeter (ECAL), which both together are placed in a 0.5 T magnetic field. Besides the capability to measure exiting muons from ND-LAr that already TMS has, ND-GAr has the capability of measuring charged final state particles at lower energies than the ND or FD LArTPCs. This enables the detection of lower energy neutrino interactions occurring within the HPgTPC volume and thus helps to further reduce systematic uncertainties of the long-baseline oscillation analysis.

PRISM As highlighted before, the main focus of the ND is to reduce systematic uncertainties for the oscillation measurements. The prediction of the FD beam spectrum based on the ND measurements is a significant challenge due to the broad on-axis beam energy range. The particular issue is understanding the relationship between the measured energies of final-state particles and the reconstructed energy of the incident neutrino. This relationship is highly model-dependent since undetectable or misidentified particles must be considered. The PRISM concept approaches this challenge in a novel way [8]. By moving ND-LAr and TMS/ND-GAr off-axis in a controlled manner, PRISM effectively samples different parts of the neutrino spectrum as shown in Figure 2.10. Neutrinos emitted at smaller angles relative to the beam direction tend to have higher energies, whereas those emitted at larger angles have lower energies. By combining measurements from multiple off-axis positions, PRISM enables a direct reconstruction of the oscillated far detector spectrum by applying linear combinations of different off-axis spectra without relying on model-dependent extrapolations. By reducing the issue to measurements of much narrower beam spectra, this approach provides a robust way to mitigate flux and cross-section uncertainties, improving the overall precision of the oscillation measurements.

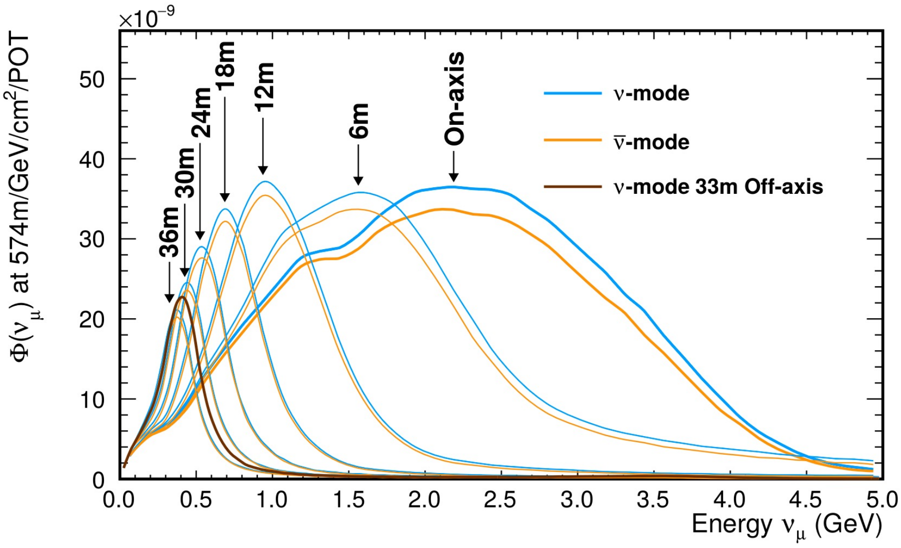

Figure 2.10 – DUNE ND energy spectra for various off-axis positions accessible by the PRISM system. [4]

ND-LAr and the spectrometer are placed on a movable support structure, enabling off-axis measurements with a narrower neutrino energy spectrum, while the beam monitor stays on the axis.

SAND SAND [8] is a permanent on-axis detector that continuously monitors the neutrino beam flux and composition. It consists of a high-granularity tracker and an ECAL placed within a 0.6 T magnetic field. The high-granularity tracker is designed to precisely reconstruct charged particle trajectories, allowing for accurate neutrino interaction vertex identification and momentum measurements. By providing real-time measurements of beam stability and flux variations, SAND ensures precise monitoring of beam variations in time, particularly when the two other detectors are moved off-axis by PRISM. The detector reuses the solenoid and ECAL from the KLOE experiment [61]. The high-granularity tracker is implemented as a Straw Tube Tracker (STT), including additional CH_2 and C target layers. An additional 1 t LAr target with an optical imaging system is planned to be placed upstream of the tracker and would add the ability to measure neutrino-argon interactions [62].

Chapter 3

A Modular Liquid Argon Near Detector for DUNE

Neutrino detection requires two fundamental components: First, a target medium in which neutrino interactions occur, leading to the production of final-state particles. Second, a detection mechanism capable of identifying and reconstructing these secondary particles. The detector development discussed in this thesis is based on the Liquid Argon Time Projection Chamber (LArTPC) technology, in which argon acts as both the interaction target and the detection medium. In the first part, this chapter provides a detailed introduction to this technology. In order to understand the physics processes involved, a basic introduction to how final state particles interact with matter is given and based on this, the working principle of LArTPCs is elucidated in detail. In Section 3.4, a review of existing LArTPC technologies is given based on former experiments.

For the application of the LArTPC technology in the DUNE ND, a novel modular detector design is applied. This modular approach, developed in the so-called ArgonCube concept, brings major advantages in the high-intensity environment of DUNE's LBNF beam. The second part of this chapter outlines the dimension requirements, introduces the modular ArgonCube concept adopted for ND-LAr, and summarises the extensive prototyping campaign conducted to validate the detector design and ensure robust performance.

3.1 Final state particles in matter

In the following, the fundamental processes by which particles interact with matter are reviewed. The discussion will primarily focus on electromagnetically interacting particles, as these are of particular relevance for LArTPCs.

3.1.1 Interaction of charged particles

For charged particles, the key interaction mechanisms relevant in the context of LArTPCs is the inelastic scattering with atomic electrons, which can lead to excitation or ionisation of the atom. The energy loss per unit distance travelled by a charged particle with a mass significantly greater than that of an electron ($m >> m_e$) is well described by the Bethe-Bloch formula, which quantifies the ionisation energy loss as a function of the particle's velocity and the properties of the medium:

$$-\left\langle \frac{dE}{dx} \right\rangle_{\text{ion.}} = Kz^2 \frac{Z}{A} \frac{1}{\beta^2} \left[\frac{1}{2} \text{Ln} \left(\frac{2m_e c^2 \beta^2 \gamma^2 T_{\text{max}}}{I^2} \right) - \beta^2 - \frac{\delta}{2} \right], \tag{3.1}$$

where

- $K = 4\pi N_{\text{A}} r_e^2 m_e c^2 \approx 0.307\,\text{MeV}\,\text{cm}^2/\text{mol}$ is a constant,
- z the charge of the incident particle,
- Z the atomic number of the medium,
- A the atomic mass of the medium,
- $\beta = \frac{v}{c}$ the velocity of the incident particle,
- $\gamma = \frac{1}{\sqrt{1-\beta^2}} \approx \frac{E}{m_0 c^2}$ the Lorentz factor of the incident particle,
- m_e the electron mass,
- I the mean excitation energy in the medium,
- T_{max} the maximum kinetic energy which can be transferred to an electron in a single collision,
- δ a density correction factor (because of electromagnetic screening effects in the medium relevant at high $\beta\gamma$).

Figure 3.1 presents the energy loss of an incident muon in argon as described by the Bethe-Bloch formula. The plot reveals the presence of a minimum in the ionisation energy loss. In liquid argon (LAr), this minimum occurs at approximately 2.1 MeV/cm. A charged particle exhibiting this characteristic energy loss is referred to as a minimum ionising particle (MIP).
If the momentum of a particle falls below that of a Minimum Ionising Particle (MIP), the energy loss rapidly increases due to the $1/\beta^2$ term until the particle eventually stops. This phenomenon, where a large amount of energy is deposited within a relatively short distance, is called the Bragg peak.

For very high relativistic incident particles, radiative energy losses become dominant over the inelastic collisions with shell electrons. The threshold where the stopping power of the two processes is equal, the so-called critical energy $E_{\text{crit.}}$, is at 483 GeV [64] for muons in liquid argon and even much higher for hadrons.

For incident electrons (and positrons), two things need to be considered. Due to the unfulfilled $m >> m_e$ assumption, the Bethe-Bloch formula (Eq. 3.1) needs to be adapted and results in a much more uniform stopping power relative to the momentum of the incident particle. Also, as $E_{\text{crit.}}$ lies much lower at $\mathcal{O}(10\,\text{MeV})$, radiative energy loss becomes dominant at much lower energies.

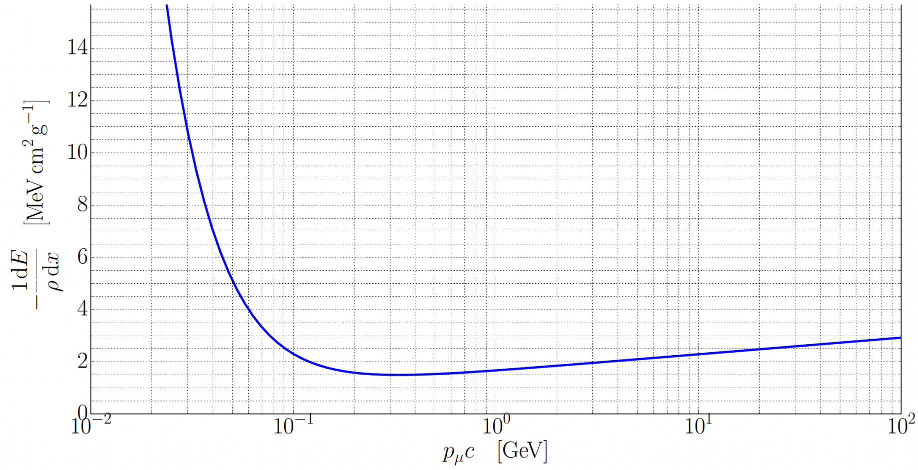

Figure 3.1 – Energy loss of a muon per distance travelled in argon due to ionisation, calculated using the Bethe-Bloch formula (without density correction δ). Figure taken from [63].

The radiative energy loss, also called Bremsstrahlung, is due to the interaction of the incident particle with the Coulomb field of the nuclei (or shell electrons for incident electrons) in the medium through the interaction shown in Figure 3.2. The energy loss per distance can be parametrised as

$$-\left\langle \frac{dE}{dx} \right\rangle = \frac{E}{X_0}, \tag{3.2}$$

where X_0 is the so-called radiation length characterising the stopping power of the medium. For LAr the radiation length is 14.0 cm [65].

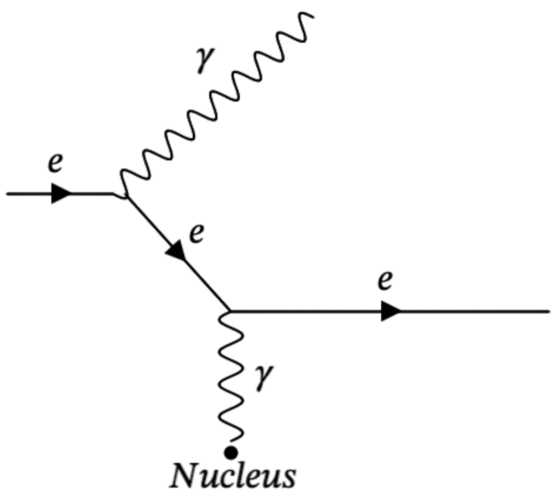

Figure 3.2 – Feynman diagram of the Bremsstrahlung process

3.1.2 Interaction of photons

In the context of the experiments described in this thesis, photons with energies below the ionisation energy (E_γ<15.7 eV or λ>79.0 nm for Argon) produced in primary neutrino interactions are negligible for calorimetric measurements. However, photons in this energy range produced through scintillation processes play an important role in the event reconstruction of LArTPC. Therefore, one particular effect such photons are subject to should be mentioned here: Rayleigh scattering occurs when photons interact elastically with shell electrons of atoms in the medium, leading to a change in their propagation direction without significantly altering their energy. In liquid argon, this effect influences the spatial distribution of scintillation light, affecting the timing and position resolution of light detection systems. The characteristic scattering length, which depends on the refractive index and wavelength of the photon, dictates how frequently these scattering events occur. Since Rayleigh scattering is more pronounced for shorter wavelengths, it impacts the transport of the Vacuum Ultra Violet (VUV) scintillation light in LAr. A detailed discussion of the scintillation process is given in Section 3.2.
High-energetic photons with energies at $\mathcal{O}$(MeV) play an important role in LArTPCs. Although they do not leave a direct ionisation track in the argon, they can induce the production of secondary charge particles and contribute significantly to the calorimetric measurement. Similar to Equation 3.2, an attenuation length λ_0 can be introduced to parametrise the intensity loss after a distance x as

$$I(x) = I_0 \cdot e^{-\frac{x}{\lambda_0}}. \tag{3.3}$$

Figure 3.3 illustrates the inverse of the radiation length $\mu = 1/\lambda_0$ for the three different processes in gaseous argon. In the following the three mechanism through which photons can produce secondary charged particles are elucidated.

Ordered by dominance relative to the photon's energy, the first process is the photoelectric effect. When a photon possesses energy exceeding the ionisation threshold of an atom in the absorber medium, it can transfer its entire energy to an atomic electron and eject the electron from its bound state. This effect is called the photoelectric effect. It primarily occurs in the inner atomic shells (e.g., K-shell or L-shell), where binding energies are relatively high. The kinetic energy (E_e) of the ejected electron is given by:

$$E_e = E_\gamma - B, \tag{3.4}$$

where E_γ is the incident photon energy, and B is the binding energy of the electron in the atom.
Since the photon transfers all of its energy to the electron, the photoelectric effect does not involve a scattered photon. Instead, the entire photon energy is either used to free the electron or converted into the kinetic energy of the ejected electron.

At around 100 keV, Compton scattering becomes dominant. In this interaction, an incident photon undergoes an inelastic scattering with a shell electron in the absorber medium. As a result, the photon transfers part of its energy to the electron, ejecting it from the atom, while the photon itself is scattered at an angle θ with reduced energy.

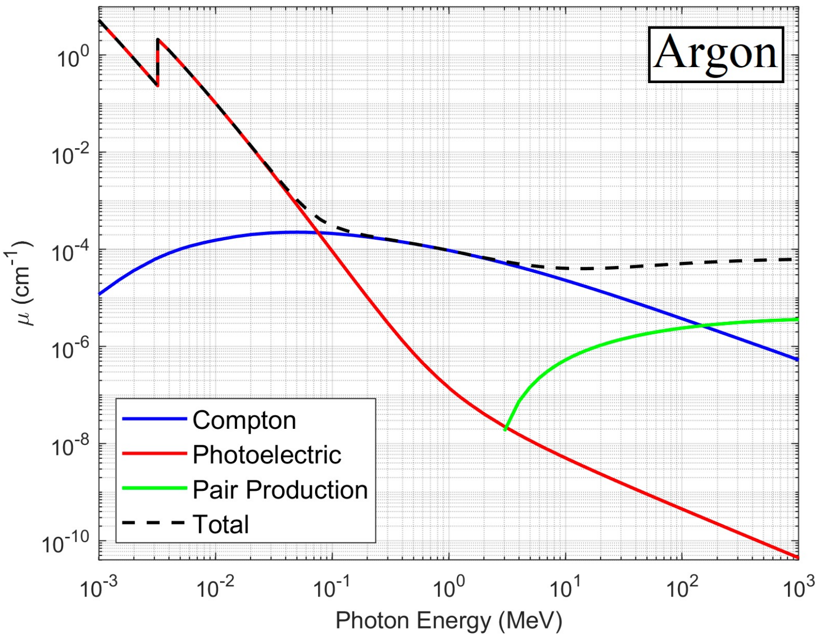

Figure 3.3 – Attenuation coefficient for high-energetic photons in gaseous argon with the individual contributions from the photoelectric effect, Compton scattering and pair production. [66]

The energy of the ejected electron, E'_γ, is given by

$$E'_e = E_\gamma \left(1 - \frac{1}{1 + \frac{E_\gamma}{m_e c^2}(1 - \cos\theta)} \right), \tag{3.5}$$

where E_γ is the energy of the incident photon and θ is the scattering angle of the photon.

As soon as a photon reaches the energy equivalent to the rest mass of $2 \cdot m_e$ and the electromagnetic field of a nucleus is present, the photon can convert into an electron-positron pair. In this so-called pair production, the excess photon energy above the 1.022 MeV threshold is distributed to the kinetic energy of the produced electron and positron. Since pair production requires the conservation of energy and momentum, it cannot occur in free space and must take place in the Coulomb field of a nucleus. The nucleus absorbs the recoil momentum, ensuring conservation laws are satisfied.

3.1.3 Electromagnetic Showers

For highly energetic photons, the resulting electron and positron themselves enter an energy regime where they emit additional photons through Bremsstrahlung or annihilation. This particle multiplication process can trigger a cascade effect, commonly referred to as electromagnetic showering. Since the photon attenuation length λ_0 and the radiation length X_0 are almost identical, the number of particles in an electromagnetic shower approximately doubles with each radiation length. The multiplication continues until the

electron energies drop below $E_{\text{crit.}}$, below which ionisation losses start dominating. For liquid argon, $E_{\text{crit.}} = 38.0\,\text{MeV}$ [44]. At each stage of the shower, the number of particles increases while the average energy per particle decreases.
The number of particles N at a given shower depth t (measured in units of radiation length X_0) follows an exponential growth, described by:

$$N(t) = 2^t, \tag{3.6}$$

where the shower maximum occurs. The shower depth at this maximum, t_{max} can be estimated by

$$t_{\text{max}} = \frac{\ln\left(\frac{E_\gamma}{E_c}\right)}{\ln(2)}, \tag{3.7}$$

where E_γ is the initial photon energy. Beyond the shower maximum, energy loss is dominated by ionisation and Compton scattering, causing the shower to dissipate gradually. An approximation for the length at which 95% of the shower is contained is given by

$$X_{95} \approx X_0 \left(t_{\text{max}} + 0.08Z + 9.6\right) \ \text{[67]}. \tag{3.8}$$

E.g. for a 500 MeV photon $X_{95} \approx 206\,\text{cm}$. This expression provides an estimate of the shower length required for full energy containment.
The transverse width of an electromagnetic shower at its maximum can be approximated by the Molière radius, given by

$$r_{\text{Mol.}} = \frac{21.1\,\text{MeV}}{E_{\text{crit.}}} X_0. \tag{3.9}$$

$r_{\text{Mol.}}$ defines the region within which approximately 90 % of the shower's energy is deposited. To achieve 95 % energy containment, a transverse width of $2r_{\text{Mol.}}$ must be considered. Importantly, the Molière radius depends only on the medium's properties—specifically, the radiation length X_0 and the critical energy $E_{\text{crit.}}$. It is independent of the initial energy of the primary particle. For liquid argon (LAr), the Molière radius is $r_{\text{Mol.−LAr}} = 9.04\,\text{cm}$ [65].

3.1.4 Hadronic showers

For hadronic interactions, highly energetic hadrons, such as protons, neutrons, or pions, undergo multiple nuclear collisions and can lead to the production of secondary particles and the development of a hadronic shower. Unlike electromagnetic showers, which primarily involve bremsstrahlung and pair production, hadronic showers consist of a mixture of nuclear interactions, particle decays, and secondary electromagnetic sub-showers. The primary hadron interacts inelastically with nuclei in the medium, producing mesons, baryons, and nuclear fragments. Among these, neutral pions π^0 decay rapidly into photons, initiating electromagnetic cascades within the hadronic shower.
Since the nuclear interaction length λ_{I} determines the typical scale of hadronic interactions, the number of particles in a hadronic shower approximately doubles with each interaction length ($\lambda_{\text{I}} \approx 85.7\,\text{cm}$ for LAr [65]). The multiplication process continues until the secondary particles' energies drop below the pion critical energy $E_{\pi,\text{crit.}}$, where ionisation losses become the dominant energy loss mechanism. At each stage of the shower,

the number of particles increases while the average energy per particle decreases. The shower depth at this maximum in units of λ_{I} can be estimated by

$$t_{\max} \approx 0.2 \ln\left(E_{\mathrm{h}}\right) + 0.7, \tag{3.10}$$

where E_{h} is the initial hadron energy in GeV [68]. Beyond the shower maximum, energy loss occurs mainly through ionisation, nuclear fragmentation, and neutron interactions, leading to the gradual dissipation of the shower. An approximation for the length (in units of λ_{I}) at which 95 % of the shower energy is contained is given by

$$\lambda_{95} \approx \lambda_{\mathrm{I}} \left(t_{\max} + E_{\mathrm{h}}^{0.3}\right) [68]. \tag{3.11}$$

E.g. for a 0.5 GeV hadron, $\lambda_{95} \approx 118$ cm.

3.2 LArTPC Detection principle

LArTPC tracking detectors are being employed to meet the requirements of future neutrino experiments as they provide a high-density target that combines precise tracking and calorimetry. In this section, the working principle of a LArTPCs is described.
A Time Projection Chamber (TPC) is a 3D tracking detector based on a noble gas or liquid as the sensitive medium. The concept was first proposed by Charpak et al. in 1970 [69], and later realised and named TPC by David Nygren in 1974 [70]. A schematic depicted in Figure 3.4 illustrates the detection principle.

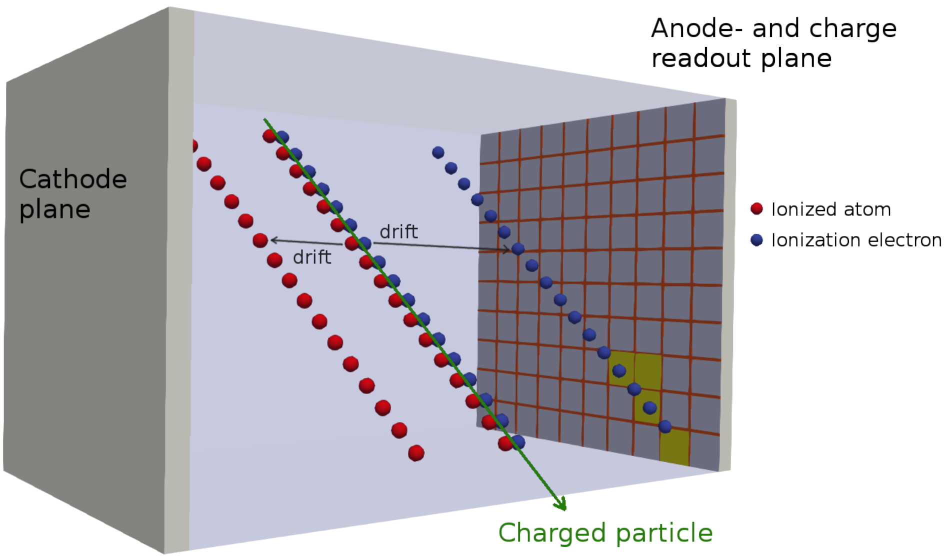

Figure 3.4 – Scheme of the LAr TPC detection principle. A charged particle crossing the detector (green) leaves a track of ionised atoms (red) and free electrons (blue). The electrons drift towards the anode, which hosts the charge readout, and get detected. Here, a pixelated charge readout is illustrated. [13]

A TPC consists of two planes, a cathode and an anode plane, that are held at different potentials, forcing free charged particles in the medium to drift in one or another direction. When a charged particle crosses the active volume of a TPC, it loses kinetic energy through ionisation as described in the Bethe-Bloch formula (Eq. 3.1) and leaves a track of ionised atoms and ionisation electrons. In the electric field between the cathode and the anode of the TPC, the ionised atoms and ionisation electrons drift in opposite directions, preventing them from recombining instantly. If the lifetime of a free ionisation electron in the medium is long enough, the electrons can drift all the way to the charge readout plane. Therefore, only noble gases or liquids can be applied as the sensitive medium since only those can provide a long electron lifetime due to their low electronegativity. The timing information of the charge arriving at the readout plane enables the conversion of the projection on the anode plane into three-dimensional information. However, by measuring only the collected charge, the absolute position of the reconstructed track in the drift direction is unknown. This issue can be solved by also measuring prompt scintillation light that occurs within $\mathcal{O}$(ns) after the interaction. Since the drift velocity is known, the delay ΔT between the obtained timestamp, T_0, of the scintillation light and the charge arrival time at the anode, can be used to set the coordinate position of the interaction within the TPC volume. An external trigger can replace the scintillation timestamp if it can provide the exact timing of the interaction, e.g. a precise beam trigger. Any uncertainty in T_0 is reflected in an uncertainty of the drift coordinate of a track.

In 1974, Willis and Radeka started using LAr in ionisation chambers [71]. Two years later, Herbert H. Chen et al. proposed the use of LArTPCs to study neutrino-electron scattering [9]. LAr has excellent properties to study neutrino interactions in TPCs. A list of the main properties relevant to the application in a TPC is given in Tab. 3.1. In particular, LAr has a high density of $1399\,\mathrm{kg/m^3}$, which helps to overcome the low neutrino cross-section. The presence of argon in earth's atmosphere (0.93 % [72]) and the fact that it is widely used in industry makes it cheaply available in large amounts and thus applicable for large-scale detectors (compared to xenon). Argon has its boiling point at $\sim 87\,\mathrm{K}$ (at atmospheric pressure), which requires a cryogenic detector setup with proper isolation and cooling for LAr applications.

In order to enable an accurate charge readout, the ionisation and charge transport properties are crucial.

The energy deposited through ionisation can be quantified by the total amount of charge collected. Thus, the required energy per electron-ion pair W_i sets the theoretical maximum on the possible energy resolution by charge collection. The resolution expressed as the Full Width at Half Maximum (FWHM) is

$$\delta_\mathrm{E} = 2.35\sqrt{F\frac{W_\mathrm{i}}{\Delta E}}, \tag{3.12}$$

where F is the Fano factor (see Tab. 3.1) and ΔE is the deposited energy. For LAr, W_i is $23.6\,\mathrm{eV}$, which yields 9k electron-ion pairs per mm for a MIP.

Due to the recombination of produced electron-ion pairs, not the full charge produced arrives at the readout plane. The amount of charge that can be collected (assuming zero

Symbol	Property	Value
ρ_{BP}	Density (@ boiling point)	1399 kg/m^3 [73]
T_{B}	Boiling point (@ 1 bar)	87.30 K [73]
X_0	Radiation length	14.0 cm [65]
W_{i}	Required energy per electron-ion pair	23.6 eV [74, 75]
F	Fano factor	0.107 [76]
μ	Electron mobility (@ E=500 V/cm)	329.66 cm^2/Vs [77–80]
v	Electron drift velocity (@ E=500 V/cm)	0.165 cm/µs [77–80]
λ	Scintillation emission wavelength	128 nm [81]
$W_{\mathrm{ph,max}}$	Required energy per photon (@E=0)	19.5 eV [82]
L_{R}	Rayleigh scattering length	55 cm to 95 cm† [83–86]
D_{L}	Longitudinal diffusion coefficient	6.82 cm^2/s [87, 88]
D_{T}	Transverse diffusion coefficient	13.16 cm^2/s [87, 89]

Table 3.1 – List of liquid argon properties. †The measured Rayleigh scattering length varies greatly between the values obtained in ProtoDUNE and measurements done in dark matter experiments. Thus, not a single value can be stated here.

ion mobility) can be described by the so-called modified-box model as

$$Q = Q_0 \cdot \frac{Ln(\alpha + \frac{dE}{dx}\frac{\beta}{\rho\epsilon})}{\frac{dE}{dx}\frac{\beta}{\rho\epsilon}}, \tag{3.13}$$

where Q_0 is the initially produced charge by ionisation and $\alpha = (0.93 \pm 0.02)$, $\beta = (0.212 \pm 0.002)\,\mathrm{kV\,g/(cm\,cm^2\,MeV)}$ are model parameters [90]. The model shows that with a stronger drift field, more charge can be collected. Furthermore, the fraction of charge that arrives at the readout plane is reduced by impurities, as free electrons can attach to them. Impurities with high electronegativity can reduce the mean electron lifetime in LAr drastically; in the worst case, no tracks are observable.

The velocity of an electron in an electric field in a medium is $v = \epsilon \cdot \mu$, where μ is the electron mobility in the medium. E.g. for $\epsilon = 500\,\mathrm{V/cm}$ and a maximum drift length of 50 cm, the maximum drift time of an electron is 303 µs. Within this time, the electrons also move in the transverse direction to the drift direction due to diffusion. Also, in the drift direction, diffusion causes smearing in the electron velocity and, thus, a coordinate smearing. Depending upon its magnitude, diffusion can limit or enhance the spatial resolution of the charge readout. The smearing due to diffusion for a drift time t is

$$\sigma_{\mathrm{L/T}} = \sqrt{2D_{\mathrm{L/T}}t}, \tag{3.14}$$

where $D_{\mathrm{L/T}}$ is the the longitudinal or transversal diffusion coefficient, respectively [91]. Thus, at the same field strength, shorter drift lengths reduce the effect of diffusion.

The scintillation process in liquid argon emits light at a single peak around 128 nm. The photon emission is induced by the decay of the singlet or triplet state of an excited dimer. Thus, also two decay time constants are observable, a fast time component in $\mathcal{O}(5\,\mathrm{ns})$

and a slow component in $\mathcal{O}(1.5\,\mu\text{s})$ [92]. These excited dimer states can be induced by directly excited atoms A^*

$$\begin{aligned} A^* + A + A &\rightarrow A_2^* + A, \\ A_2^* &\rightarrow 2A + h\nu, \end{aligned} \tag{3.15}$$

or by recombination of ionised atoms A^+

$$\begin{aligned} A^+ + A &\rightarrow A_2^+, \\ A_2^+ + e^- &\rightarrow A^{**} + A, \\ A^{**} &\rightarrow A^* + heat, \\ A^* + A + A &\rightarrow A_2^* + A, \\ A_2^* &\rightarrow 2A + h\nu, \end{aligned} \tag{3.16}$$

where $h\nu$ represents an emitted VUV photon and *heat* denotes a non-radiative de-excitation [82]. Singlet and triplet states can be formed through both of the processes, however, not at the same rate [93]. Due to the low binding energy of A_2 of 12.3 meV, a non-negligible fraction of the Argon atoms is permanently in a dimer state, which could lead to reabsorption of the scintillation light [94]. However, the binding energy of the A_2^* state is significantly stronger than that of A_2. This leads to a massive Stokes' shift, and thus, reabsorption hardly ever occurs.

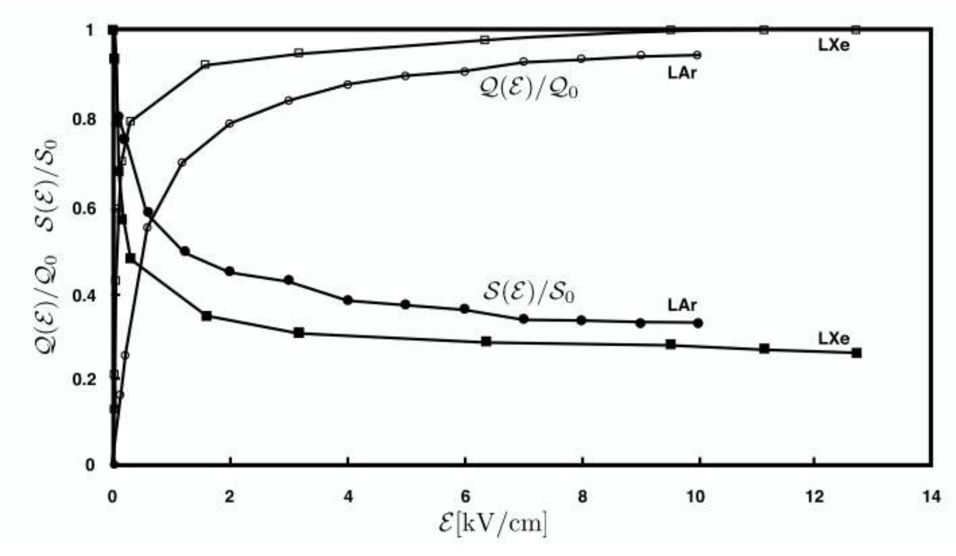

Figure 3.5 – Ionisation (non-filled symbols) and scintillation yield (filled symbols) in LAr and liquid xenon (LXe). $S(\epsilon)/S_0$ is the relative light yield to zero-field conditions and $Q(\epsilon)/Q0$ is the relative ionisation yield compared to infinite-field conditions. Used with permission of IOP Publishing, Ltd, from [82]; permission conveyed through Copyright Clearance Center, Inc.

As the scintillation process can be induced by recombination (Eq. 3.16), any process reducing the recombination rate reduces the light yield. Thus, applying an electric field reduces the number of photons that can be collected at the light detectors [82]. At the same time, the amount of collected charge increases. This anti-correlation is shown in

Figure 3.5.

In the absence of an electric field, ideally, each produced electron-ion pair undergoes recombination and produces a VUV photon. Since additionally VUV photons can be produced through direct excitation, the average energy needed to produce one photon $W_{\mathrm{ph}}(\epsilon = 0) = (19.5 \pm 1.0)\,\mathrm{eV}$ is lower than W_{i} [82]. Besides providing the timing information, the scintillation light can be used to perform calorimetry.

Similar to the charge collection, impurities in the LAr can have a significant impact on the scintillation light. One particular to mention here is nitrogen. Nitrogen impurities in liquid argon can significantly impact scintillation light yield and timing characteristics by introducing additional non-radiative de-excitation channels. Even at low concentrations in $\mathcal{O}(1\mathrm{ppm})$, nitrogen molecules can quench the argon excimer states by efficiently absorbing the excitation energy and dissipating it without photon emission [95]. This quenching primarily affects the slow triplet component of the scintillation light, leading to a reduction in overall light yield and a reduction of the slow scintillation component.

3.3 General requirements on charge and light detectors for LArTPCs

The fundamental principles of TPCs and the properties of LAr as a detection medium impose specific requirements on charge and light readout systems. These requirements are further shaped by the operational environment and the sensitivity needed for a given experiment. The following discussion outlines general design considerations for charge and light detection in LArTPCs.
The charge readout of a LArTPC must be capable of measuring small charge deposits with high spatial resolution. For a MIP traversing the detector, the amount of collectable charge per unit track length can be estimated using Eq. 3.13 as:

$$\begin{aligned}
\frac{\mathrm{d}Q}{\mathrm{d}x} &= \frac{\left(\frac{dE}{dx}\right)_{\mathrm{MIP}}}{W_{\mathrm{i}}} \frac{Ln\left[\alpha + \frac{\beta}{\rho\epsilon} \cdot \left(\frac{dE}{dx}\right)_{\mathrm{MIP}}\right]}{\frac{\beta}{\rho\epsilon} \cdot \left(\frac{dE}{dx}\right)_{\mathrm{MIP}}} \cdot e && (3.17)\\
&\approx \frac{2.1\,\mathrm{MeV/cm}}{23.6\,\mathrm{eV}} 0.71 \cdot e && (3.18)\\
&\approx 6.3 \times 10^{3}\,\mathrm{e/mm} && (3.19)\\
&\approx 1.0\,\mathrm{fC/mm}, && (3.20)
\end{aligned}$$

for a $\epsilon = 500\,\mathrm{V/cm}$ drift field.

Increasing the number of readout channels per unit anode area reduces the charge collected by each individual channel, thereby necessitating higher sensitivity for each channel. Simultaneously, the density of readout channels directly determines the spatial resolution of the system. Traditionally, for the charge collection, wire-based readout systems were used, where multiple layers of wires are arranged at different orientations. By correlating charge signals from different layers, a 3D particle interaction can be reconstructed from multiple 2D projections. While this method has proven effective in several experiments, its intrinsic ambiguities can become limiting in high-energy, high-multiplicity environments where overlapping events occur.

The purpose of the light detection system is to provide accurate timing information, which requires it to be sensitive to the LAr scintillation light at 128 nm. Given the high photon yield of approximately 4.7×10^4 photons per cm for a MIP (at $\epsilon = 500\,\mathrm{V/cm}$), a relatively low Photon Detection Efficiency (PDE) ($\mathcal{O}(1\,\%)$) can suffice for timing measurements. However, detecting VUV photons directly is challenging, necessitating the use of Wavelength Shiftings (WLSs) materials to shift them to the visible spectrum. PMTs coated with WLS, such as Tetraphenyl Butadiene (TPB), can achieve a reasonable PDE ($\approx 6.5\,\%$ [96]). Despite their advantages, PMTs present drawbacks, including high voltage operation (typically around 1 kV) and significant space requirements within the detector volume.
Beyond providing a T_0 reference for track reconstruction, which requires $\mathcal{O}(\mu\mathrm{s})$ resolution, the light detection system also plays a crucial role in distinguishing overlapping interactions. In high-multiplicity environments, multiple particle interactions can occur within a short time frame, leading to an overlap of ionisation tracks due to their relatively slow drift towards the anode plane. By leveraging precise scintillation light timing and spatial information to match occurring ionisation tracks with a precise interaction time, it is possible to separate interactions that would otherwise be indistinguishable based solely on charge readout. Retrieving spatial information from the light signal gets complicated for large detectors due to Rayleigh scattering. Advanced light collection and timing techniques, such as segmented photon detection systems or fast-timing photosensors, can significantly improve event reconstruction in these conditions. These techniques will be discussed in Chapter 4.

The cryogenic operating conditions of LArTPCs impose further constraints on both charge and light detection systems. All components must remain mechanically and electronically stable at cryogenic temperatures, and materials used in the detector must be carefully selected to accommodate differing thermal expansion coefficients. Failure to account for these effects could lead to structural damage during cool-down or warm-up cycles. Further, any heat dissipated in the liquid argon needs to be compensated by active cooling. Thus, electronic readout components placed inside the detector need to be optimised for minimal power consumption.

3.4 Review of former LArTPC experiments

Over the past few decades, LArTPCs have been extensively studied and successfully implemented in various neutrino experiments. The following section provides a brief review of these experiments, summarising the current state of LArTPC technology and its applications. This is a purely technological review; no physics motivation or outcome will be discussed.
The first ever operated large-scale LArTPC, the Imaging Cosmic And Rare Underground

Signals (ICARUS) T600, pioneered several technologies that have shaped current detector designs. Following three decades of prototyping, the detector was successfully built and operated at Gran Sasso Laboratory between 2004 and 2013 [56, 97], and subsequently moved to Fermilab as part of the SBN programme [98], ICARUS demonstrated long-term operational stability and introduced a three-wire plane charge readout system, where the first two planes, oriented at specific angles relative to each other, provide two-dimensional position measurements, and the third plane collects charge signals, enabling precise spatial reconstruction of particle trajectories. For the operation at Fermilab, its light readout system was refurbished by installing new PMTs along with a laser-based calibration system, which delivered short light pulses to all PMTs, significantly improving their timing response calibration [99, 100].

The smaller-scale Argon Neutrino Teststand (ArgoNeuT) detector was operational from 2009 to 2010, and marked the first LArTPC in the United States at Fermilab. It contributed extensively to neutrino cross-section measurements. Although ArgoNeuT lacked internal photon detection, relying instead on external scintillator planes for event timing, its results provided essential data and insights into neutrino cross-sections with argon [101].

In 2014, the ArgonTube experiment at the University of Bern first demonstrated the implementation of a LArTPC with a drift distance of over 5 m, playing a crucial role in testing the feasibility of detectors with extended drift lengths [102]. Using a Greinacher voltage multiplier stack directly attached to the TPC, the experiment probed HV stability and performed studies of the electron lifetime in liquid argon using ionisation tracks generated by a UV laser [103].

Based on the experiences with these detectors, the Micro Booster Neutrino Experiment (MicroBooNE) was constructed at Fermilab [57]. The primary physics goal of MicroBooNE was to investigate the nature of the low-energy electron-like events previously observed by MiniBooNE [104], aiming to clarify whether these anomalies result from new physics, such as sterile neutrinos, or from misidentified backgrounds. Operating at Fermilab from 2015 until 2021, it was a monolithic LArTPC with a total active mass of 85 tons and a drift length of 2.56 meters, housed within a cryostat to maintain ultra-pure liquid argon.

The detector incorporated a three-wire-based charge readout with a wire pitch of 3 mm, providing high spatial resolution. A major innovation in MicroBooNE was its use of cold electronics, meaning that the front-end analogue electronics were submerged in liquid argon and operated at cryogenic temperatures. The cold electronics system in MicroBooNE consisted of a low-noise Complementary Metal-Oxide-Semiconductor (CMOS) Application-Specific Integrated Circuitss (ASICs) designed to function reliably in cryogenic conditions [105]. These ASICs performed pre-amplification and signal shaping of the induced signals from the TPC wire planes before transmitting them outside the cryostat for further processing and digitisation. In order to avoid liquid argon boil-off, these ASICs were designed to have a very low power consumption of 6 mW per channel. The design significantly minimised thermal noise, leading to a higher signal-to-noise ratio compared to warm electronics setups. This improvement allowed to measure charge signals of below 400 electrons [106] and thus study events with energy deposits below 3 MeV [107].

This effort was supported by the MicroBooNE light detection system, which, besides providing the interaction timing information, helped reject noise events by requiring a matching light pulse to the observed ionisation tracks. The primary light detection system consisted of 32 PMTs. Unlike in other experiments, these PMTs were not directly coated with TPB but had TPB-coated acrylic plates mounted in front of each unit. Light pulses generated by Light-Emitting Diodes (LEDs) and guided through optical fibres to the PMTs were used for calibration. A secondary light detection system was installed, consisting of four PMTs, each coupled to a set of six 50 cm long light guides with a WLS coating [108]. This system was installed for R&D purposes to inform future experiments with more restricted spatial requirements, making the application of PMTs inconceivable.
Since the MicroBooNE detector was located at the surface, a key challenge was the rejection of the cosmic-ray background. For this purpose, a dedicated cosmic-ray tagging system was developed by the University of Bern [109]. The CRT was composed of plastic scintillator panels surrounding the cryostat, arranged in multiple layers to ensure a high geometric coverage. The system was segmented into modules, with each module containing wavelength-shifting optical fibres embedded in the scintillator material to collect the emitted light and guide it to SiPMs for precise signal readout. When a cosmic-ray muon passed through the detector, the CRT recorded its spatial and temporal coordinates, allowing for the identification and rejection of events.
MicroBooNE featured a laser calibration system designed to correct distortions in the electric field within the TPC volume [110]. These distortions are primarily caused by space charge effects, where slow-moving argon ions accumulate due to high cosmic-ray activity and could lead to misreconstructions of particle trajectories [111]. The laser system developed by the University of Bern consisted of two laser beam injection points that directed UV laser pulses into the liquid argon. The system used steerable optical mirrors to scan various regions of the detector, producing well-defined ionisation tracks at known locations. By comparing these artificially generated ionisation tracks with their expected positions, the distortions in the drift field could be mapped and corrected in data reconstruction.
MicroBooNE pioneered several significant reconstruction techniques and methodologies that greatly advanced event analysis in liquid argon detectors. The experiment developed and refined algorithms for three-dimensional track reconstruction, particle identification, and electromagnetic shower reconstruction, establishing a benchmark for subsequent neutrino experiments. These advancements not only enhanced MicroBooNE's sensitivity to neutrino interactions but also provided critical foundations for the reconstruction frameworks adopted in current and future neutrino experiments utilising LArTPC technology [112–114].

Moving towards the installation of the detectors for DUNE, large R&D efforts and prototyping campaigns were conducted in recent years or are still ongoing.
The ProtoDUNE-SP (or also ProtoDUNE-HD) detector at CERN served as a large-scale demonstrator for one of the DUNE far detector modules (details see sec. 2.4.1) [115]. It was first operated between 2018 and 2020 [59] and ran again in 2024 with upgraded hardware [116]. With a total active mass of 770 tonnes of LAr, ProtoDUNE-SP was the largest LArTPC ever operated to date. The large detector volume and long drift distance of 3.6 m required exceptional argon purity to reach an electron lifetime sufficient

to see ionisation tracks over the entire volume. A sophisticated liquid argon purification system made it possible to reach an electron lifetime consistently exceeding 30 ms, far above the requirements [59]. This marks an important milestone regarding operating the multi-kilotonne DUNE far detectors.
Its charge readout system featured modular wire-based APAs with four wire planes, one shielding plane, two induction planes, and one collection plane, wrapped symmetrically around steel frames. Cold analogue and digital ASICs, based on the MicroBooNE design, amplified and digitised signals directly in cold, facilitating the management of a large number of channels.
ProtoDUNE-SP was the first large-scale detector which applied a SiPM based light readout. For the second run of ProtoDUNE-SP in 2024, the light detection system was completely refurbished, and all light traps were replaced by so-called X-ARAPUCAS [117]. The X-ARAPUCA modules feature a highly reflective cavity with a TPB-coated outer surface. Incoming VUV scintillation light from liquid argon is absorbed by the TPB and re-emitted at a longer wavelength, allowing it to enter the cavity. Once inside, the light undergoes a second wavelength shift. Dichroic mirrors prevent the light from escaping, ensuring multiple reflections within the cavity to enhance light collection efficiency. Finally, the trapped light is eventually detected by an array of SiPMs mounted along the cavity edges. This design significantly improves photon detection by providing a large sensitive area while maintaining a compact volume. No performance results from the 2024 ProtoDUNE-SP run have been published yet. However, in previous small-setup tests, an overall PDE of about 2 % was measured for the X-ARAPUCA [118].

Parallel to single-phase developments, dual-phase LArTPC concepts were explored, motivated by technologies established in xenon-based dark matter detectors (e.g. LUX [119], LUX-ZEPLIN [120]). The dual-phase approach aimed to amplify ionisation signals by a charge multiplication mechanism at the liquid to gas interface, enhancing sensitivity. The dual-phase prototype at CERN, ProtoDUNE-DP, aimed to validate large-scale dual-phase technology for DUNE [121]. However, the experiment faced significant technical challenges, including charge extraction inefficiencies and HV stability issues. The lessons learned from ProtoDUNE-DP highlight the importance of rigorous testing in large cryogenic volumes before committing to full-scale implementations. The DUNE collaboration refocused on different design approaches, and the dual-phase concept was not pursued further.

Although wire-based charge readouts have been successfully deployed in several large-scale detectors, their construction and handling remain challenging. Each wire must be precisely tensioned to avoid sagging, which can alter the intended electric field and affect signal integrity. The breakage of a single wire can potentially affect an extensive area and needs to be avoided at any cost. In particular, for the very large detectors of DUNE, the sheer number of wires required increases the complexity and cost of the construction tremendously. Novel concepts of charge readout planes have been developed in the past and are finally getting to a mature enough level to be applied on a large scale.
The first concept to be mentioned is the CRPs developed for the application in one of the DUNE far detectors [58]. In the CRPs, the wires are replaced with copper strips placed on a perforated Printed Circuit Boards (PCBs). This more rigid construction facilitates

the assembly and handling processes significantly, leading to comparably low production costs. The stack of PCB incorporates a shield, two induction and a collection plane. Same as for the APAs, the copper strips on the CRPs are set at different angles to enable the reconstruction of incoming charge tracks. One of the main drawbacks of the design is its opacity for scintillation light. Light detectors can no longer be placed behind the anode plane but need to be moved to other locations.

While the CRP design mitigates many disadvantages associated with wire-based readouts, two significant issues persist. First, ambiguities remain in wire-based readouts because charge signals are recorded as 2D projections rather than precise spatial points, complicating 3D event reconstruction. When multiple tracks overlap or cross at steep angles, their signals can merge on the same wires, making it difficult to distinguish individual particles. Second, wire-based planes (or also CRPs) have relatively high capacitance, leading to higher noise levels and reducing sensitivity to low-energy signals.

Both these issues can be alleviated by implementing a pixelated readout. If each pixel independently records charge signals, this eliminates the need for complex signal deconvolution and reduces the risk of track overlap issues. However, the number of channels that need to be read out for the same anode area increases quadratically and thus requires new readout electronics. The development of the first ASIC designed specifically for such a pixelated readout, the LArPix chip [11], represents a major milestone in detector technology. Research and development efforts aimed at achieving this technological breakthrough have spanned over a decade (preceding the development of the CRPs).

As LArTPCs evolve to accommodate more complex event topologies and higher interaction rates, innovative readout technologies are required to enhance spatial resolution, reduce ambiguities, and improve the efficiency of charge and light detection. The next chapter discusses a novel detector design aimed at addressing these challenges in high-multiplicity environments.

3.5 Modular Near Detector for DUNE

As discussed in Section 2.4, in order to reach the physics goals and reduce systematic uncertainties, the ND complex requires a liquid argon detector part. In the following, the requirements for such a detector are discussed. Based on the experiences and the technologies developed in former experiments, a modular design approach was developed, which will be applied for the ND-LAr.

3.5.1 Dimensional requirements

To fulfil the physics goals of DUNE, the requirement was set that the ND detectors need to be able to reconstruct the neutrino energy as well as or better than the FD. To avoid an excessively large ND-LAr, it was decided to limit its dimensions to ensure effective containment of hadronic and electromagnetic showers. Therefore, the TMS/ND-GAr was positioned downstream of ND-LAr to measure exiting muons (see Fig. 2.9b).

The minimum dimensions of the active LAr region were determined using simulations to optimise hadronic shower containment. Figure 3.6 shows the fraction of neutrino events with 95 % hadronic energy containment as a function of the height and depth of the detector. Given the high number of expected interactions, it is sufficient to ensure transverse containment along one axis, allowing for an asymmetrical transverse detector geometry. A minimum transverse area of 3 m × 4 m and a depth of 5 m were found sufficient to achieve >99 % hadronic containment for neutrinos with energies up to 5 GeV. As discussed in Section 3.1, ensuring hadronic shower containment also ensures containment of electromagnetic showers with the same initial energy.

Since the downstream muon spectrometer can only cover low-angle outgoing muons, the transverse area of the detector was extended to 3 m × 7 m to be able to reconstruct muons emitted at larger angles. To reduce the height of the required cavern, the detector dimensions will be 7 m wide and 3 m tall. [8]

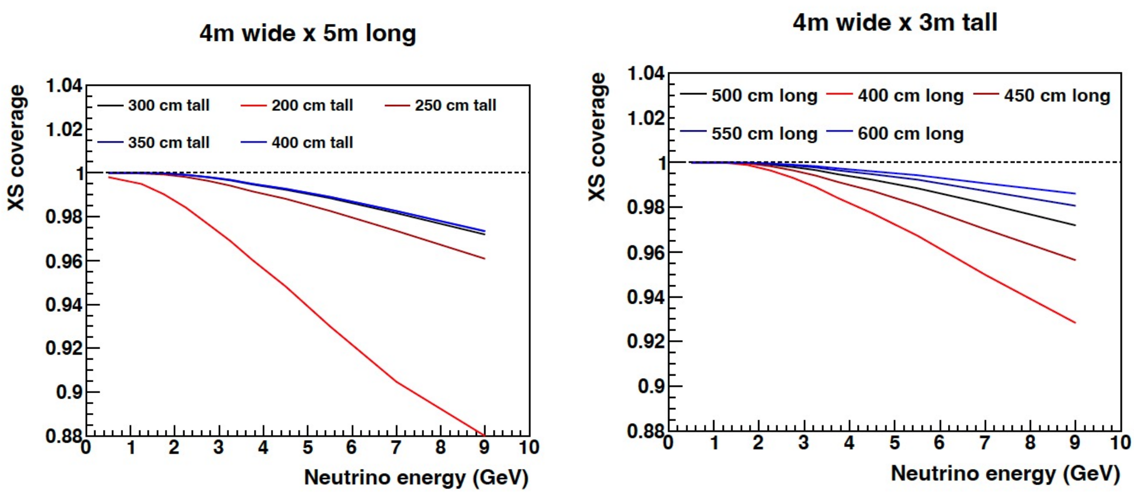

(a) (b)

Figure 3.6 – Coverage fraction of events with a minimum 95% containment, called cross-section (XS) coverage, for different (a) heights and (b) depths of ND-LAr depending on the neutrino energy. [8]

Given the derived dimensions, the liquid argon density and the beam energy and intensity, an average pile-up of 55 neutrino interactions (originating from targets inside and outside the detector) is expected per beam spill in ND-LAr (at 1.2 MW beam power). With a beam spill duration of 10 µs in the DUNE beam, a neutrino interaction is expected on average every ∼200 ns. Due to the large detector volume needed, the photon propagation paths to the edge of a monolithic detector would be well above the Rayleigh scattering length (see Tab 3.1). Rayleigh scattering has an impact on the spatial resolution of the light readout and thus limits the charge-light matching capabilities needed to resolve the pile-up.
To effectively address these challenges, the next section introduces the ArgonCube concept, a modular TPC design concept initially developed to enhance performance and

operational flexibility, which also effectively mitigates pile-up by segmenting the detector into smaller modules.

3.5.2 The ArgonCube concept at ND-LAr

The ArgonCube concept [10] was initially developed based on the experiences gained with the ArgonTube experiment at the University of Bern [102]. After probing the feasibility of drift distances of 5 m and experiencing the risks included in such an operation, it was concluded that a much more robust operation can be achieved with much shorter drift distances. The ArgonCube approach is a fully modular detector design, with a number of TPCs sharing a common cryostat. The full active volume gets split up into shorter drift volumes, making in particular the HV operation simpler as lower bias voltages need to be applied on the cathode planes. This also reduces the stored energy per TPC and prevents damage in the case of an HV discharge. Further, due to the shorter drift lengths, the demanded electron lifetime is lower, which reduces the requirements on the argon purity, making the detector more robust against contamination.

Although initially motivated to improve operational robustness, the modular approach brings major advantages in the high pile-up environment of ND-LAr. Most importantly, the module structure is opaque, meaning that scintillation light is contained within each TPC. For ND-LAr, the full $5\,\mathrm{m} \times 7\,\mathrm{m} \times 3\,\mathrm{m}$ active volume is split up into 35 modules, each with a footprint of $1\,\mathrm{m} \times 1\,\mathrm{m}$ and a height of 3 m. Each module hosts two symmetrical TPCs with a shared central cathode, thus resulting in a total number of 70 TPCs. These dimensions were chosen not only to limit the maximum cathode voltage required to 25 kV (for a nominal drift field of 0.5 kV/cm) but also to keep the propagation paths of scitillation photons below the Rayleigh scattering length. Figure 3.7 shows the design of the ND-LAr with its 35 modules packed in seven rows of five modules each.

With the segmented detector, the number of scintillation light flashes per beam spill per TPC can be reduced. This is demonstrated with simulation data in Figure 3.8. It is shown that, e.g. for a timing resolution of 12.5 ns, only due to the modularisation itself the flash pile-up is below 2 % for the modular detector, while it would be $\sim$16 % for a monolithic detector [8]. Accounting for the reduced Rayleigh scattering further improves the situation.

The drawback of the modular approach is the introduction of inactive volumes needed for the module structures and module-individual readout systems, increasing the total number of readout channels drastically. To reduce this effect, novel compact readout technologies and field-shaping structures had to be developed or adapted. Since the adaptation of the light readout to the modular design and the high-pile up environment brought major challenges, the entire Chapter 4 is devoted to this topic. Figure 3.9 shows an overview of a single ND-LAr module illustrating the placement of the readout systems in the TPC structure. The depicted Light Collection Module (LCM) light detectors, developed at Joint Institute for Nuclear Research (JINR) are briefly described in Section 5.5. The ArCLight detector will be covered in Chapter 4.

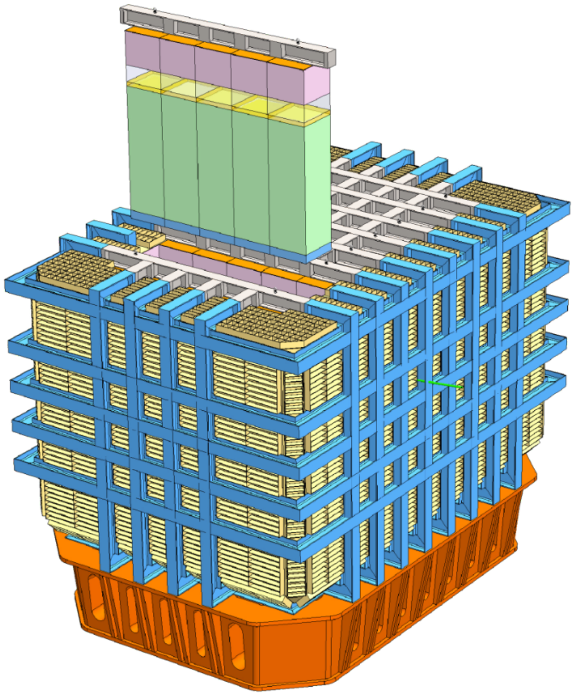

Figure 3.7 – LAr-TPC detector design for the DUNE ND. The LAr ND consists of seven rows with five modules each. A single ND module has a size of 1 m × 1 m × 3 m.

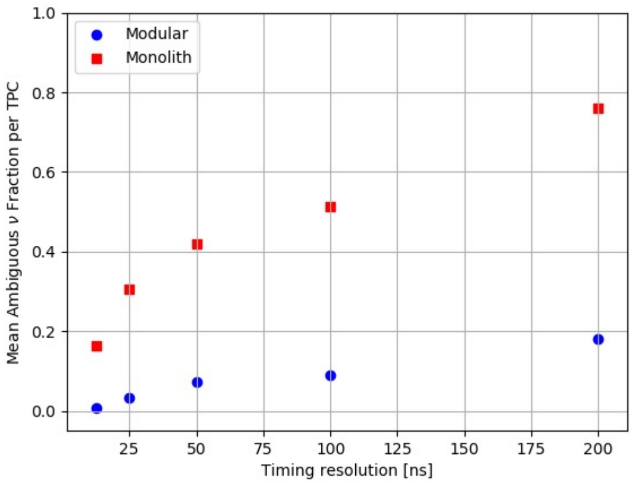

Figure 3.8 – Fraction of neutrino interactions per TPC drift region that cannot be resolved using timing information from the light for a given resolution (ambiguous ν fraction). This plot is based on simulations assuming a 1 MeV threshold for the light readout. [8]

Electric Field Shaping The uniformity of the electric field in a TPC has a major impact on the resolution of the charge reconstruction. For the modular design, a new compact approach to field shaping was needed to maximise active volume.

In the course of the ArgonCube R&D phase, a field-shaping technology using a resistive shell was developed [13]. A carbon-loaded polyimide foil replaces the conventionally used field-shaping cage structures. A similar technique has previously been used for the

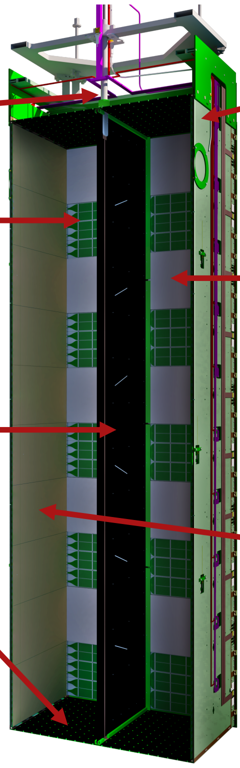

Figure 3.9 – Technical drawing of a sliced single ND-LAr module. The illustrated resistive shell field shaping technology is not part of the final design and was later replaced with a technology based on Zinc strips.

ProtoDUNE-SP cathode planes [115]. This technology reduces the risk of catastrophic damages in case of an HV breakdown since the material leads to a gradual and not sudden discharge of the entire field shell structures. The used DR8 foil[1] can be directly laminated on the G10 structure of the module, minimising the amount of dead material. Further, the risk of an electric breakdown is minimised by reducing the number of components (compared to conventional field shaping) and thus the potential points of failure.

However, during the prototyping phase for ND-LAr, the lamination process of the high-resistive foil on the module structure has appeared to be very challenging and minor imperfections in the manufacturing process have led to localised discharges during TPC operation. For the final ND-LAr modules, a novel approach with Zinc strips, acting as field shaping rings, will be used. The Zinc strips can be directly coated on the G10 module structure using an arc coating method carried out by Vivid Inc., Campbell CA, USA. To drop the voltage between the individual Zinc strip rings, a resistor chain is attached at each corner. Using four individual resistor chains in each corner, and not only one, adds redundancy and thus helps to prevent a catastrophic HV discharge. Compared to the resistive shell technology, this approach, due to the low resistivity of the Zinc, ensures the same electric potential along each Zinc ring. With the resistive shell technology, the uniformity along the drift direction is dependent on the uniformity of resistivity in the

[1] DuPont™, DR8 polyimide film, `www.dupont.com`

material.

Charge readout As mentioned in Chapter 1, the commonly used wire readouts in LArTPCs have the big drawback of ambiguities in the 3D reconstruction. The ArgonCube concept includes a pixelated charge readout providing unambiguous 3D images of particle interactions [11, 122, 123]. The pixelated charge readout is formed of a PCB and thus is mechanically robust to temperature deformation as occurring in the detector cool down and warm up. This is not the case for a traditional wire readout as slight differences in the wire tension can lead to sagging of wires, which can lead to wires touching. Due to the increased number of readout channels for a fully pixelated charge readout, the amplification and digitisation of the signal directly in the cold is unavoidable. This is achieved by the Liquid Argon Pixelate charge readout (LArPix) ASIC technology [11]. LArPix is based on a system-on-a-chip ASIC, providing a charge-sensitive amplification and a self-triggering digitisation system. Even for EM-showering events with a large amount of induced charge over a large area, the majority of channels have no signal. Thus, even in the intense DUNE ND environment, the expected pixel occupancy is below the percent level [124]. The self-triggering effectively functions as zero suppression on the ASIC level, keeping the data stream relatively low. A digital data acquisition rate of $\mathcal{O}(0.5)$ $\mathrm{MB\,s^{-1}\,m^{-2}}$ is expected when exposed to the flux of surface cosmic rays with a metre-scale drift length. For underground beam operation, the data rate is much lower. With LArPIXp to 256, ASICs can be run with a single external connection by connecting them in an optimised I/O network (Hydra I/O). More details on the LArPix implementation on the pixel tile design will be given on a prototype design in Sec. 5.6.

3.5.3 Prototyping campaign

To ensure the successful operation and optimal performance of the DUNE ND-LAr detector, an extensive prototyping campaign has been conducted.

In the first phase, until 2018, the individual detector technologies were produced and tested. These tests were conducted in small-scale setups at various institutes as part of the ArgonCube R&D program. In particular, the novel techniques developed for this detector design, including LArPix, the field shell structure, the ArCLight, and the LCM, underwent intensive prototyping at the component level [11–13, 125, 126].

In the second phase, the individual technologies were integrated into test setups of different sizes and configurations.
The first setup tested, called SingleCube, represented a single "cell" of the final detector design. This smallest unit consisted of one LArPix pixel board ($32\,\mathrm{cm} \times 32\,\mathrm{cm}$) and one light readout unit. Each light readout unit comprised either three LCM panels or one ArCLight panel. The single-drift TPC structure for SingleCube was built using FR4 PCB-like panels with copper traces connected by a resistor chain to generate the electric field. With this setup, the basic-level combination of charge and light readout was tested. The first SingleCube test was performed in October 2020 at the University of Bern.

After the successful test of the SingleCube, two large-scale demonstrators were developed and built: the 2x2 demonstrator and the Full Size Demonstrator (FSD).

The 2x2 demonstrator consists of a 2x2 arrangement of four prototype modules, which are scaled-down versions of the final ND-LAr modules. Each module includes 16 of the "cells" tested in SingleCube, distributed over two symmetrical TPCs. The drift lengths were reduced to 60 % of the final 50 cm, and the height to 40 % of the final 3 m. By placing the 2x2 detector in a neutrino beam, it can demonstrate successful multi-module operation and also serve as a physics demonstrator. The 2x2 demonstrator development, operation, and performance will be discussed in detail in Chapters 5 and 6.

The FSD was developed as the final prototyping stage before producing the actual detector modules. The full-scale module allows for the validation of complete integration of all final-design detector components, including the module structure. All components are built to their final scale. Comprehensive testing of this demonstrator ensures detection performance, robustness of mechanical structures, and reliability of integrated systems under conditions representative of the final experimental environment. To test the FSD, a dedicated setup was built at the University of Bern, including a detector cryostat, a storage cryostat, a liquid argon recirculation system, and all cryogenic infrastructure required for operation. The FSD was successfully operated for the first time in October 2024. The FSD is mentioned here for completeness, though its evaluation is beyond the timeline of this thesis.

Chapter 4

Light Readout for a Modular LArTPC

As seen in the previous Chapter, the modularisation of LArTPCs has significant advantages in high-intensity environments. However, designing the readout systems for modular detectors presents a range of challenges, particularly in adapting to the spatial constraints and demands of high-intensity environments. In this chapter, the development of a light readout system addressing these challenges is presented. This includes not only the design and production of the light detector itself but also the full readout chain, incorporating a Data Aquisition (DAQ) system and calibration methods. The system design was specifically driven by the ND-LAr development but is adaptable to any modular TPC design in a high-intensity environment.

To allow actual measurements of physics parameters using light data, a reliable simulation from photon creation, through the interaction with the light detector, up to the response of the readout electronics and the DAQ system is necessary. Basic signal processing and light-specific low-level reconstruction must be applied to feed the data to algorithms that combine charge and light information and reconstruct physics interactions. In the second part of this chapter, the entire processing from signal creation (either in real data or simulation) up to the output of the low-level reconstruction is presented.

4.1 Requirements for the light readout in high-intensity environments

In Chapter 3, it was discussed why the detection of scintillation light in LArTPCs is needed to accurately reconstruct particle tracks in 3D. A measurement of the T0 timestamp with a precision of $\mathcal{O}(\mu s)$ is required to achieve a $\mathcal{O}(mm)$ precision of the hit position in the drift direction.

However, placing a LArTPC detector in a high pile-up environment, such as for the DUNE ND-LAr, imposes significantly stricter requirements for the light readout. In Section 3.5, the advantage of optical segmentation to operate in such an environment was discussed. The key prerequisite for successful operation is efficient in-spill timing for each tracklet

recorded in the charge readout. Only if an accurate interaction time for each tracklet can be measured, detached energy deposits spread over multiple TPCs can be matched with their original interaction vertex or tagged as not associated with any vertex within the active volume. Figure 4.1 illustrates how the charge and light information must be combined to associate each tracklet with an individual timestamp within a single beam spill.
It becomes evident that adding an exact timestamp to each tracklet enables a transition to a 4D level of information (3D coordinates + time), opening up new methods for event selection and physics analyses. For instance, in decay processes, the time delay between the incidence of a particle and the occurrence of its decay product can be leveraged to tag and study specific interactions.

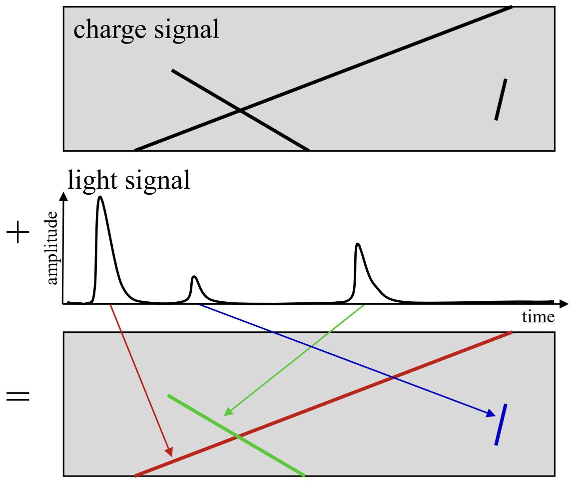

Figure 4.1 – Illustration of the charge-light matching to achieve an in-spill timing. Here, only one light readout channel is illustrated; by combining the information from multiple channels, also spatial information can be extracted from the light.

To define the direct requirements a complying light readout must fulfil, it needs to be further expounded on how efficient in-spill timing can be achieved. The key factor is that light signals that are not simultaneous can be identified as individual events, called "flashes" in the following. In the first order, this needs to be possible within a single readout channel. The upper part of Figure 4.2 illustrates this separation based on the temporal resolution. By deconvolving the two overlaying signals, each can be associated with an amplitude. Comparing this with the energy deposited by the tracklets from the charge readout and the consequential expected light yield, in most cases, the observed flashes can already be matched with the tracklets. This method reaches its limit once the expected light yield from multiple tracklets falls within the amplitude resolution of the readout or when deconvolution becomes unfeasible.

Combining information from multiple readout channels within the same TPC can significantly improve the charge-light matching efficiency. In cases where the above-mentioned method fails, such as when the temporal resolution of a single channel is insufficient to deconvolve two peaks, combining information from multiple channels becomes particularly helpful, especially if the two tracklets are spatially well-separated. By integrating

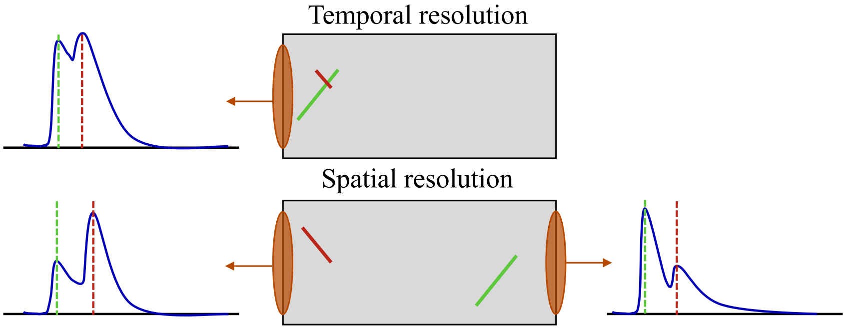

Figure 4.2 – Illustration of the usage of the temporal and spatial resolution for charge-light matching. The top figure shows the separation of signals using only the temporal resolution of a single channel. By combining information from multiple channels in the bottom figure, spatial information can be extracted.

data from multiple channels, it becomes possible to reconstruct the origin of the light emission, enabling discussion of the spatial resolution of the light readout. This spatial resolution is crucial when the light yield of two tracklets falls within a similar range, but they are spatially distinct. This scenario is illustrated in the lower part of Figure 4.2. In summary, both temporal and spatial resolution are essential for efficient charge-light matching. The temporal resolution is inherently limited by the time characteristics of the scintillation process in argon (see Ch. 3), while the spatial resolution is constrained by the isotropic and undirected nature of scintillation light emission (compared to the Charge Readout System (CRS)) and the effects of Rayleigh scattering (see Sec. 3.1.2.

The fundamental parameter that directly influences all other performance aspects is the Photon Detection Efficiency (PDE). It defines the fraction of incident photons successfully detected by the sensor and, consequently, determines the overall light yield available for event reconstruction. Both temporal and spatial resolution depend on the PDE, as the number of detected photons per event directly impacts their precision. Moreover, PDE plays a crucial role in energy resolution, as it dictates the fidelity with which the light signal can be correlated with charge-based energy deposits. Thus, optimising PDE is not only a requirement in itself but also a key driver for meeting all other resolution criteria in the light readout system.

While the modular design is essential to achieve charge-light matching and in-spill timing, it introduces significant challenges for the design of light detectors. Since every module needs to be equipped with an individual charge and light readout, these components must be compact enough to minimise dead areas in the detector volume. For ND-LAr, the pixelated charge readout prohibits placing the light detector behind the anode plane (as is possible with wire-based charge readouts) or outside the field shaping structure since this is directly integrated into the module. As a result, the only viable option is to position the light detectors within the drift volume itself.

Placing a detector in the drift field requires a fully dielectric design for the light detector to prevent discharges in the electric field. Conducting materials in the active volume are permissible only in regions located at or behind the anode. Even with a dielectric design, materials placed within the drift field accumulate surface charges by accumulating ionisation charge from particle interactions. If the surface resistance is too low, these charges can start migrating, causing field non-uniformities.

Not only the light detectors but also the entire readout electronics define the performance of the light readout. The choice of the light sensor is driven by minimal space requirements. The only viable option that provides single-photon sensitivity while maintaining a sufficient dynamic range are Silicon Photo Multipliers (SiPMs) (see Sec. 4.3). Their typical signal rise time is approximately 0.5 ns, which is sufficiently fast given the timing characteristics of LAr scintillation.

To avoid any information loss from the light signals, it is necessary to record the full waveforms. This allows for the use of pulse shape discrimination and optimised offline signal processing. Due to the large size of the TPC modules, long cables are required to transfer the analogue signal outside the module. A simple pre-amplifier is positioned directly after the SiPM to prevent signal degradation during transfer. Since this pre-amplifier is submerged in LAr, its heat load must be minimised to avoid boiling. Another amplification stage is required outside the cryostat to adapt the signal range to the input voltage range of the Analogue-to-Digital Converter (ADC).

The scintillation process largely determines the rise time of the readout signal ($\sim$5 ns), along with the timing characteristics of the light trap and the analogue readout electronics, both of which are design-dependent. The $\sim$0.5 ns rise time of the SiPM contributes only marginally. Overall, a typical signal rise time of $\sim$30 ns is anticipated. This parameter influences the selection of the ADC sampling rate. A compromise must be struck between achieving a sufficiently high sampling rate, ensuring adequate amplitude resolution, and managing an overall data rate that remains practical.

For the particular case of ND-LAr, collecting all the considerations described above, a quantified list of requirements was created, which is shown in Tab. 4.1. Of particular importance is the single hit resolution of $<$10 ns. This value is particularly motivated to enable the tagging of detached neutron recoils with the primary neutrino vertex, which poses a particular challenge in the beam environment at the DUNE ND. To achieve such a tagging, proton recoils caused by high energetic neutrons need to be resolved with high resolution [127]. A particular analysis to verify that this requirement can be met will be presented in Section 6.5.

Table 4.1 – Overview of the main requirements for the ND-LAr light readout system.

Property	Value
ADC sampling rate	>50 MS/s
ADC synchronisation	<1 ns
Single hit resolution	<10 ns
Pile-up resolution	<200 ns
Photon detection efficiency	>0.6 %
Spatial resolution	<10 cm
Cold amplifier heat dissipation	<65 mW/ch

4.2 Overview

Based on the requirements stated in the previous section, I co-developed a complete light readout system including light detectors, the full readout chain, a calibration system, and the DAQ software. This section provides an overview of its primary components and their interfaces. In Figure 4.3, the readout chain is illustrated in a block diagram. At large, the system is divided into three parts: the cold section within the cryostat, the warm electronics section located immediately outside the cryostat, and the computer-based DAQ system distributed across multiple locations.

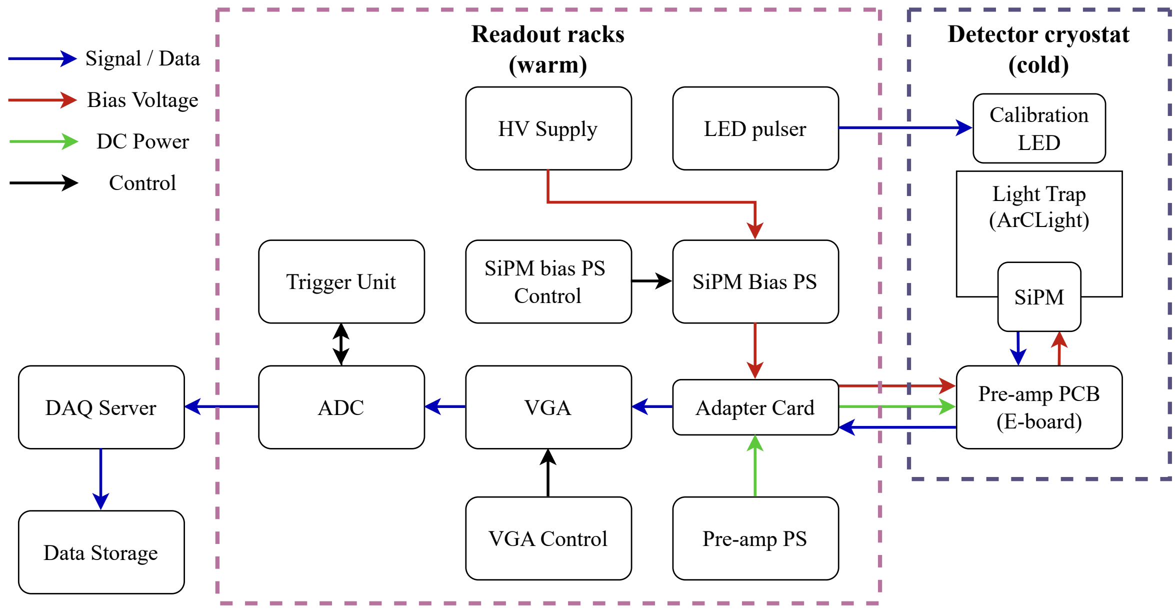

Figure 4.3 – Block diagram of the entire light readout chain as implemented for the ND-LAr prototypes together with the LED calibration system. (PS = power supply)

Besides the readout chain, Figure 4.3 also highlights the components of the LED calibration system, which was implemented to measure and optimise the SiPM response, particularly the SiPM gain. The subsequent sections discuss the individual components in greater detail.

4.3 ArClight

4.3.1 Concept and Design

The ArgonCube Light detector (ArCLight) is a VUV light detector developed at the University of Bern that meets the requirements outlined in the previous section [125]. Inspired by the ARAPUCA concept [128], the ArCLight features a bulk structure made of wavelength-shifting plastic, which forms a trap for incoming photons. These trapped photons eventually reach the sensitive surface of a SiPM that is directly attached to the structure. Figure 4.4 illustrates the detection principle of the ArCLight detector.

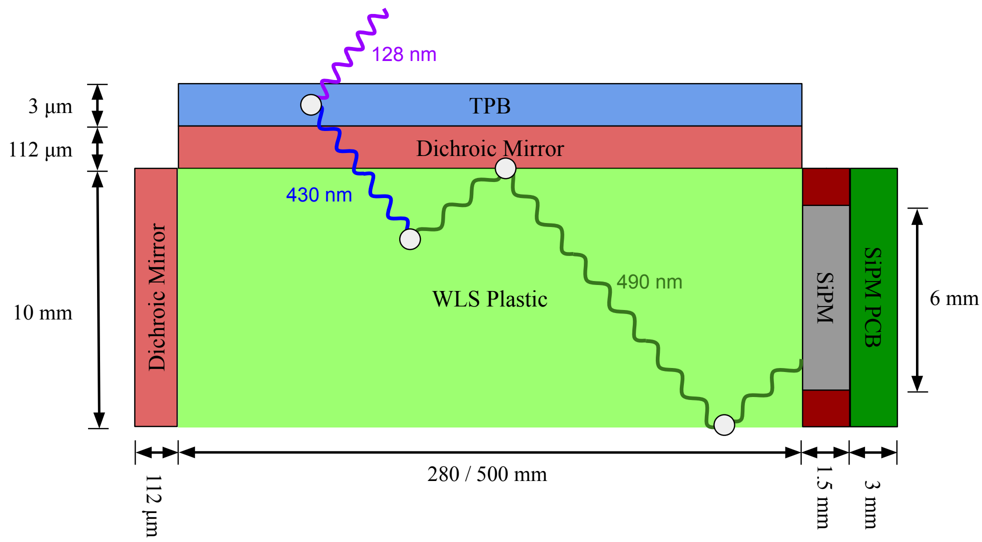

Figure 4.4 – Diagram of an ArCLight illustrating the path of a VUV photon. The photon passes through the TPB, shifting to blue light (peak wavelength: 430 nm), and then enters the dichroic mirror. Inside the WLS plastic, the photon shifts to green light (peak wavelength: 490 nm). Finally, the green photons travelling within the plastic are detected by the SiPM.

The scintillation light in LAr is emitted at approximately 128 nm within a relatively narrow spectrum. At this wavelength, effective photon trapping is not possible because the light is absorbed by most materials. To address this, Tetraphenyl Butadiene (TPB) is utilised as a wavelength shifter, transforming the light into the blue range, around 430 nm, with very high efficiency ($\geq 100\,\%$ [129]). TPB operates on the principle of a Stokes shift, where absorbed VUV photons excite the molecules. During the relaxation process, part of the energy dissipates non-radiatively, causing the remitted photons to be at lower energy and longer wavelengths compared to the originally absorbed VUV photon. The emission spectrum of TPB peaks at around 430 nm, which corresponds to visible blue light. The TPB must be applied as a very thin layer, approximately $\sim$3 µm, to avoid reabsorption [130] (see Sec. 4.3.2). While TPB generally exhibits a very fast decay time of less than one ns, studies have shown that VUV photons can induce TPB triplet (rather than singlet) excitation states, leading to a slower decay time of 50 ns to 100 ns, which negatively impacts the time response of the light trap [131].

A second wavelength-shifting process is required to enable photon trapping with dichroic mirrors. For this purpose, a WLS plastic is used as the bulk structure of the ArCLight. The 300 mm × 500 mm × 10 mm plate is composed of EJ-280, produced by Eljen Technology[1]. As shown in Figure 4.5, its absorption spectrum significantly overlaps with the emission spectrum of TPB, resulting in a high conversion efficiency. With a decay time of 8.5 ns, the photons are reemitted around 490 nm (green).

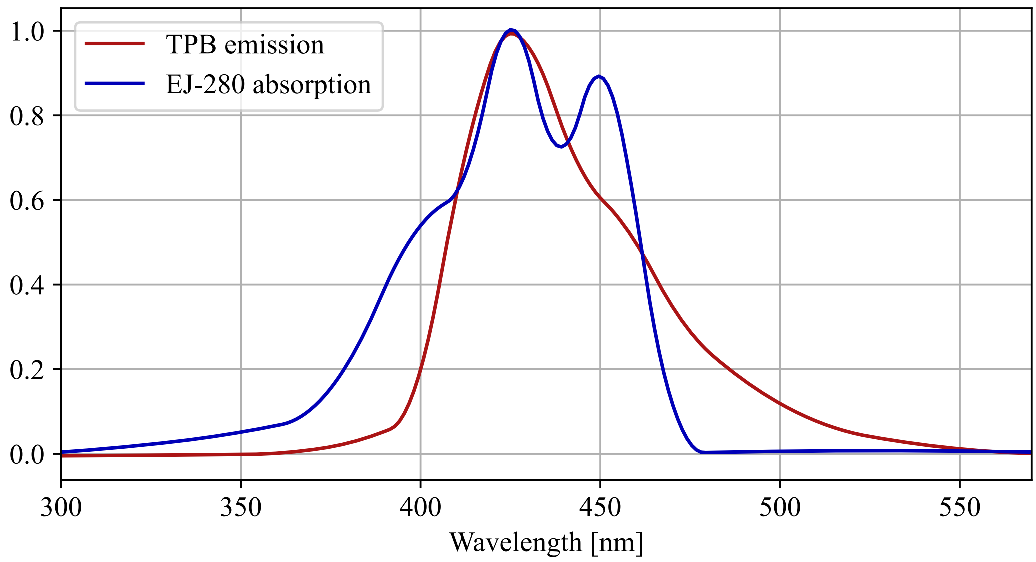

Figure 4.5 – Normalised emission spectrum of TPB and absorption spectrum of EJ280 WLS plastic.[12]

To prevent the 490 nm green light from escaping the WLS plastic, dichroic mirrors are applied. The selected material exhibits high reflectivity at 490 nm and high transmissivity at 430 nm. This ensures that TPB emission light can enter the structure, while photons emitted by the WLS plastic are reflected back into it. The 3M DF-PA Chill[2] foil meets these requirements. Moreover, it is composed entirely of dielectric material, making it suitable for use within the drift field. Figure 4.6 shows that the DF-PA foil has high transparency across the entire TPB emission spectrum.

Figure 4.6 shows that the transparency window does not significantly overlap with the EJ-280 emission spectrum at larger incidence angles. Some loss in trapping efficiency must be accepted at lower incidence angles, which cannot be avoided due to the isotropic emission of TPB. The dichroic mirror foil includes an adhesive layer, allowing it to be directly laminated onto the WLS plastic.

[1] Eljen, EJ-280, `eljentechnology.com`
[2] 3M, DF-PA Chill, `3m.com`

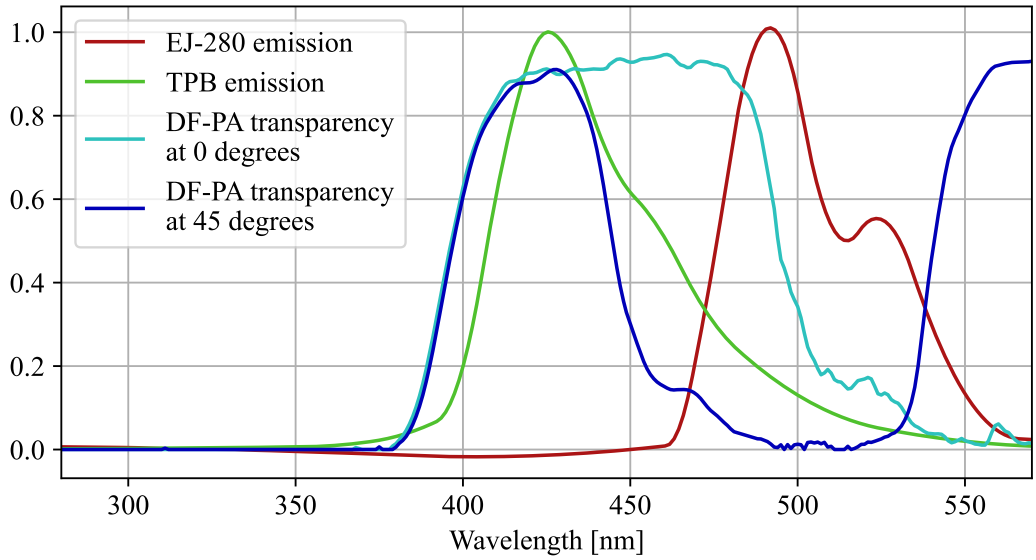

Figure 4.6 – Normalised emission spectra of EJ-280 (WLS plastic) and TPB together with the DF-PA dichroic mirror transparency at two different incidence angles (0°/45°). [12]

Due to the difference in refractive index between the WLS plastic (~ 1.58) and LAr (~ 1.25) at 430 nm, photons have a natural probability of being trapped even without a dichroic mirror. At incidence angles above 52°, total internal reflection occurs. Applying the dichroic mirror foil to both large surfaces of the WLS plastic has proven problematic due to differing Coefficient of Thermal Expansion (CTE). During cooldown to LAr temperature, this discrepancy can create significant mechanical stress, leading to delamination of the foil or breakage of the WLS plastic. To enhance the mechanical robustness of the assembly, the mirror foil is applied to only one of the two large surfaces, which can lead to a minor bending of the structure but no delamination. On the sensitive side, the application of the dichroic foil is necessary because if TPB is deposited directly onto the WLS plastic surface, the direct WLS plastic-LAr interface is eliminated. Initially, mirror foils were also removed from the narrow faces, but measurements showed that these foils significantly improved trapping efficiency (see Sec. 6.1).

At one of the narrow faces of the WLS plastic, a PCB holding six SiPMs is attached. The PCB is secured to the WLS plastic using Polyether Ether Ketone (PEEK) screws. Eight millimetre-long holes with M3 threads are cut directly into the WLS plastic, ensuring direct contact between the SiPMs and the light trap. A spacer PCB is included to prevent the SiPMs from being crushed. To further enhance trapping efficiency, the area around the SiPMs is covered with dielectric mirror foil (3M Vikuiti ESR[3]).

4.3.2 Evaporation Coating

The TPB deposition on the large surface of the ArCLight forms one of the key steps in its production. As highlighted above, the thickness, but also the uniformity, of the

[3] 3M, Vikuiti ESR, `3m.com`

TPB layer significantly affect the overall performance of the ArCLight. To achieve this, a vacuum evaporation deposition procedure was developed to coat the dichroic mirror foil with TPB, which is then laminated onto the WLS plastic structure. Direct coating on the final ArCLight structure is not feasible because the WLS plastic would deform during the heating phase of the coating process.

In early prototypes, TPB was dissolved in toluene and mixed with polystyrene. This solution was directly airbrushed onto the ArCLight. However, compared to vacuum evaporation deposition, this method resulted in approximately $\sim$50 % lower photon detection efficiency and was subsequently replaced by evaporation coating [132][125]. The reduced efficiency of this method can be attributed to less uniform crystal formation and, thus, lower surface coverage (see Fig. 4.7).

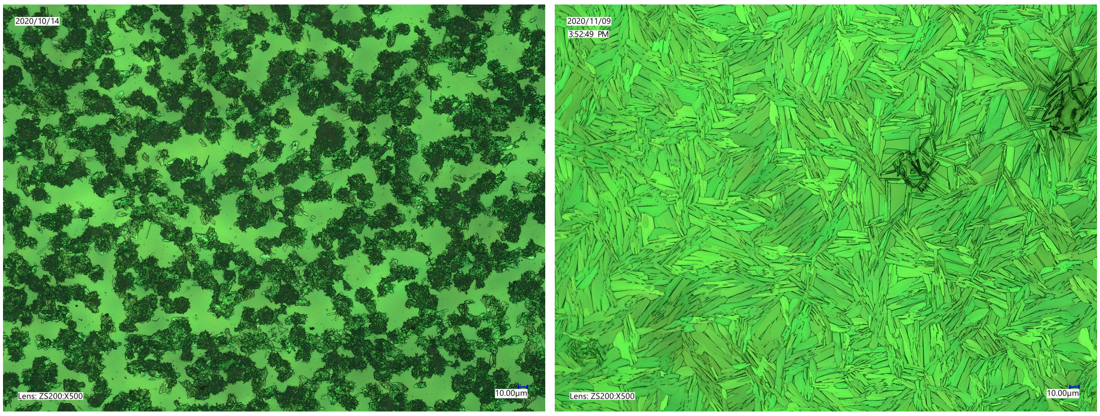

Figure 4.7 – Microscopic images of the TPB layer achieved with airbrush (left) and evaporation deposition (right). Both images are magnified by a factor of 500.[125]

In evaporation deposition coating, the TPB is heated in a vacuum chamber until it evaporates, creating a vapour phase. The vaporised molecules then condense onto the substrate, in this case, the dichroic mirror foil, forming a uniform thin coating. The vacuum environment minimises contamination and ensures a high-purity film, while precise control of the evaporation rate and substrate temperature enables reproducible thickness and coverage. This technique is widely employed in noble liquid TPC detectors for applying wavelength-shifter coatings [133].

In previous work, a prototype coating chamber was developed and utilised for producing various prototype versions for ND-LAr [132]. In this thesis, a production-level chamber was designed and constructed to coat full-size ArCLight panels, as will be deployed in the final ND-LAr detector modules. A picture of the production-level chamber is shown in Figure 4.8.
The setup is placed in a cubic high-vacuum chamber and equipped with multiple pressure and temperature sensors for monitoring. At the core of the setup is the heating table, which uses a series of power resistors to heat up the TPB powder. A Proportional–Integral –Derivative (PID) processor maintains a constant temperature on the table throughout the coating process. The TPB is distributed on a tray clamped onto the heating table

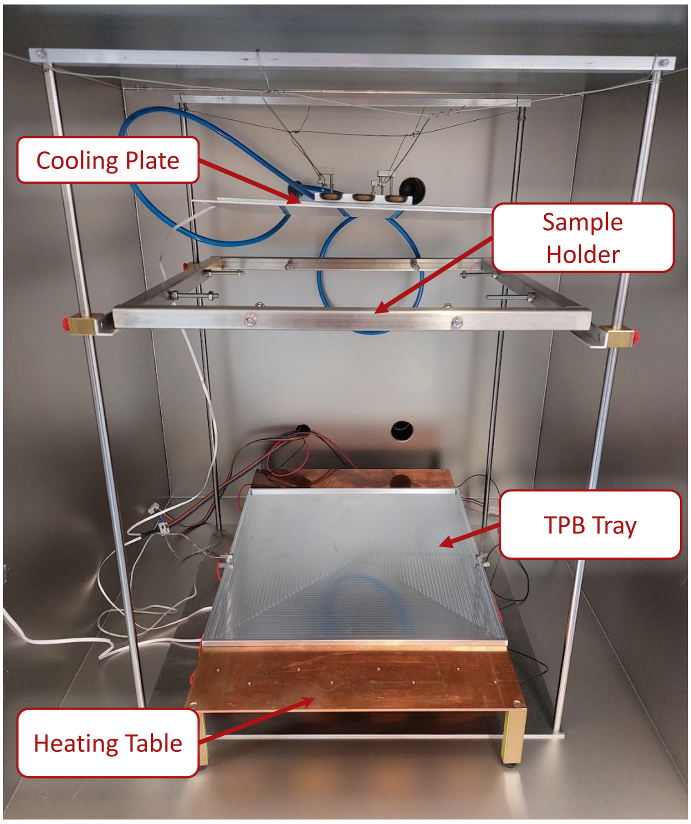

Figure 4.8 – Evaporation deposition setup inside a vacuum chamber, showing the heating table for TPB evaporation, the cooling plate, and the aluminium plate holder for substrate positioning.

to ensure efficient heat conduction. For the coating process, the dichroic foil is attached to an aluminium sample holder, which is mounted on a movable sample holder. The optimal distance between the TPB tray and the sample was determined to be 13 cm. To enhance the coating process efficiency, the sample can be cooled. An external chiller provides cooling via a closed water cycle, and a cooling plate can be placed on top of the aluminium plate to deliver uniform cooling power across the surface.

Figure 4.9 shows the temperature and pressure progression over an entire coating cycle. After positioning the sample and TPB in the chamber, a pump-down is initiated. Once the pressure drops well below 10^{-2} mbar, heating is activated, leading to a pressure increase due to TPB evaporation. During the 3 h to 4 h heating phase, the TPB is maintained at a constant temperature of 200 °C. The sample temperature experiences a significant but non-destructive rise, peaking at 50 °C before the heater is turned off. The sample is left in the chamber overnight, allowing it to cool down.

While the described setup enables good control over most parameters, the reproducibility of the coating process is still constrained by factors that are either inherently difficult to regulate or not yet fully characterised (e.g. lab humidity, TPB grain size). It has been observed that the cleaning process of the dichroic foil prior to coating significantly affects the results. Since TPB does not sublimate perfectly and undergoes minimal melting

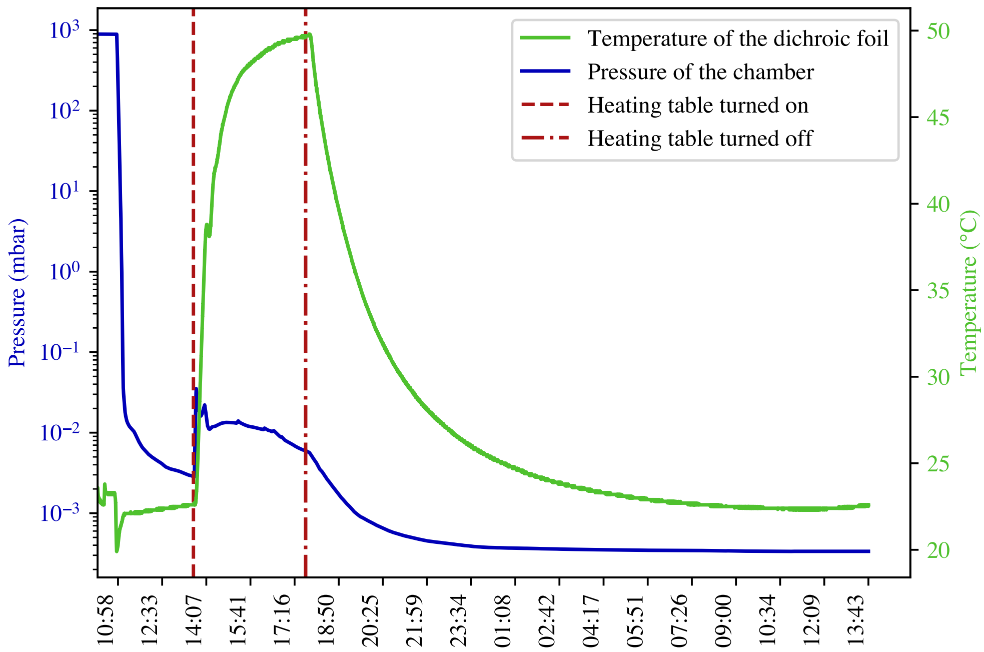

Figure 4.9 – A TPB evaporation cycle overview, illustrating the chamber pressure (blue), the temperatures of the dichroic mirror (green) and the turning on and off of the heating table (red). The first blue peak represents the moment the chamber is opened to place the dichroic mirror inside. The pumping process lowers the pressure before the heating table is activated. Once the heater is turned on, water and TPB evaporate, leading to increased pressure within the chamber. The temperature of the foil increases as the heating table operates.

during the coating process, reusing it across multiple coating cycles can be problematic. Crushing the TPB powder by pushing it through a fine mesh has been shown to improve the results.

4.3.3 Quality control scanning

Due to the limited reproducibility of the coating process and potential quality defects, a quality control mechanism was required. For this purpose, a three-axis LED scanning stage was developed. The scanner is based on a modified commercial 3D printer[4], where the printer head was replaced with an LED setup. A UV LED with a wavelength of 270 nm was used to probe the TPB layer, preventing direct absorption in the WLS plastic layer. The setup is shown in Figure 4.10.

A collimator with an adjustable aperture defines the size of the light cone projected onto

[4] Creality, Ender 5 Plus, `creality.com`

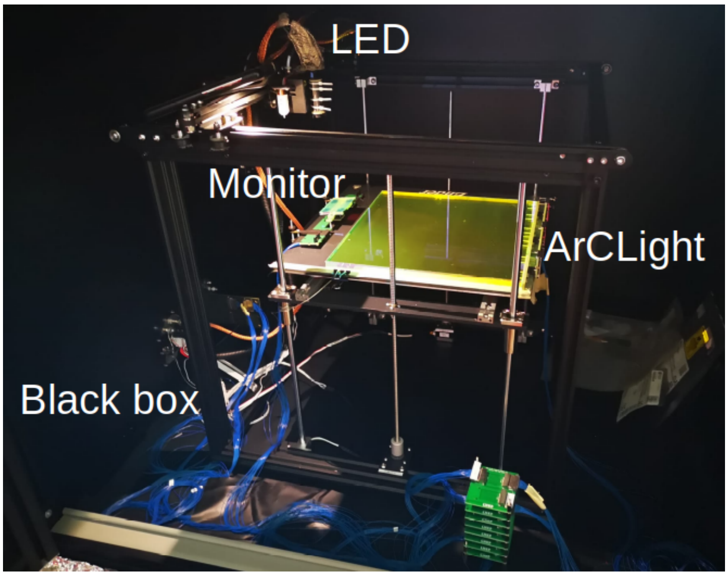

Figure 4.10 – Scanning setup for the ArCLight quality control. A calibration LED is mounted on a three-axis Computer Numerical Control (CNC) stage, which allows scanning of the ArCLight surface. A fixed monitoring system is placed at the edge, allowing long-term monitoring of the LED intensity.

the ArCLight surface. By adjusting the aperture and the distance to the sample using the CNC stage, the light cone size can be tailored to match the desired scanning step size, minimising overlap.

A fixed monitoring system was installed adjacent to the scanned sample. This system includes two SiPMs attached to a WLS plastic slab coated with TPB. The scanning LED can be periodically moved to the monitoring stage, enabling comparisons of LED intensity over extended periods.

At each position, the LED is pulsed 15k times at a fixed intensity to measure the average collected light on each of the six SiPMs. Details on how the light signals are recorded are discussed in Sections 4.4 and 4.5. Figure 4.11 illustrates an example showing the response of each individual SiPM for all positions. Each SiPM has a distinct cone-shaped region where it is most sensitive to incoming light, allowing for a spatial reconstruction of incoming light within a single ArCLight panel.

Looking at the sum of the signals from all six SiPMs provides a visual representation of the overall performance of an ArCLight panel (see Fig. 4.12). It is evident that the light yield primarily depends on the distance to the SiPMs, with areas of reduced light observed between two adjacent SiPMs. This visualisation can also identify regions with low or absent TPB coverage. In the example shown, this is the case in the upper left corner.

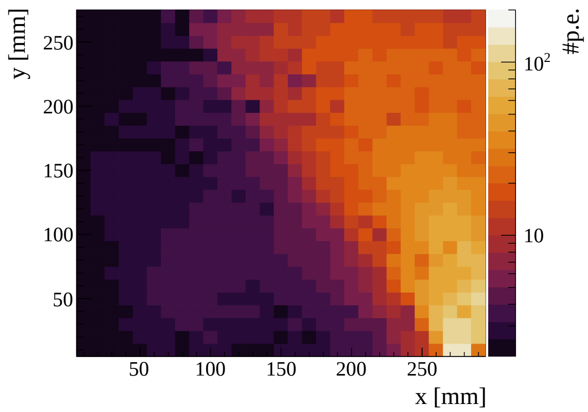

(a) SiPM 0

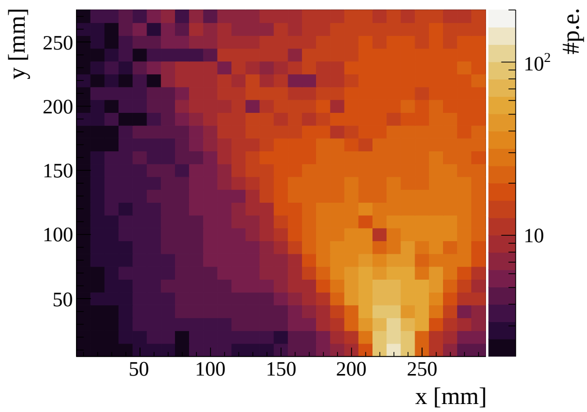

(b) SiPM 1

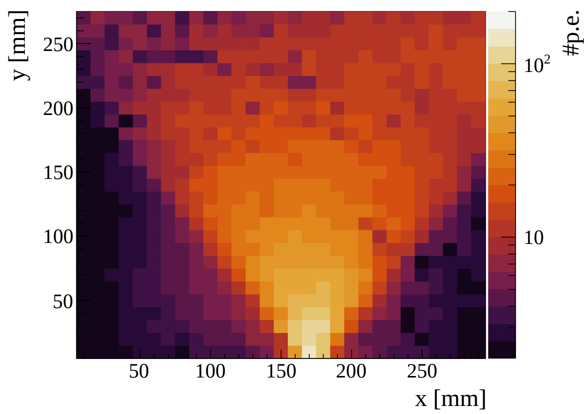

(c) SiPM 2

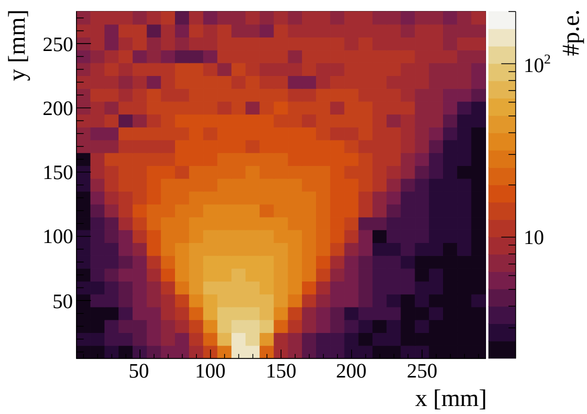

(d) SiPM 3

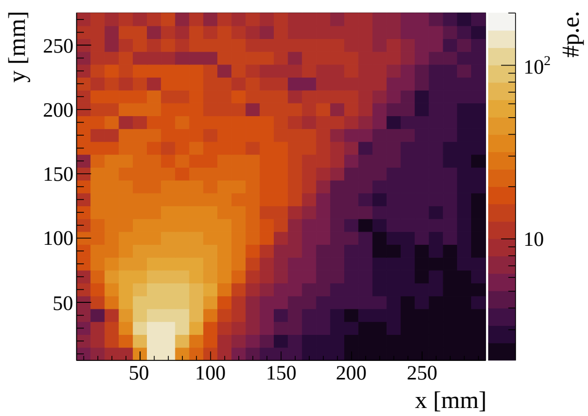

(e) SiPM 4

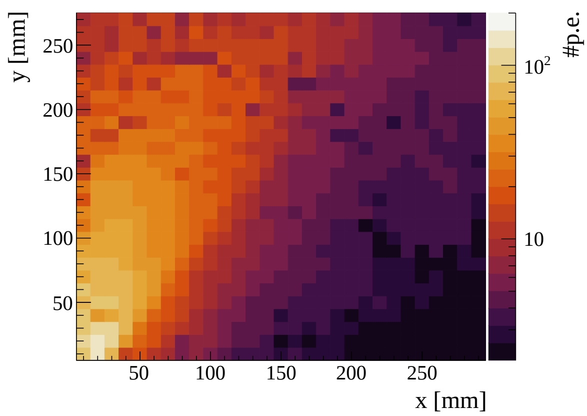

(f) SiPM 5

Figure 4.11 – The detected number of p.e. in a high-resolution scan by each of the six SiPM channels for the LED at a distance of 20 mm, with the SiPMs positioned on the x-axis. The colour scale represents the detected number of photoelectrons (p.e.). The absolute signal strength is arbitrary and depends on the LED light emission power, which is kept constant for the different scans.

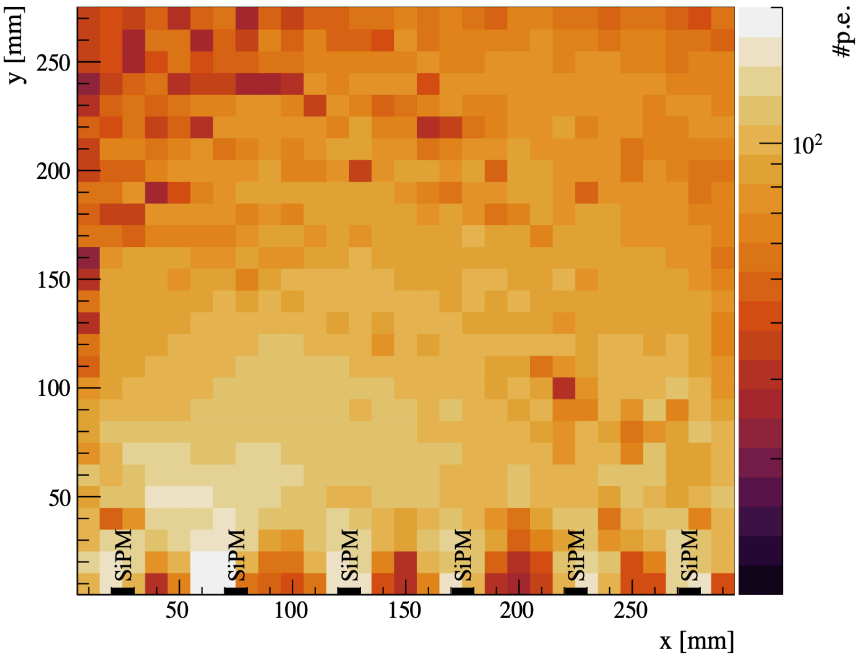

Figure 4.12 – Total light yield summed over all six SiPMs for each scanning position of a sample ArCLight (corrected using the monitoring stage). Above the x-axis, the SiPM positions are indicated.

4.4 Readout electronics

The light readout electronics are designed to process signals from their generation at the SiPM through to digitisation and transmission to the DAQ system. For the system developed and tested in this thesis, both commercial and custom-built components were utilised. The custom parts were developed and produced by JINR and the University of Bern. The readout chain starts with the SiPMs[5], which convert scintillation light into electrical signals. To explain the readout in detail, it is essential to understand the basic principle of a SiPM.

A SiPM comprises an array of microcells, each functioning as an independent avalanche photodiode. Figure 4.13 illustrates a SiPM. Each microcell features a depletion zone (π) and an avalanche region with a higher electric field intensity. When an incoming photon strikes the reverse-biased SiPM, it creates an electron-hole pair within a microcell. Electrons drifting towards the anode trigger an avalanche effect in the high field region (Geiger mode), producing an amplified electrical pulse. A quenching resistor (R_{Q}) connected to each microcell halts the avalanche by limiting the current draw, resetting the microcell for subsequent photon detection. The summed signals from all microcells constitute the SiPM output. The output signal of a SiPM exhibits a quantised structure, as it is the sum of discrete pulses generated by individual microcells triggered by single photons.

[5]Hamamatsu, Hamamatsu S13360-60XXCS, `hamamatsu.com`

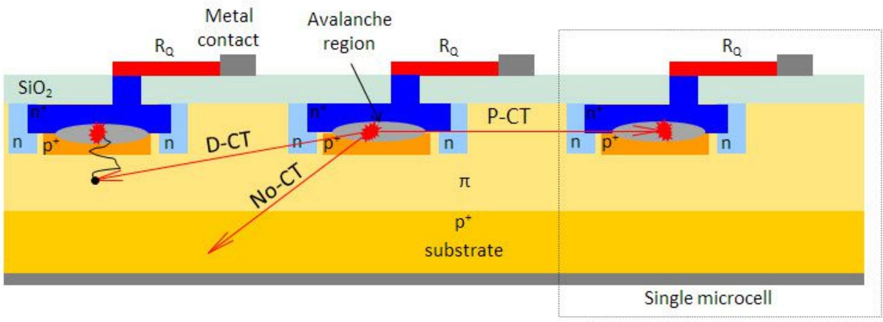

Figure 4.13 – Schematic of a SiPM microcell structure showing avalanche regions, quenching resistors R_Q, and all silicon doping regions. Additionally, the two potential crosstalk mechanisms, prompt crosstalk (P-CT) and delayed crosstalk (D-CT), are shown. The third mechanism shown, no-crosstalk (No-CT), does not lead to an actual signal induction. [134]

To operate in Geiger mode, the bias voltage applied to the SiPM must exceed its breakdown voltage. The difference between the breakdown voltage and the operating voltage is referred to as the overvoltage, which is the primary parameter defining the gain of the SiPM. Crosstalk between neighbouring microcells can occur in various forms, as illustrated in Figure 4.13. During the avalanche process, high-energy photons may be generated and penetrate a neighbouring microcell. If the secondary photon directly interacts within the avalanche region of the second microcell, it triggers a prompt crosstalk signal. Delayed crosstalk signals occur when the secondary photon generates an electron-hole pair in the depleted zone of a microcell, resulting in afterpulses approximately $\mathcal{O}(10\,\mathrm{ns})$ after the main pulse. The probability of crosstalk increases with higher overvoltage. Balancing the gain against the crosstalk probability enables finding an optimal operation point with maximum resolution.

Since the breakdown voltage of a SiPM varies slightly from unit to unit due to production differences, the bias voltage for each SiPM must be individually adjustable to achieve optimal resolution. To address this, a custom-built SiPM bias supply was developed, featuring 128 individually adjustable channels. The device incorporates 14-bit high-voltage Digital-to-Analogue converters (DACs)[6], capable of outputting up to 200 V per channel. Packaged as a 6U Versa Module Eurocard (VME) unit, the device requires an external HV DC supply that exceeds the maximum bias voltage needed per channel.

As outlined in the requirements section above, a first pre-amplification stage must be positioned in close proximity to the SiPM to ensure proper signal transmission from the detector module. This is accomplished using a custom-built pre-amplifier PCB directly connected to the SiPMs PCB via a pin connector. The OpAmp-based inverting amplifier circuit is designed for high-speed, low-noise operation and configured with a gain of approximately 18. The pre-amplifier requires ±5 V power, supplied from outside the detector. During testing, significant noise interference from adjacent charge readout circuits

[6] Analog Devices, AD5535, `analog.com`

was observed. To mitigate this, the pre-amp board was equipped with metal shields. A drawing of the pre-amp board with and without shielding is shown in Figure 4.14.

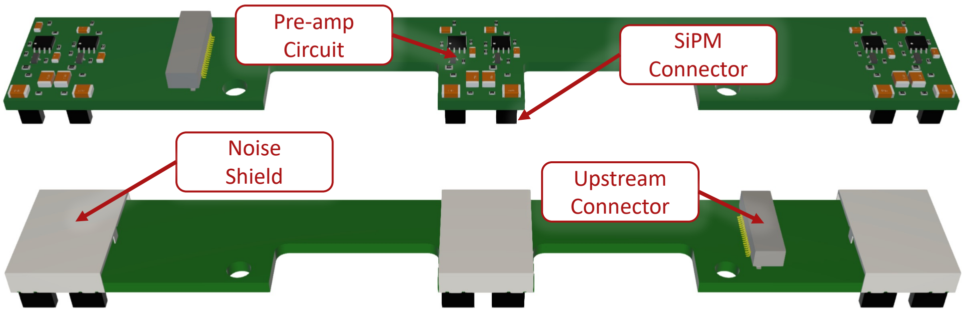

Figure 4.14 – Drawing of the pre-amp board with (top) and without noise shield (bottom).

All transmission lines between the pre-amplifier board (output signal, bias voltage supply, $\pm 5\,\mathrm{V}$ DC power) are sensitive to noise pickup. To avoid excessive noise pickup and reduce potential line-to-line cross-talk (micro)coaxial cables[7] are used. The shielding of these cables is referenced to the detector ground at the feedthrough of the cryostat.

Outside the cryostat, the signals are routed to a Variable Gain Amplifier (VGA), which adjusts the signal amplitude to account for variations in light intensity and detector conditions. This custom-built device ensures that signals stay within the dynamic range of the subsequent electronics, preventing saturation or signal loss. A dedicated VGA control system allows fine-tuning of the gain, making the system adaptable to different operational scenarios. For LED calibration runs (see details in Sec. 4.6), the amplification gain can be increased to optimise resolution in the single-photon regime. In addition to the amplified single-channel signals, the VGA outputs an analogue sum signal for each set of six channels. These sum signals are used for threshold-based triggering.

The final device in the electronics readout chain is the Analogue-to-Digital Converter (ADC) unit. Here, the amplified signal from the VGA is digitised and forwarded to the DAQ system. The commercial ADC unit[8] used in this setup features 64 input channels and a sampling rate of 62.5 MHz. A 10 Gbit fibre interface enables rapid data transfer to the DAQ servers, preventing ADC buffer overflows. The integration of the White Rabbit (WR) timing system [135] synchronises all ADCs to a sub-nanosecond level, as required. An additional ADC unit can digitise the VGA sum signals and issue threshold-based triggers.

The analogue signals are not continuously recorded but are captured only when a trigger is issued. A dedicated trigger unit[9] provides synchronous trigger signals to all ADCs.

[7]Samtec, FCF8, `samtec.com`
[8]AFI Electronics, ADC64, `afi.jinr.ru`
[9]AFI Electronics, UT24, `afi.jinr.ru`

Additionally, the trigger unit receives busy signals from each ADC and only issues a trigger when all ADCs have completed processing and are ready for new triggers. Triggers can originate from threshold-based signals from the ADC or from external sources, such as a beam trigger.

4.5 DAQ and detector configuration

The DAQ system is responsible for receiving the data stream from the ADC units and storing it in a structured format for efficient analysis. In addition to storing raw signals from the light detectors, it retrieves and records relevant information about the readout configuration and status, ensuring this metadata can be correlated with the corresponding data. This includes critical parameters such as SiPM bias settings, amplification gains, trigger thresholds, and details of known dead or malfunctioning channels.

Since the light readout does not operate as a standalone system but functions as part of a broader detector system, its DAQ system is interfacing with the other detector DAQ systems and an overall run control unit.

The ADC and trigger unit manufacturer, AFI Electronics, provides a commercial software package for unit configuration and data acquisition. This package includes three main tools: an ADC configuration utility, a trigger unit configuration utility, and an event builder. The event builder is responsible for writing data from all ADCs to file and dividing data runs into subrun files. For ease of integration, the commercial software package is run in a separate container environment with a Transmission Control Protocol (TCP) link to start and stop data acquisition. This AFI package has been integrated into a custom light readout control package, enabling all the functionalities mentioned above. An overview of the developed framework, including the interconnections between tools, is shown in Figure 4.15.

The Light Readout System (LRS) run control package[10] consists of two core tool packages. The first, *lrsctrl*, serves as the interface to the AFI package to start and stop runs. It supports running different configurations tailored for either normal physics data-taking or calibration runs (see details in Sec. 4.6). Additionally, it automatically generates and stores metadata files for each recorded data file. These metadata files include crucial information for downstream data management tools and a direct reference to the active detector configuration. The metadata is also saved to a LRS run database, allowing fast access for data analysts. Runs can be started via a user-friendly command-line interface or a specific Application Programming Interface (API). The latter can also be used by an overall run control software to coordinate runs across multiple readout systems.
The second tool package, *lrscfg*, enables centralised configuration of the full light readout electronics. This tool facilitates direct control of the SiPM bias Power Supplys (PSs), the VGAs, and the calibration pulser. Using this tool, the detector configuration can be unified into a single file called the Mother Of All Spreadsheets (MOAS). This tool fetches the

[10] `github.com/LHEP-neutrino/2x2_LRS_runcontrol`

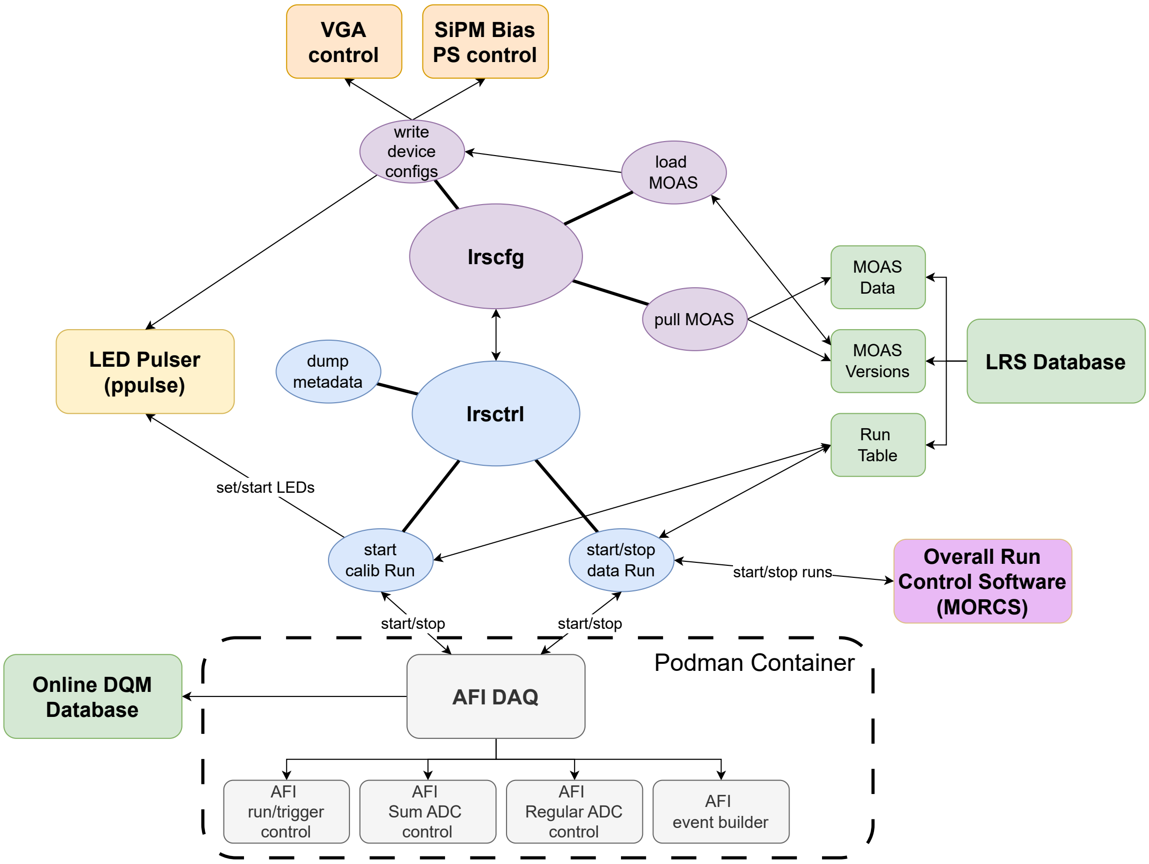

Figure 4.15 – Overview of the light readout control software, including the two main packages 'lrsctrl' and 'lrscfg'. The first manages data taking, and the latter handles loading and activating detector configurations. Both tools write relevant information into a set of configurations and run databases. The MOAS is a centralised collection of the full detector configuration, including settings such as SiPM bias and other device parameters.

configuration file from a web-based editor, parses it into device-specific formats, and activates it. Configurations are tagged with unique labels and saved in dedicated databases, allowing analysts to verify the active configuration for any recorded data retrospectively.

To ensure reliable data-taking, continuous monitoring of the system status and data quality is essential. For the light readout system, monitoring tasks are divided into two main components.

The first involves online tracking of all relevant system parameters during data-taking. This framework provides real-time feedback on system performance and alerts operators to anomalies that require immediate attention. It includes a periodic readout of the bias voltage on each SiPM. Large fluctuations in the read-back voltage could indicate the malfunctioning of single channels or transmission lines. Additionally, environmental factors such as temperature variations are monitored to ensure stable operation. Further, a large set of parameters is extracted from the ADC control and event builder stages in the AFI software. Key indicators such as trigger and data rates are monitored. Excessive trigger rates could indicate the occurrence of spurious signals not originating from actual particle interactions but, e.g., from HV discharges in the TPC volumes. By comparing these rates with reference values from calibration runs, potential issues can be quickly identified and addressed.

The second part of the monitoring is a Data Quality Monitoring (DQM) run after a data file has been completely written. It consists of a set of data quality plots extracted from the recorded raw waveforms. This nearline monitoring operates independently of the online system to allow more detailed offline analysis of data quality. A key parameter monitored is the noise amplitudes for each channel. Using Fast Fourier Transform (FFT), the noise frequency spectrum is analysed to identify potential sources of interference. Further, signal baselines and amplitudes are inspected for each channel individually.

4.6 In-situ SiPM calibration

The intrinsic gain of a SiPM is not directly fixed by its design but can vary depending on operating conditions such as temperature and bias voltage. Furthermore, small production variations between individual SiPMs result in differences in breakdown voltages. These variations necessitate accurate and consistent calibration of the gain of each individual SiPM. One effective method for achieving this is through the use of LEDs to deliver controlled and reproducible light pulses. This section describes an LED calibration setup optimised for modular TPCs, including the design of a custom LED pulser.

With the described readout system, one aims to achieve an effective calibration of the number of photoelectron (p.e.) to counts in ADC units. This factor will hereafter be referred to as the "SiPM gain" G_{SiPM} (in units of p.e. per ADC units), although it does not directly refer to the intrinsic gain of the SiPM but an overall calibration factor including the full readout chain. The most straightforward way to determine G_{SiPM} is to measure light in the single-photon regime and compare the integrated response statistically. An example is shown in Figure 4.16, where the integrated ADC counts for a light pulse are plotted as a histogram. The clearly identifiable peaks correspond to the SiPM response for no p.e. (pedestal), one p.e., two p.e., and so on. Thus, the distance between two neighbouring peaks represents G_{SiPM}. In a first approach, the centre of each peak can be extracted using, for instance, single Gaussian fits. Due to the linear response of the SiPM in this regime, G_{SiPM} can be calculated using linear regression on the peak centres. For this work, more sophisticated models that include crosstalk and afterpulsing effects can be simultaneously fitted over all peaks were used, which provided more accurate G_{SiPM} values [136].

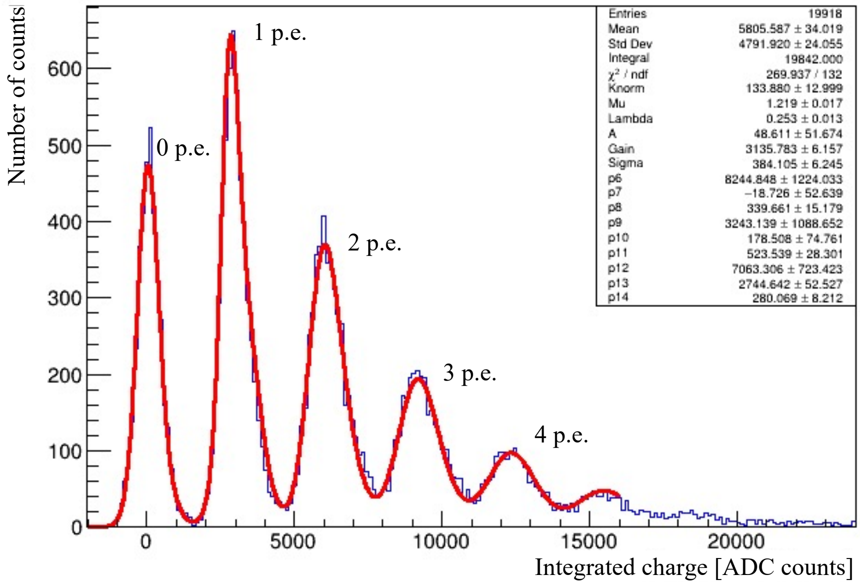

Figure 4.16 – Example ADC integral spectrum with fitted single p.e. peaks. The fit, according to the model described in [136], outputs the SiPM gain and other parameters. The peaks according to 0 (pedestal), 1, 2, 3, 4 p.e. are labelled.

4.6.1 LED setup

LEDs are a convenient light source for achieving single-photon light yield in the modular TPC setup. They are compact, operable at LAr temperature, and have a tunable light yield. As only single photons need to reach the SiPMs, a small number of LEDs per TPC is sufficient. In the setup shown in Figure 4.17, cylindrical diffusers made of Polytetrafluoroethylene (PTFE) are placed in front of the LED to distribute the light isotropically across the entire TPC volume. For this purpose, the tip of the diffuser is designed to protrude slightly into the TPC volume. An LED emitting in the visible blue spectrum was selected as the most efficient option for ArCLight calibration.

To operate in the single-photon regime, very short $\mathcal{O}$(ns) voltage pulses are sent to the LED. To avoid reflections in the transmission lines, the LED PCB is equipped with two resistors to match the input impedance to the 50 Ω coaxial cable used to deliver the pulse from outside the detector to the calibration LED.
However, the higher impedance introduces challenges for the device providing the voltage pulse. Significantly higher signal amplitudes are required compared to configurations without the additional resistors. During cryogenic testing, it was found that peak voltages of 10 V to 60 V are needed to achieve a single-photon light yield for SiPMs at various positions relative to the calibration LED.

To optimise the light yield for each SiPM in a modular detector, the LED pulse amplitude is individually tuned. These adjustments result in a large set of LED settings to be scanned to generate a full calibration dataset for the entire detector. Furthermore, to fine-tune the SiPM bias voltage for optimal resolution, multiple calibration datasets at different settings are recorded. This large number of required LED configurations and

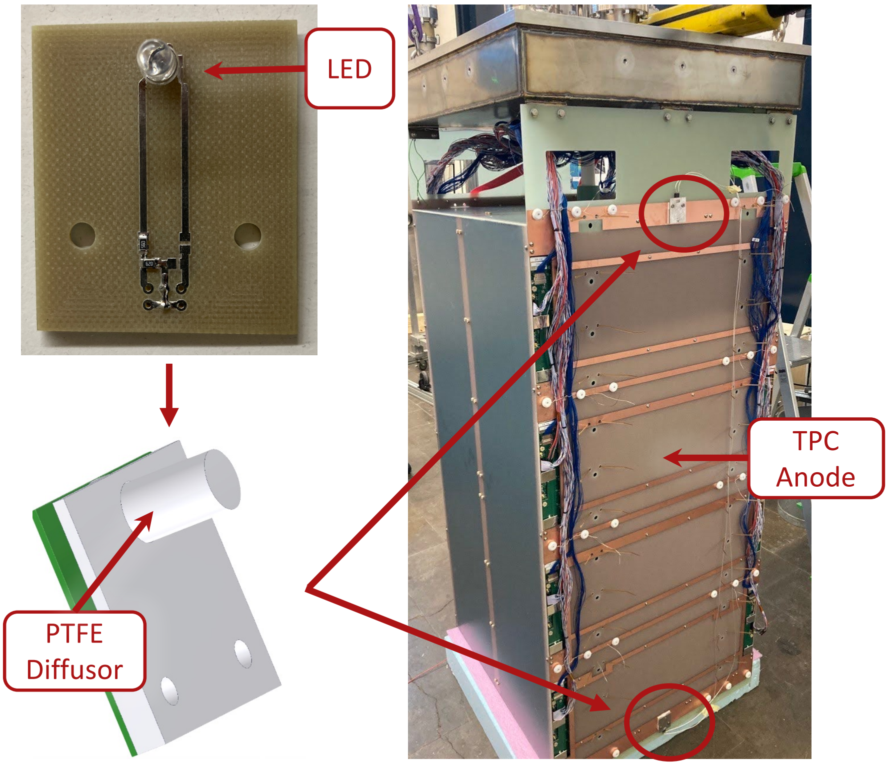

Figure 4.17 – Calibration LED setup. The LED mounted on a PCB (top left) is inserted in a PTFE diffuser (bottom left), which together can be mounted at multiple locations of a TPC anode plane (right). Here, as an example, the setup for a single module of the 2x2 demonstrator is shown.

the need for reproducibility make manual tuning impractical, necessitating fast digital control of amplitude settings. Since no commercial pulser unit with > 10 output channels meeting all these requirements was available, a custom LED pulser device was developed in the course of this thesis.

Achieving a high-voltage pulse with a nanosecond pulse length is challenging since most commercial electronics designed for this speed are built for low-voltage applications. After evaluating multiple methods, the use of a Bipolar Junction Transistor (BJT) transistor in avalanche mode was chosen as the most effective solution. In the avalanche (or Geiger-mode) configuration, the transistor is biased beyond its breakdown voltage. In this state, the high electric field across the base-collector junction accelerates free carriers, such as electrons, to energies sufficient to generate further charge carriers, resulting in an avalanche effect in the depletion zone of the transistor. Initiated by a small trigger pulse, the rapid buildup of carriers generates a sharp current pulse through the transistor. Since this avalanche process is self-sustaining, it must be controlled by the circuit design to avoid damage to the transistor. This is achieved by providing the current to the transistor from a capacitor and limiting the recharging of the capacitor with a resistor. The complete schematic of the developed pulser stage is shown in Figure 4.18.

To tune the output amplitude of the pulse stage, two Metal Oxide Semiconductor Field

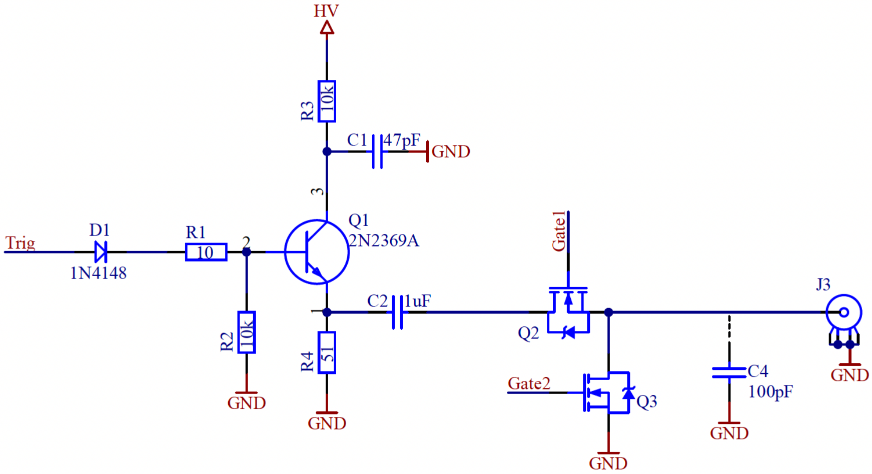

Figure 4.18 – Schematic of a single-channel pulser stage based on a avalanche-mode BJT transistor Q1.

Effect Transistors (MOSFETs), effectively acting as variable resistors, are placed at the output. The first MOSFET is in series with the output signal, and by applying a bias voltage to its gate terminal, the output voltage is increased. The second MOSFET is connecting to ground, resulting in a reduction of the output voltage once the gate is biased.

Sixteen individual pulser stages are mounted on a shared main board. The main board provides a common trigger signal and the HV required to operate the avalanche transistor. A compact single-board computer[11] interfaces with the pulser device, controlling the trigger pulse and managing a set of DACs that supply bias voltages to all MOSFET attenuators on the pulser stages. The entire setup, including the required AC-to-DC converters, is housed in a compact single-unit standard rack case, as shown in Figure 4.19. The developed control software[12] incorporates an API, allowing direct and remote control of the pulser. The LRS control software, using the previously tuned optimal LED settings for each SiPM, calculates the minimal number of calibration runs required to cover all channels. This calculation takes into account that calibration runs can be executed simultaneously across multiple TPCs, streamlining the process.

[11] Raspberry Pi, Model 4A, `raspberrypi.com`

[12] `github.com/LHEP-neutrino/2x2PulserSoft`

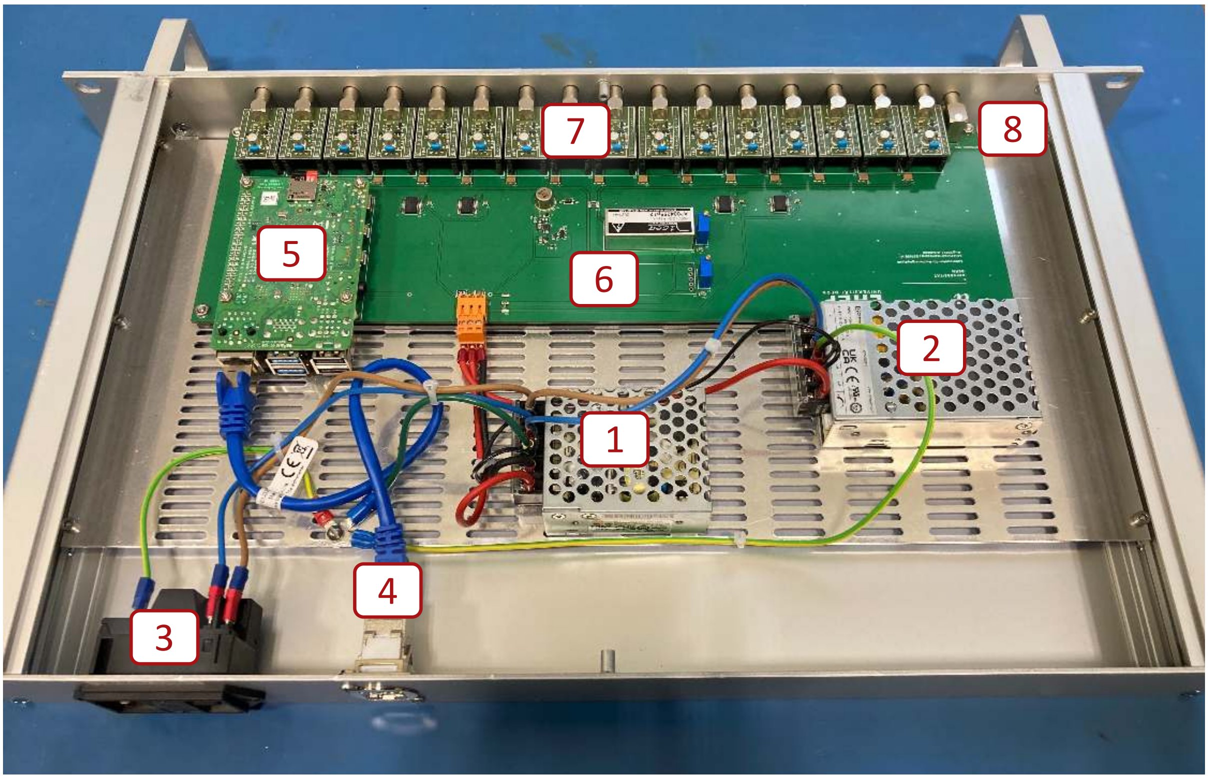

Figure 4.19 – Setup of the 16-channel LED pulser. 1: 5V AC/DC, 2: 12V AC/DC, 3: Fused AC input, 4: Ethernet port, 5: Controller (Raspberry Pi 4A), 6: Main board, 7: Single-channel pulser units, 8: Trigger In/Out

4.7 Light Simulation

Simulations play a critical role, as they enable comparisons between model-based expectations and experimental data. In addition to simulating primary neutrino interactions, it is essential to accurately model the detector's interaction with particles and its response. An accurate detector simulation enables simulation-based performance studies to analyse the impact of single design parameters that are not easily tunable in experimental setups. Reconstruction and analysis algorithms can be developed and validated using simulation data before applying them on data. This section focuses on the light simulation developed specifically for a modular detector, which is part of the ND-LAr simulation. For completeness, a short overview of the ND-LAr simulation is given.

4.7.1 Photon creation

At the start of the simulation chain, a Monte Carlo (MC) particle generator produces the primary particles resulting from the initial interaction between the incident particles and the liquid argon. The incident particles normally originate from neutrino beam generators like GENIE [137] but can also be replaced with different sources, e.g. cosmic event generators like COsmic Ray SImulations for KAscade (CORSIKA) [138]. To simulate the propagation and energy deposition of the resulting particles, a GEometry ANd Tracking 4 (GEANT4) wrapper called energy deposition simulation (edep-sim) [139] was used. GEANT4 [140] is a software toolkit used for simulating the passage of particles through matter, which is widely applied in particle physics.

The edep-sim stage does not include the LArTPC specific processes of ionisation charge propagation and scintillation light creation. For this purpose *larnd-sim*, a GPU-accelerated detector simulation, was developed by the ND-LAr consortium[141, 142]. *larnd-sim* was specifically written for the modular detector of ND-LAr. Due to the very large number of charge and light readout channels, a highly-parallelised implementation was needed, which could not be achieved by existing frameworks such as LArSoft [143].

For the light simulation, *larnd-sim* includes a scintillation model to simulate the photon emission based on the energy deposit given by the edep-sim stage. The calculation of the scintillation light yield is based on the recombination factor, which is evaluated with the Box model as described in Section 3.2. The time profile of the photon creation is based on a two-component exponential model accounting for the fast and slow components of the LAr scintillation process.

4.7.2 Photon propagation

The MC simulation of the photon propagation through the detector volume and the light detectors until reaching the SiPM is computationally very intensive. Since the PDE of the light detectors is relatively low ($\mathcal{O}(1\,\%)$) and the majority of photons are absorbed by various materials, the tracking of every single photon for each simulated neutrino interaction is very inefficient. Due to this fact, this part of the simulation was disengaged from *larnd-sim* and only included as a Look-Up-Table (LUT). The LUT contains voxelised information for the entire detector volume on the probability of detecting a photon created at a certain location on a specific SiPM (visibility), and an average time profile of the photon arrivals for each channel. By combining the light yield information with visibility from the LUT, the mean number of p.e. expected per SiPM can be calculated. By convoluting the scintillation time profile with the photon propagation time distribution from the LUT, the time of arrival of every single photon per channel is modelled.

The LUT is based on a photon propagation simulation implemented in GEANT4. An initial version of the ArgonCube Optical Simulation (ArCubeOptSim)[13] was developed in previous work [127, 132]; in the course of this thesis, further improvements were conducted, and the final production versions for the 2x2 demonstrator and the full-size ND-LAr detector were produced.

The GEANT4 implementation requires a geometry description of the detector as a Geometry Description Markup Language (GDML) file. To generate this, a tool was developed by the DUNE ND consortium[14] based on the GGD toolkit[15]. Engineering Computer-

[13] `github.com/Frappa/ArCubeOptSim`
[14] `github.com/DUNE/dunendggd`
[15] `github.com/brettviren/gegede`

Aided Design (CAD) drawings were used to generate GDML files for the 2x2 demonstrator modules and the full-size ND-LAr modules.

Besides the geometry file containing information on the materials and volumes, an optical properties description is needed. This includes the optical properties of each material and interface occurring in the detector. The implementation uses the Optical Photon Processes library[16] included in GEANT4. For the definition of optical interfaces, one can either rely on the model calculations based on the refractive indices of the two materials involved (e.g. WLS plastic - LAr) or define own interfaces by providing detailed angle and wavelength-dependent information on the reflectivity and transmittance of the interface (e.g. dichroic mirror). Wavelength-shifting processes and material absorption can be defined for any material.

For the production of the LUT, the active volume of a TPC is split into voxels of about $10\,\mathrm{mm} \times 10\,\mathrm{mm} \times 10\,\mathrm{mm}$ (for 2x2 TPCs) or $15\,\mathrm{mm} \times 15\,\mathrm{mm} \times 15\,\mathrm{mm}$ (for full-size TPCs). In each voxel, 10^3 positions are randomly selected, and 10^4 photons are simulated per position, resulting in 10^7 photons simulated per voxel. Each photon is propagated through the detector until it either gets absorbed in a material or hits the surface of a SiPM. The number of photons that eventually hit a certain SiPM surface is multiplied by the wavelength-dependent quantum efficiency of the SiPMs to get the mean number of detected p.e. per voxel. Dividing this number by the total number of photons emitted per voxel results in the visibility expressed in units of average number of p.e. per emitted photon. Figure 4.20 shows the total visibility of each voxel for a full-size ND-LAr TPC.

The ND-LAr includes not only ArCLights but also LCMs, a complementary light trap design, which will be described in Section 5.5. Due to the difference in PDE between the LCM and ArCLight, a clear pattern with spots of higher visibility close to the SiPMs of the LCMs can be identified. The visibility simulation allows the extraction of the fraction of the active volume, in which a certain amount of deposited energy can be detected for a given threshold in number of p.e.. This is shown in Figure 4.21. For comparison, the plot includes a typical energy threshold per pixel of the CRS (as achieved in the 2x2). Even when assuming a conservative threshold of 10 p.e., for any energy deposit above 0.6 MeV the detector has a full spatial coverage to detect the emitted light.

Besides the visibility information, the distribution of the time interval between photon creation and detection at the SiPM per voxel and channel is stored in the LUT. This information enables an accurate T_0 simulation in *larnd-sim*.

[16] `geant4-userdoc.web.cern.ch/UsersGuides/ForApplicationDeveloper/html/TrackingAndPhysics/physicsProcess.html#optical-photon-processes`

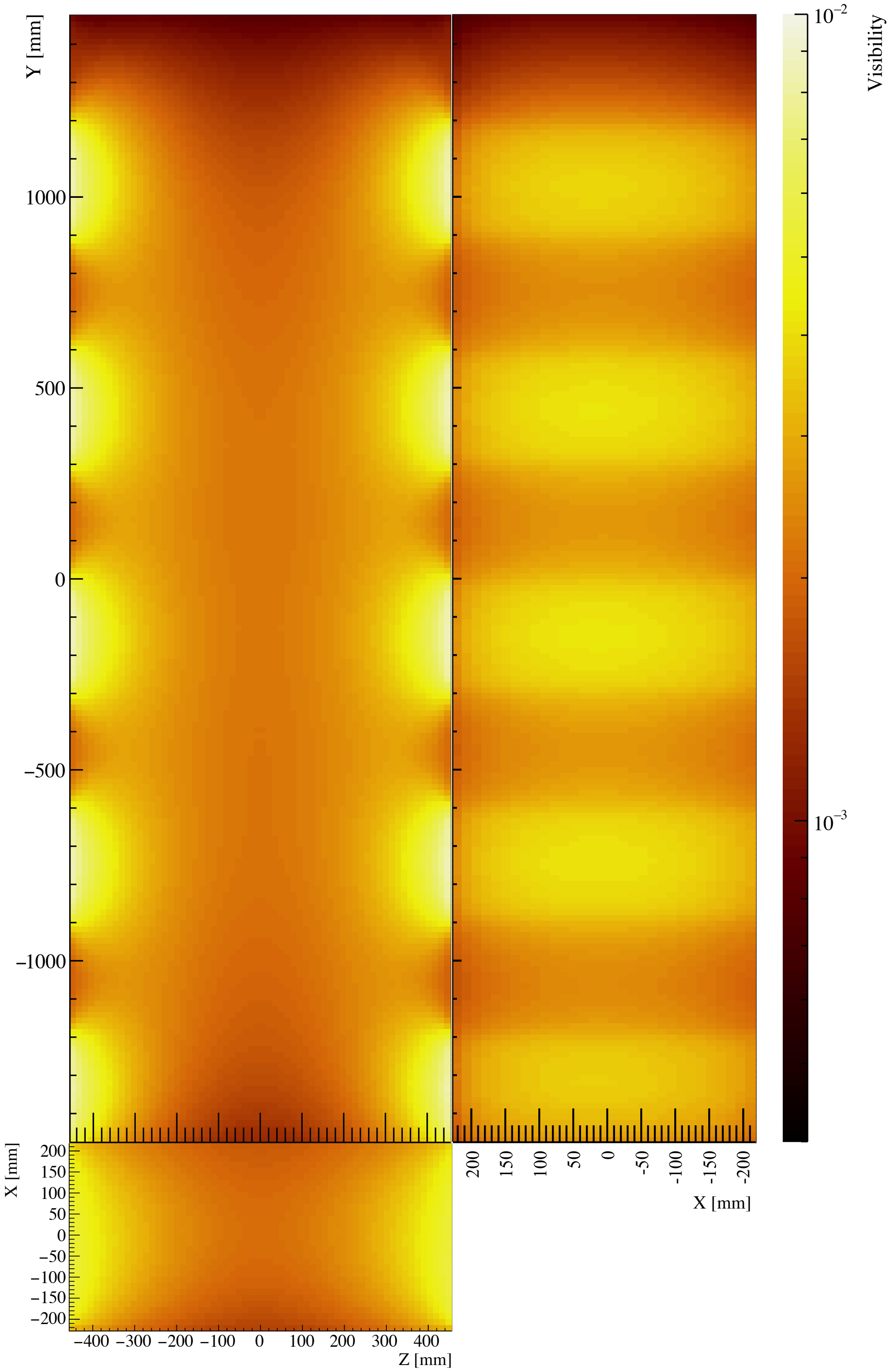

Figure 4.20 – Visibilty map for a full-size ND-LAr TPC in all three projections. The visibility drawn is averaged over all voxels in the projection direction and summed over all SiPM channels.

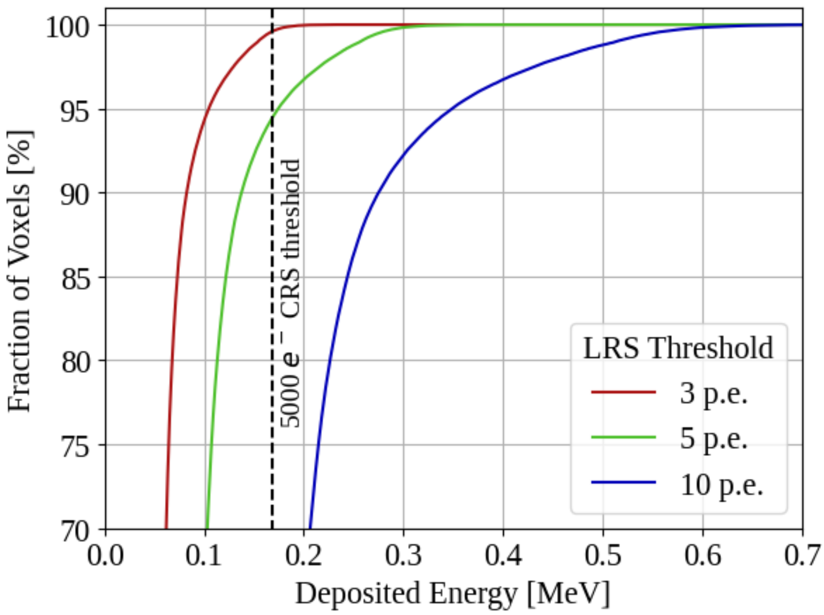

Figure 4.21 – Detector coverage versus total deposited energy for different light thresholds based on the visibility simulation for an ND-LAr module. The indicated 5000 e^- CRS pixel threshold is a typical threshold achieved in the 2x2 demonstrator.

4.7.3 Electronics response

Based on the average number of expected p.e. on the SiPM and their temporal distribution, the response of the readout electronics can be simulated. A Poisson random generator is used to calculate the effective number of p.e. per time bin. The probability of direct and delayed crosstalk can also be included at this step by using an appropriate model [144]. A linear ADC model with a realistic SiPM gain factor is applied to the simulated waveform. The ADC sampling rate and resolution are applied by linearly interpolating the simulated waveform. The waveform is overlayed with a simulated noise, which is based on a Fourier spectrum extracted from real prototype data, including channel-by-channel variations. The noise is randomised by applying an individual phase for each noise frequency.

The simulated readout window is triggered, as in real, by either a threshold crossing on a simulated sum channel or an external enforced trigger (e.g. beam). The final product of the light simulation are the simulated waveforms and several truth parameters, such as the number of photons created, which are saved for each event. An example for a simulated waveform is shown in Figure 4.22.

4.8 Light Reconstruction

The raw waveforms, either recorded in detector data or generated by the MC simulation, are processed by reconstruction algorithms to retrieve the relevant information contained. The goal is to feed the light data to high-level reconstruction algorithms, such as Pandora [145] or MLreco [146], which identify particles and reconstruct their energies using both charge and light data. To achieve this, the light data must first undergo a low-level reconstruction to produce so-called flash objects. A flash is a collection of temporally and spatially isolated light hits on multiple SiPMs. In its current implementation, spatially isolated is defined as contained within a single TPC.

For this purpose, a software toolkit was developed called *ndlar-flow*[17], which can process both charge and light data. The ndlar-flow package is based on *h5flow*[18], a framework for creating simple sequential workflows for HDF5 datasets, with parallelisation capabilities to run on High-Performance Computing (HPC) clusters. The light reconstruction in *ndlar-flow* was originally developed and described in [142]. In the course of this thesis, the reconstruction was refined and extended, as well as adapted for 2x2 and ND-LAr. While charge and light data are processed separately initially, they are later cross-referenced. This section focuses exclusively on light data processing.

The first stage of the light processing is an event builder, which can parse data from both the MC simulation input and the detector data input. The main goal is to produce a common output format, enabling the application of identical reconstruction stages to both data and MC. For data inputs, binary files written by the DAQ system are parsed into two datasets: one for raw waveforms and another for event-level information, such as trigger timestamps. An event here is equivalent to a single readout window, defined as the period of data acquisition initiated by a trigger signal and encompassing the recorded data from all readout channels (For 2x2, a readout window was 16 µs long). For MC simulation, the *larnd-sim* output file is reformatted into the same structure with additional truth information.

Due to the slow component of the scintillation light ($\mathcal{O}(1\,\mu\text{s})$), light signals often overlap even if their associated interaction times are separated by hundreds of ns. To disentangle these overlapping signals on a single SiPM, the waveforms are deconvolved to remove the scintillation time profile. Further precision can be achieved by additionally deconvolving the electronic response profile. In *ndlar-flow*, the deconvolution is performed using a Wiener filter. Based on noise and signal frequency spectra extracted directly from data, the Wiener filter simultaneously subtracts noise and applies the deconvolution (details in [142]). Extracting signal spectra directly from data ensures that both scintillation and electronics response are included simultaneously. Alternatively, if the goal is to preserve the scintillation pulse shape information, only the electronics response can be deconvolved from the raw waveform. To do so, LED calibration data is used to extract the pure electronics response (without an underlying scintillation pattern). Figure 4.22 shows an example waveform with overlapping hits before and after deconvolution of both the scintillation profile and electronics response.

By normalising the integral over the signal and noise spectra fed to the Wiener filter to one, the integrated charge of a waveform peak before and after deconvolution remains consistent. After applying the SiPM gain G_{SiPM} factor extracted from LED calibration

[17] `github.com/DUNE/ndlar_flow`
[18] `github.com/larpix/h5flow`

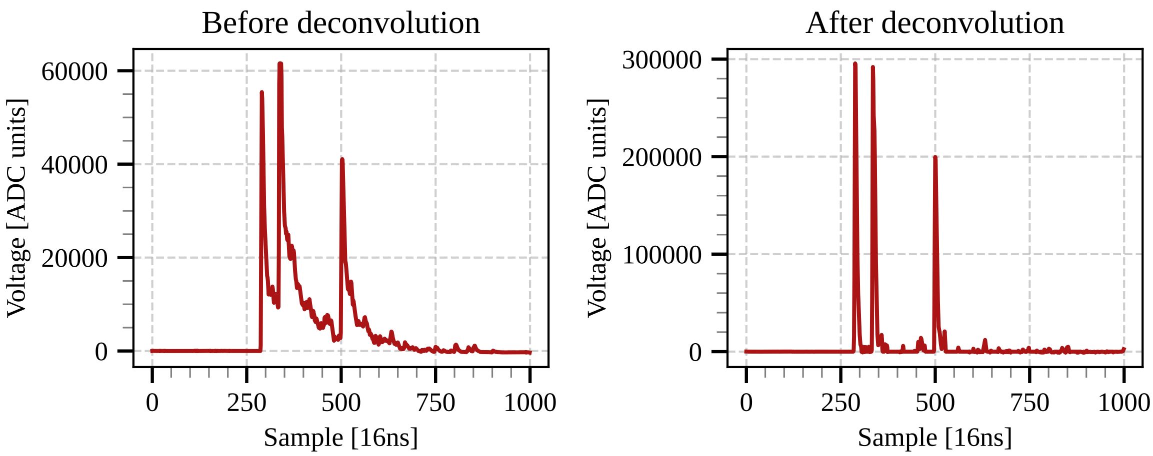

Figure 4.22 – Single SiPM waveform with multiple overlapping hits before (left) and after (right) deconvolution.

runs (see Sec. 4.6), the deconvoluted waveform can be translated into units of p.e. per time tick, allowing for the total number of p.e. per peak to be extracted by summing over the waveform section.

With the first prototype module for ND-LAr (Module-0), significant noise pickup from the CRS was observed on the light readout. Although this issue was resolved later (see Sec. 4.4), an additional noise filtering was implemented before the actual Wiener filter. The designed noise filter specifically targets coherent 10 MHz noise pickup. Using the pre-trigger portion of each waveform, an interpolated pattern is extracted and subtracted from the full waveform. This filter is dedicated solely to removing the 10 MHz noise while leaving the noise pattern else unaffected. Examples of waveforms before and after applying the noise filter are shown in Figure 4.23.

Based on the deconvolved waveforms after the Wiener filter, light hits can be extracted. A simple threshold-based hit finder is used to identify local maxima in the deconvolved waveforms. Beyond the location and amplitude of each peak, further information is obtained by integrating over the entire peak.

To obtain timing information for each hit with a precision below the sampling rate, various methods were explored. Finally selected was a method previously applied by MicroBoone [147], which extracts timing information by fitting the rising edge of the raw waveform with the function

$$f(t) = A * exp\left(-\frac{(t - T_{\max})^N}{B}\right), \tag{4.1}$$

where A, B and $t_{\max}$ are free fitting parameters and $N = 2, 4, 6, ...$ is a fixed parameter. From the fitting function, two different ways were examined to define the reconstructed T_0 value. In the first definition, the timestamp at the half-max value (HM) of the fitting function is chosen as T_0. From the fitting function, this value can analytically be

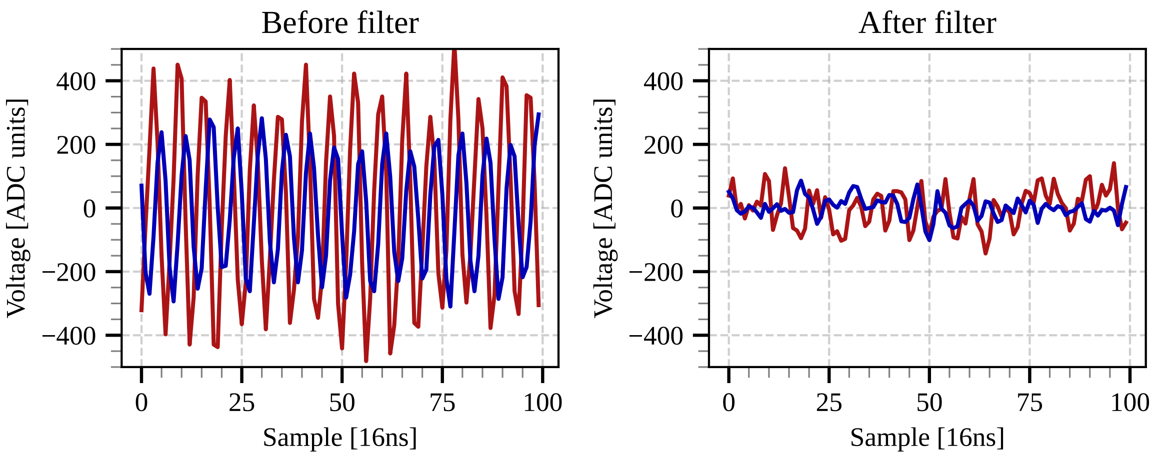

Figure 4.23 – Two example noise-only SiPM waveforms (blue and red) before (left) and after (right) the 10 MHz filter for Module-0.

calculated as

$$T_0^{\mathrm{HM}} \stackrel{\mathrm{def}}{=} T_{1/2} = T_{\max} - (B * log(2))^{1/N}. \tag{4.2}$$

For the second, more sophisticated method, the derivative at the half-max point is calculated

$$\left.\frac{\partial f}{\partial t}\right|_{t=T_{1/2}} = \frac{AN \log^{\frac{N-1}{N}}(2)}{2B^{1/N}}, \tag{4.3}$$

which is used to construct a linear extrapolation to the rising edge

$$g(t) = \frac{A}{2} + \left(t - T_{1/2}\right) \cdot \left.\frac{\partial f}{\partial t}\right|_{t=T_{1/2}}. \tag{4.4}$$

T_0 is then defined as the crossing point of this linear extrapolation (EX) with the signal baseline

$$g(t = T_0^{\mathrm{EX}}) \stackrel{!}{=} T_{1/2} \quad \Rightarrow \quad T_0^{\mathrm{EX}} = T_{1/2} - \frac{A}{2}\left(\left.\frac{\partial f}{\partial t}\right|_{t=T_{1/2}}\right)^{-1}. \tag{4.5}$$

The two definitions are illustrated in Figure 4.24.
Both possible definitions with different parameter values of N were studied extensively on simulation data. To do so, the reconstructed $T_{0,\mathrm{reco}}$ values were compared to true photon emission times $T_{0,\mathrm{true}}$. For both T_0 definitions, the reconstruction performances were almost identical for $N = 4, 6, 8$, but significantly better compared to $N = 2$. For all further studies, $N = 4$ was chosen.

For the simulation truth studies, the timing resolution of the ArCLight was compared to the LCM, an alternative light detector design described in Section 5.5. The results for the discussed T_0 definitions are shown in Figure 4.25. The precision of the half-max method is significantly superior with an observed FWHM of the residual $\Delta T_0 = (T_{0,\mathrm{reco}} - T_{0,\mathrm{true}})$ of 4.6 ns (0.29 samples) for the ArCLight and 3.4 ns (0.21 samples) for the LCM.

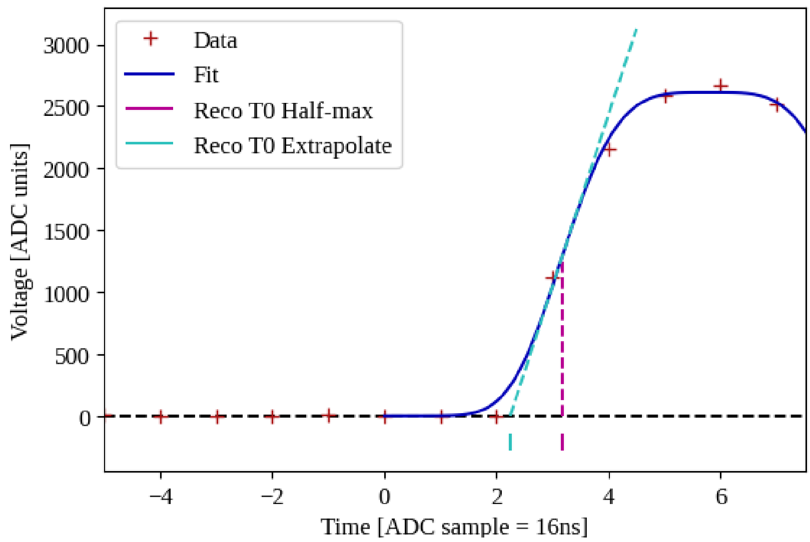

Figure 4.24 – Hit level T_0 reconstruction with the half-max method and the extrapolation method shown on a hit waveform.

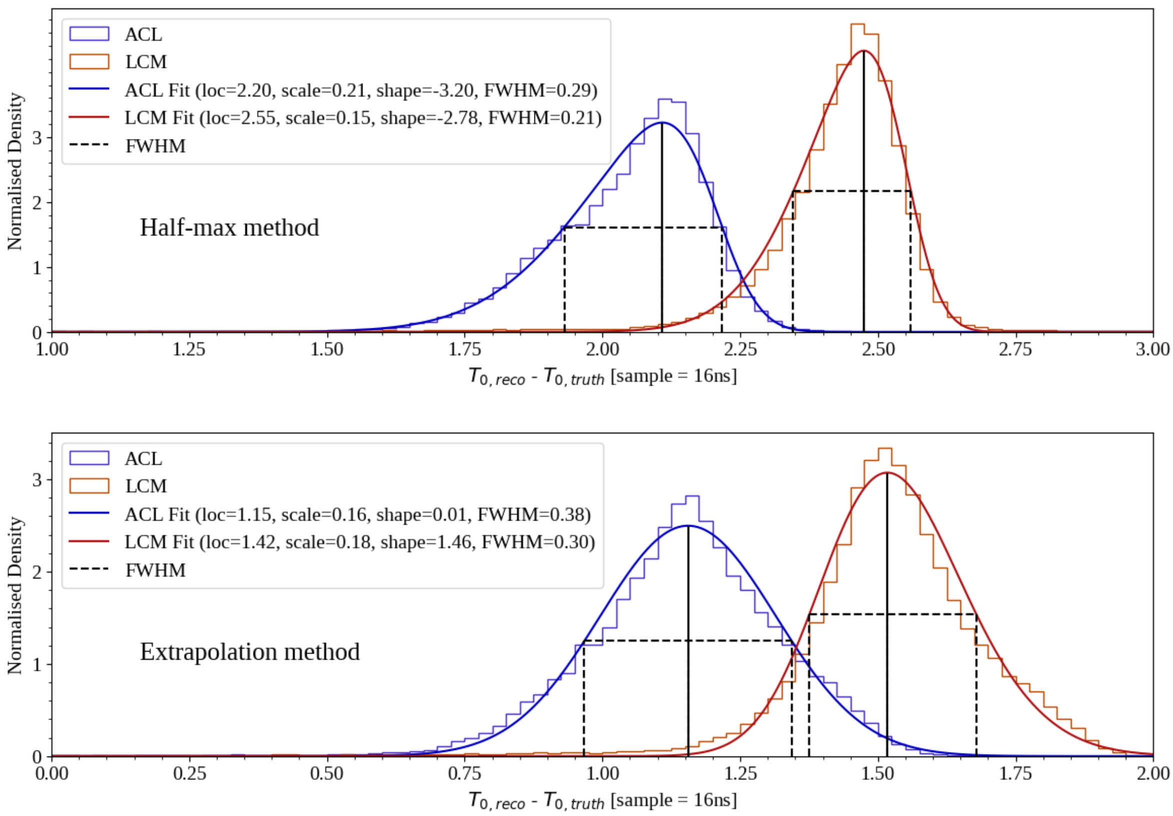

Figure 4.25 – Reconstruction to truth comparison of the T_0 hit time for the ArCLight and LCM. Upper: Half-max method; Lower: Extrapolation method.

Although the absolute residuals for the extrapolation method are lower, its precision is notably worse with a FWHM of 6.1 ns (0.38 samples) for the ArCLight and 4.8 ns (0.30 samples) for the LCM.

In the reconstruction, light hits are extracted for each single SiPM waveform. To combine the information from multiple channels, these hits are clustered into flashes. Clusters are identified per optically isolated TPC of a modular detector. An example of raw waveforms together with the detected SiPM hits and flashes are shown in Figure 4.26.

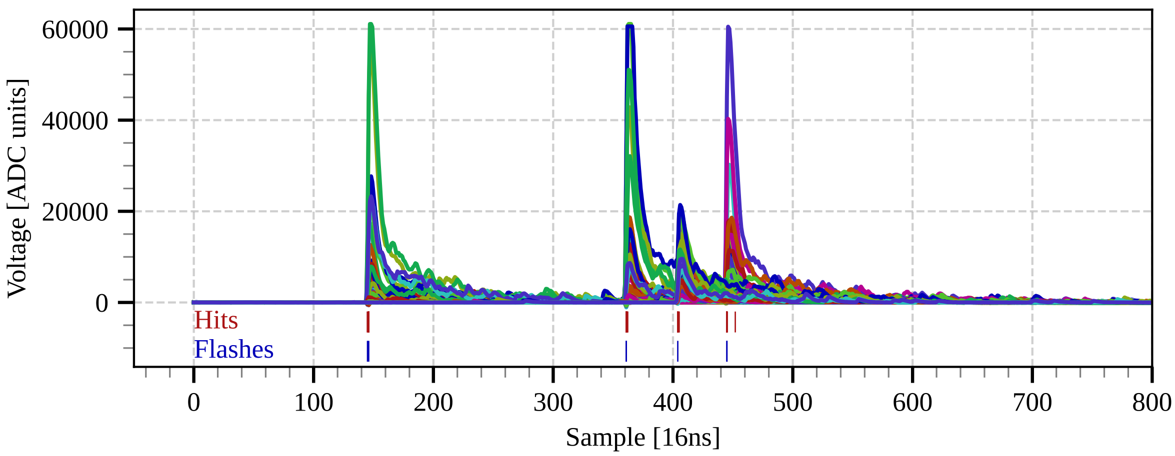

Figure 4.26 – Example raw SiPM waveforms with detected hits (red) and flashes (blue). For the plotted waveforms each channel is identified with a separate color.

Future improvements could include clustering of light hits below this boundary by identifying spatial hit clusters within a TPC. Flash objects contain information on the total light and time distribution of individual hits, which can be directly fed into high-level reconstruction algorithms to match flashes with identified charge tracks.

Chapter 5

The 2x2 Demonstrator - Motivation and Design

The most straightforward geometric arrangement to test the modular principle of ND-LAr and the interoperability of such modules is to put four modules in a two-by-two arrangement. Named after this arrangement, the 2x2 demonstrator consists of four scaled-down prototype versions of an ND-LAr module and forms a vital component of the prototyping campaign for the final ND-LAr. By placing the 2x2 in the neutrino beam of the NuMI facility at FNAL, the detector can not only serve as a technology demonstrator but also as a physics demonstrator. In this chapter, the experiment setup is discussed in detail, covering all subsystems. In the following, the 2x2 demonstrator will simply be referred to as the "2x2".

5.1 Overview and Motivation

The 2x2 is designed to test the modular principle of ND-LAr and evaluate the interoperability of such modules. By arranging four scaled-down modules in a two-by-two configuration, the setup offers valuable insights into how well the individual components function both independently and in coordination with one another. One of the primary motivations is to assess interactions which are spread over multiple modules, particularly in terms of shared spaces like dead volumes, and how these influence the event reconstruction and overall detector performance. Being able to reconstruct these shared interactions is critical for optimising the reconstruction in the full ND-LAr detector.

With 2x2, the full ND-LAr event reconstruction chain can be tested. This includes the capability to process data from multiple TPCs for track finding, calorimetry, and vertex reconstruction, ensuring that the algorithms designed for the full ND-LAr detector will work efficiently in the multi-module environment. The demonstrator also focuses on pile-up reconstruction, testing the ability of the system to accurately reconstruct events where multiple interactions overlap in time, a necessary feature for handling data from a high-intensity neutrino beam.

The NuMI beam, in detail described in Section 5.2, allows not only testing the detector performance in detecting and reconstructing neutrino interactions but also conducting stand-alone physics analyses. Such studies are vitally needed to improve current models on neutrino-argon interactions and thereby ensure the success of the DUNE program. Details about the physics potential of the 2x2 will be discussed in Section 5.2. Another key goal of the 2x2 program is to evaluate the long-term operation of the TPC modules. The 2x2 will run for extended periods, allowing for the evaluation of the detector's reliability and performance over time, which is essential for the successful operation of the full ND-LAr detector. During this long-term operation, the stability and performance of both the light and charge readout systems are evaluated. In particular, for the light readout, studying the potential degrading of the photon detection efficiency is relevant as issues with the robustness of WLS substrates on the light detectors have been observed previously [148].

In DUNE, the ND-LAr detector will not be a stand-alone experiment but will be integrated into the ND complex (see Ch. 2.4.2). The interoperability with the other detectors in this complex is vital for the success of DUNE. In particular, the downstream-placed muon tracker (Phase I: TMS, Phase II: ND-GAr) is required to measure outgoing muons from ND-LAr, and its data needs to be matched with ND-LAr at a single interaction level. The 2x2 detector faces the same issue but at an even more severe level: due to its relatively small size, muons (and also other particles) will be even less contained in the active volume. To mitigate this, scintillator planes are placed downstream of the TPCs to track outgoing particles. Additional tracking planes upstream help to tag incoming particles, such as muons generated in beam interactions with rock. These tracking planes are repurposed from the MINERνA experiment, wherefore they are referred to as "Mx2" within the 2x2 project (see Sec 5.4). With Mx2 installed, the 2x2 can also be used to test combined operations within a detector complex.

Additionally, the 2x2 focuses on setting up and testing the auxiliary systems needed for its operation, including triggering, timing synchronisation, data management, combined run controls, and slow control monitoring. These systems are vital for ensuring efficient data acquisition and operation throughout the experiment. Similar systems will be needed for the ND-LAr operation.

Although the cryogenic system for ND-LAr will be substantially different from that of the 2x2, certain operational aspects can still be tested. In particular, the filling and emptying procedures can be tested given the requirements for maximal temporal and spatial gradients of the temperature over the detector. The cryogenic system will be further discussed in Section 5.3.

The core of the 2x2 are the LArTPC modules mounted in the main cryostat. Figure 5.1 provides an overview of these main components of the 2x2 and their arrangement along the NuMI beamline. The detectors are centred around the beamline to have the maximum possible flux through the active volume.

Fig 5.2 shows an illustration of the entire 2x2 setup, including the access platforms. The detector platform gives direct access to the cryostat top flange. Since the space on this detector platform is very limited, most of the electronics had to be placed in racks on the

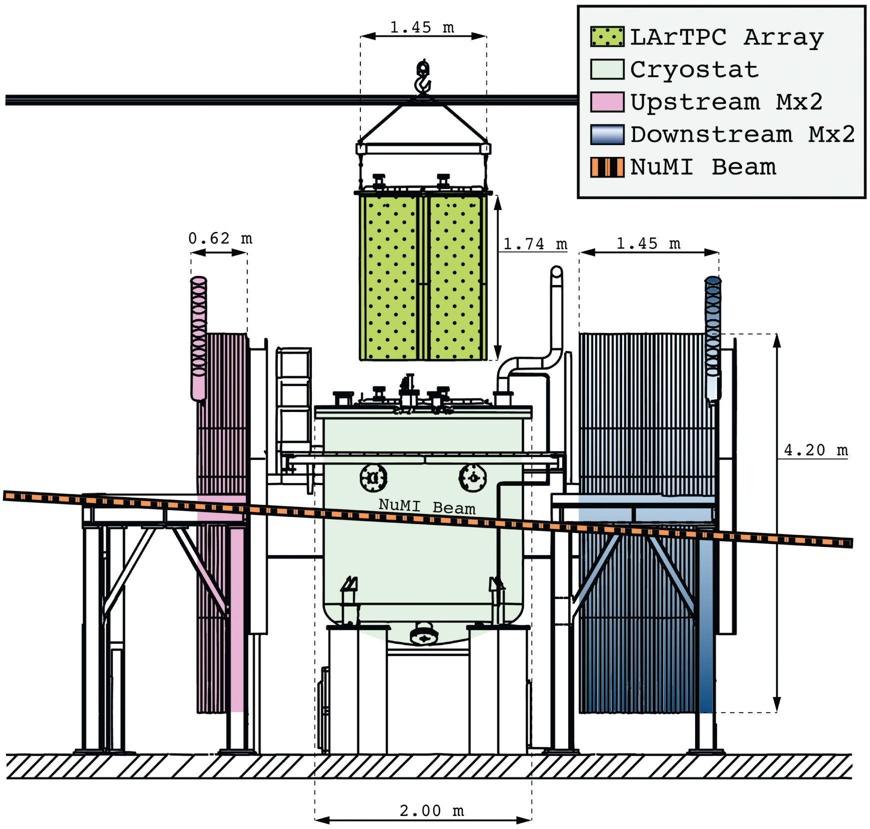

Figure 5.1 – Overview of the main components of the 2x2, including dimensions to scale. To get a better impression of the dimensions, the LArTPC array is depicted hanging on a crane before they are inserted into the cryostat. The centre of the incoming NuMI beam (from left to right) is shown in its relative position to the detector components.

catwalk from which the detector platform is accessed. One single rack could be placed just next to the cryostat top flange, which is used by the light readout to minimise the cable length of the analogue signal to the amplifiers (details see Sec. 5.5).

The four prototype modules installed in the 2x2 have outer dimensions of 67 cm × 67 cm × 175 cm. Each module consists of two TPCs with a central cathode placed along the beam axis. An anode plane has a total surface of 62.0 cm × 124.0 cm. With a distance of 30.3 cm between the cathode and anode, the active volume per TPC is 0.233 m^3. A technical drawing of a single module is shown in Figure 5.3. Figure 5.4 shows a picture of the inside of a single module. Combining the 8 TPCs of all modules, we get a total active LAr volume of 1.864 m^3, equivalent to an active mass of 2.6 t.

The main structure of the TPC modules is made of 3.2 mm thick G10 sheets. G10 is the material of choice since it has ideal properties for cryogenic applications (very low thermal contraction), a high dielectric strength (200 kV/cm) and has a similar radiative and hadronic interaction length as the surrounding argon [149], which reduces unwanted effects on particle tracks at the module borders. At the same time, the G10 body serves as the electric field-shaping structure [13]. For this purpose, the side, top and bottom sheets

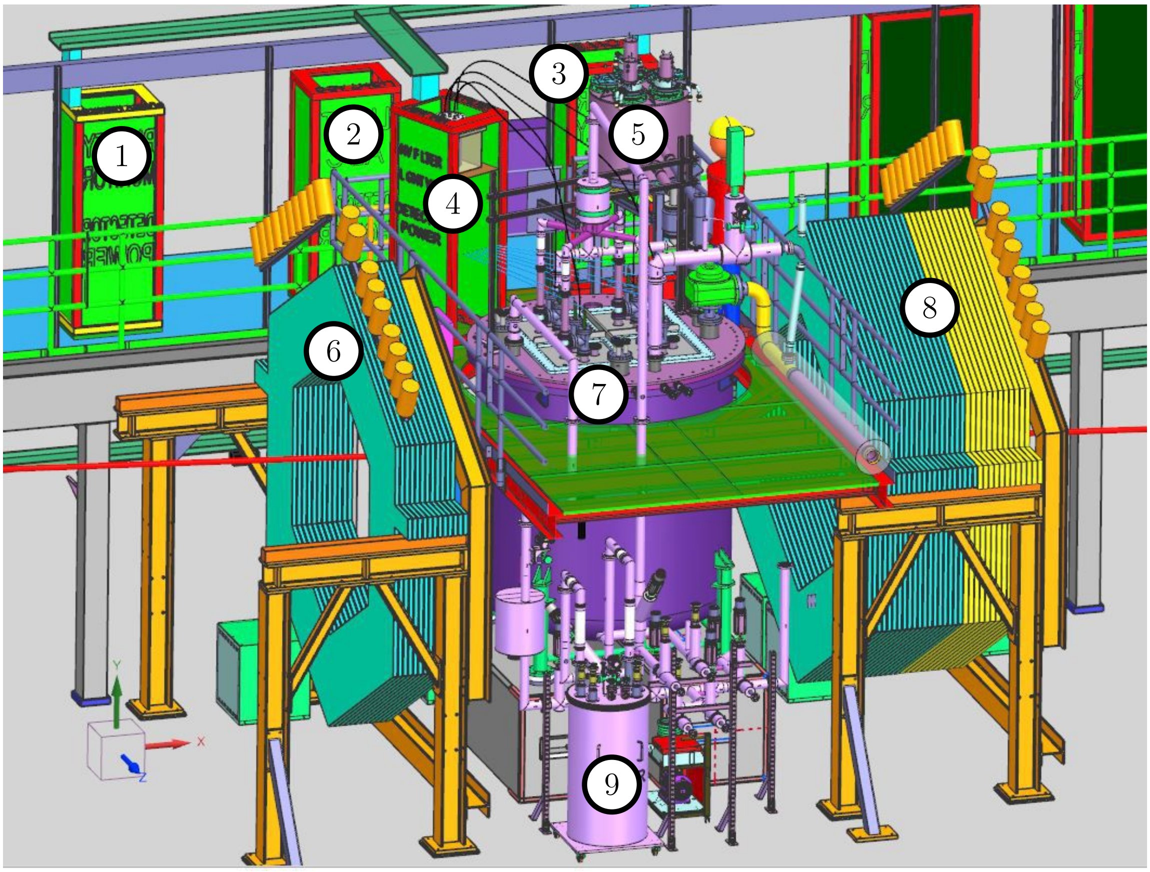

Figure 5.2 – CAD drawing of the 2x2 including the access platforms and electronics racks. **(1)** Purity monitor rack; **(2)** LRS ADC rack; **(3)** DC power supply rack; **(4)** LRS VGA rack; **(5)** Argon condenser; **(6)** Upstream Mx2; **(7)** Main cryostat; **(8)** Downstream Minerva trackers in 2x2 (Mx2); **(9)** LAr filter cryostat.

are laminated with a resistive layer of carbon-loaded Kapton film (DR8[1]). The film has a sheet resistance of $\mathcal{O}(1\,\mathrm{G}\Omega/\mathrm{sq})$ at operational conditions (87 K, -15.1 kV at the cathode) ensuring a uniform gradient of the electric potential along the drift direction. The same type of material but with a $\mathcal{O}(1\,\mathrm{M}\Omega/\mathrm{sq})$ sheet resistance is laminated on both sides of the cathode to ensure a uniform potential on the entire surface. The top and bottom sheet is equipped with uniformly distributed 4 mm holes to allow circulation of liquid argon from top to bottom (see Sec. 5.3). To improve the top-to-bottom LAr circulation, the module is inserted in a G10 sleeve, which also helps to protect the electronics mounted on the anode planes.

For all four modules, a single HV power supply[2] is used. An HV filter that also serves as a distribution box is placed in between the power supply and the modules. It consists of a container filled with transformer oil equipped with an RC low-pass filter ($10\,\mathrm{M}\Omega$, 2 nF) designed for up to 60 kV. A voltage divider attached to each output line of the filter can be used to monitor the voltage present on the cathode.

[1] DuPont™, DR8 polyimide film, `www.dupont.com`
[2] Spellman, SL50x300, `www.spellmanhv.com`

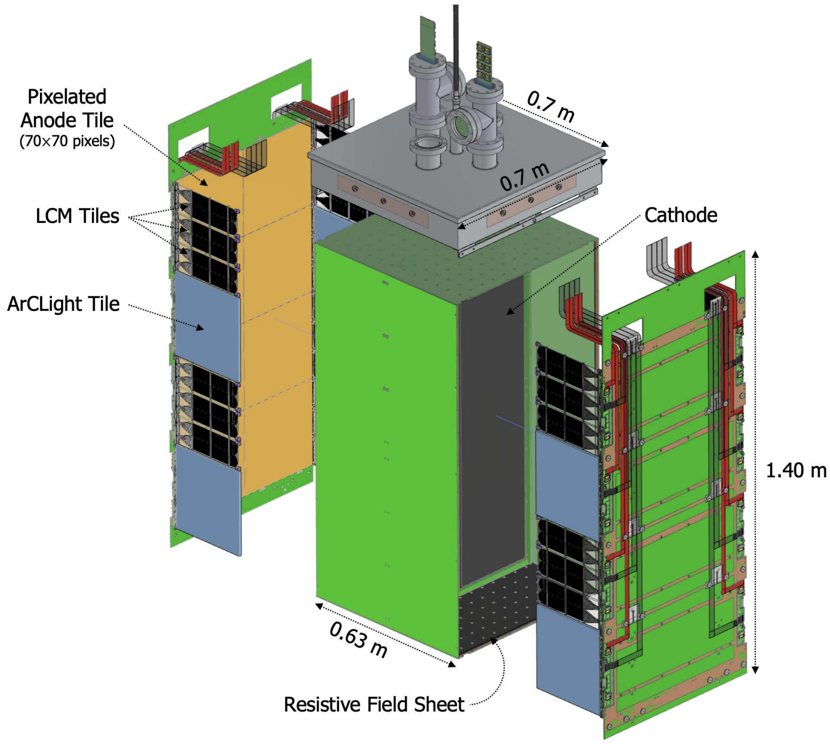

Figure 5.3 – Technical drawing of a single 2x2 module including cables and top flange. For clarity, the two anode planes (with the attached instrumentation) are extracted from the field structure.

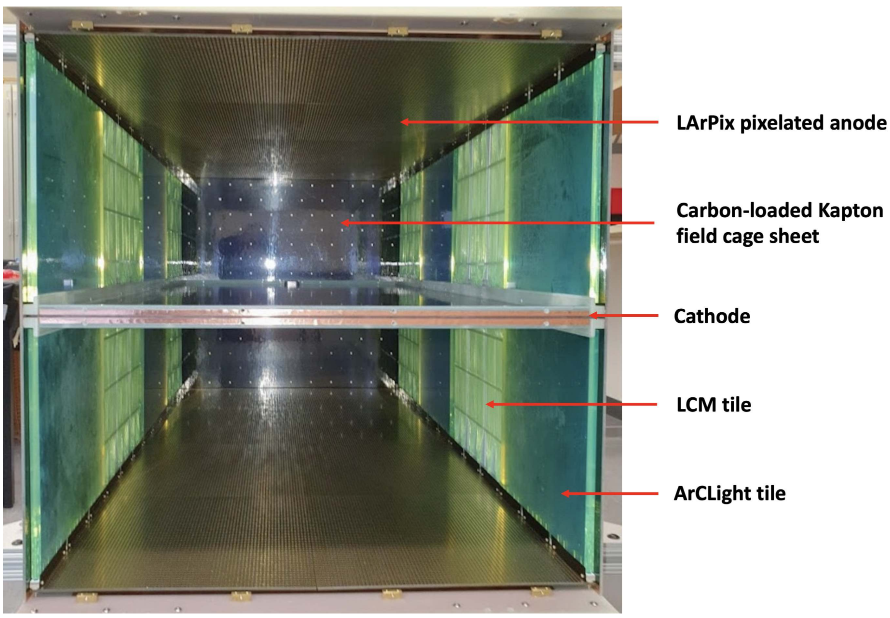

Figure 5.4 – View into a 2x2 module module with the bottom panel removed. In operation, the central cathode is brought to a negative potential, creating two symmetrical drift chambers with the anodes on the top and bottom of the picture. The light detectors are mounted on the left and right sides.

5.2 NuMI beam and backgrounds

The 2x2 is located in the MINOS ND underground facility at FNAL at ∼102 m below the surface. The 225 meters water equivalent (m.w.e.) [150] of rock provide efficient shielding from cosmic radiation backgrounds. Based on Mei and Hime [151], the cosmic muon flux can be approximated with

$$I_\mu(h_0) = 67.97 \times 10^{-6} e^{-\frac{h_0}{285}} + 2.071 \times 10^{-6} e^{-\frac{h_0}{698}}, \tag{5.1}$$

where h_0 is the vertical depth in m.w.e. and $I_\mu(h_0)$ is the muon flux at this depth in $\mathrm{cm}^{-2}\mathrm{s}^{-1}$. For the 2x2, the estimated muon flux at its location is ∼0.50 Hz. This calculation is not accounting for the vertical expansion of the detector, therefore can only be used for an order of magnitude estimation.

The 2x2 has energy thresholds for charge and light readout low enough that ^{39}Ar decays become a significant source of background. ^{39}Ar with a half-life of 268 y is produced through the interaction of cosmic rays with atmosphere of the Earth and is therefore present in trace amounts in the atmospheric argon that is used in the 2x2. The isotope decays by beta decay, emitting electrons with an energy of up 565 keV. The specific activity of ^{39}Ar in atmospheric Argon is $(1.01 \pm 0.02\ \text{(stat)} \pm 0.08\ \text{(sys)})$ Bq/kg [152], which for the active mass of 2x2 results in 2.6 kBq. The fraction of decays that can be detected can be calculated by integrating over the energy distribution of the beta electron[153]. Assuming an energy threshold of 200 keV for the charge readout, 53 % of the decays should be detectable. Thus, a background event rate of ∼1.4 kHz on the charge readout is expected. The energy threshold for the light readout is dependent on the position of the interaction in the detector. Only ^{39}Ar decays occurring very close to the light traps can be detected. Nevertheless, using charge and light event matching to eliminate noise events, the ^{39}Ar activity can be used to probe the electric field uniformity close to the light traps. The ^{39}Ar activity is uniformly distributed over the detector. Thus, detecting areas with lower or no activity gives a strong indication that the charge from this area can not drift to the anode due to field non-uniformities.

The 2x2 is placed on the NuMI beam axis as shown in Figure 5.5. To get a better understanding of the structure of the beam, it is necessary to look at how it is produced [154].

The NuMI beam is currently one of the most intense neutrino beams in the world. To achieve such a beam, highly energetic protons are directed at a fixed target to ultimately generate the neutrinos. In the case of the NuMI, a complex chain of accelerator stages is needed to reach the desired energy and intensity ranges. An overview of the FNAL accelerator complex is shown in Figure 5.6. At the very start, hydrogen ions H^- are pre-accelerated to 750 keV using a Radio-Frequency Quadrupole (RFQ) and fed into the Linear Accelorator (Linac) which accelerates them to 400 MeV. At the subsequent Booster stage, the two electrons are stripped from the ion to have pure protons, which are then accelerated to 8 GeV. The Booster is a 468 m circumference rapid-cycling synchrotron, which operates at 53 MHz and can hold up to 84 proton bunches. The following Main Injector is a synchrotron with a seven times larger circumference than the Booster.

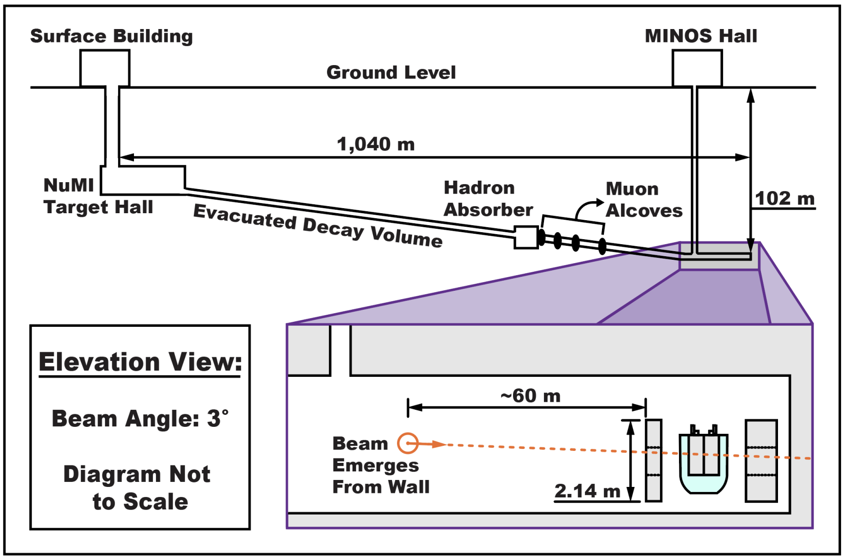

Figure 5.5 – The 2x2 is placed in the former MINOS ND cavern ~1040 m downstream of the NuMI target. The cavern is at 102 m (or 225 m.w.e.) below surface. In the "muon alcoves" after the hadron absorber, muon trackers are placed to do beam monitoring and extract precise beam timing information.

Thus, six "batches" of 84 proton bunches can be stored after each other, and one slot is needed for the pulse kicker rise time. Using the so-called "slip-stacking" technique, multiple Booster batches can be stacked into the same Main Injector bunches, resulting in a higher beam intensity. The protons in the Main Injector are accelerated to 120 GeV before the beam pulses with a total length of 9.6 µs are distributed to the different beamlines. The period between two beam pulses can vary depending on the beam configuration, but commonly is ~1.2 s.

One of these beamlines directs the protons to the 350 m away NuMI target hall. In the target stage, the protons strike an arrangement of graphite fins with a sophisticated cooling infrastructure. The outcomming particles are focused with a set of two magnetic horns. By setting the current direction on these horns, one can decide to focus either π^+/K^+ or π^-/K^- particles, which are dominantly produced. The π^+/K^+ (π^-/K^-) are then led into a 675 m long decay pipe where they decay into μ^+ (μ^-) and ν_μ ($\overline{\nu}_\mu$). The residual hadrons are absorbed by a 5 m thick absorber. The following 240 m of rock absorb most of the muons produced in the decay processes. Muon tracker stages, referred to as Resistive Wall Monitor (RWM), are placed in four alcoves in the rock to monitor the beam. These trackers are also used to get a sub-nanosecond timing of the beam (see Sec. 5.7 for details). The ν_μ ($\overline{\nu}_\mu$) pass the absorber stations and enter as a directed beam into the MINOS cavern.

The on-axis neutrino energy spectrum peaks at approximately 5.6 GeV. The beam flux and expected event rates for 2x2 compared with ND-LAr are shown in Figure 5.7a. The NuMI peak energy is almost three times as high as the LBNF beam but of much lower intensity. However, since there is roughly a linear relationship between neutrino energy and cross-section, the expected neutrino event rate is in a comparable range for 2x2 and

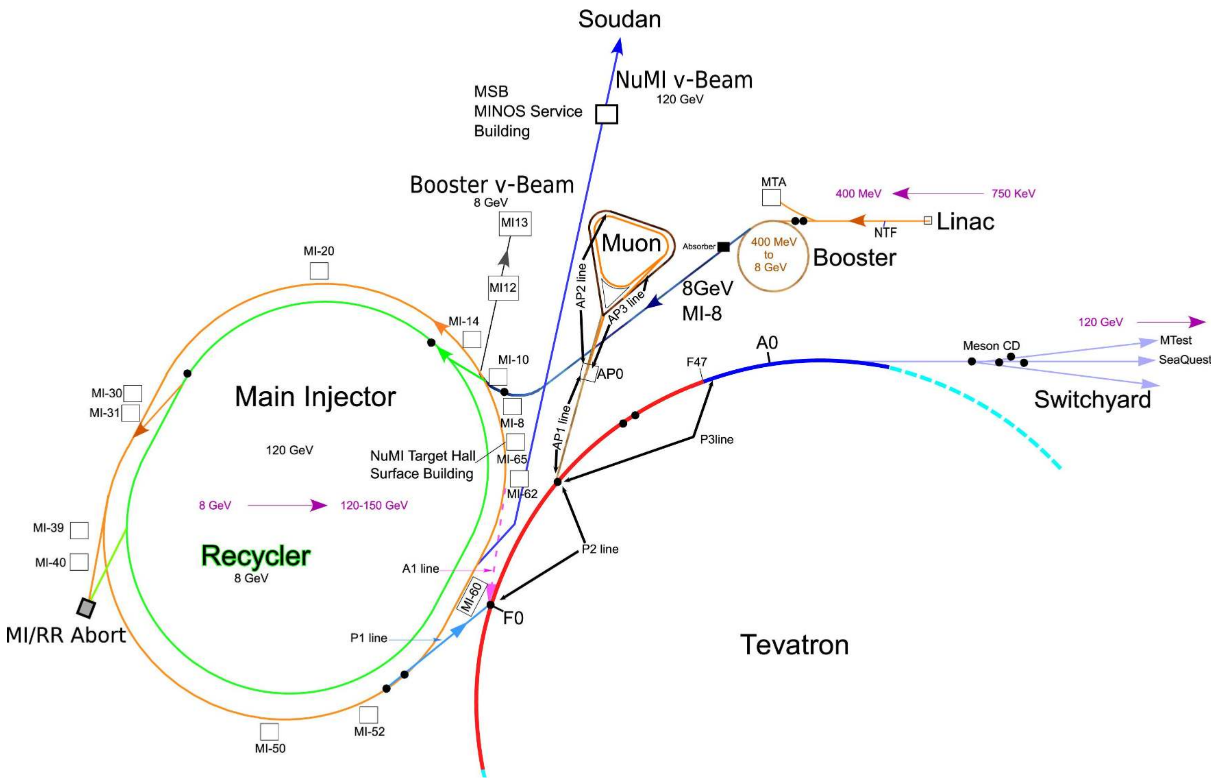

Figure 5.6 – The FNAL accelerator complex is a network of different accelerator and storage stages which are used by a broad spectrum of experiments. For the NuMI beam, the Linac, the Booster and the Main Injector are most relevant. With these three stages, protons with an energy of 120 GeV can be produced, which are used to create the high-intensity NuMI beam. The shown Tevatron was decommissioned in 2011. [154]

DUNE ND-LAr, as shown in Figure 5.7b. In the event rate plot (and all the following plots), a fiducial mass of 1.7 t is assumed, which is likely underestimated compared to the total active mass of 2.6 t.

Figure 5.8 shows that, based on simulations, the number of ionisation tracks coming out of a primary neutrino vertex is comparable for 2x2 and ND-LAr. The similar complexity of the interaction topologies allows the verification of the reconstruction methods, which can later be directly applied to ND-LAr data. This statement also holds when looking at the production rates of important final state particles, as shown in Figure 5.9. Although, in particular, for μ, the momentum distribution is broader, the overlap of the spectra is significant. Therefore, the 2x2 provides real-data samples to verify the reconstruction performance. [8]

The broad-energy spectrum of the NuMI beam enables neutrino-argon cross-section measurements at energies that are not covered by existing experiments [8]. The experiments in the Booster Neutrino Beam (BNB) beam at Fermilab (MicroBoone [57], SBND/ICARUS [53]) only cover lower energy ranges as shown in Figure 2.4. Some of the most relevant cross-section measurements were taken by ArgoNeuT [101], which took data in a lower energy mode of NuMI beamline with a peak neutrino energy of $\sim$3 GeV. Although

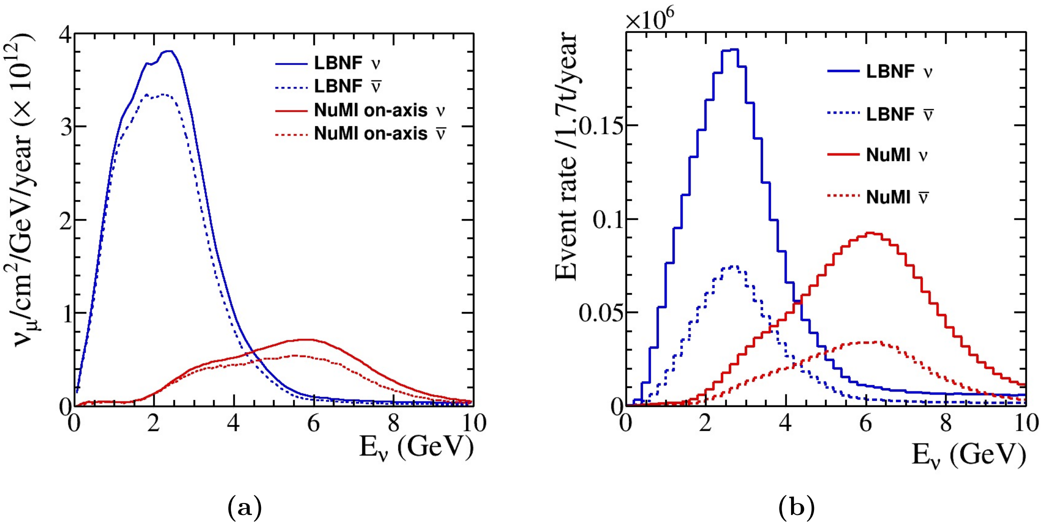

Figure 5.7 – Comparison of absolutely normalised beam fluxes (a) and expected rates (for a fiducial mass of ∼1.7 t) (b) for ND-LAr (in the LBNF beam) and 2x2 (in the NuMI on-axis beam). [8]

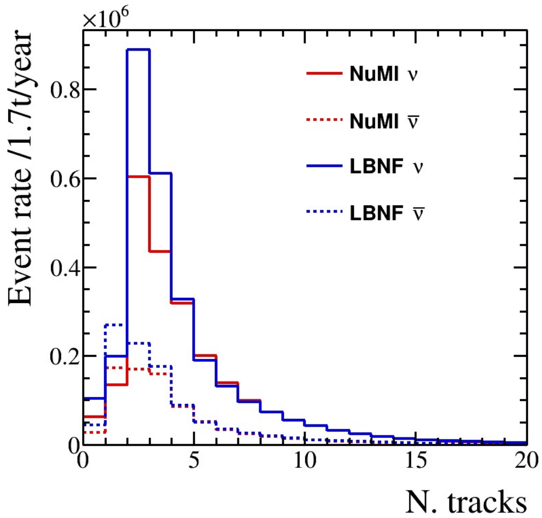

Figure 5.8 – Expected track multiplicity at the primary neutrino vertex for 2x2 (in NuMI) and DUNE ND (in LBNF beam). [8]

the detector itself had, due to its small size, a poor event containment, by making use of the downstream placed MINOS-ND, an excellent reconstruction of exiting muons could be achieved. The experiment predominantly took data in the $\overline{\nu}_\mu$ beam configuration.

Neutrino-argon cross-section measurements are crucial for reducing uncertainties in DUNE oscillation studies. While neutrino interactions with single nucleons are generally considered to be better understood, significant uncertainties remain, especially in the energy regions dominated by baryonic resonance production (RES) and in the transition range to Deep Inelastic Scattering (DIS) interactions. Moreover, particles produced in these interactions can undergo further interactions within the nucleus before exiting (Final State Interaction (FSI)), which can substantially alter the final-state particle topology. Current

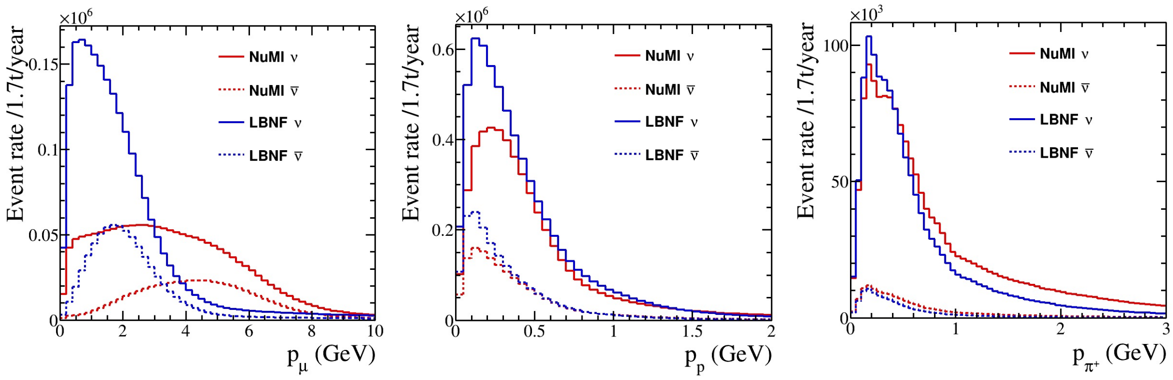

(a) μ **(b)** p **(c)** π^+

Figure 5.9 – Expected production rates for μ, p, π^+ (for a fiducial mass of $\sim$1.7 t), as a function of their momentum, in 2x2 (in NuMI beam) and DUNE ND (in LBNF beam). [8]

models describing such intranuclear dynamics in argon exhibit considerable uncertainties. This is illustrated in Figure 5.10, which shows the impact of these model uncertainties on the δ_{CP} sensitivity.

Accessing higher energy regions has a direct impact on the complexity of final-state particle topologies. In existing LAr experiments like SBND, the pion multiplicity in CC interactions is significantly lower than in 2x2 or later in ND-LAr, as shown in Figure 5.11. The 2x2 gives the unique opportunity to perform cross-section measurements of CC1π and CC2π interactions, vitally needed to improve the model uncertainties for DUNE oscillation analyses as described above. E.g. for CC2π the only existing measurements

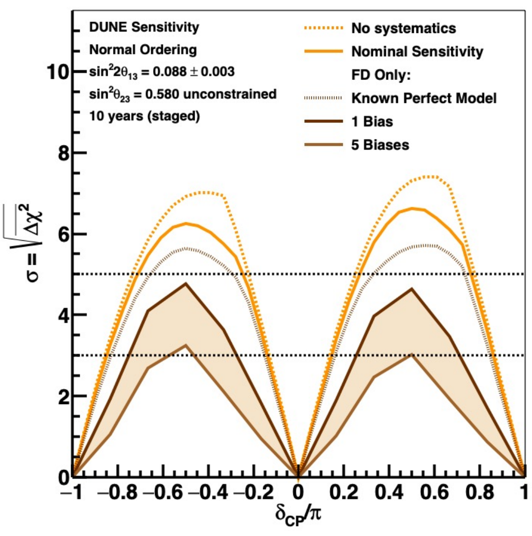

Figure 5.10 – DUNE δ_{CP} sensitivity for different levels of systematic uncertainties. To illustrate the impact of the cross-section model, the difference between two existing models (GENIE and NuWro) is used to introduce a reconstruction bias (1 bias) leading to systematic uncertainties. Since, conservatively, even larger biases have to be assumed, the impact of a five times higher bias is plotted as well. [8]

are exclusively from deuterium-filled bubble chamber experiments from the '70s and '80s with very low statistics [155, 156]

A major challenge for these potential physics measurements in 2×2 is the limited containment capability of the detector. In particular, for high-energy events, the relatively small size of the detector results in a large fraction of interactions producing final-state particles that exit the active volume. Although the downstream Mx2 planes assist in tagging such particles, particularly muons, the absence of a magnetic field prevents precise momentum reconstruction. It is noteworthy that final states with higher particle multiplicities, such as multi-pion production, can exhibit improved containment efficiency compared to low-multiplicity topologies. This is due to the distribution of the available energy among several particles, which reduces the individual particle momenta and, consequently, the probability of all products escaping the detector volume.

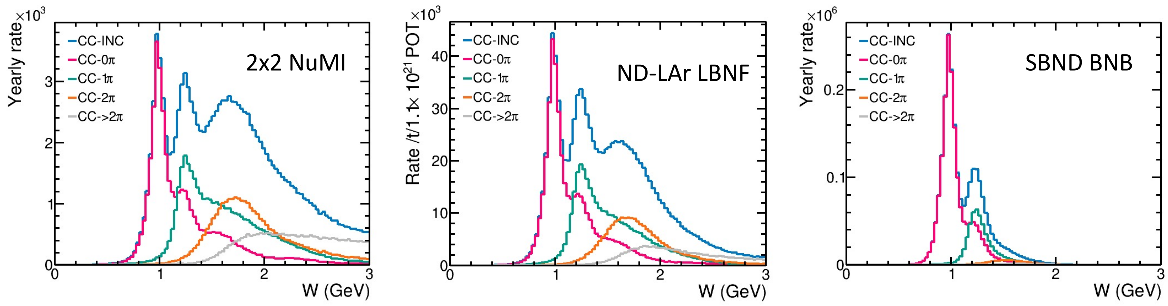

(a) (b) (c)

Figure 5.11 – Expected pion multiplicity rates in CC final state particles, as a function of the hadronic invariant mass (W) for 2x2 (in NuMI beam), ND-LAr (in LBNF beam) and SBND [53] (in BNB beam). Plots provided by C. Wilkinson.

5.3 Cryogenics

The TPC modules of 2x2 are operated in a common liquid argon bath. The four modules are hosted in a $\sim$6 m^3 cryostat, which is reused from previous experiments. Having this existing cryostat with a diameter of $\sim$2.2 m, the upper limit for the size of the footprint of the prototype module was set. For long-term operation, access to the cryostat for maintenance work is required every year. To allow this, the modules were installed in the cryostat using indium seals. The four modules are directly attached to a stainless steel frame, which allows the installation and extraction of all modules together. A 2.5 mm diameter indium wire is placed between the module top flange and the frame in a dedicated grove. Indium is a very soft metal and, under compression, starts flowing away and filling up every potential leak spot between the two objects. The same technique is used to attach the frame to the cryostat. After re-extracting the frame (or a single module from the frame), the indium seal can be replaced, and no welds or similar have to be cut and re-welded.

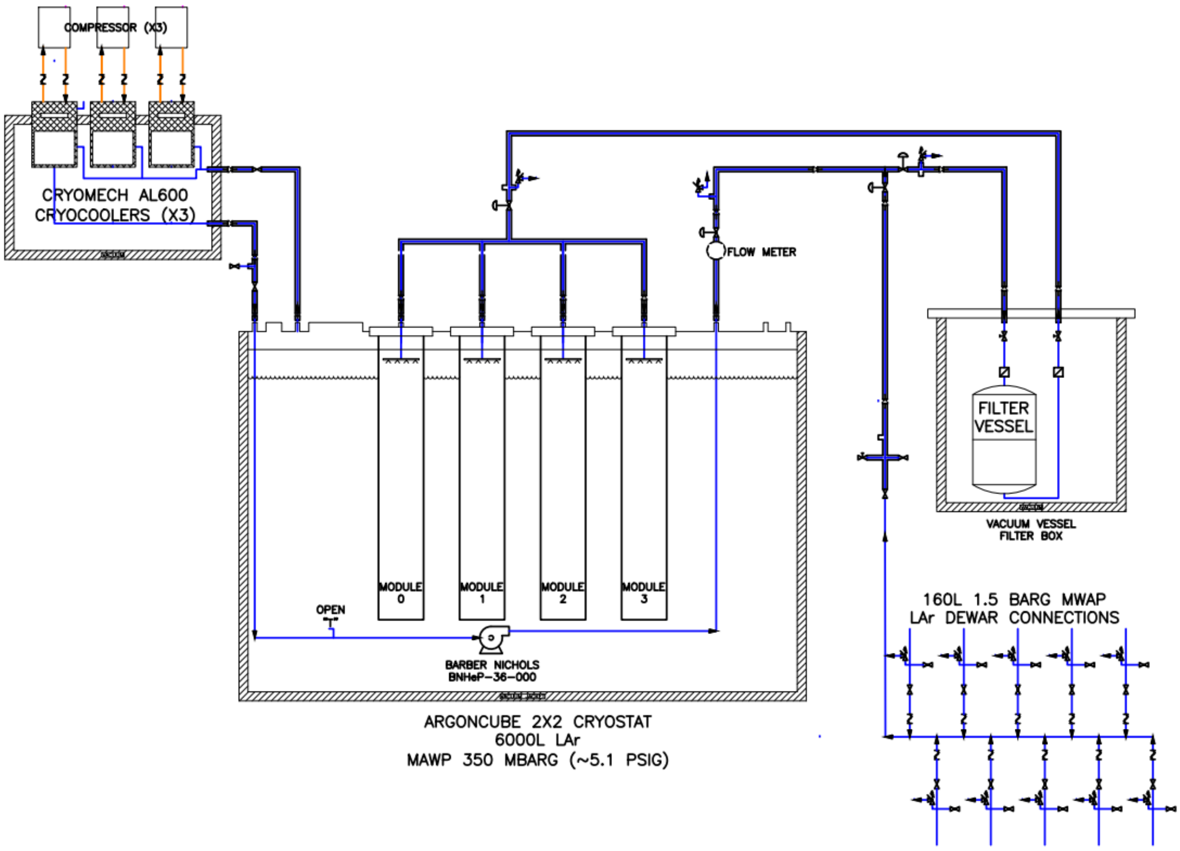

Figure 5.12 – Simplified Piping and Instrumentation Diagram (P&ID) for 2x2. LAr from the main cryostat is pumped to the external filter vessel (top right) and inserted back through sprayer bars at the top of each detector module. A second external vessel hosts three cryocoolers (top left), which pull gaseous argon from the ullage. The reliquified argon gets directly inserted into the submerged pump and pushed through the filter recirculation. The manifold with ten dewar connections (bottom right) is used for the cool-down and filling. Original drawing provided by FNAL.

Figure 5.12 shows the P&ID for the 2x2 cryogenic setup. Three key requirements have driven the design. First, LAr can not be delivered to MINOS ND facility underground with a cryogenic line from the surface due to the high height difference. The only possibility to bring LAr to the 2x2 is with small portable dewars. To cool down the cryostat and fill it, about 9600 L of LAr are needed, which is equivalent to ∼60 of the used ∼180 L-dewars. To perform an efficient cool-down and filling, a station was set up where up to 10 dewars in parallel can be attached. Each connection slot has a shut-off valve, allowing one to swap out empty dewars while others are still running.

Second, there is no large supply of Liquid Nitrogen (LN) available at the detector location. LN is commonly used to provide cooling for LAr experiments, as the nitrogen boiling point is ∼10 K lower than the one of argon. Since this option was unavailable, cryogenic refrigerators, more commonly called cryocoolers, were used. Cooling is needed to compensate for several heat inputs into the system, e.g. from the readout electronics or the recirculation pump. The heat inputs cause evaporation of the LAr, which needs to be compensated by recondensing gaseous argon at the cryocoolers. For the 2x2, three units of the Bluefors Cryomech AL600 were installed. The AL600, a single-stage Gifford-McMahon cryocooler, operates on a regenerative refrigeration cycle, using helium gas to transfer heat. The system consists of a compressor and an expansion stage. Helium is compressed and heated, then cooled in a heat exchanger before entering the expansion stage. As the gas expands, it cools due to the Joule-Thomson effect, cooling the cold head. The cycle repeats, maintaining a low temperature at the cold head. The cold heads are installed in a special vessel outside of the cryostat. Gaseous argon from the ullage of the main cryostat can condense on the cold heads and be returned to the system as a liquid. A heater unit installed in each of the three cold heads can be used to regulate the cooling power per head from maximum 600 W down to 400 W.

Third, the argon needs to be purified to reach a sufficient electron lifetime to collect charge from the full drift length of the TPC (see Chap. 3). To reach this goal, the argon needs to be recirculated through a filtration system. The recirculation is driven by a pump[3] submerged in the main cryostat. The pump outlet is connected to a pipe going to the cryostat top flange. From there, a vacuum isolated line brings the LAr to the vacuum vessel holding the filtration system. The mass flow to the filter can be monitored with a Coriolis flow meter.

The filtration system comprises a 20 L filter vessel and a particulate filter. The filter vessel is filled half with a 3 Å molecular sieve[4], which efficiently removes water and other contaminants. The other half is filled with an activated copper catalyst[5]. The copper catalyst, as received from the supplier, must first be activated. To do so, the copper oxide in the catalyst is flushed with a mixture of argon (carrier) and hydrogen while it is heated up to start the reaction

$$\mathrm{CuO} + \mathrm{H_2} \longrightarrow \mathrm{Cu} + \mathrm{H_2O}. \tag{5.2}$$

During operation, the activated copper can then filter out the oxygen contamination from the LAr via

$$2\,\mathrm{Cu} + \mathrm{O_2} \longrightarrow 2\,\mathrm{CuO}. \tag{5.3}$$

The filter material can be reactivated following the same procedure as for the initial activation.

Reliable monitoring of the argon purity is vital, especially during the filling and cold commissioning phase of the detector. For 2x2, two different monitoring systems were implemented. The first system comprises a set of gas analysers that provide a precise measurement of impurities in the ullage of the cryostat. Dedicated sensors for N_2, H_2O and O_2, which are the most common impurities, are assembled in a gas analyser panel. With this, not only the cryostat ullage gas but also the quality of the received argon before filling can be tested.

[3] Barber-Nichols Inc., BNHeP-36-000
[4] Research Catalysts Inc., RCI-DRI 4A
[5] Research Catalysts Inc., Q-5 Copper Catalyst

The second system is a dedicated LAr purity monitor. It consists of a single-channel drift chamber used to measure electronegative impurities by detecting the attenuation of drifting electrons from a cathode to an anode electrode. Light pulses created with a xenon flash lamp outside of the cryostat are guided through a quartz fibre to the photocathode of the device. At the cathode, due to the photoelectric effect, electrons are knocked out and subsequently start drifting towards the anode. By comparing the charge current arriving at the anode with the initial charge knocked out of the cathode, the total attenuation factor can be distinguished. While it cannot distinguish between different types of impurities, it can provide a direct measurement of the electron lifetime, which is the crucial parameter for the charge collection in the detector TPCs. The device is very insensitive to N_2 contaminations since they only attenuate the charge collection if present at the percent-level [157]. However, N_2 contaminations are critical for the light yield as they attenuate the slow component of the LAr scintillation process [95].

5.4 MINERνA trackers in the 2x2 (Mx2)

The Mx2 system is an integral part of the 2x2 Demonstrator, providing additional particle tracking capabilities to enhance the identification and discrimination of charged pions and muons, which are important for studying neutrino interactions. Positioned both upstream and downstream of the LArTPC modules, the Mx2 planes are repurposed from the MINERνA detector [158], a fine-grained plastic scintillator detector originally designed for precise cross-section measurements on various nuclear targets. The Mx2 system serves primarily as a muon tagging system, although it also performs calorimetric functions to improve particle identification for uncontained particles.

The Mx2 system consists of three types of modules. Each type of module contributes differently to the tracking and identification of particles:

- Tracker modules comprise two scintillator planes and provide high-resolution tracking of charged particles.
- ECAL modules add a 1.99 mm thick sheet of lead in front of each scintillator plane, enabling the detection of electromagnetic showers produced by high-energy electrons or photons.
- Hadronic Calorimeter (HCAL) modules consist of a single scintillator plane preceded by a 26 mm thick steel plate designed to stop most outgoing hadrons, particularly pions.

In the context of the 2x2 Demonstrator, the Mx2 system is composed of 22 tracker modules, 10 ECAL modules, and 12 HCAL modules. These modules are arranged to cover both upstream and downstream sections of the LArTPC detector. Upstream of the LArTPCs, 12 tracker modules are positioned approximately 75 cm away from the cryostat, where they help identify particles produced in neutrino interactions in the rock upstream of the detector. Downstream of the cryostat, 10 tracker modules, 10 ECAL modules, and 12 HCAL modules are placed approximately 45 cm away from the cryostat, providing comprehensive tracking and calorimetric coverage for particles that interact with the LArTPC but are not fully contained within it. The arrangement of upstream and downstream Mx2 around the main cryostat is shown in Figure 5.13.

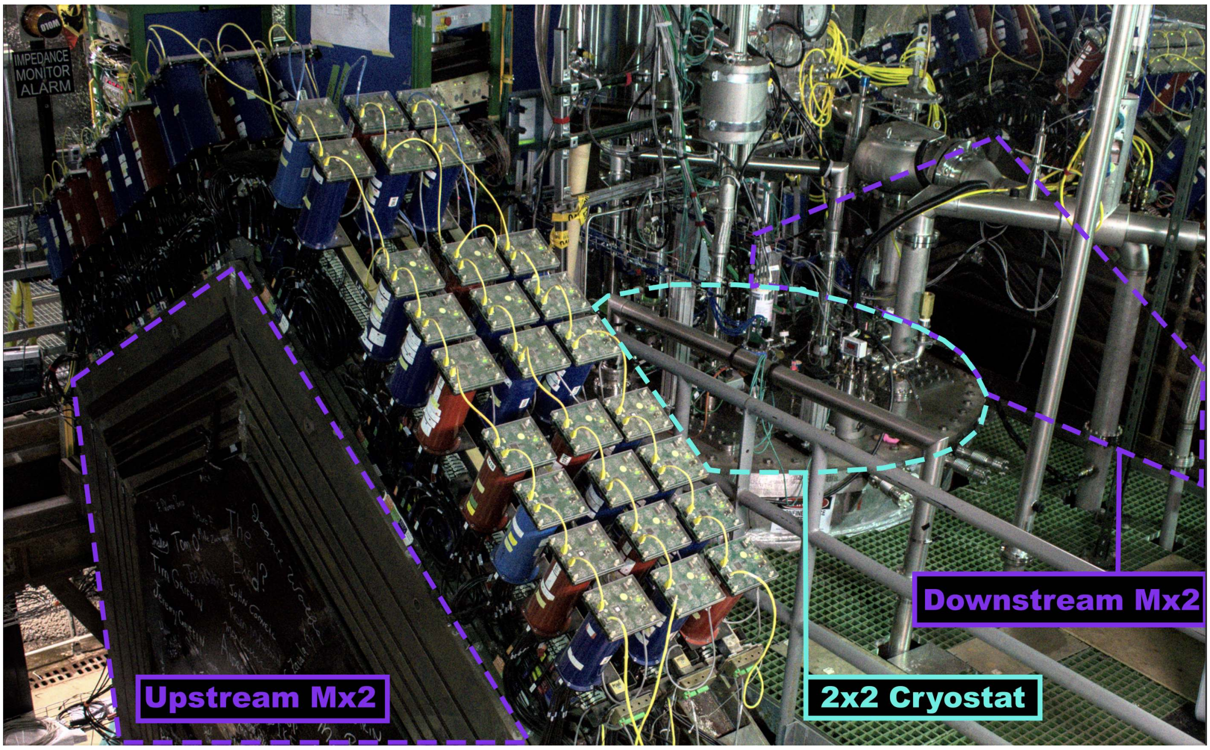

Figure 5.13 – The 2x2 main cryostat is flanked both upstream and downstream with a set of Mx2 planes. On top of the Mx2 planes, the daisy-chained front end boards are shown, each attached to a PMT reading out the optical signal from the scintillator planes.

The total active mass of the Mx2 system is approximately 5.6 t, composed mainly of hydrogen and carbon atoms (7.8% and 92.2%, respectively). The tracker planes, which are essential for precise particle tracking, contain 127 strips of plastic scintillator with a triangular cross-section. Each strip has a height of 1.7 cm and a width of 3.3 cm along the base, providing a spatial resolution of 3.1 mm. Wavelength-shifting fibres capture and funnel scintillation signals to 185 photomultiplier tubes (PMTs) located at the edges of each hexagonal panel. This configuration allows for high-efficiency tracking of charged particles passing through the system.

A key function of Mx2 is to track particles that pass through the LArTPC and identify those that exit the detector. This is especially useful for tagging muons, as particles that punch out of the downstream portion of the detector are highly likely to be muons. The ECAL and HCAL modules provide additional information on particles that are not fully contained within the LArTPC. These modules can also contribute to the overall calorimetry of the system. The ECAL modules detect electromagnetic showers, typically produced by electrons and photons, while the HCAL modules are designed to stop hadrons such as pions. While the LArTPC itself does not have the physical scale to contain all secondary particles produced by neutrino interactions, the combination of tracker, ECAL, and HCAL modules in the Mx2 system can significantly improve the overall particle identification for uncontained particles.

By repurposing modules from the MINERνA experiment, Mx2 enhances the overall particle identification and tracking capabilities of the 2x2 detector, making it a crucial tool for studying neutrino interactions and improving the precision of the 2x2's measurements.

5.5 Light readout

In 2x2, a version of the light system described in Ch. 4 is deployed. In the following, only the specific details for the 2x2 are elucidated; for a general description of the readout system, see the aforementioned Chapter.

In addition to the ArCLight, thoroughly described in Sec. 4.3, the 2x2 hosts a second complementary VUV-light trap: The Light Collection Module (LCM) [126], which is designed and produced by JINR (Dubna, Russia). The LCM utilises wavelength-shifting fibres coated with TPB to detect the VUV scintillation light. As for the ArCLight, the TPB coating absorbs the VUV light and re-emits it in the blue range. The fibres, made from Kuraray Y-11[6] material, shift the light further to ∼510 nm green light, which is then guided towards the readout system by total internal reflection. At each end of the fibre bundle, the light is detected by Hamamatsu S13360-6050CS SiPMs (same as for ArCLight), which are optimised for the green emission of the fibres. Figure 5.14 shows a schematic of the LCM working principle. The LCM has a surface of 10 cm × 30 cm, and a overall PDE approximately 0.6 % [159]. The spatial resolution of a single LCM for reconstructing the point where the light was emitted is, due to its design, limited to its size. Same as the ArCLight, the dielectric design of the LCM allows it to be placed in the drift field of a TPC.

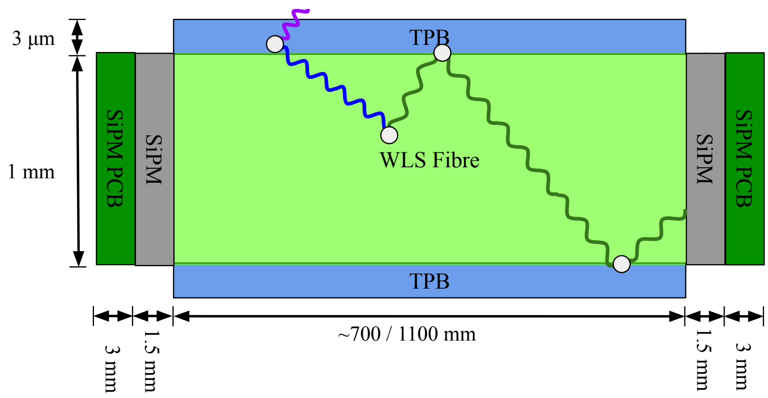

Figure 5.14 – Schematic of the LCM detection principle. The incident VUV photon (Violet wave) gets shifted to the blue spectrum by the TPB layer. The wavelength-shifting fibre absorbs the blue photon and re-emits it as a green photon, which remains trapped and eventually guided to a SiPM placed at either end of the fibre.

[6]Kuraray, Y-11, `www.kuraray.com`

As shown in Figure 5.15, the light traps are placed in the direction of the drift field at the side walls of the TPCs. Since three LCMs make up the size of an ArCLight, the detector is equipped alternately with a set of three LCM and an ArCLight, starting with an ArCLight at the bottom. The calibration LEDs discussed in Sec. 4.6 are placed on the centre-top and centre-bottom of the anode plane of each TPC.

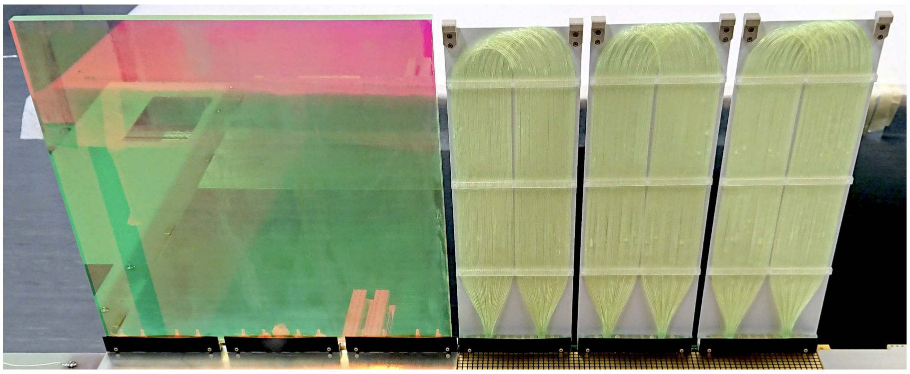

Figure 5.15 – An ArCLight (left) and a set of three LCMs assembled in the TPC structure. At the interface of the light trap and the anode, where the SiPM is placed, a small kapton shield is mounted to shield the charge readout from noise from the SiPM electronics.

The two light traps use the same interface to the TPC structure and are read out by the same front-end electronics (see Ch. 4). A total of 384 SiPMs are placed in the four modules. To operate and read them, 64 pre-amplifier boards, 16 VGAs, (8 regular + 1 sum) = 9 ADCs, 2 SiPM bias supplies, 2 SiPM bias controllers and 2 VGA controllers are needed. Figure 5.16 gives an overview of the mapping of the detector.

Since the only pre-amplified analogue signal is transmitted out of the cryostat, a proximity rack is placed next to the cryostat to maintain the signal quality (see Fig. 5.2). The proximity rack hosts all of the above-mentioned devices except the ADCs. The ADCs, due to lack of space, are located in a dedicated rack on the access catwalk.

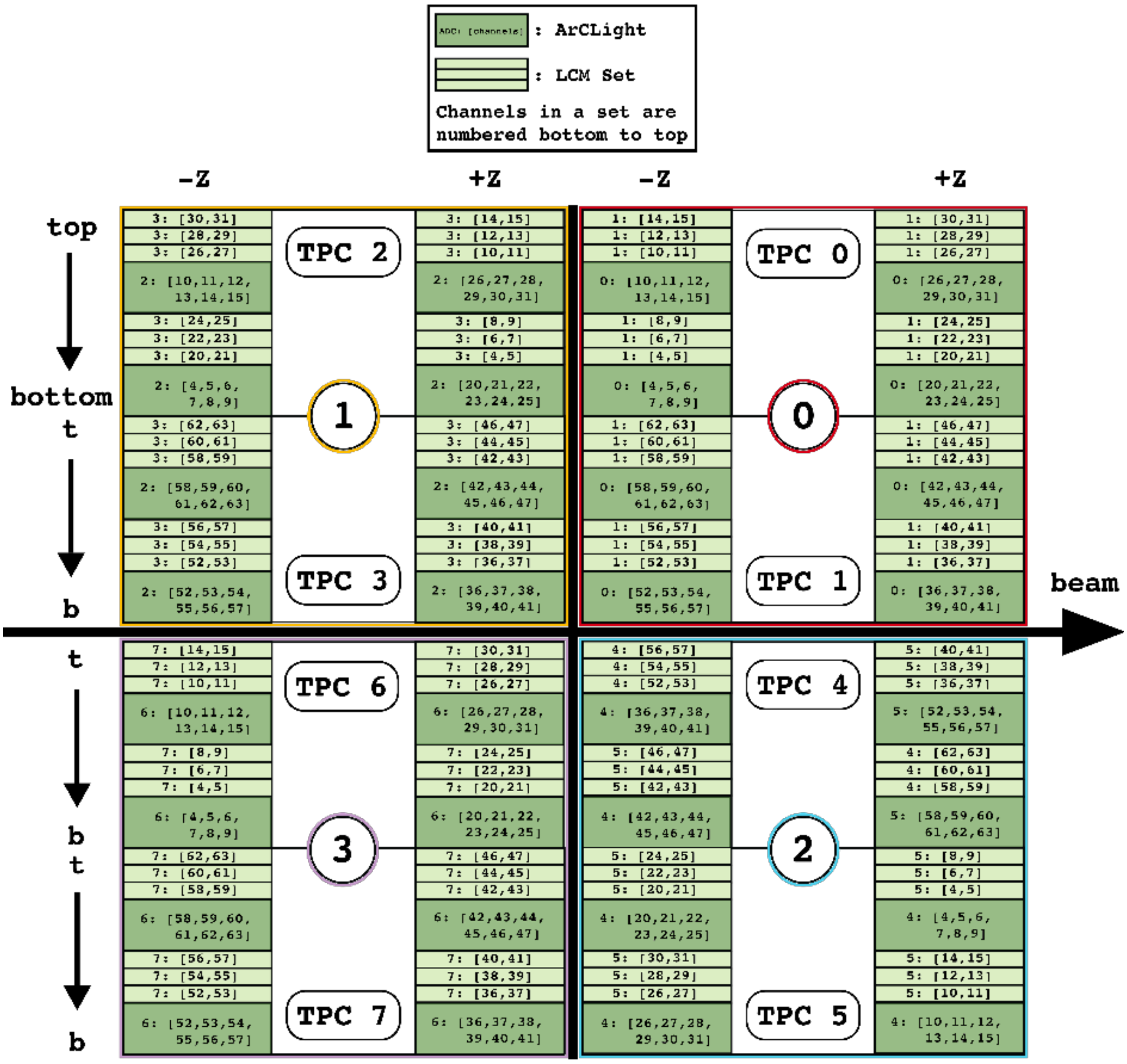

Figure 5.16 – Arrangement of the LRS SiPM channels in the four modules (circled number = module number)

5.6 Charge readout

As described in Section 3.5.2, DUNE applies a 3D pixelated charge readout to enable high-precision tracking and event reconstruction in ND-LAr with minimal inactive volume. The Charge Readout System (CRS) used in the 2x2 is based on the same Liquid Argon Pixelate charge readout (LArPix) architecture [11].

Each of the eight TPCs in the 2x2 employs eight charge-sensitive anode tiles, each of which is equipped with a 10×10 grid of LArPix ASICs. These anode tiles are arranged in a 2×4 array, providing 4900 charge-sensitive pixels per tile. The pixel pitch is set at 4.43 mm, allowing for a 1.28 mm spatial resolution, which is crucial for distinguishing the trajectories of high-energy particles in the detector. The front and back side of a pixel tile is shown in Figure 5.17. The pixel tiles in the two TPCs of Module-2 have a slightly different design than the remaining modules. Here, the pixel pitch is 3.8 mm, and 6400 pixels are placed per tile. The entire 2x2 has a total of 337.6k pixels.

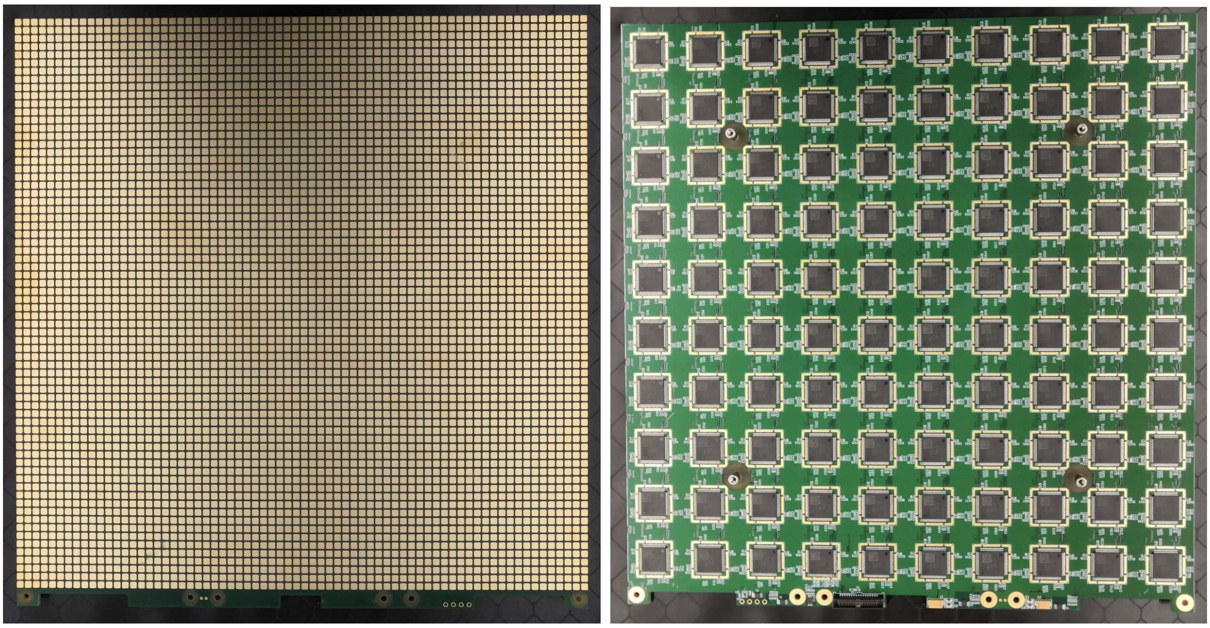

Figure 5.17 – The CRS pixel tiles in the 2x2 are 31 cm × 32 cm large. Here, the version deployed in Module-0, 1, and 3 with a pixel pitch of 4.43 mm is shown. The gold-plated pixel pads on the front side (**left**) are connected to the input channels of the ASICs mounted on the backside of the tile (**right**). The non-quadratic shape of the tile is due to the connectors and mounting holes placed outside of the drift field (see the bottom of the two pictures).

The LArPix ASICs are central to the functionality of the CRS. Each ASIC can handle up to 64 pixels, and it performs analogue signal amplification, analogue-to-digital conversion, and data transmission. In the 2x2, two different versions of the ASIC were used. Version v2a deployed in Module-0, 1, and 3 could only read 49 of the possible 64 input channels due to a design issue. This issue was fixed in version v2b, which allowed the use of more pixels per tile, as described above. The ASICs are designed to operate at cryogenic temperatures, as required for the liquid argon environment. The LArPix ASIC is a mixed-signal chip consisting of 64 analogue front-end amplifiers and 64 ADCs, along with a digital core responsible for managing configuration and data I/O. The integrated self-triggering mechanism is crucial for minimising dead time and ensuring efficient data acquisition, as it allows the system to focus only on significant ionisation events. The v2 ASICs reach a noise level of below 800 e^- Equivalent-Noise-Charge (ENC).

An essential requirement for the CRS is to have a minimal heat dissipation in liquid argon. Excessive power consumption would lead to warm-up and potential boiling of the argon. With this very high number of individual readout channels, achieving a low power consumption is challenging and was a driving factor in the ASIC design. Having a self-triggering mode and keeping the digital part of the circuit else in a sleep mode helped significantly to achieve this goal. Overall, the LArPix system achieves a static power dissipation of <200 mW per channel.

The self-triggering threshold for each individual channel of an LArPix ASIC can be tuned. For the 2x2, different threshold configurations are used depending on the focus of each study. To explore the low energy regime, e.g. from ^{39}Ar decays, the threshold can be lowered to a range where the readout starts to pick up noise ($\mathcal{O}$(5k) electrons). This data then needs more offline reconstruction to get a high-purity hit sample. In normal operation, the thresholds are optimised to achieve a perfect balance between collection efficiency and hit purity. In this mode, the threshold is set at $\mathcal{O}$(10k) electrons.

The self-triggering mechanism allows the detector to collect data continuously without dead time, which is essential for high-rate experiments where rapid particle interactions occur. For a single module in a high-rate environment, e.g. exposed to cosmic radiation at surface, a total data rate of approximately 2.5 MB/s is expected. If conventional trigger schemes were applied, like external triggering of full TPCs, the expected data rate would be orders of magnitude higher since the overall low occupancy would not be exploited. Figure 5.18 shows a simplified block diagram of the ASIC visualising all the functions described above.

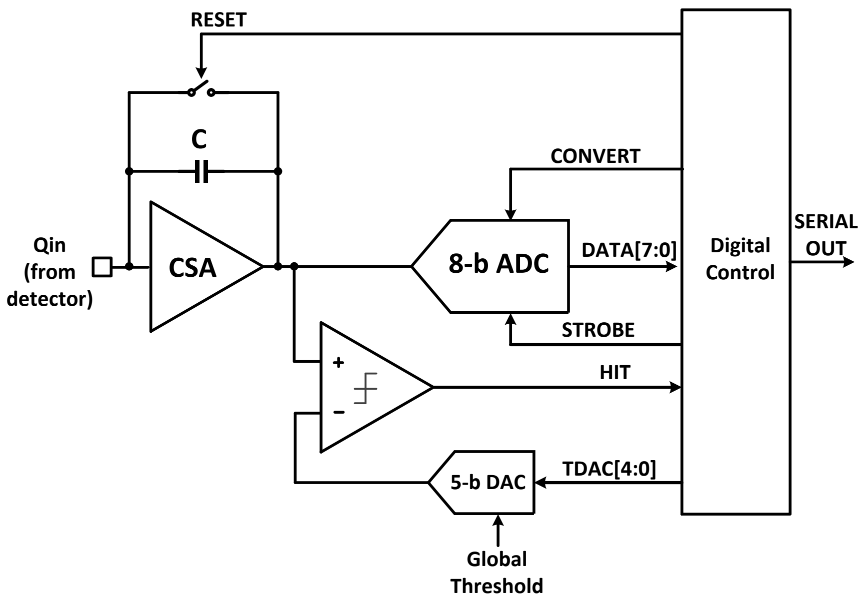

Figure 5.18 – The simplified block diagram for a single channel on the LArPix ASIC shows the way the self-triggering is implemented. A central threshold unit activates the digital part of the chip once the accumulated charge overcomes a certain level. The threshold can be defined by the DAC unit shown at the bottom of the diagram. The digital part of the chip only gets activated once the threshold is reached, and otherwise, is in sleep mode to prevent unnecessary heat emission. At the end of a digitisation cycle, the integrator is reset. This reset function can also be used periodically to prevent long-term charge accumulation caused by noise.[11]

Each charge-sensitive pixel in the CRS functions independently, and data are streamed continuously via serial data packets. These data packets are timestamped at the ASIC level to ensure accurate synchronisation between the charge readout and the light readout systems. The I/O communication to all LArPix chips for a full TPC is handled by a single Pixel Array Controller and Network (PACMAN) front-end board located at the warm side of the top flange feedthrough. The PACMAN not only handles the collection and packaging of the hit-level data from the ASICs but also is the interface for the downstream propagation of configuration settings. In particular, the I/O network mapping of the individual chips on a pixel tile can be set dynamically, which allows the mitigation of a faulty ASIC.

The benefits of using a pixelated readout, which enables true 3D imaging, have already been elaborated in Section 3.5.2. The resolution of such a system is partly determined by the size of the pixels, which defines the spatial resolution in two of three axes. In the third direction, however, the spatial resolution is determined by the time-binning of the readout electronics. The LArPix system operates with a 10 MHz clock. A full digitisation cycle takes 11 clock ticks, resulting in a maximum sampling rate of 1.1 µs, equivalent to 1.76 mm spatial resolution assuming a nominal drift field of 0.5 kV/cm. The fast clock speed is not only beneficial for spatial resolution but mainly enables setting a precise timestamp of the threshold crossing event, allowing better synchronisation with the light readout. Besides the pixel pitch and maximum sampling rate, the resolution is limited by transverse and longitudinal diffusion as discussed in Section 3.2. However, this effect is typically at $\mathcal{O}(1\,\mathrm{mm})$ per meter of drift for the nominal drift field and thus only has a minor impact for the chosen design [160].

5.7 Trigger and Timing System

The three readout subsystems of the 2x2 (LRS, CRS, Mx2) operate for the most part independently of each other. All three run a separate DAQ system. In order to match the data taken by each subsystem offline, a reliable trigger and timing distribution system is needed.

At large, there are two main event types for 2x2: beam events and non-beam events. The primary focus of the 2x2 physics program is on beam events, so the system is designed to ensure no beam trigger is missed. However, non-beam events like ^{39}Ar decays or cosmic interactions can have significant importance, particularly for detector performance studies, and are therefore also recorded as much as possible. The three subsystems have fundamental differences in how these two types of events are recorded. The Mx2 only records beam events, the CRS records both without differentiating between the two, and the LRS records both but uses different trigger logics for the two. An overview of the trigger and timing system is shown in Figure 5.19.

A trigger signal from the accelerator is required to record beam events in the 2x2 system. Specifically, an early warning signal ($A9) provided by the FNAL accelerator division is

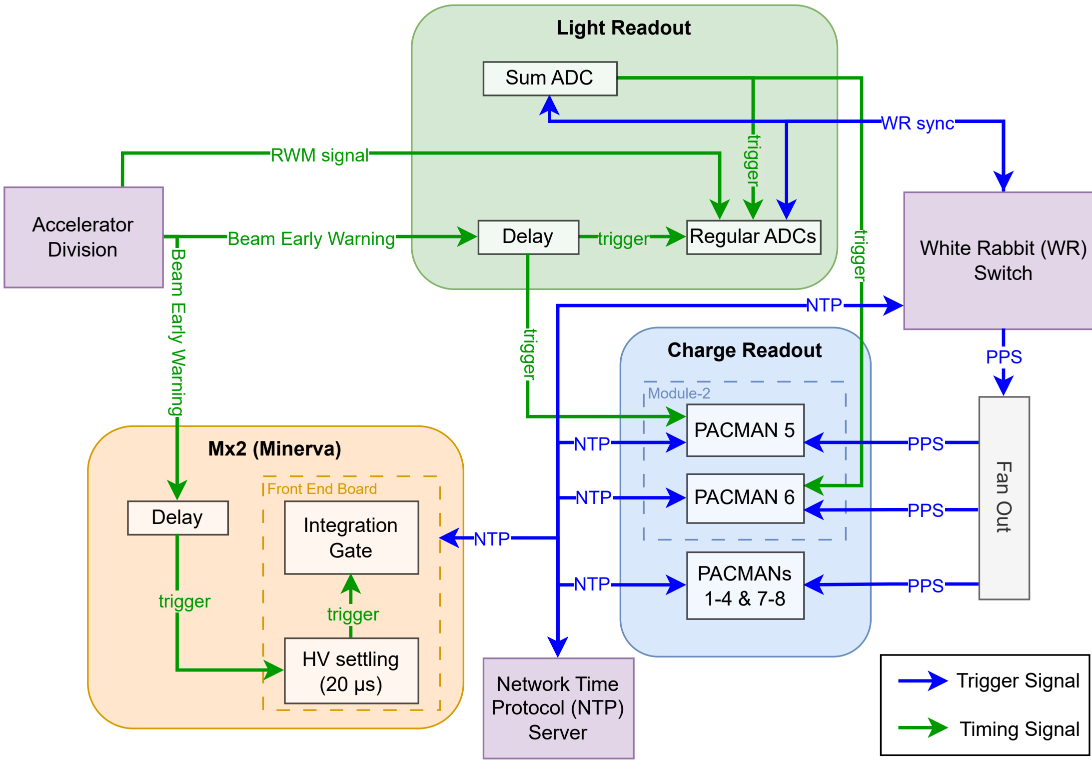

Figure 5.19 – Overview of the trigger and timing signal distribution in 2x2. The original beam triggers are provided by the accelerator division of FNAL. The LRS and Mx2 use different delay units, and their readout windows, therefore, are not perfectly aligned. The timing synchronisation is based on two complementary systems: The Network Time Protocol (NTP) and the WR system.

used, which arrives at the underground cavern approximately ∼213 µs before the particle beam. This signal is generated when the kicker magnet of the Main Injector extracts the beam into the NuMI beamline (see Sec. 5.2). The early warning signal allows the systems to prepare for potential incoming signals from beam-related interactions. Both the LRS and Mx2 systems use this signal to ensure they are ready for data acquisition and not occupied with processing and transmitting previous events. In parallel to preparing for incoming data, a delay unit gets started, which later triggers the actual data-taking.

In the case of the LRS, the delay unit is integrated into the LRS trigger unit (UT24), which is the central unit in the LRS coordinating all triggers. Once the LRS trigger unit receives the early warning, no other triggers are accepted anymore. Approximately 100 ADC samples (=1.6 µs) before the arrival of the beam particles on the detector, the trigger is issued to the individual ADCs recording the regular SiPM signals. At the same time, a trigger signal is forwarded to the CRS.

The CRS continuously runs in a self-triggering mode. Externally received trigger signals are recorded as timestamped markers in the data stream and do not initiate a readout of the charge-sensitive pixels directly. These markers are later used in offline analysis to correlate charge and light events. In 2x2, the external markers for beam triggers are only sent to a single PACMAN located at Module-2 (PACMAN 5). This setup is sufficient to tag beam-related events across the entire charge dataset during offline processing.

Similar to the LRS, the Mx2 system uses the early warning signal to prepare the system. Here, in particular, the HV of the PMTs needs to be raised early enough to have stable conditions for the incoming beam. Mx2 starts acquiring data ∼500 ns before the neutrinos penetrate the detector.

For non-beam events, the LRS uses an additional threshold-based trigger mode. As described in Section 5.5, a separate ADC is used to record the analogue signal sums from groups of six SiPMs, with each group corresponding to a full ArCLight or a set of three LCMs. These summed signals are generated by the VGAs. The ADC is configured to issue a trigger signal whenever a sum exceeds a tunable threshold, which can be set individually for each sum channel. The central trigger unit ensures all regular ADCs are ready and not busy processing data before a non-beam trigger is issued. As for beam events, the trigger is forwarded to the CRS. However, here the trigger is sent to a different trigger input channel of a separate PACMAN to make sure the different trigger modes can be identified in the CRS data stream. Otherwise, the CRS handles non-beam data exactly the same way as beam data.

The early warning signal $A9 has a jitter of ∼50 ns relative to the actual arrival time of the beam particles in the detector (see measurements in Sec. 6.5). While this is not a particular issue to define the readout window, which is chosen large enough, this timing reference can not be used to do studies on the beam structure. As mentioned in Section 5.2, a more accurate beam signal can be obtained using the Resistive Wall Monitor (RWM) placed in the alcoves after the beam target. The RWM can not be directly used to trigger the readouts of the systems since it arrives after the beam and does not allow the systems to prepare. A spare channel on a regular LRS ADC is used to record the RWM signal. In order to increase the precision of the timestamp when the RWM arrives, a signal shaping is applied that slows its rising edge down to ∼100 ns. With this measure, more ADC samples within the rising edge can be recorded, which can later be used to apply a fit and get precise timing. With the RWM signal in the LRS data stream, one can directly compare the beam timing with the fast incidence of scintillation from potential interactions in the detector.

To allow an offline matching of the data from the individual subsystems, a reliable synchronisation of the timestamps issued by each system is implemented. For 2x2, two complementary systems are used.

Since the overall event rate in the 2x2 is relatively low ($\mathcal{O}(10\,\mathrm{Hz})$), coarse time synchronisation at the microsecond level is already sufficient to match the majority of system triggers across all three systems, though not all. The Network Time Protocol (NTP) is used to achieve exactly such a coarse synchronisation. As the name suggests, the time signal here is distributed to each device directly via the network connection. NTP allows devices to synchronise their system clocks with a reference time source, such as an atomic clock or GPS. At FNAL, a central NTP service is provided by the computing division.

For the CRS and LRS, the NTP synchronisation is not sufficient. To handle multiple interactions within one readout window of the light system, a higher level of synchronisation is needed within the LRS and CRS but also across the two systems. Within the LRS, it is vital to have a sub-nanosecond level of time synchronisation to be able to do detailed timing studies. To achieve this, the White Rabbit (WR) system is used. WR has been used in various particle physics experiments with a high demand for high-precision timing synchronisation, such as LHC at CERN [161]. It incorporates a hardware-based absolute time synchronisation using a master-slave architecture. In the 2x2, a WR switch runs as grand master, which gets its date and coarse time from the central NTP server, but otherwise runs a stand-alone clock. All ADCs in the LRS have a direct WR interface and are connected via fibre to the switch. A two-way communication protocol is used to calibrate out the signal delay between the two units.

The CRS PACMANs do not have a direct WR interface. However, they can receive an external pulse to reset their internal clock counter. A Pulse-per-Second (PPS) signal is extracted from the WR switch and distributed to all PACMANs. This not only ensures the synchronisation between charge and light readout but also within the CRS itself. The precision of the PPS synchronisation (<1 ns) is much higher than the clock speed of the PACMAN itself. Thus, the only source of potential mismatch between multiple PACMANs is their relative clock drift within one second.

The Mx2 system triggers only on beam events, and only a trigger-level synchronisation to the other systems is required. To achieve this, the NTP integration is already sufficient. To ensure time synchronisation within the Mx2 system, a common clock is distributed to all front-end electronics using a hierarchical distribution scheme. The source of the clock signal is a 53.1 MHz clock on the MINERνA Timing Module, which is synchronised to the accelerator RF clock system.

Chapter 6

The 2x2 Demonstrator - Operation and First Results

The 2×2 neutrino detector, described in the previous chapter, was successfully operated for the first time in 2024. This chapter details the assembly and commissioning procedure, outlining the entire process of getting the detector ready for data collection. Additionally, it presents the first 2x2 results obtained from data taken with the NuMI beam, offering an initial assessment of the detector's performance. The chapter also provides an overview of the run period, including key operational parameters. In the last section, the known spill structure of the beam is exploited to analyse the time resolution performance of the light readout.

6.1 Single module assembly and testing

All detector modules for the 2x2 were assembled at the University of Bern. For the assembly, each CRS pixel tile was paired with an LRS unit, consisting of either one ArCLight or three LCMs. These detector units were then attached to one of the G10 anode planes. Using a custom-built assembly structure, the TPC unit was inserted into the pre-assembled field shell. This process is illustrated in Figure 6.1. Once the first TPC was assembled, the module could be rotated to repeat the steps for the second TPC.

After assembly, the detector module was positioned upright, and the stainless steel top flange was attached. At this stage, both the charge and light readout systems were cabled, and all signal feedthroughs were installed. The LED calibration system was mounted and cabled. Additionally, a set of Resistance Temperature Detectors (RTDs) was installed at the anode plane and above the active volume to monitor the detector cool-down and warm-up phases and to have redundant control of the liquid level besides the dedicated level meter. Once fully equipped, the detector was inserted into its G10 sleeve.

Before shipping to FNAL, each module was individually tested in LAr between 2021 and 2023. For this purpose, a dedicated test facility was constructed at the University of Bern. Besides the main cryostat holding the detector module, the facility includes a second cryostat for cooling and filtering the LAr. Similar to the final 2x2 setup, the filter system uses a molecular sieve and a copper catalyst (details in Sec. 5.3). For cooling, the

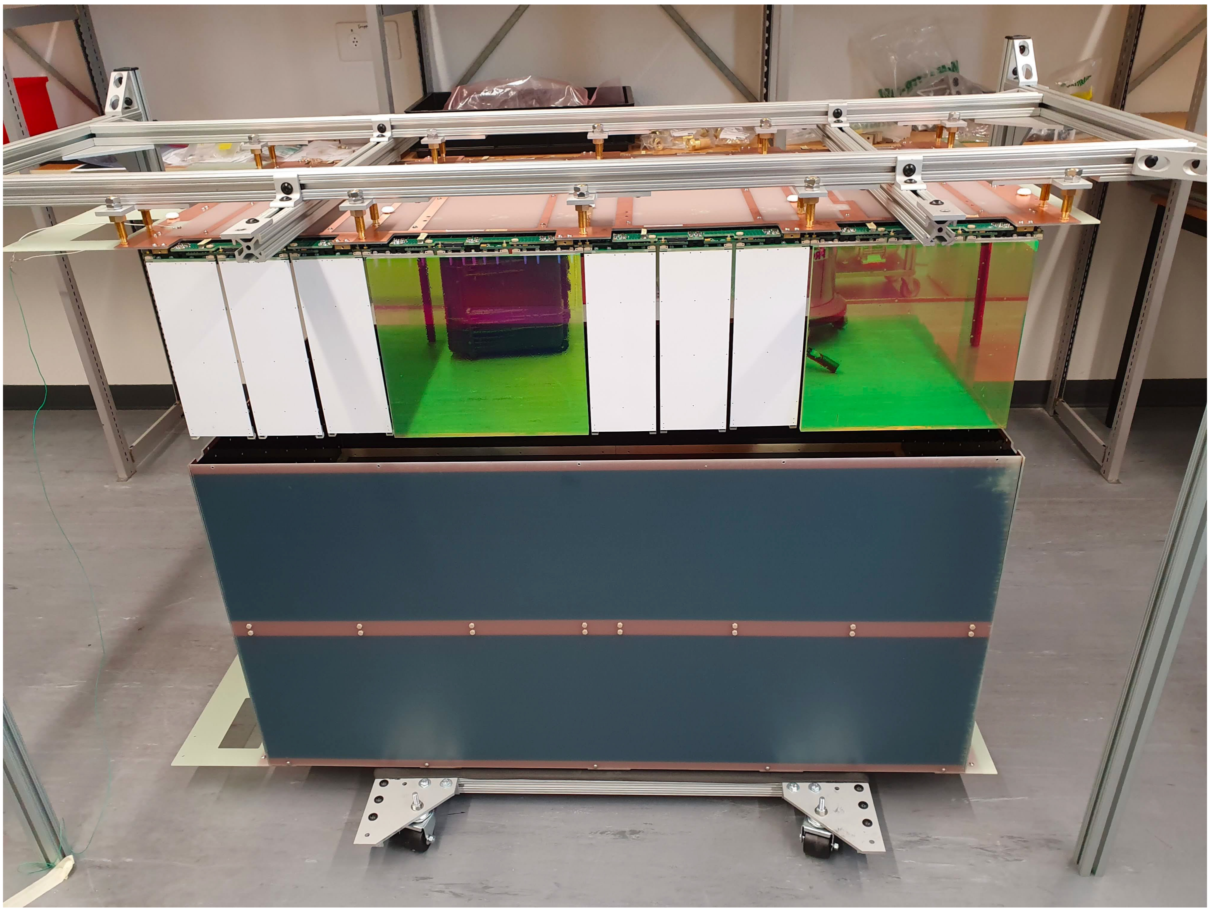

Figure 6.1 – Single module assembly structure. The light and charge detectors are attached to the anode plane on the top, held by the assembly frame. The pre-assembled field shell structure, on the bottom, can be pulled up using threaded rods (not shown), so the detector structure gets inserted into it.

filter cryostat is filled with liquid nitrogen and pressurised to 2.25 bar to reach 85 K. To enhance cooling efficiency, a heat exchanger is installed before the filter material. The cooling capacity can be regulated either by adjusting the liquid nitrogen pressure or by controlling the speed of the recirculation pump located in the main cryostat. Figure 6.2 shows the facility with a module just before insertion into the cryostat.

Instead of a neutrino beam, interactions induced by cosmic radiation were used to validate the performance of each module. Table 6.1 summarises the test runs conducted for all four modules. Each module underwent multiple test runs to identify and resolve minor or major issues.

Module-0 displayed minor noise issues on the CRS, which were addressed during a second run by implementing an improved grounding scheme. This second run also allowed for additional data collection for performance studies. From Module-1 onwards, shielding was added to the LRS pre-amplifiers to resolve a clock signal pickup from the CRS (see Sec. 4.4). Moreover, Module-1 featured an improved ArCLight design with dichroic mirrors on the side surfaces, significantly enhancing the photon detection efficiency. Im-

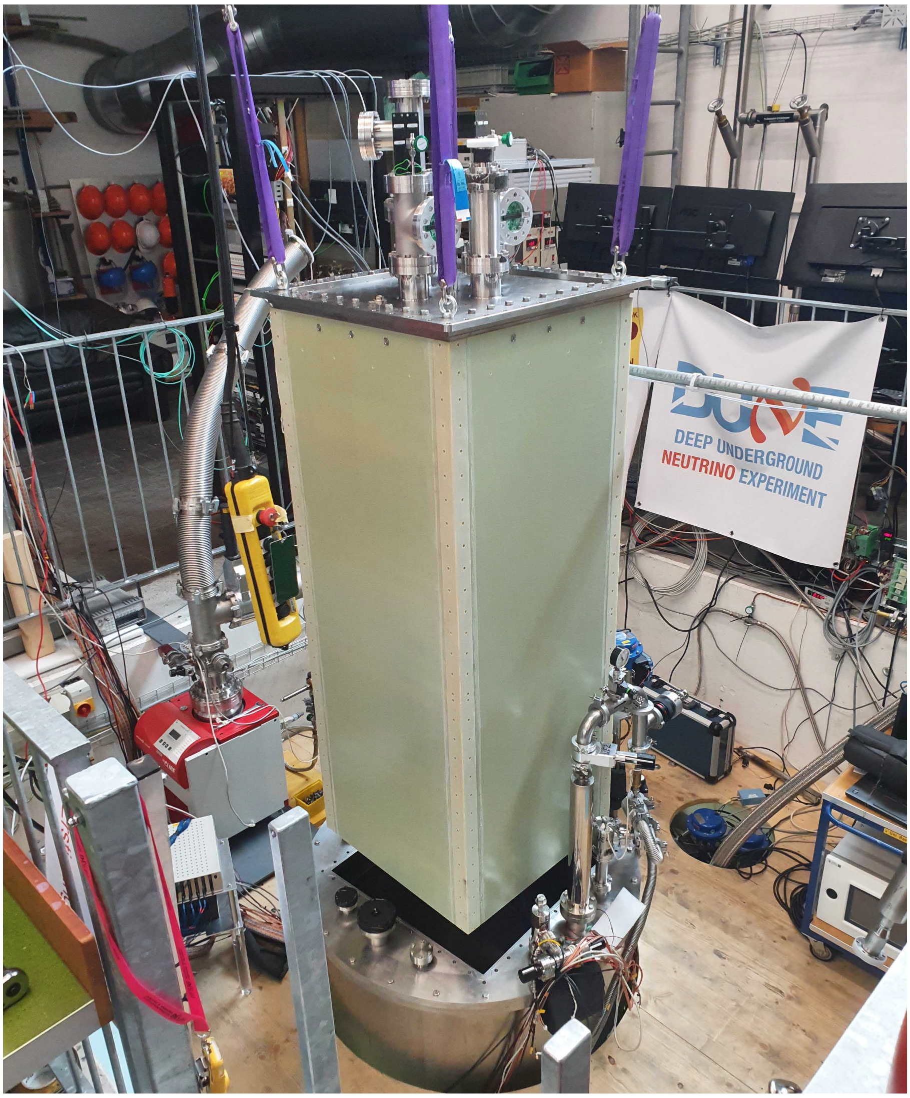

Figure 6.2 – Single module testing facility at the University of Bern. The picture shows a 2x2 module in its protection sleeve just before insertion into the cryostat. The filter cryostat is situated below the wooden platform and is connected to the main cryostat by vacuum-isolated pipes.

plementing Hamamatsu S13360-6050CS SiPMs with a larger pixel pitch (50 µm instead of 25 µm) for both the ArCLight and the LCM increased the quantum efficiency per SiPM channel and thus had a positive impact on the PDE.

For Module-2, a new ASIC chip design (v2b) for the CRS was introduced, featuring a smaller pixel pitch and a larger number of readout channels (102.4k in Module-2 compared to 78.4k in Modules 0, 1, and 3). However, this version has a known issue: it can only be configured under warm conditions and loses its configuration settings in the event of a power outage when operating in the cold. Consequently, Module-3 reverted to the older v2a version. Both Module-2 and Module-3 encountered significant issues requiring additional test runs in LAr. For Module-2, a modified sleeve design caused major vibrations, which were picked up as noise by the CRS, particularly on edge pixels. Repairs to

Table 6.1 – Overview of single-module test runs conducted at the University of Bern.

Module	LRS Differences	CRS Differences	Run Periods / Notes
0	• ArCLights without side mirrors • Pre-amp without shielding • SiPM Hamamatsu S13360-6025CS	• LArPix v2a • 4.4 mm pixel pitch	• 27.03–12.04.21 First Run • 21.06–27.06.21 Improved grounding scheme
1	• ArCLights with side mirrors • Pre-amp with shielding • SiPM Hamamatsu S13360-6050CS	• LArPix v2a • 4.4 mm pixel pitch	• 05.02–14.02.22 First Run • 04.04–07.04.22 Cold gas test only, fix broken pixel tile
2	• ArCLights with side mirrors • Pre-amp with shielding • SiPM Hamamatsu S13360-6050CS	• LArPix v2b • 3.8 mm pixel pitch	• 13.11–23.11.22 First Run • 28.11–06.12.22 Sleeve fixed to eliminate vibrations
3	• ArCLights with side mirrors • Pre-amp with shielding • SiPM Hamamatsu S13360-6050CS	• LArPix v2a • 4.4 mm pixel pitch	• 27.01–08.02.23 First Run • 20.02–28.02.23 Swap field shell side panels to eliminate discharges, failed • 12.03–19.03.23 Fix cathode-side panel copper connection to eliminate discharges

the sleeve design resolved the problem.

During the initial HV ramp-up, electric discharges were detected in Module-3 by the LRS and later confirmed by the CRS. Using the LRS data, the discharges were traced to the interface between the cathode and the field cage side panel. Despite swapping side panels to rule out assembly issues, the problem persisted, confirming a manufacturing defect in the side panel. After a thorough inspection, it could be concluded that there was an excess of epoxy from the lamination process, allowing for a localised region of DR8 to charge at a slower rate than the surrounding material and, eventually, the discharges observed. Since no damages could be observed, the side panel was modified with an additional layer of copper, recovering proper contact. The third and last test run of Module-3 was then successful, and the proper operation of the module could be confirmed.

Across all test runs, approximately 140 million cosmic ray interactions were recorded, providing a vast dataset for studying detector performance. Using data from Module-0, a paper presenting detailed performance results and basic physics studies was published [159]. Some of these results are shown in the following.

To highlight the capabilities of the pixelated readout, Figure 6.3 showcases a gallery of raw data events collected during the second Module-0 run.

To extract the Photon Detection Efficiency (PDE) of the LRS, scintillation light induced by tracks reconstructed from TPC charge readout data was used. A Density-Based Spatial Clustering of Applications with Noise (DBSCAN) algorithm identified vertically throughgoing muon tracks. In a 3D reconstruction, the charge of a track was discretised to single points with 1 mm steps along the track, assuming an infinitely thin trajectory. For each track point, the solid angle to each light detector tile was calculated, enabling the estimation of geometrical light acceptance. This calculation assumed isotropic scintillation light emission and integrated over the full track length, neglecting the effect of Rayleigh scattering, which is of minor relevance for such low distances (see Sec. 3.1).
The overall efficiency of the light detection system was estimated by comparing the mea-

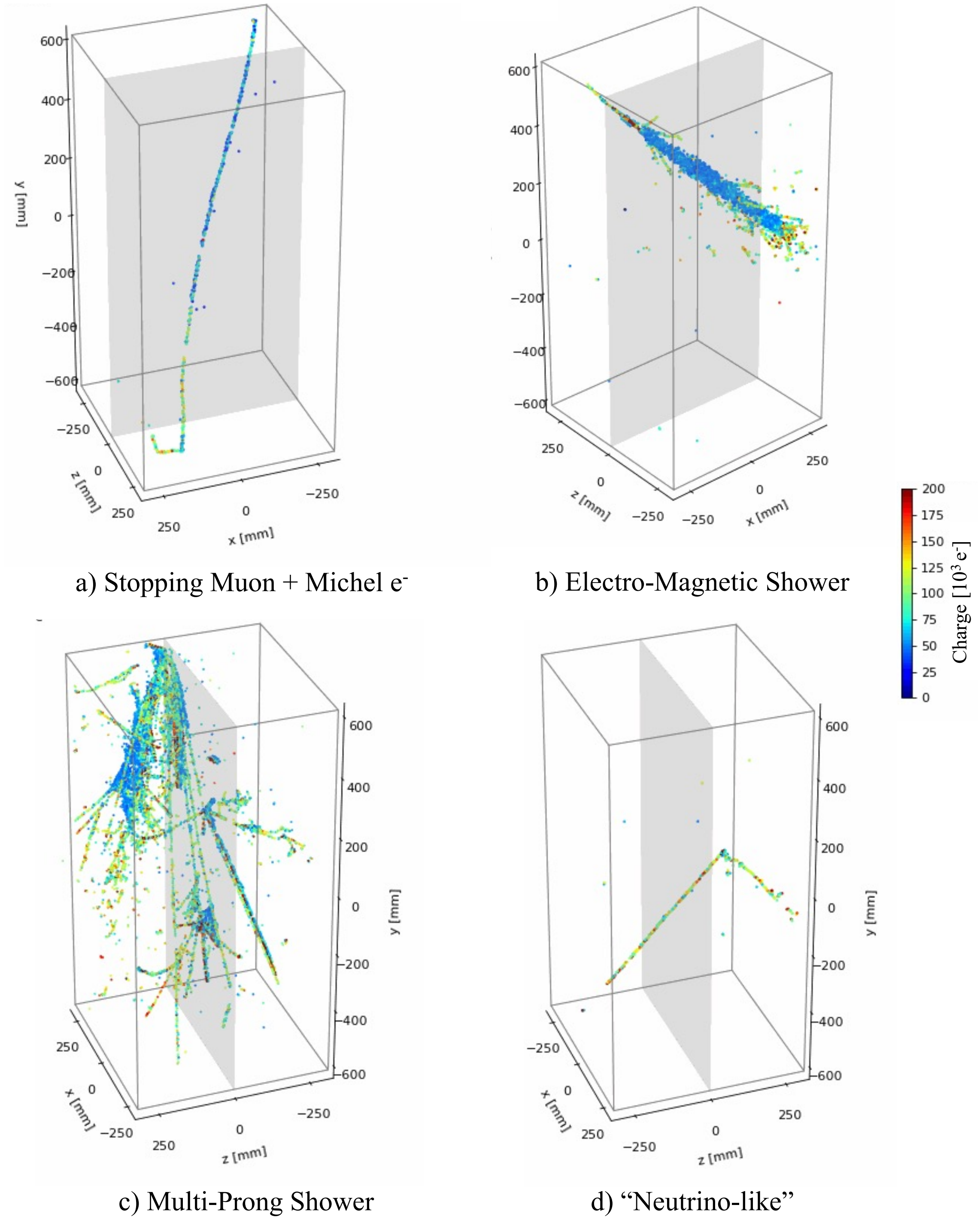

Figure 6.3 – Gallery of four representative cosmic ray-induced events collected with Module-0, as recorded in the raw event data, with collected charge converted to units of thousands of electrons. The central plane in grey denotes the cathode. (a) shows a stopping muon and the subsequent Michel electron decay, (b) denotes an electromagnetic (EM) shower, (c) is a multi-prong shower, and (d) is “neutrino-like” in that the vertex of this interaction appears to be inside the active volume. Published in [159].

sured number of p.e. with the estimated number of photons hitting the detector surface. Since the waveforms obtained with the light detectors have been integrated using a limited gate length, a correction factor was applied to account for scintillation light outside the integration window. Figure 6.4 shows the measured detection efficiency for all ArCLights and LCMs tiles used in Module-0 and Module-1. The improvements on the ArCLight design and the implementation of the higher-efficiency SiPMs resulted in an increase of the average PDE from $(0.056 \pm 0.017)\,\%$ to $(0.187 \pm 0.022)\,\%$. The LCM shows an average efficiency of $(0.63 \pm 0.13)\,\%$ for Module-1, where the increase compared to Module-0 is as expected due to the improved SiPMs.

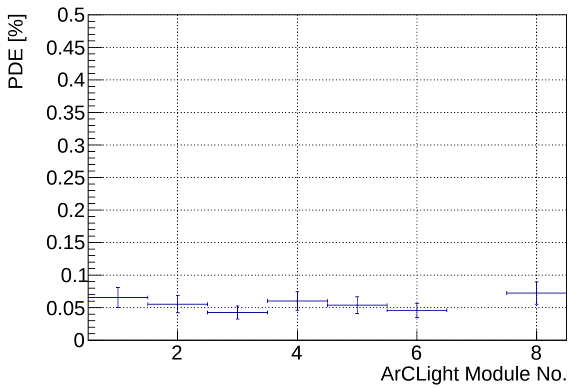

(a) Module-0 ArCLight

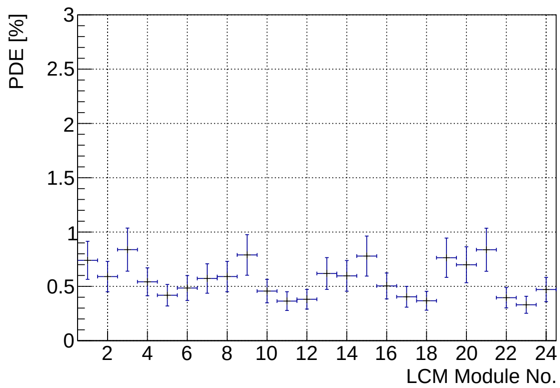

(b) Module-0 LCM

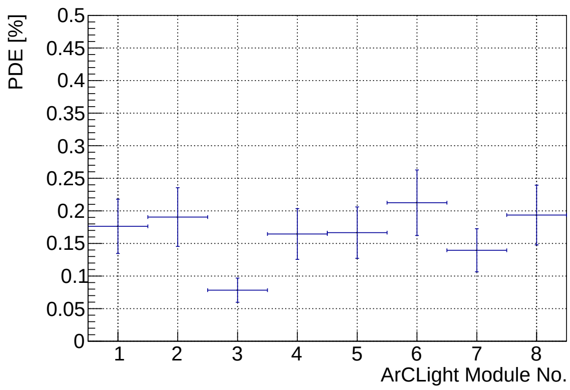

(c) Module-1 ArCLight

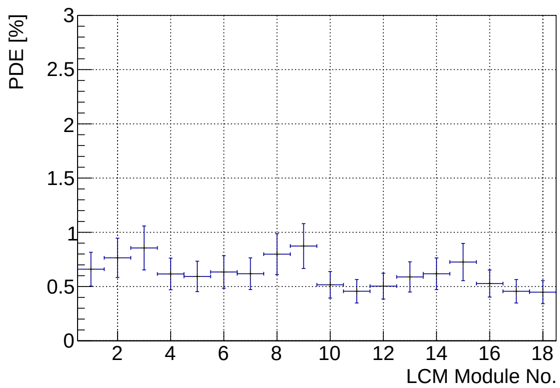

(d) Module-1 LCM

Figure 6.4 – Absolute PDE of all ArCLights (left) and LCMs (right) measured during the Module-0 and Module-1 cosmic runs at University of Bern. For Module-0, ArCLight tile #7 was disabled. For Module-1, the failure of a CRS pixel tile led to a too low track coverage in the region of LCM tiles #19 till #24 for a PDE extraction. Module-0 results were published in [159].

The importance of the high timing resolution in the LRS (compared to the CRS) can be demonstrated by examining muons that stop in the active volume and decay with the emission of a Michel electron. Figure 6.5 illustrates a candidate for such an event. Given the $\sim 2\,\mu\text{s}$ lifetime of the muon, in the case of a μ^+, a gap between the stopping point of the muon track and the starting point of the electron track is expected. However, this gap cannot be resolved using the charge readout alone due to the slow drift speed of electrons. The light detectors, on the other hand, enable clear differentiation between the two signals, providing a perfect example of how light information can be applied to tag specific interactions effectively. The energy distribution of Michel electrons can serve as a standard candle for detector calibration and performance validation.

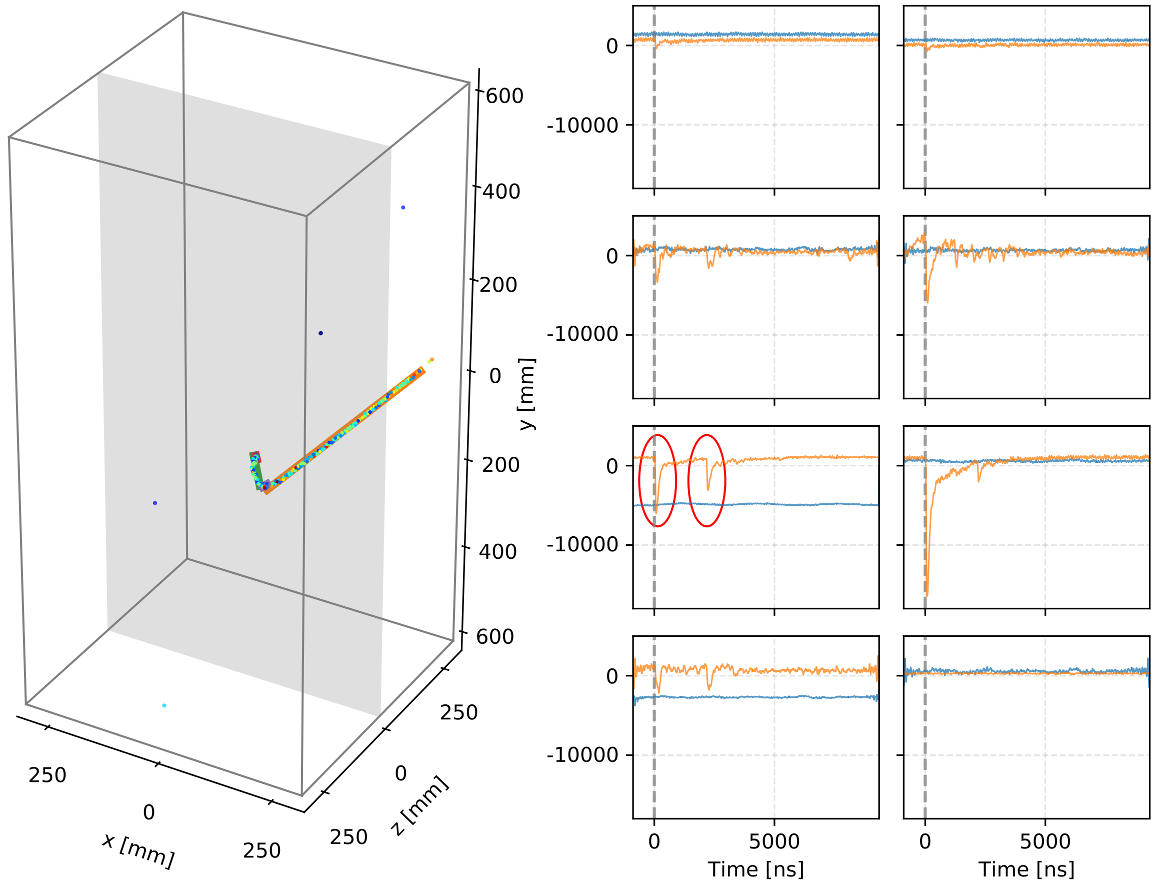

Figure 6.5 – Event display of a Michel electron candidate shown in a 3D view (left) and with associated waveforms from photon detectors (right). In the right panel, orange and blue indicate the two optically isolated TPCs. The red circles highlight an example of the two pulses on the photon detectors that correspond to the entering muon and the electron resulting from its decay. Published in [159].

6.2 Installation at MINOS

The detector modules were shipped individually to FNAL in a custom-designed shipping frame to protect them from potentially harmful impacts. After reception at FNAL, each module was tested to identify potential damage during the shipping process. These tests involved a communication and functionality test of all pixel readout tiles. For the light readout tests, the module was wrapped in a light-tight material, allowing the testing of the functionality of each SiPM by looking at light signals generated with the calibration LED. No damage to any of the modules was detected.

During the original assembly of Module-0, it was equipped with a top flange, which was designed for a Maximum Allowable Working Pressure (MAWP) of 50 mbar. Since the MAWP of 2x2 was later raised to 350 mbar, stronger reinforcement structures were required in the module top flange. To mitigate this, after receiving at FNAL, the module was extracted from its G10 sleeve, and the top flange was replaced. A further issue was discovered during the Module-0 and Module-1 test runs at Bern, where a high energetic shower event led to a drop in the stability of the supply voltage of the LArPix ASICs. A simple swap of a single capacitor on each pixel tile was identified as an effective solution to the issue. Consequently, Module-1 was also extracted from its sleeve at FNAL and the necessary modifications were applied. Both modified modules underwent the testing discussed above and did not show any damage from the modification process.

In October 2024, the four modules were lowered through the 102 m access shaft to the MINOS underground hall. The top flanges of the modules were then, one by one, attached to a common support frame structure with an indium seal placed in between. All four modules could be lowered together into the main detector cryostat, where the support frame was again sealed to the cryostat with an indium seal. A picture of the insertion process is shown in Figure 6.6.

Figure 6.6 – Picture of the 2x2 detector modules insertion process. On the left and right of the access platform, the installed up- and downstream Mx2 sections are visible.

After the module insertion, the cryogenic infrastructure on the detector cryostat was installed. This involved, in particular, the LAr distribution system of the recirculation return line located centrally above the top flange. During the leak-checking process, the inner indium seal between the support frame and the module top flanges was found to be leaking. Several rounds of successively increasing the torque on the connecting bolts did improve the situation, but left a leak rate of $\sim 30\,\mathrm{L/min}$ through the seal. This issue is most likely attributed to the fact that the support frame and the module top flanges were slightly warped due to welding processes. The impact of this leak on the operations will be discussed in the next subsection.

Due to the high density of feedthroughs and installations on the top flange, the cabling process required thorough planning. Several cable support structures were installed to ensure proper strain relief and routing of all cables. A picture of the fully assembled top flange is shown in Figure 6.7.

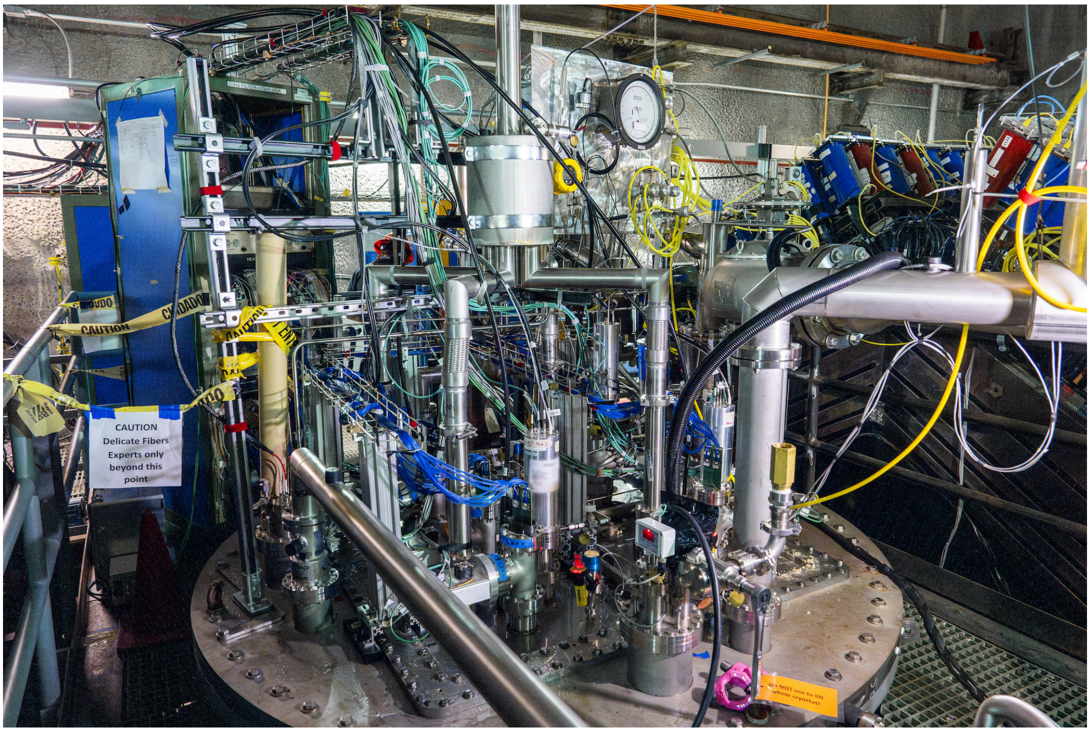

Figure 6.7 – Picture of the fully assembled top flange of the main cryostat, including all cabling and cryogenic infrastructure.

With the detector fully cabled, the warm commissioning of the detector was started. The entire commissioning process of the LRS is described in the next subsection. The Mx2 and CRS commissioning will be presented in other publications since they were not part of this thesis.

6.3 Light readout commissioning

To achieve a fully functional and performance-optimised LRS, a dedicated commissioning procedure was established and executed. This procedure included several configuration tasks and performance checks, conducted both before and after the detector cooldown.

After the LRS was fully cabled, the first part of the LRS commissioning at room temperature involved basic connectivity and functionality testing of all 384 SiPMs and the entire readout chain. A default bias voltage was applied to all channels. At this stage, the SiPMs signals were dominated by dark counts occurring at a rate of $\sim$2 kHz, which could be used to verify the functionality of the readout chain. Dark counts result from the spontaneous generation of charge carriers in the SiPM depletion zone due to thermal excitation. These carriers trigger an avalanche reaction similar to that caused by an incoming photon. During this warm commissioning phase, five SiPM readout channels were identified as broken (1.3 % of all channels). Subsequent investigations revealed that two of these channels had faulty SiPMs, while the remaining three suffered from readout chain issues. The identified broken channels fully matched those already marked as malfunctioning during the Bern test runs, and no additional channels were broken during the transport from Bern to Fermilab.

Following the dark count functionality checks, all calibration LEDs were tested for proper operation. To streamline the later cold commissioning, the optimal LED light yield for each SiPM was determined at this stage. Due to unforeseen delays and time restrictions related to the limited beamtime, the warm commissioning phase concluded here, and the detector transitioned into the cooldown phase. No additional commissioning tasks were performed during the cooldown since the SiPM breakdown voltage is highly temperature dependent and, thus, cannot be regulated during this period.

After the cooldown, the single-channel functionality checks conducted during the warm phase were repeated. While dark counts decrease significantly at cryogenic temperatures, they still occur at a low rate ($\sim$1 Hz) due to band-to-band tunnelling effects, which dominate at low temperatures [162]. However, due to the low rate, dark counts become impractical for the functionality checks. Instead, signals induced by the calibration LEDs were used. These tests were again performed at a common bias voltage of 47 V. The SiPM breakdown voltage was observed to decrease by approximately 12 V compared to warm operation during earlier operation in Bern. No new broken channels were identified during these tests.

To enable reproducible automatic LED calibration runs for each SiPM, an LED setting was tuned to produce a single p.e. range light yield. Due to the reduced PDE and sub-optimal LED locations in Module-0 (as discussed in previous sections), some ArCLight channels could not be illuminated with sufficiently intense light. Ongoing efforts aim to achieve a data-driven gain calibration to address this limitation.

The individual breakdown voltage U_{br} was first determined for each SiPM. This involved scanning across various bias voltages, with the SiPM gain extracted at each step using the automatic LED calibration. Figure 6.8 illustrates the result of such a scan for a single channel. This procedure was systematically repeated for all channels.

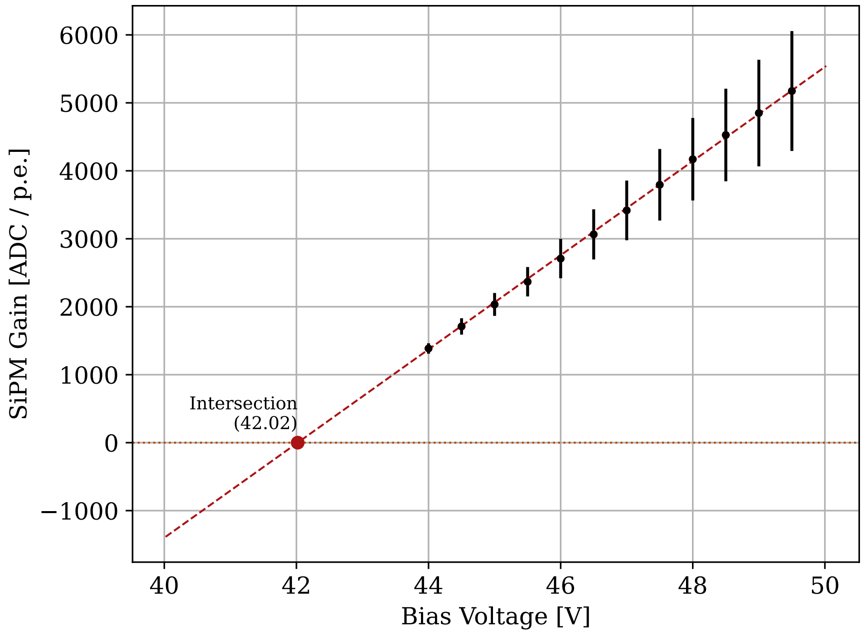

Figure 6.8 – Example of the breakdown voltage extraction based on SiPM gain measurements at various bias voltages. The linear fit through the individual gain measurements is extrapolated to determine its zero-crossing value, which is equivalent to the breakdown voltage.

To determine the optimal overvoltage, U_{ov}, the point with the maximal SiPM resolution is identified. Compared to the breakdown voltage, the optimal overvoltage remains the same for all SiPMs of the same type, assuming nearly identical operational conditions across the detector. Therefore, this value was extracted only for a few channels of each of the two SiPM types used in 2x2. For the selected channels, data is recorded at a fixed LED light yield. Unlike for the gain calibration, the data is taken at a high (but not saturating) light yield to ensure the photon distribution is Gaussian rather than Poissonian. The resolution is defined as the standard deviation of the integrated charge divided by the mean, which is measured over a sample of 15,000 pulses at each voltage.

The results for the two different types of SiPMs, one used in Module-0 and the other in all subsequent modules, are shown in Figure 6.9. The optimal overvoltages at LAr temperature are determined to be 3.0 V for the Hamamatsu S13360-6025CS (used in Module-0) and 5.0 V for the Hamamatsu S13360-6050CS (used in Modules 1, 2, and 3).

Once the optimal operation voltage $U_{\mathrm{op}} = U_{\mathrm{br}} + U_{\mathrm{ov}}$ had been determined for all channels, the final SiPM gain values were measured. By choosing a common overvoltage for each SiPM type, the gain values are expected to be the same. Figure 6.10 illustrates the distribution of the gain values for all four modules.

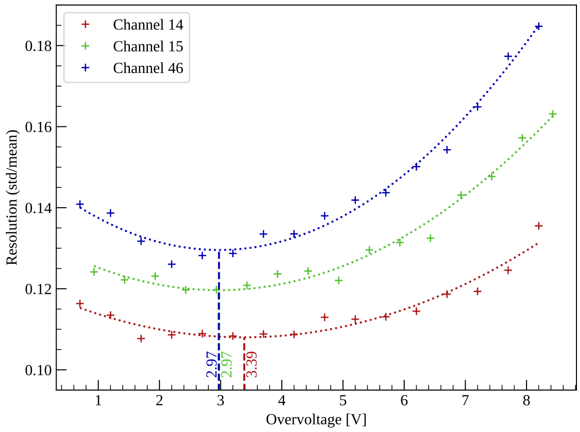

(a) S13360-6025CS (Module-0)

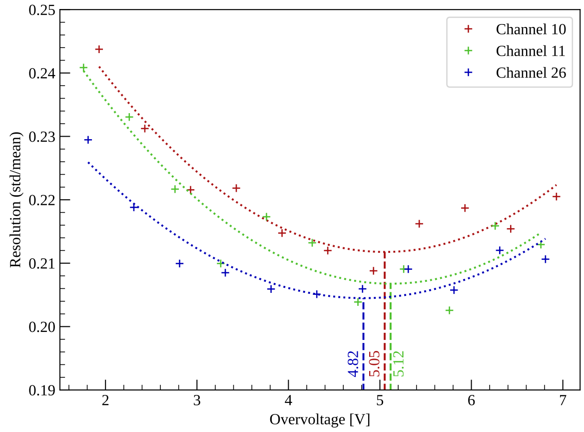

(b) S13360-6050CS (Module-1,2,3)

Figure 6.9 – Measured resolution (std/mean) for three channels of each of the two SiPM types used in 2x2. Left: Hamamatsu S13360-6025CS used in Module-0. Right: Hamamatsu S13360-6050CS used in Modules-1,2,3.

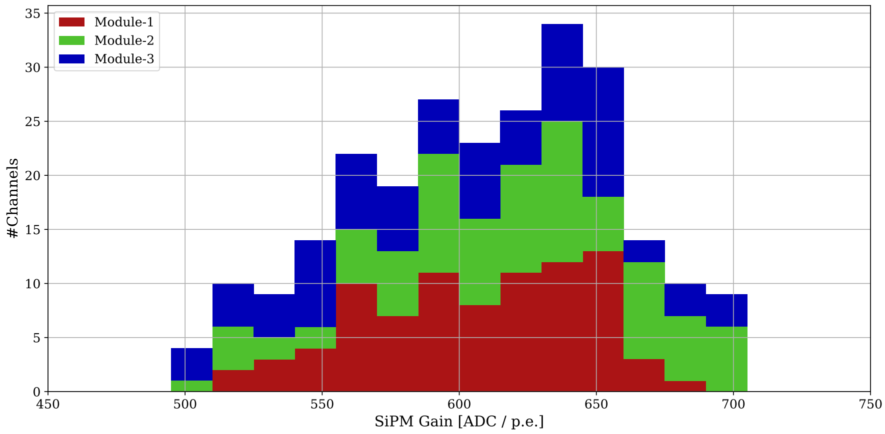

Figure 6.10 – SiPM gain distribution for Module-1,2,3. On Module-0, for only a fraction of the channels, a gain value could be extracted due to the nonoptimal LED placement, resulting in an insufficient light yield for calibration. Inactive channels are also excluded from the plot.

6.4 Operation in the NuMI beamline

After the successful installation and warm commissioning of the TPC modules, in late May 2024, the detector cooldown process was initiated. Prior to this, the detector was purged for over a week with gaseous argon to remove impurities. In the first phase of the cooldown, the goal was to uniformly cool the cryostat in the gas phase down to the LAr temperature without building up a large temperature gradient ($< 1\,\mathrm{K/cm}$). An excessive spatial temperature gradient could potentially damage the ArCLight light traps, which are prone to cracks and delamination of their mirror foils due to mechanical stress induced by temperature changes.

From the portable dewars attached to the filling manifold, a small but constant flow of LAr was pushed through the filter to the inlet on the top of each module. Due to the latent heat of the filling line and the module, the liquid was evaporated, and a constant vertical gas flow through each module could be established. The evaporation was further enhanced by diffuser nozzles attached to the end of the filling lines. Achieving a cooling rate sufficient for the process while avoiding liquid flow directly through the module posed significant challenges, and occasional splashes of liquid were unavoidable. Activating the cryocoolers added cooling to the cryostat bottom where the condenser vessel's return line is directed to (see Fig. 5.12). A limited LAr supply due to procurement issues aggravated the situation, causing periods where, due to a too-low input flow, the detector warmed up instead of cooling down. Despite these hurdles, excessive temperature gradients could be avoided throughout the gaseous cooldown phase.

Once the LAr supply constraints were resolved, within two days, the entire volume reached a state sufficiently close to LAr temperature, enabling a controlled increase in inlet flow to fill with liquid without risking temperature gradients. Within four additional days, the entire cryostat was filled with liquid, submerging the TPCs and reaching the necessary level to activate the HV system. Subsequently, the recirculation system was engaged to push argon through the filter. Figure 6.11 provides an overview of the entire cooldown process. At the end of the filling process, an unforeseen issue arose. The gas inlet line leading to the condenser vessel turned out to be installed too low, allowing liquid instead of gaseous argon to be sucked into the condenser vessel. This resulted in argon freezing at the cold heads. To prevent a recurrence, the level was maintained below this inlet, leaving a very narrow operational margin of only a few cm for the safe operation of the HV system. To ramp up the HV, a minimum layer of LAr is needed above the coupling point of the HV cable to the TPC cathode to prevent a catastrophic breakdown.

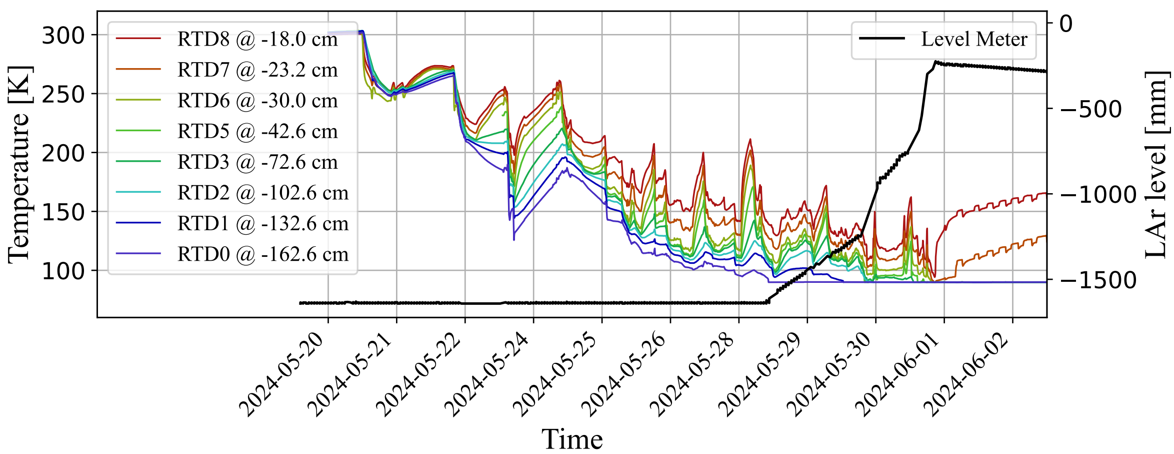

Figure 6.11 – Overview of the 2x2 main cryostat cooldown. The temperature data (left axis) from Module-2 is shown together with the LAr level (right axis). Both the level and RTD positions are relative to the top flange. The range of the level meter did not cover the full cryostat height, and thus, the start of the liquid fill is not visible.

During the purging phase, tests of temporarily maintaining the overpressure in the detector indicated remaining leaks in the inner indium seal (see Sec. 6.2). Due to expected thermal-induced movements of the top flange structure during the cooldown, further sealing efforts were deferred until post-cooldown. After completing the cooldown, a liquid loss was measured at ~2.4 L/h at an ullage pressure of 100 mbar. A constant gas injection into the condenser vessel was implemented to compensate for the loss and enable TPCs operation.

Despite the persistent cryogenic issues, on June 11th the recirculation and the level were stabilised, and a first attempt to ramp the HV of all four TPCs was initiated. However, the electron lifetime remained poor due to constant impurity ingress via the gas makeup line. The installed purity monitor confirmed this and measured an electron lifetime of ~50 µs, insufficient for efficient charge collection across the drift region. The ramp was halted at the half nominal voltage (0.25 kV/cm) following recurrent high event rates observed in the light readout system, indicative of potential electric discharges occurring in the active volume. It was decided to ramp down the HV and conduct a thorough analysis of the collected data. Figure 6.12 summarises the first ramp. Analysis of the charge and light data confirmed occurrences of discharge events similar to those observed in the Module-3 test runs at Bern, albeit with lower amplitude. It has to be considered that in 2x2, lower LRS thresholds could be applied due to the absence of cosmic background radiation, thus increasing the sensitivity also for discharge-like events. Based on the experiences with Module-3, it was concluded that there was a low probability that the discharges could lead to catastrophic damage to the detectors, so a second ramp was prepared. Additional monitoring tools were implemented, which allowed faster localisation of anomalous events in the light data stream. Further, changes to the ramp procedure were applied, including a lower ramp rate.

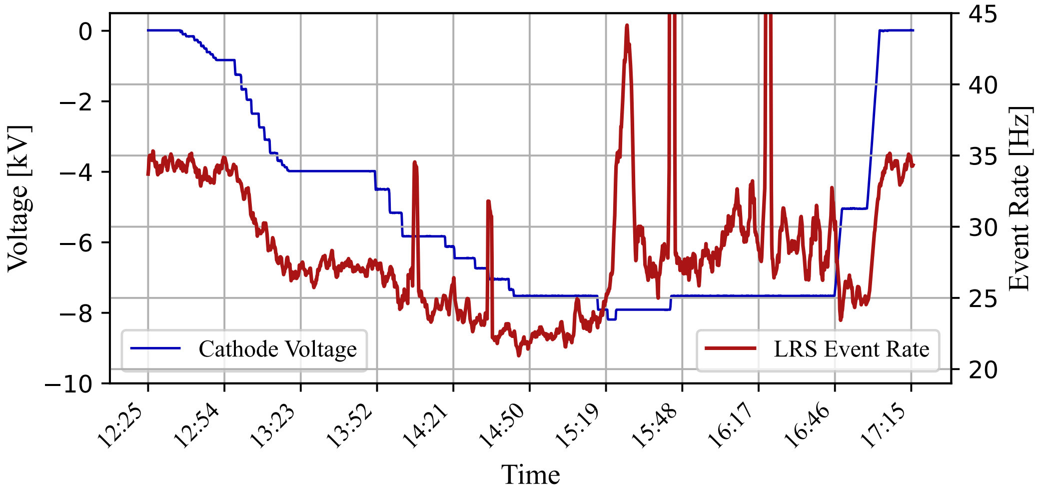

Figure 6.12 – Overview of the first HV ramp on June 11th, 2024. The light event rate (red) initially decreases as expected when the negative bias voltage on the cathode (blue) increases. At around −6 kV, light event rate anomalies begin. At the half nominal voltage of −7.5 kV starts to be elevated without recovering by itself for over half an hour. Consequently, the cathode voltage was ramped back to zero.

The time needed for these investigations was used by the cryogenic experts to resolve the remaining issues. Besides the previously mentioned issues, a malfunctioning cryo cooler was identified, and a grounding issue caused the liquid level probe to fail while running the recirculation pump. Both those issues could be resolved. Further, the copper catalyst filter material was regenerated to recover its full filtering capacity, and a O2 getter was installed in the gas makeup line to reduce the amount of impurities injected into the system.

At the beginning of July 2024, the fixes on the cryogenic system were concluded, and a second HV could be attempted. Within two days, cathode voltages were raised to 15.1 kV without observing any light event rate anomalies. At nominal field, the event rate stabilised at 16 Hz. However, after two days at nominal voltage, a malfunction in the gas makeup system caused the liquid level to drop, leading to an automatic HV system shutdown. Corrective measures, including improving the O2 getter system, stabilised the cryogenics and led to a major improvement in the argon purity as shown in Figure 6.13.

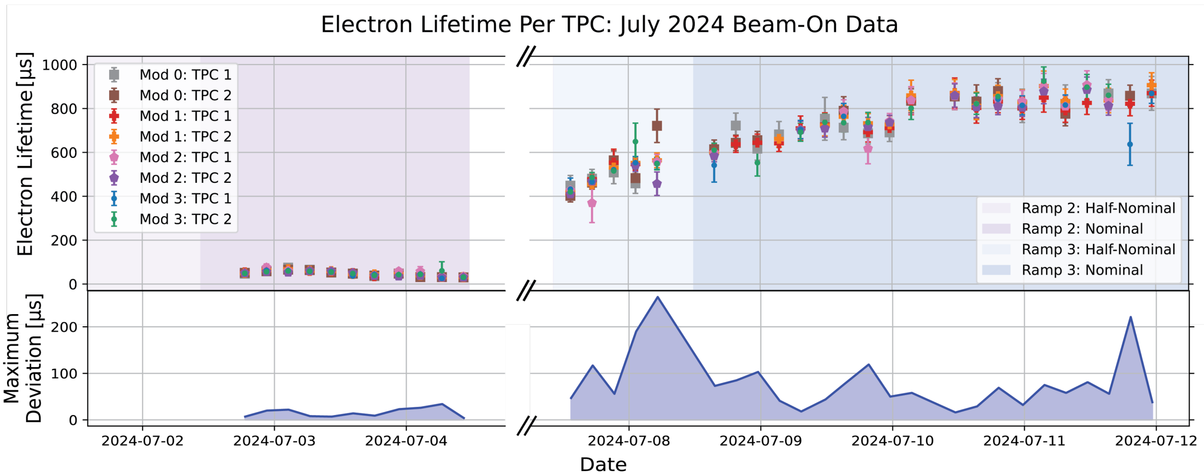

Figure 6.13 – Electron lifetimes extracted using TPC data over the beam-on data taking phase of the 2x2.

On July 8th, the third and final HV ramp was concluded, allowing four days of uninterrupted data collection before the NuMI beam shutdown. During this period, a 100 % detector uptime was achieved, recording interactions corresponding to over 1.1×10^{19} POT. Based on simulations, approximately 2.8×10^{4} neutrino interactions with a vertex in the active LAr volume are expected to be contained in this dataset. Figure 6.14 provides an overview of all the beam periods recorded.

In the following, three event displays are presented containing neutrino candidate events (Figures 6.15,6.17,6.16). Each display comprises the interactions recorded over a full beam spill. Since at the time of writing, no physics reconstruction algorithm containing particle identification was available for 2x2 data, the events were selected by hand scanning. The event displays combine data from all three subsystems: charge, light and Mx2. For both charge and light readout, the displays show raw data. For the charge displays, the hit intensities were translated to a number of electrons. The light readout data is

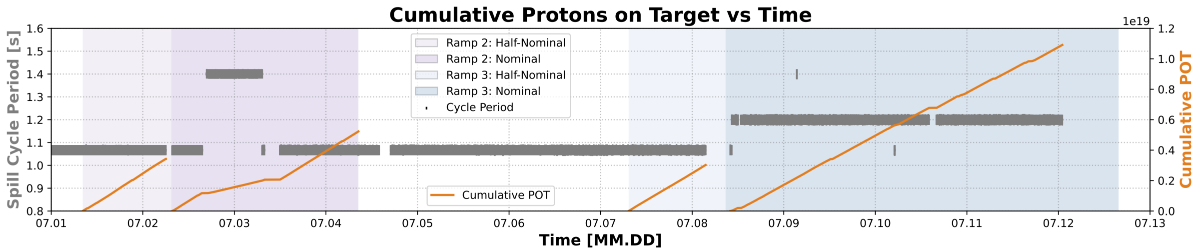

Figure 6.14 – Cumulative Protons On Target (POT) and spill period data throughout the TPC data taking.

depicted in ADC units and thus can only be interpreted as relative intensities.

Although the event displays do not constitute a quantitative analysis, they offer compelling qualitative evidence for the capability and coherence of the modular detector concept. All three events feature interactions that extend across multiple TPCs or modules, yet can be clearly combined “by eye”, illustrating the viability of the modular approach. Even complex interaction topologies spanning several modules are resolved with remarkable clarity. The segmentation introduced by the modular design does not substantially fragment events or obscure their topology.

Within each individual TPC, the observed charge and light signals show good spatial and temporal alignment. E.g. in Figure 6.16 from the summed light waveforms per TPC, three clearly separated light flashes are identified, which could be matched with the neutrino interaction occurring in Module-0 and Module-1, and the two passing rock muons. The fact that only one light flash can be identified in Module-0 and Module-1 together gives a clear indication that the observed tracks originate from the same neutrino vertex. Flashes with the same timing can be observed in both TPCs of Module-2, which enable matching detached deposits to the neutrino interaction and separating them from the throughgoing muons. Notable differences in the amount of collected light can be seen between the ArCLights (first and third sets of six SiPMs from the bottom) and the LCMs (second and fourth sets), which is expected due to their different PDEs.

Beyond the internal performance of the 2×2 system, the event displays also show successful matching of tracks between the 2×2 and M×2 detectors. In shared beam spills, track segments can be followed visually as they propagate from one system into the other. The observed geometrical consistency and timing alignment support the feasibility of integrated reconstruction across detector subsystems. In particular, Figure 6.16 shows two muons traversing the upstream M×2, Module-3, Module-2, and the downstream M×2 without stopping. Such through-going tracks provide valuable constraints for improving the spatial and temporal alignment of detector components in reconstruction algorithms. While these observations are not yet based on quantitative reconstruction, they offer strong visual confirmation that the reconstruction algorithms under development can be expected to achieve excellent performance.

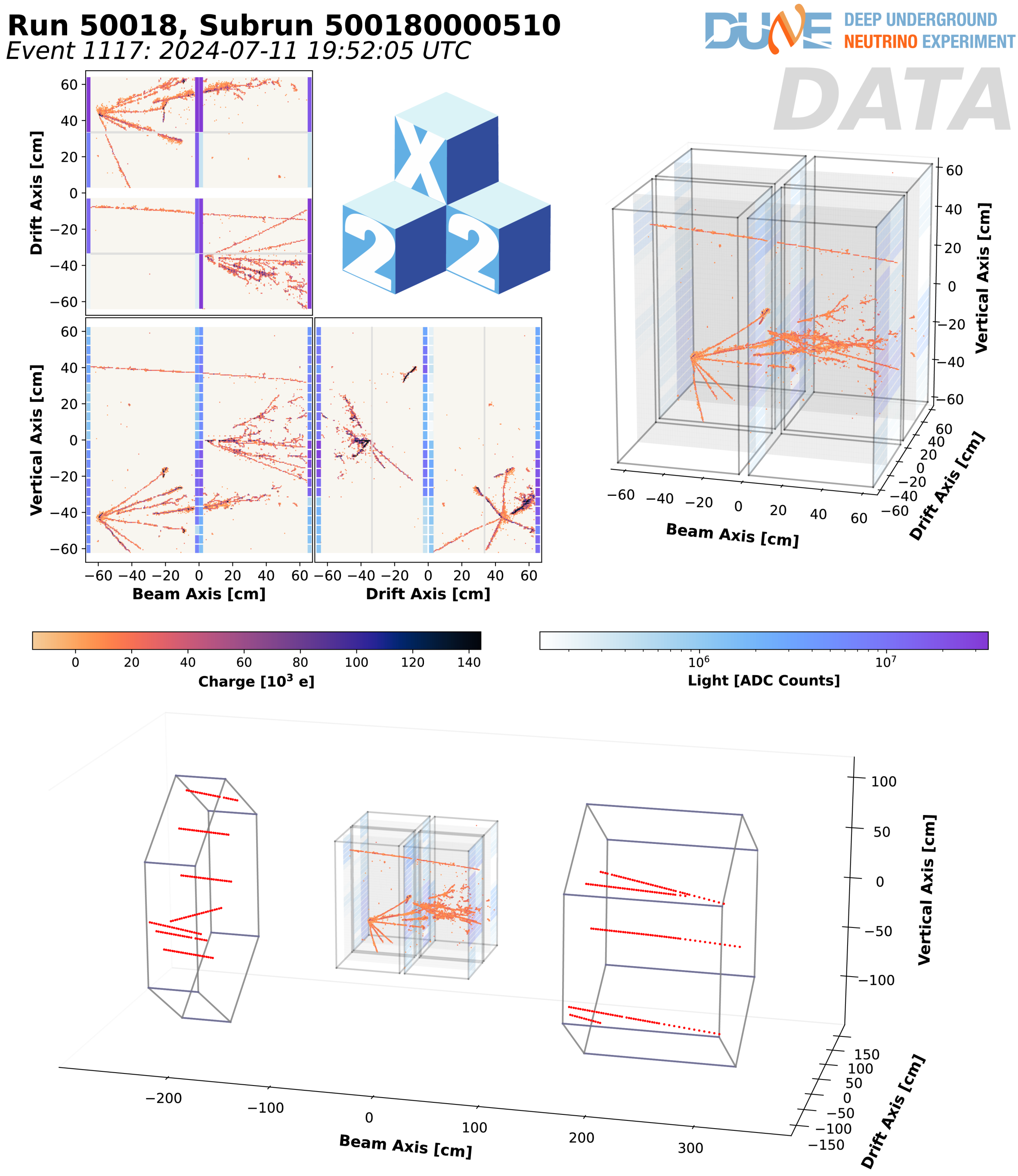

Figure 6.15 – Raw data event display with two neutrino-candidate interactions, in Module-1 and Module-2, within a single beam spill. An additional rock muon passing through both Module-2 and Module-3 is registered by both the upstream and downstream Mx2 trackers (bottom plot).

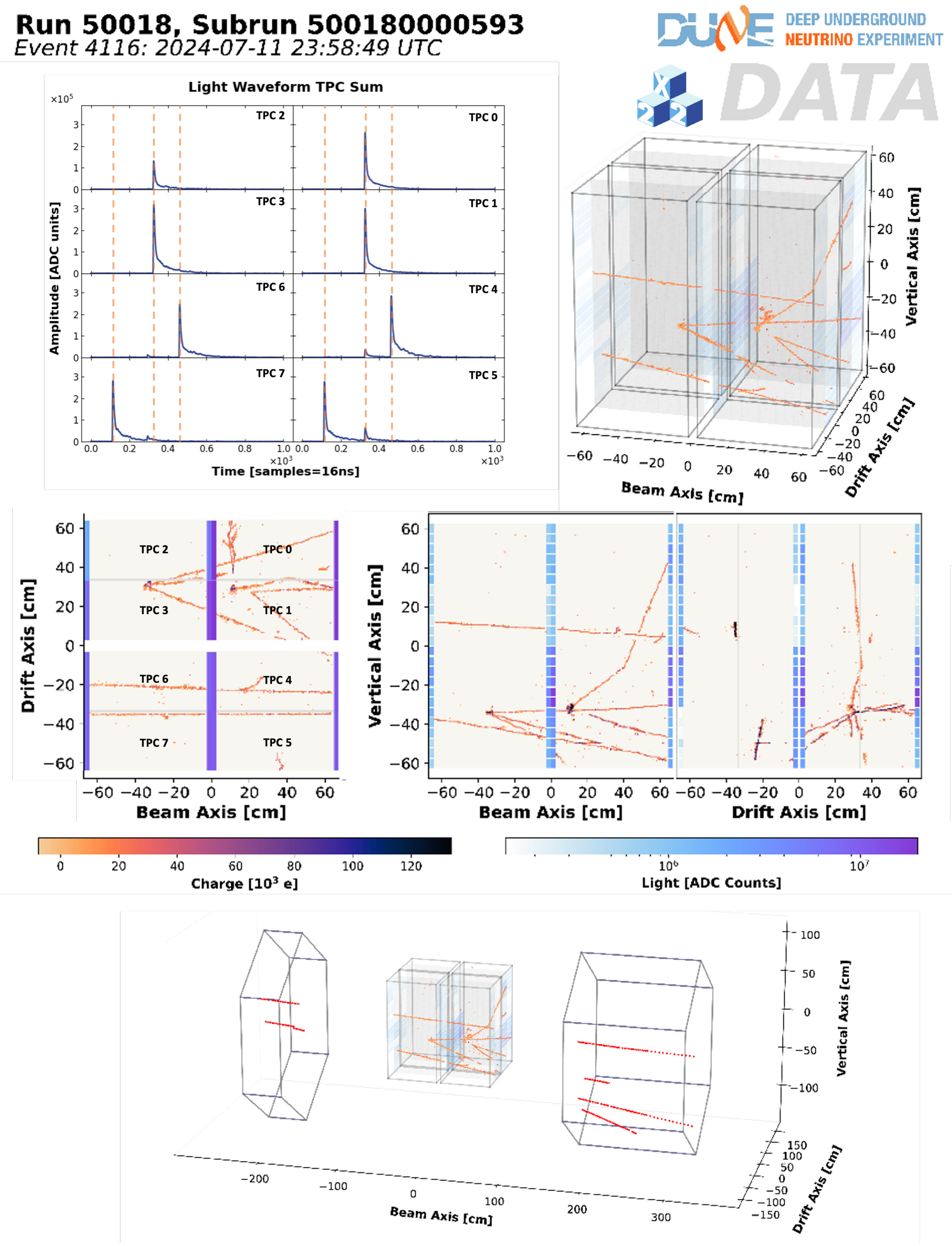

Figure 6.16 – Raw data event display with a neutrino-candidate interaction in Module-0 and Module-1. On the additional two throughgoing muon interactions in Module-2 and Module-3, delta electrons splitting of the muon tracks can be identified. The two muons can be matched to interactions recorded in the Mx2 planes. Three separate light flashes can be identified, indicating that a total of three independent interactions occurred.

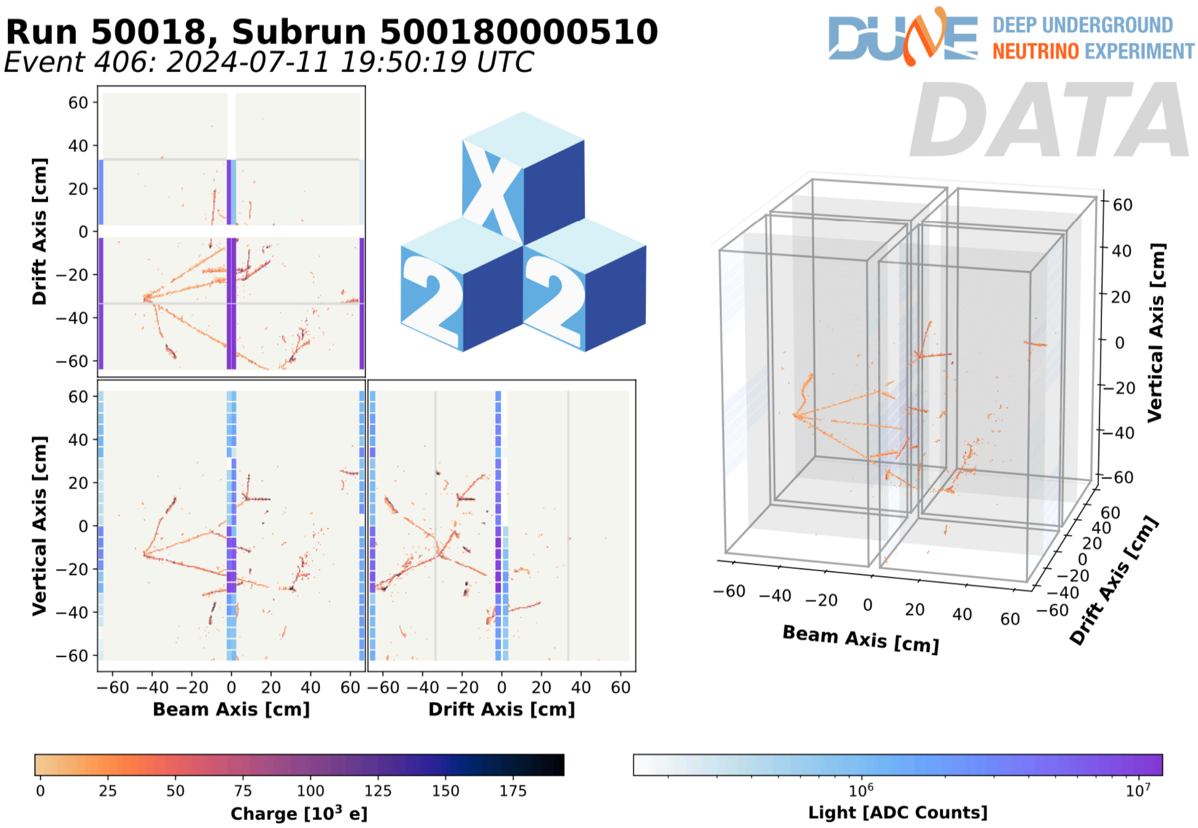

Figure 6.17 – Raw data event display with a single neutrino-candidate induced vertex close to the cathode in Module-3. The Mx2 system is not visualised since no incoming or outgoing interactions were matched with the event.

6.5 Extraction of the T_0 resolution using the NuMI beam structure

As previously highlighted in Section 4.1, timing resolution represents one of the most critical performance metrics for the light readout system. Precise determination of the interaction time (T_0) is essential for efficiently matching light signals across multiple TPCs. Particularly in the case of event pile-ups, precise timing information helps to associate individual tracklets with their respective interaction vertices.

To establish constraints on the precision achievable for T_0 reconstruction, an analysis of the temporal structure of the NuMI neutrino beam spills is conducted. As thoroughly described in Section 5.2, this structure directly arises from the proton storage and acceleration procedures within the main injector. Specifically, a spill comprises six batches, with each batch containing 81 proton-filled bunches followed by 3 empty bunches. The temporal spacing between consecutive bunches is governed by the main injector RF frequency of 53.1 MHz, corresponding to 18.83 ns. Each bunch has a width of 0.8 ns RMS [163]. A schematic representation of this beam spill structure is presented in Figure 6.18.

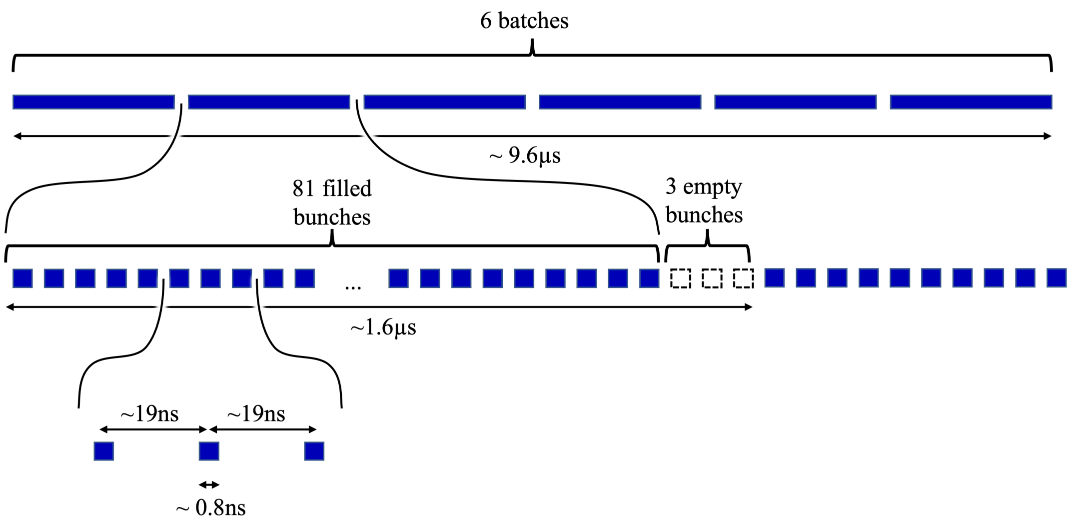

Figure 6.18 – Illustration of the NuMI beam spill structure including the batch and bunch structure.

I aim to resolve this spill structure using the reconstructed T_0 times of beam-related interactions. By measuring the width of the reconstructed bunch structures, an upper limit for the achieved T_0 resolution can be extracted. Since the ADC sampling rate of 16 ns used in 2x2 is only slightly lower than the time structure of the bunches, resolving the bunch structure is challenging. To address this, the approaches described in Section 4.8 are employed. These use fitting methods to achieve a resolution beyond the limit imposed by the ADC sampling rate. Due to its demonstrated superior resolution on simulation data, only the half-max method is used here.

To avoid including T_0 timestamps from secondary particles with delayed emission relative to the beam incidence, only the first light hit per beam spill is considered in this analysis. The first light hit is defined by selecting the first SiPM channel exceeding a threshold of 3000 ADC units, corresponding to ∼7 p.e. Furthermore, signals saturating the ADC are discarded. Any impurity in the hit selection of this analysis is expected to contribute to a constant background, which degrades the T_0 resolution. The inclusion of such a background in the fitting procedure, therefore, allows the determination of an upper limit for the precision of the T_0 reconstruction.

No time-of-flight correction was applied for the incident neutrino (or rock muon) and for the scintillation photon propagation. Due to the small TPC size, the maximum propagation path of a photon to the next light trap is 30 cm, equivalent to a maximum time delay of ∼1 ns.

Resolving the NuMI spill structure requires not only precise reconstruction of the light hit in the recorded waveforms but also an accurate beam trigger for time reference. As discussed in Section 5.7, the early-warning beam trigger used to start the LRS DAQ is subject to a time jitter on the order of tens of nanoseconds; thus, additionally, the RWM beam monitor signal is recorded, providing a nanosecond-level time reference for the incoming beam. Figure 6.19 shows the RWM signals recorded over 250 beam spills and the extracted time correction for the T_0 reconstruction for a larger dataset. A significant variation exceeding 50 ns can be observed in the RWM distribution, underscoring the necessity of this correction for accurately resolving the beam bunch structure. It is notable that the distribution of the RWM corrections has two distinct peaks separated by ∼19 ns, indicating a shift corresponding precisely to one beam bunch. This can be explained by the fact that in the process of the slip-stacking, the first bunch is only partially filled and does not reach the RWM trigger threshold, which delays the signal to the subsequent bunch. In either scenario, such a shift by one bunch cycle does not impact the results of the subsequent analysis since it preserves the reference to the RF structure.

A second correction was performed to compensate for variations in cable length between the SiPM and the ADC. Table 6.2 details the cable lengths used inside (cold side) and outside (warm side) the detector cryostat. For the warm side, only cables between the module feedthrough and the VGA are listed, as identical cable lengths were used for all channels between the VGA and ADC; thus, no correction is required for these. According to measurements provided by the cable manufacturer[1], a signal delay of 5.0 ns per meter of cable length is expected. The varying cable lengths result in a maximum delay difference of approximately 7 ns. All extracted T_0 timestamps are corrected accordingly.

For the following analysis, the full LRS dataset recorded during stable, nominal data-taking between July 8 and July 12, 2025, is used. The dataset includes a total of 1.08×10^{19} POT. Applying the selection criteria described above, 42% of the first light hits are detected by an ArCLight and 58% by an LCM. In total, about 170,000 first light hits are reconstructed.

[1] Samtec Inc., FCF8 High Speed Characterization Report, `samtec.com/products/fcf8`

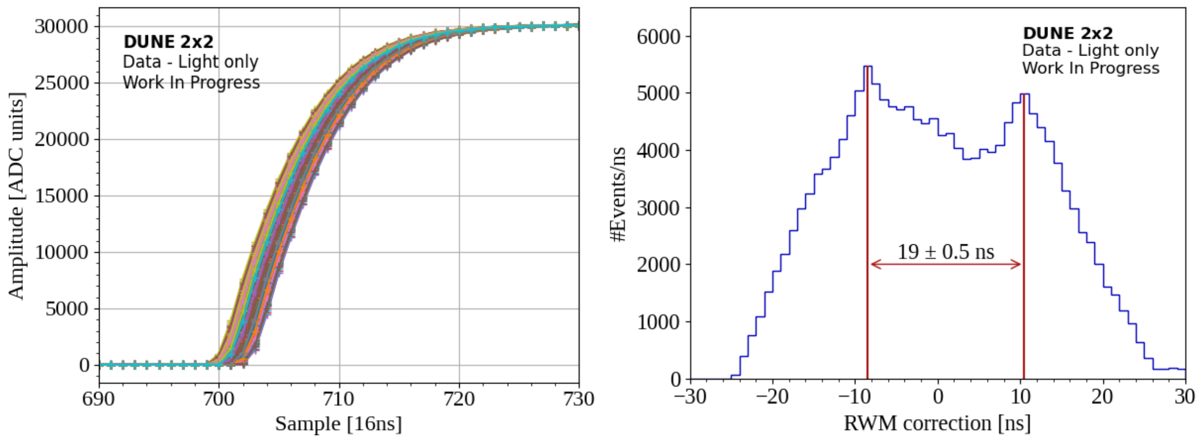

(a) **(b)**

Figure 6.19 – (a) Spread of the raw RWM signal over a 5 min period (250 spills) as recorded on the LRS ADC. (b) Distribution of the beam jitter correction calculated based on the threshold crossing time of the RWM signal. Two peaks can be observed with a (19.0±0.5) ns distance, which corresponds to the NuMI beam bunch separation time.

Table 6.2 – Signal propagation delays caused by variations in the used cable lengths on the cold and warm side of the detector.

Module	Light detector	Cold side cable length [in]	Warm side cable length [in]	Total delay [ns]
0	Bottom ArCLight	80	87	21.2
	All other detectors	60	87	18.7
1	Bottom ArCLight	80	87	21.2
	All other detectors	60	87	18.7
2	Bottom ArCLight	80	118	25.2
	All other detectors	60	118	22.6
3	Bottom ArCLight	80	84	20.8
	All other detectors	60	84	18.3

Figure 6.20 displays the distribution of reconstructed T_0 timestamps over the full beam spill length. Separated by the three empty bunches, causing a gap of approximately 56 ns, the six batches can be clearly distinguished. The overall decrease in the number of events per time bin is attributed to the selection of only the first light hit per spill, resulting in a beta distribution with parameters $\alpha = 1$ and β equal to the number of neutrino or beam-related interactions per spill.

A detailed view of the timestamp distribution within a single beam batch is presented in Figure 6.21, revealing the 18.8 ns bunch structure. When the timestamps obtained from ArCLights and LCMs are examined separately, this periodic structure is readily apparent. However, once these two datasets are combined, the clear identification of individual bunches is no longer possible, suggesting a relative timing offset between ArCLights and

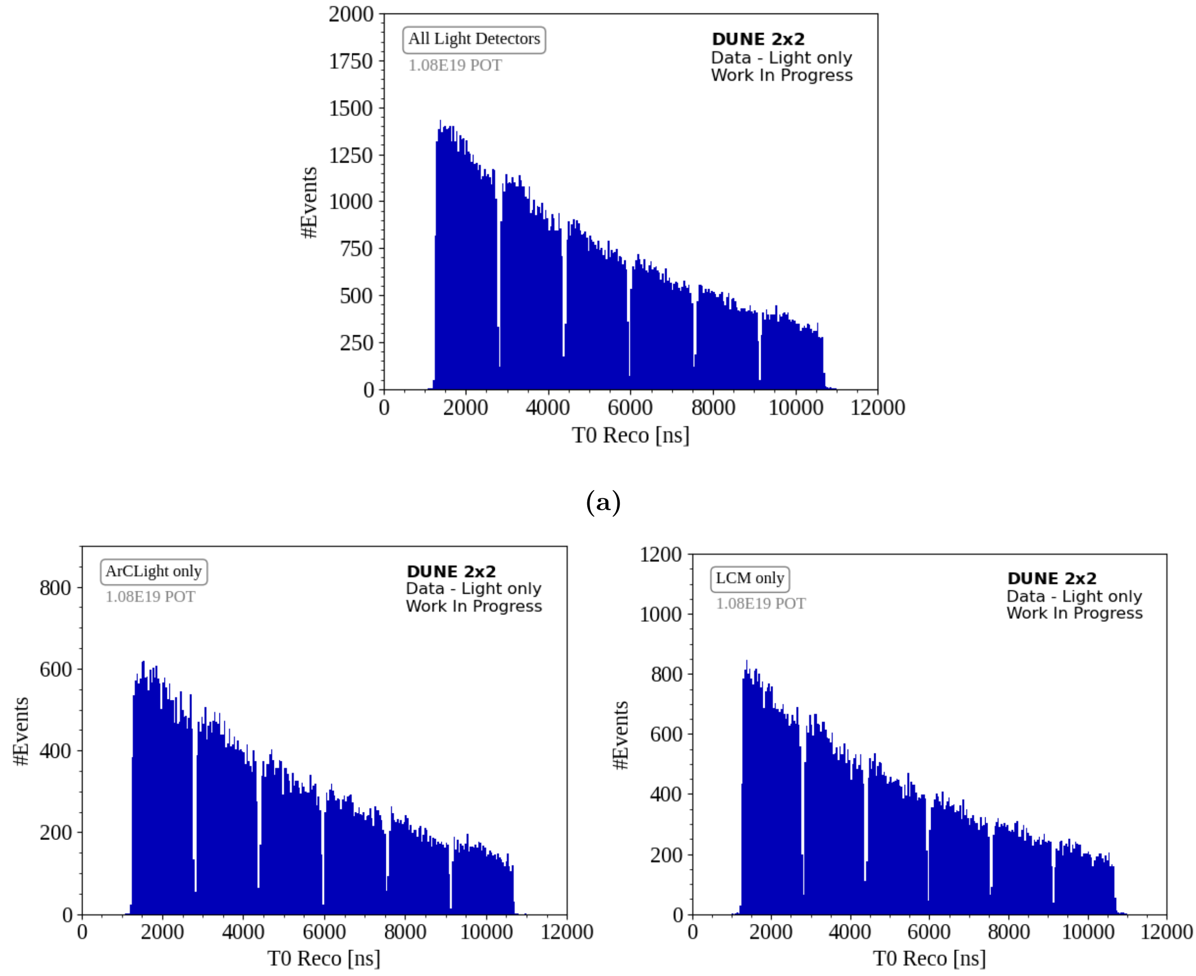

(b) (c)

Figure 6.20 – Reconstructed first hit T_0 timestamps for a full NuMI spill including (a) all light detectors, (b) only ArCLights, (c) only LCMs. The timestamps were corrected for beam trigger jitter using RWM and for cable propagation delays.

LCMs.

To confirm that the observed structures correspond to beam bunches and are not artefacts resulting from the ADC sampling rate, the spacing between the bunches is extracted and compared with the expected value. A Fourier transform is applied to the histogram to determine the frequency of the observed bunch structure precisely. Figure 6.22 illustrates this method applied to the LCM data. The extracted frequency of (53.093 ± 0.053) MHz corresponds to a bunch spacing of (18.835 ± 0.019) ns, closely matching the expected value of 18.831 ns given by the main injector RF frequency. These results confirm that the periodic structure observed indeed corresponds to the NuMI beam bunches.

The value obtained using the FFT method can be independently verified through a multi-Gaussian fit applied to the histogram. The result of this approach is shown in Figure 6.23. Performing the fit across the entire first batch, which contains the largest event statistics,

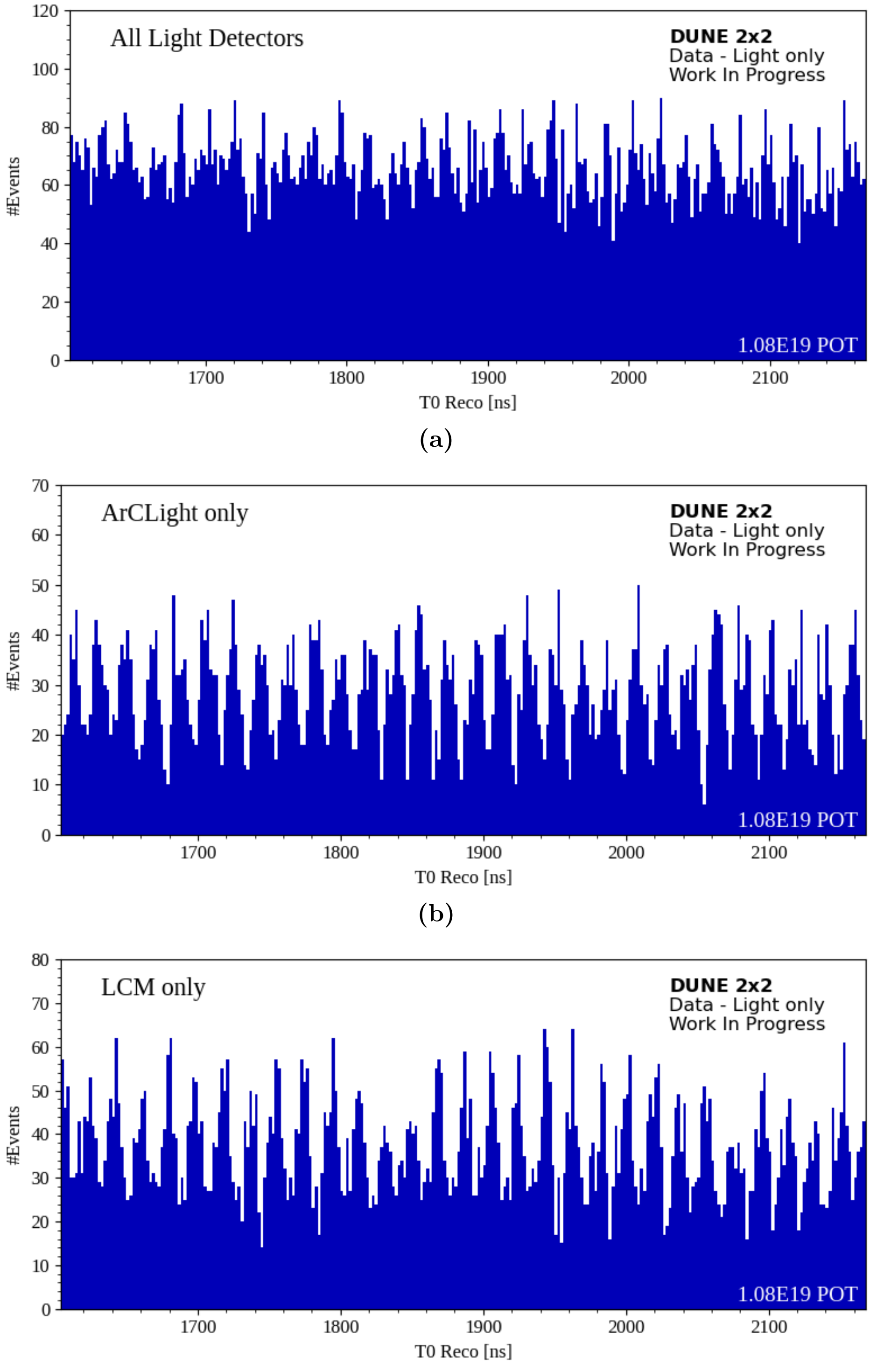

(a)

(b)

(c)

Figure 6.21 – Reconstructed first hit T_0 timestamps for a small time window in the first batch of the NuMI beam including (a) all light detectors, (b) only ArCLights, (c) only LCMs. The timestamps were corrected for beam trigger jitter using RWM and for cable propagation dealys.

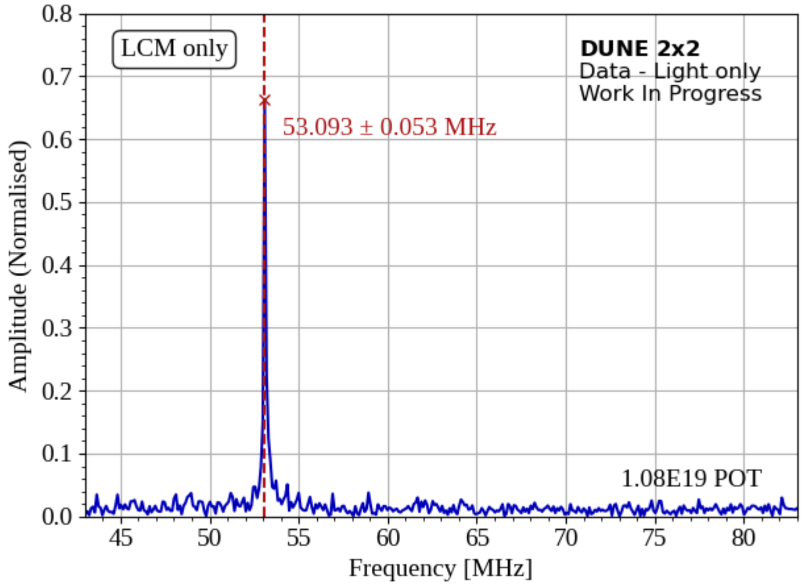

Figure 6.22 – Extracted bunch frequency using a Fourier transform of the T_0 distribution using only LCM data.

yields a mean bunch spacing of (18.81 ± 0.10) ns, agreeing with the value obtained using the Fourier analysis.

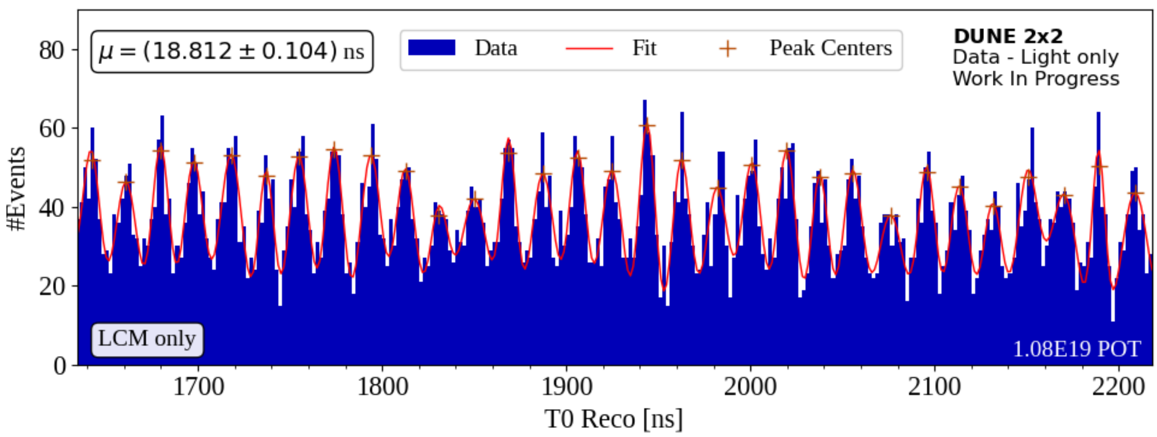

Figure 6.23 – Fitted bunch spacing using a Multi-Gaussian function. Due to better resolution, only LCM data is used here. The fit results displayed are obtained using the entire first batch. For reasons of clarity, only a smaller window is shown here.

Having determined the bunch spacing, it becomes possible to overlay the bunches, significantly increasing the statistics per bunch to extract the width of the reconstructed bunch structure. To achieve this, the T_0 timestamps are periodically shifted by applying

$$f(T_0) = T_0 \bmod(N \cdot 18.835\,\text{ns}), \tag{6.1}$$

where N denotes the number of bunches after which the timestamps are shifted. This method enables an investigation into the previously observed offset between ArCLight and LCM bunch structures. For this purpose, the bunch structure is examined separately for each ADC by dividing the histograms from ArCLights and LCMs into contributions from individual detector modules (effectively corresponding to separate ADCs). As shown in Figure 6.24, a significant timing shift on the order of ns between individual ADCs is evident. Each histogram was fitted using a triple-Gaussian function

$$f(x) = A \cdot \left[\exp\left(-\frac{(x-(\mu-\Delta_\mathrm{B}))^2}{2\sigma^2}\right) + \exp\left(-\frac{(x-\mu)^2}{2\sigma^2}\right) + \exp\left(-\frac{(x-(\mu+\Delta_\mathrm{B}))^2}{2\sigma^2}\right)\right], \tag{6.2}$$

where σ is common to all three Gaussians, and the distance between peaks is fixed at the measured bunch spacing $\Delta_\mathrm{B} = 18.835\,\mathrm{ns}$. To mitigate edge effects, the fitting was restricted to the region between the first and last peaks.

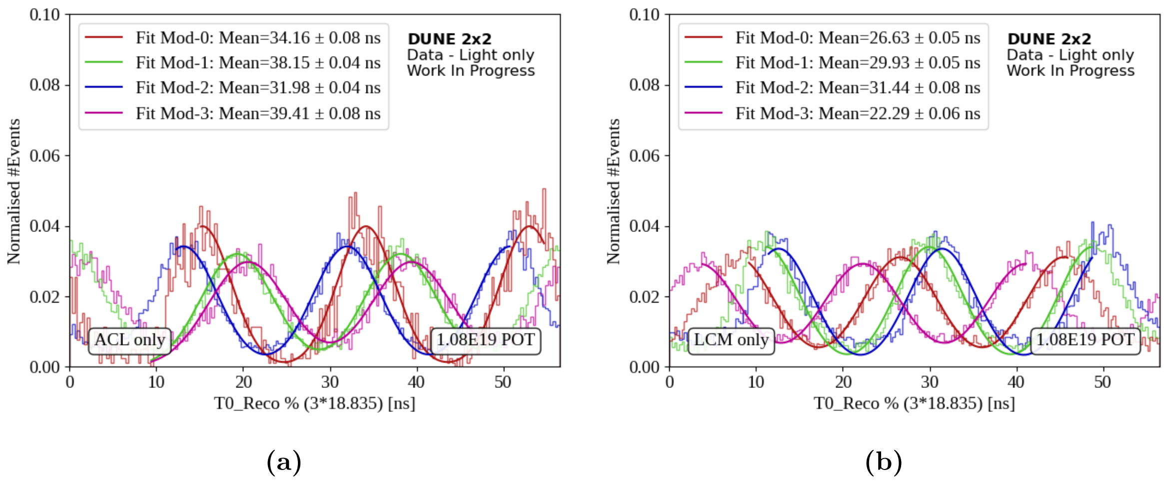

Figure 6.24 – Reconstructed T_0 timestamps overlayed into three bunches for each individual Module (= each single ADC) for (a) ArCLights and (b) LCMs. A triple-Gaussian function (described in the text) is fitted to extract the distribution parameters.

By utilising the mean parameter μ obtained from the fits, the relative timing shift of each ADC is determined. Correcting these shifts allows for precise alignment of the bunch structures from all ADCs, significantly improving the overall timing resolution, as illustrated in Figure 6.25. The figure shows the individual contributions from each module. For the ArCLights, notable inefficiencies are identified in Module-0 and Module-3. The inefficiency observed in Module-0 aligns with expectations, as its different ArCLight design and the less efficient SiPMs lead to a reduced PDE. However, the cause of the inefficiency in Module-3 is currently unclear.

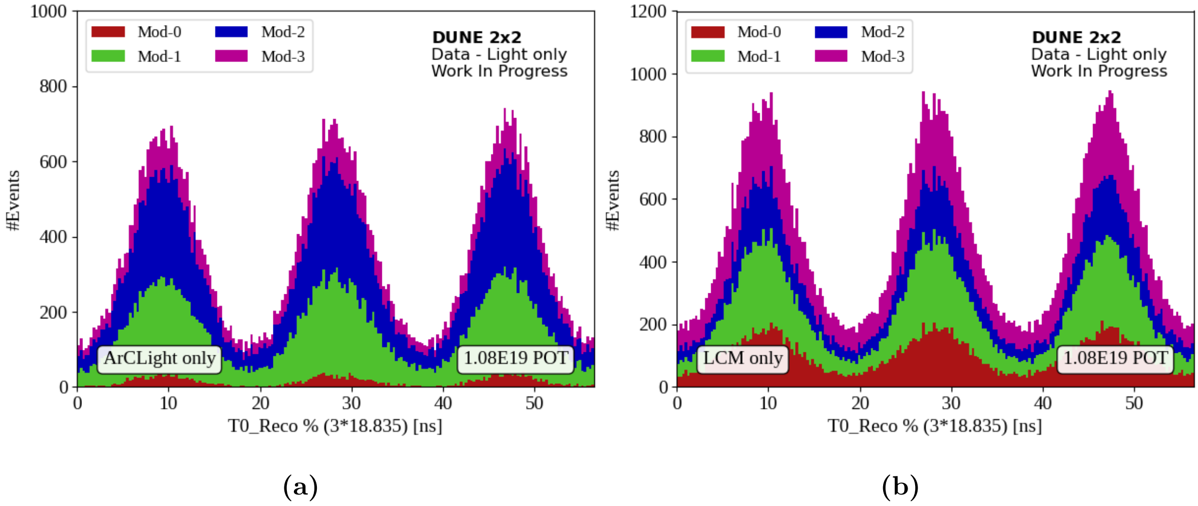

Figure 6.25 – Reconstructed T_0 timestamps overlayed into three bunches after the ADC offset correction for (a) ArCLights and (b) LCMs. The contributions of each individual module are illustrated by colour in the stacked histograms.

After correcting for the ADC offsets, the overlaid bunch structures can be fitted using the function described in Equation 6.2 to extract the resolution parameters. The results are shown in Figure 6.26, yielding sigma values of (4.04 ± 0.03) ns for the ArCLight and (4.16 ± 0.03) ns for the LCM. To establish an upper limit on the achievable T_0 resolution, the intrinsic width of the beam bunch must be subtracted

$$R \leq \sqrt{\sigma_{\mathrm{Fit}}^2 - \sigma_{\mathrm{Beam}}^2}, \tag{6.3}$$

with $\sigma_{\mathrm{Beam}} = 0.8$ ns. Consequently, this calculation yields an upper limit for the resolution of $R_{\mathrm{ArCLight}} \leq (3.96 \pm 0.03)$ ns and $R_{\mathrm{LCM}} \leq (4.08 \pm 0.03)$ ns.

Fitting the data with the triple-Gaussian function (Eq. 6.2) assumes that the observed distribution is entirely due to direct beam interactions. Specifically, the gaps between bunches must be fully represented by the overlap of the two adjacent Gaussians. Introducing a constant background term into the fit allows multiple effects to be accounted for. Firstly, this accommodates any impurity in the first light hit selection, including hits that do not originate directly from primary beam interactions but rather from delayed scintillation light. Secondly, it addresses contributions from radiological or cosmic background radiation present during the beam spill. Even if, as detailed in Section 5.2, this background contribution is expected to be minimal. Figure 6.27 illustrates the three-bunch histograms with the fits incorporating background, resulting in significantly improved fit accuracy. While the LCM exhibits a marginally smaller sigma value in this scenario, its background-to-amplitude ratio (0.24) is considerably higher compared to that of the ArCLight (0.14).

Reducing the overlay to a single bunch further enhances the statistics per bunch, as illustrated in Figure 6.28, where the fitting procedure, including a constant background, is applied. The obtained results are consistent with those from previous analyses. In

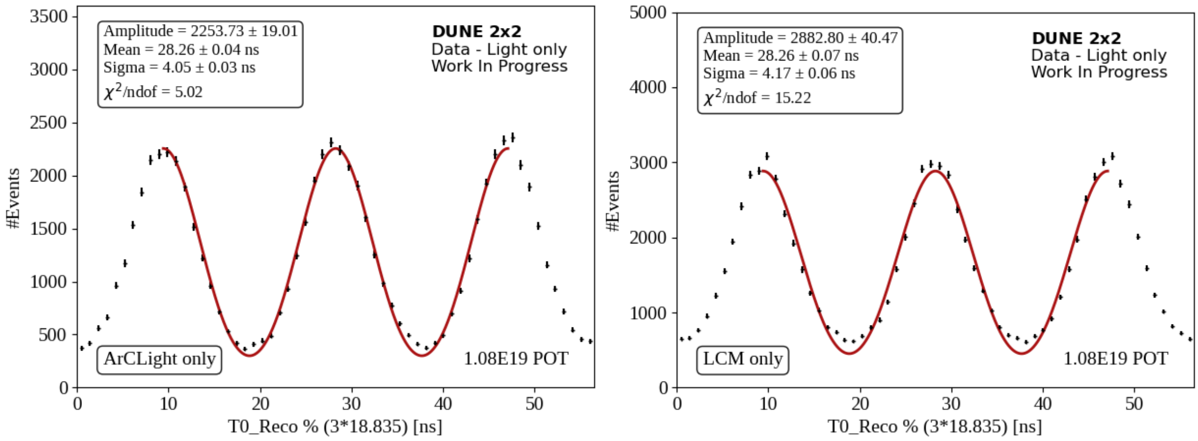

(a) **(b)**

Figure 6.26 – Reconstructed T_0 timestamps overlayed into three bunches using a modulo function from (a) ArCLights and (b) LCMs. A triple Gaussian function (described in the text) is fitted to extract the resolution parameters.

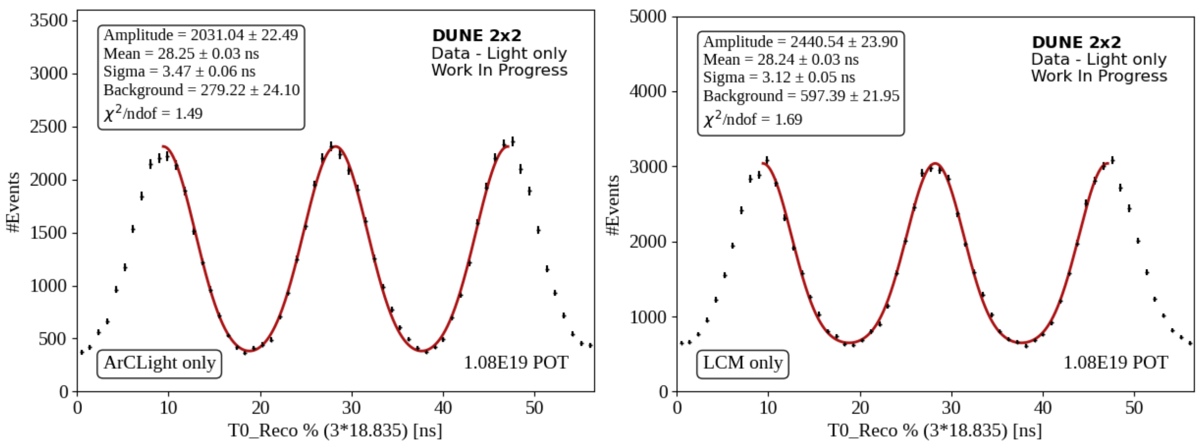

(a) **(b)**

Figure 6.27 – Reconstructed T_0 timestamps overlayed into three bunches using the modulo function from (a) ArCLights and (b) LCMs. An absolute offset is added to center the bunches in the plot. A triple Gaussian function with a constant background (described in the text) is fitted to extract the resolution parameters.

summary, the upper resolution limits are determined as $R_{\mathrm{ArCLight}} \leq (3.31 \pm 0.04)$ ns and $R_{\mathrm{LCM}} \leq (3.03 \pm 0.03)$ ns. For comparison, the intrinsic width of the beam bunches is also shown in the same figure.

The T_0 resolution is anticipated to strongly depend on the amplitude of the detected light hits. To investigate this amplitude dependence for both the ArCLight and LCM, the light hits are sorted into amplitude bins, and the resolution is calculated separately for each bin. Figures 6.30 and 6.31 present the individual fit results for the ArCLight and LCM, respectively. These findings are summarised collectively in Figure 6.29.

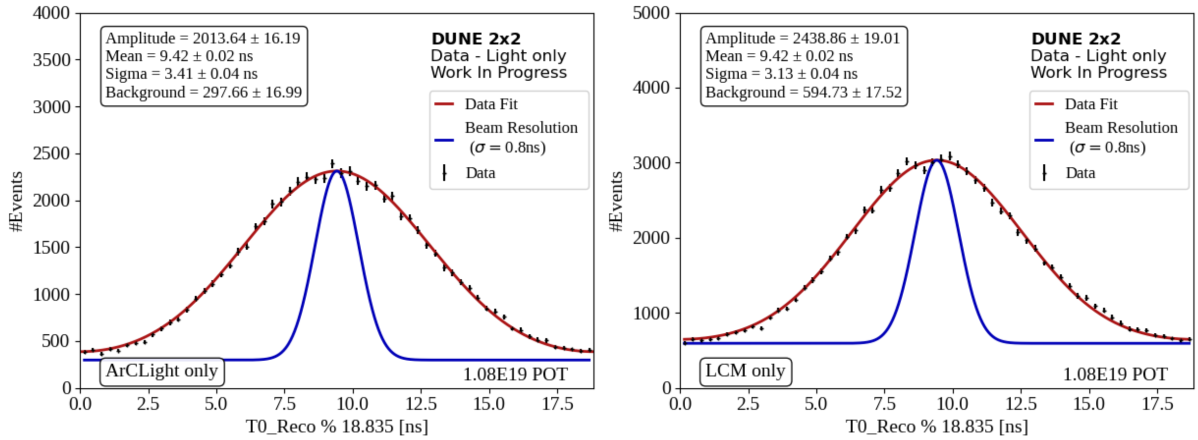

(a) **(b)**

Figure 6.28 – Reconstructed T_0 timestamps overlayed into a single bunch using the modulo function from (a) ArCLights and (b) LCMs. An absolute offset is added to centre the bunch in the plot. Although only a single bunch is displayed, a triple Gaussian function (described in the text) is fitted to properly fit the edge regions.

For the LCM, the resolution clearly improves with increasing amplitude, approaching values below 3 ns for high-amplitude signals. In contrast, for the ArCLight, a notable deterioration in resolution around 20k ADC is observed, although the uncertainties associated with these measurements are considerably larger. Currently, no definitive explanation for this observed behaviour has been identified.

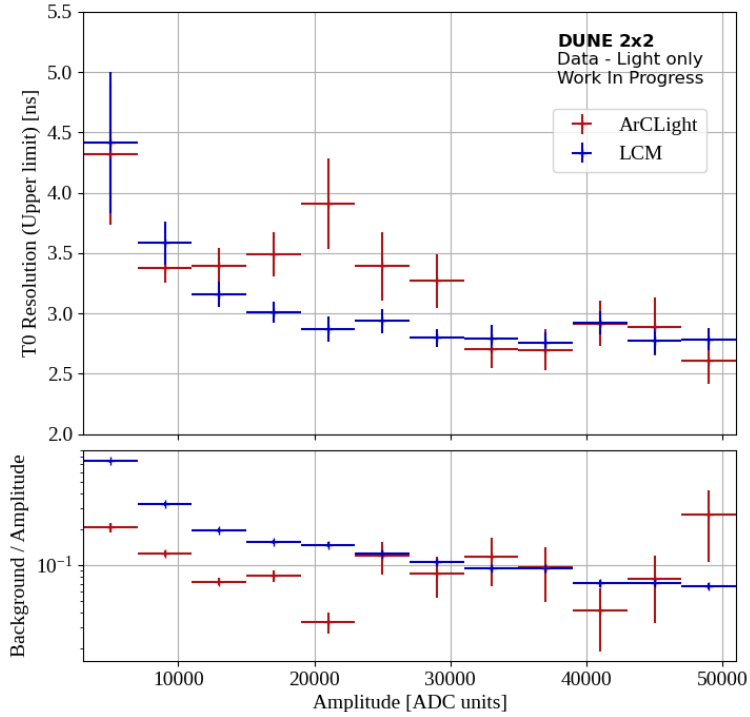

Figure 6.29 – Extracted T_0 resolution and background-to-amplitude ratio versus signal amplitude for both ArCLights and LCMs.

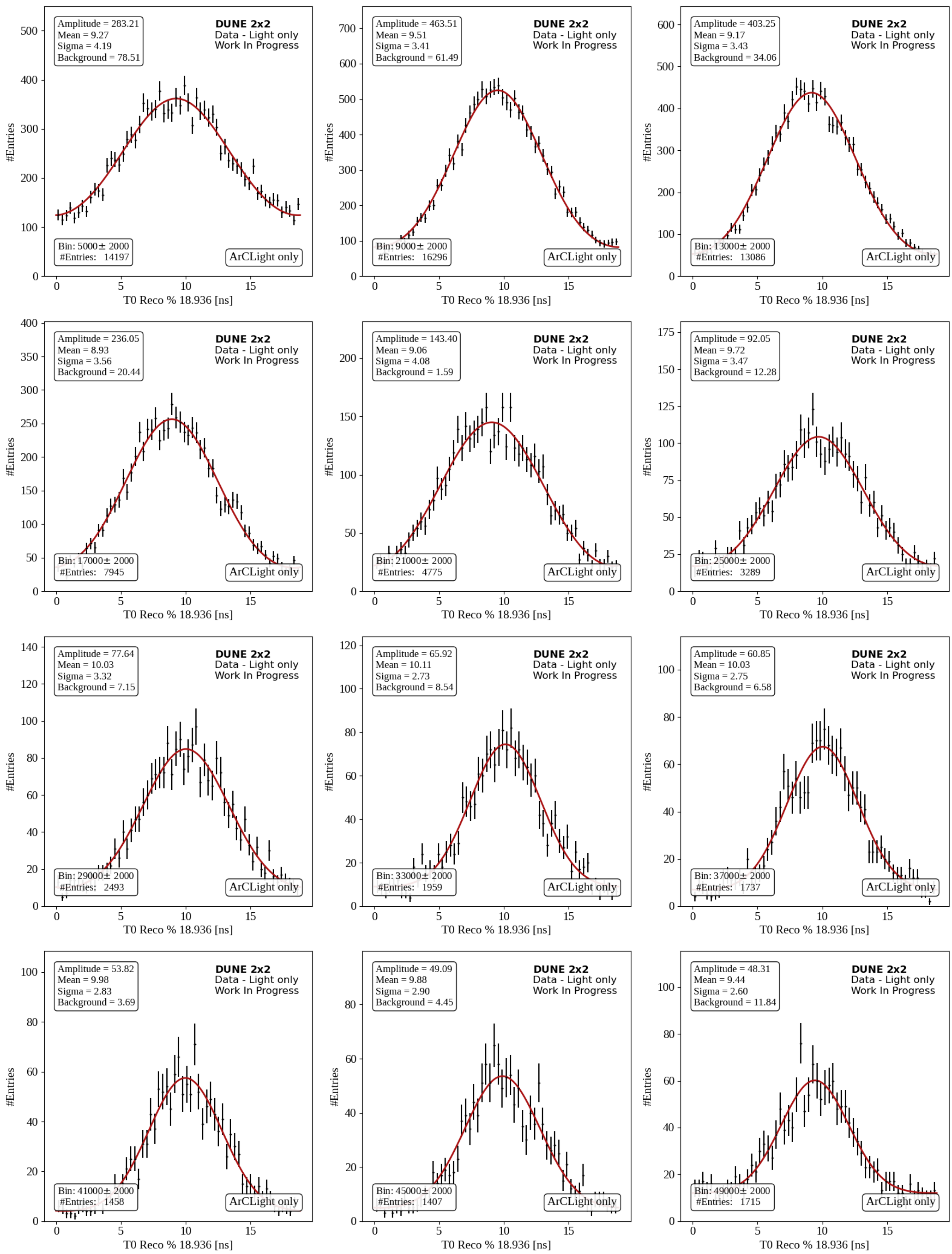

Figure 6.30 – Amplitude-binned scan of the T_0 resolution using ArCLights only.

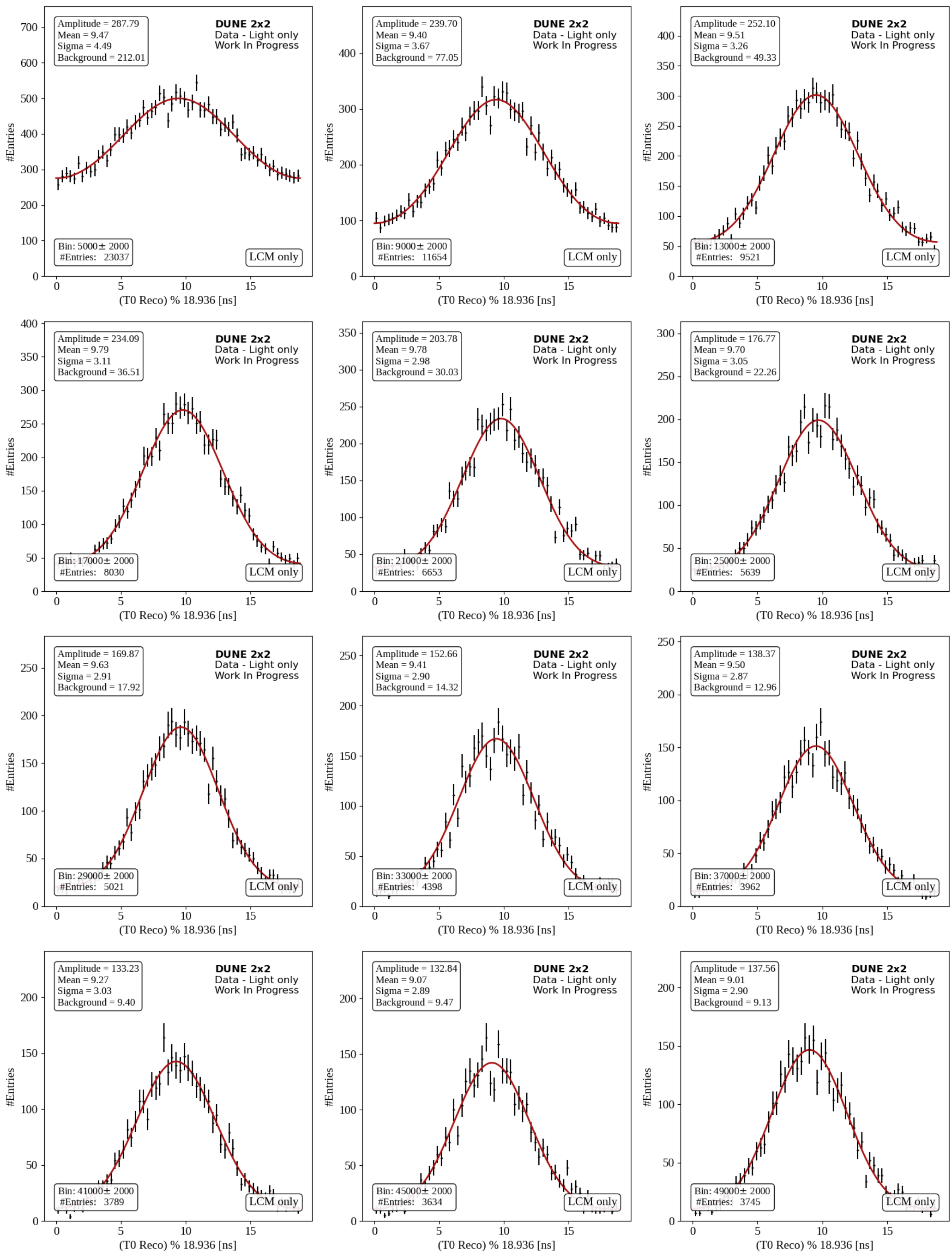

Figure 6.31 – Amplitude-binned scan of the T_0 resolution using LCMs only.

Chapter 7

Conclusion and Outlook

The work presented in this thesis describes the successful development, implementation, and validation of a novel modular LArTPC neutrino detection system capable of performing measurements in high-pileup environments. I demonstrated the advantages of adopting a modular design, as implemented in the ArgonCube concept, making it the choice for the Liquid Argon Near Detector of DUNE.

A primary objective of this research was to design and validate a robust, high-performance light readout system capable of addressing the demanding operational conditions presented by the broad-spectrum, high-intensity neutrino beam at the DUNE near detector complex. Starting from initial design concepts, the work systematically advanced through prototyping, quality assurance, system integration, and commissioning stages, culminating in the successful operation of the 2x2 Demonstrator within the NuMI beamline at Fermilab.

The development of the ArCLight modules represented a critical step forward in the detector technology, showcasing significant improvements in their photon detection efficiency by over 300% and the scaling up from $10\,\mathrm{cm} \times 10\,\mathrm{cm}$ prototypes to $30\,\mathrm{cm} \times 50\,\mathrm{cm}$ production-level versions. These improvements, including the refined coating technique and the developed quality control scanning setup, were summarised and published in [125]. The ArCLight light traps, together with the complementary LCM light traps, were installed in the 2x2 TPC modules. To operate them, a comprehensive readout system was developed, including readout electronics, an in-situ calibration system, and the necessary tools for the data acquisition and detector configuration. The calibration procedures developed, particularly the LED calibration system, allowed for a fast optimisation of the SiPM operation parameters during the detector commissioning, ensuring high-quality data taking.

The 2x2 Demonstrator was successfully assembled, commissioned, and operated in the NuMI neutrino beamline at Fermilab, demonstrating the viability of the modular LArTPC detector concept under realistic experimental conditions. The detector recorded neutrino interactions at stable nominal conditions for 4.5 days in July 2024. Following installation at the underground facility, the demonstrator achieved stable high-voltage operation and robust performance of its integrated trigger, timing, and data acquisition systems.

However, the cryogenic system faced operational challenges, including difficulties in maintaining a stable liquid argon level and achieving sufficient argon purity. While stable cryogenic conditions were eventually sustained for several consecutive days, further upgrades are required to support reliable long-term operation. Modifications are currently being implemented and involve improving the detector sealing to prevent continuous argon loss and the modification of the condenser inlet line to allow a larger liquid level range, where the HV system can be operated.

By analysing interactions induced by the neutrino beam, a detailed study of the temporal resolution was conducted. The timing distribution of detected scintillation light was compared with the known time structure of the beam to quantify the resolution across two different light collection modules and varying signal amplitudes. These studies demonstrated that the system can measure interaction times with nanosecond precision under realistic detector conditions. The upper limits of the resolution were determined to be $R_{\mathrm{ArCLight}} \leq (3.31 \pm 0.04)$ ns for the ArCLight and $R_{\mathrm{LCM}} \leq (3.03 \pm 0.03)$ ns for the LCM. Considering that the scintillation and wavelength-shifting processes involved have characteristic timescales of several nanoseconds, achieving an overall resolution below 4 ns is remarkable and far sufficient for ND-LAr.

Although the analysis performed on the extraction of the temporal resolution has already demonstrated excellent performance, there remains substantial potential for further optimisation. A particular direction involves incorporating associated charge track information for the reconstructed light hits. This correlation would allow for more refined event selection and enable time-of-flight corrections for both the incoming particle and the emitted photons, further improving the resolution. Future efforts should also include enhancements in timing calibration procedures. LED calibration runs could be used to extract a measurement of the signal propagation delay for each channel individually, replacing the ADC-by-ADC correction currently applied.

The path toward physics measurements with the 2x2 Demonstrator hinges on the finalisation and validation of the automated reconstruction algorithms, which will enable accurate identification and characterisation of neutrino interactions. Preliminary versions of these exist and show good performance on simulation data, but have to be verified and tuned for their application on detector data. This level of reconstruction has never before been achieved using native 3D data from a pixelated readout, marking a significant step forward in LArTPC technology. A comprehensive treatment of systematic uncertainties, including effects introduced through the modular design, will be essential to ensure reliable results. Parallel efforts in energy calibration, involving both charge and light signals, are needed to achieve precise energy reconstruction of the observed events. Together, these components form the foundation for extracting physics results from the 2x2 data and for benchmarking the performance of systems intended for ND-LAr.

Overall, the results demonstrate that the light readout system has reached a high level of maturity, with proven performance under realistic operating conditions, and is now ready for deployment in the ND-LAr detector. Moving towards the construction and installation of the ND-LAr, in parallel to the 2x2, major efforts have led to the successful first operation of a full-size demonstrator (FSD) module for ND-LAr in autumn 2024 at the University of Bern. While the 2x2 serves as a physics demonstrator and showcases the successful multi-module operation, the FSD marked a major milestone since the first time that production-scale components, including the final version of the ArCLight light detectors, were tested under integrated cryogenic and readout conditions. These tests offer the essential technical validation of the module design and, together with the 2×2 as the physics demonstrator, complete the overall validation programme for ND-LAr.

In summary, this research showed significant advances in the technological foundation for the ND-LAr detector within DUNE. Beyond this, the scalability demonstrated by the modular ArgonCube approach positions this technology favorably for larger-scale applications besides ND-LAr, potentially influencing future detector designs across neutrino physics. Continued innovation and rigorous experimental validation, as pursued in this thesis, remain essential for realising the full scientific potential of future neutrino experiments.

Looking ahead, further improvements in the light timing resolution should be pursued to fully exploit the capabilities of light-aided event reconstruction in LArTPCs. Achieving sub-nanosecond resolution would be a key step forward, significantly expanding the range of physics observables accessible through precise timing. Particular opportunities include the identification of short-lived particles such as the K^+, with a lifetime of 12.4 ns [44] or the performance of time-of-flight measurements of neutrons, enabling the reconstruction of their energy. This level of precision requires eliminating wavelength-shifting processes and directly employing VUV-sensitive SiPMs in combination with increased readout sampling rates. However, such an approach introduces the challenge of managing high data streams, making the implementation of (quasi-)online data reduction algorithms critical. These would need to extract light hit information in real-time, without recording full waveforms. Additionally, maintaining a high photon detection coverage while minimising the impact on charge readout remains a central design challenge. Placing SiPMs at the cathode offers a promising alternative with minimal obstruction to the drift field, though this approach requires optical readout and powering via fibre, an approach that has already been demonstrated (see e.g. [164]). These future directions, though technically demanding, offer compelling opportunities to expand the physics reach of next-generation neutrino detectors.

Acknowledgements

I would like to thank my supervisor, Prof. Dr. **Michele Weber**, for guiding me through my thesis. I really appreciated always being able to step into your office and discuss whatever I was stuck with, even in the most stressful times. Further, I would like to thank you for giving me the opportunity to work in a very international collaboration, in particular, the time I could spend at Fermilab will always be in my memory.

A big thank you goes to my former supervisor, Prof. Dr. **Igor Kreslo**, without whom I would have never even started my PhD. It was definitely you who aroused my fascination for physics again. I enjoyed every minute we spent together in the lab and am very grateful for everything I learned from you.

Also, I would like to thank my external examiner, Prof. Dr. **Mitchell Soderberg**, and the chair of my defence, Prof. Dr. **Gilberto Colangelo**.

Next, my thanks go to Dr. **Serhan Tufanli**, who supported me especially while writing my thesis and always had an open ear to discuss things I was struggling with.

I am very grateful to all the members of the Bern neutrino group, Dr. **Saba Parsa**, Dr. **Richard Diurba**, **Jonas Bürgi**, Dr. **Anja Gauch**, **Shivaraj Mulleria Babu**, **Nicolas Sallin**, and **Jan Kunzmann**. It was great to work with all of you, and I think it is really special to have a team where everybody supports each other to reach the goal all together. All the hours we spent in Grosslabor were probably sometimes stressful and frustrating, but mostly they were fun, because of all of you!

I need to specially thank all the people from the LHEP mechanics and electronics workshop, Camilla Tognina, Andri Simeon, Alexander Schait, Cyrill Jost, Silas Bosco, Lorenzo Meier, Efraim Elsholtz, and Finn Tschan. Thank you for all the patience you had with me during building all the smaller and bigger projects we had, and thank you for all the things I could learn from you.

Thank you to the (extended) 2x2 LRS onsite team, **Angela White**, Dr. **Tom Murphy**, **Karolina Wresilo** and **Elise Hinkle**, for the countless hours we spent underground, in the workshop, in the tiny meeting room, at the pub and any other place we have been working together. It was great to be alongside all of you, and I am happy to have gained not only super nice colleagues but also friendships that will hopefully last longer than my time on 2x2.

Further, I would like to thank all the people who made all the time I spent at Fermilab unforgettable. It is impossible to mention all the names without forgetting somebody. All the countless stories with all of you made me almost forget how flat Illinois really is...

A special thanks goes to Dr. **Kevin Wood** and Dr. **James Mead**, who provided me with inputs, support and feedback for the T_0 reconstruction analysis. Without you, I would have probably given up on it and never got to this result.

I also would like to thank Dr. **James Sinclair**, Dr. **Francois Drielsma** and Dr. **Callum Wilkinson** for providing me feedback, comments and moral support during the writing process for this thesis.

Last but not least, I would like to thank all my friends and family who were always there for me and supported me throughout the last four years. I need to apologise for all the times I was not there and all the things I have missed because I was stuck somewhere in this world in a lab. I really appreciate that I can still keep coming back and that you show me all your kindness and care.

General Remarks

Parts of chapters 2-3 are adapted from equivalent chapters in my master thesis[132].

The readability of this thesis was improved using ChatGPT [165], an AI-based language model. However, no content was generated by ChatGPT; all technical and scientific material was authored by me. The accuracy and integrity of the text remain the sole responsibility of the author.

Bibliography

[1] Q. R. Ahmad et al. "Direct Evidence for Neutrino Flavor Transformation from Neutral-Current Interactions in the Sudbury Neutrino Observatory". In: *Physical Review Letters* 89.1 (June 2002), p. 011301. ISSN: 0031-9007. DOI: 10.1103/PhysRevLett.89.011301. URL: https://link.aps.org/doi/10.1103/PhysRevLett.89.011301.

[2] J. A. Formaggio and G. P. Zeller. "From eV to EeV: Neutrino Cross Sections Across Energy Scales". In: *Rev. Mod. Phys.* 84 (2012), pp. 1307–1341. DOI: 10.1103/RevModPhys.84.1307. arXiv: 1305.7513 [hep-ex].

[3] A. D. Sakahrov. "Violation of CP in variance, C asymmetry, and baryon asymmetry of the universe". In: *JETP Lett* 5 (1967), pp. 24–27. DOI: 10.1070/pu1991v034n05abeh002497.

[4] B. Abi et al. "Volume I. Introduction to DUNE". In: *Journal of Instrumentation* 15.08 (Aug. 2020), T08008–T08008. DOI: 10.1088/1748-0221/15/08/t08008.

[5] B. Abi et al. *Deep Underground Neutrino Experiment (DUNE), Far Detector Technical Design Report, Volume II: DUNE Physics.* Tech. rep. FNAL, Feb. 2020. arXiv: 2002.03005 [hep-ex].

[6] B. Abi et al. "Volume III. DUNE far detector technical coordination". In: *Journal of Instrumentation* 15.08 (Aug. 2020), T08009–T08009. DOI: 10.1088/1748-0221/15/08/t08009.

[7] B. Abi et al. "Volume IV. The DUNE far detector single-phase technology". In: *Journal of Instrumentation* 15.08 (Aug. 2020), T08010–T08010. DOI: 10.1088/1748-0221/15/08/t08010.

[8] V. Hewes et al. "Deep Underground Neutrino Experiment (DUNE) Near Detector Conceptual Design Report". In: *Instruments* 5.4 (2021), p. 31. DOI: 10.3390/instruments5040031. arXiv: 2103.13910 [physics.ins-det].

[9] H. H. Chen et al. *A Neutrino Detector Sensitive to Rare Processes: I. A Study of Neutrino Electron Reactions.* May 1976.

[10] M. Auger, A. Ereditato, and J. Sinclair. *ArgonCube: a Modular Approach for Liquid Argon TPC Neutrino Detectors for Near Detector Environments.* Tech. rep. Geneva: CERN, 2017. URL: https://cds.cern.ch/record/2268439.

[11] D. A. Dwyer et al. "LArPix: Demonstration of low-power 3D pixelated charge readout for liquid argon time projection chambers". In: *Journal of Instrumentation* 13.10 (2018). ISSN: 17480221. DOI: 10.1088/1748-0221/13/10/P10007. URL: https://doi.org/10.1088/1748-0221/13/10/P10007.

[12] M. Auger et al. "ArCLight—A Compact Dielectric Large-Area Photon Detector". In: *Instruments* 2.1 (Feb. 2018), p. 3. ISSN: 2410-390X. DOI: 10.3390/instruments2010003. URL: http://www.mdpi.com/2410-390X/2/1/3.

[13] R. Berner et al. "First Operation of a Resistive Shell Liquid Argon Time Projection Chamber: A New Approach to Electric-Field Shaping". In: *Instruments* 3.2 (May 2019), p. 28. ISSN: 2410-390X. DOI: 10.3390/instruments3020028. URL: https://www.mdpi.com/2410-390X/3/2/28.

[14] J. Chadwick. "Intensitätsverteilung im magnetischen Spectrum der β-Strahlen von radium B + C". In: *Verhandl. Dtsc. Phys. Ges.* Vol. 16. 1914, p. 383. URL: https://cds.cern.ch/record/262756.

[15] W. Pauli. "Letter of the 4th December 1930". In: *Pauli Archive at CERN* (1930).

[16] J. Chadwick. "Possible Existence of a Neutron". In: *Nature* 129 (1932), p. 312. DOI: 10.1038/129312a0.

[17] F. Perrin. "Possibilité d'émission de particules neutres de masse intrinsèque nulle dans les radioactivités β". In: *Comptes rendus* 197.1625-1627 (1933), p. 6.

[18] E. Fermi. "Tentativo di una teoria dei raggi β". In: *Il Nuovo Cimento (1924-1942)* 11.1 (1934), p. 1.

[19] H. Bethe and R. Peierls. "The 'neutrino'". In: *Nature* 133 (1934), p. 532. DOI: 10.1038/133532a0.

[20] C. L. Cowan et al. "Detection of the Free Neutrino: a Confirmation". In: *Science* 124.3212 (1956), pp. 103–104. ISSN: 0036-8075. DOI: 10.1126/science.124.3212.103. eprint: https://science.sciencemag.org/content/124/3212/103.full.pdf. URL: https://science.sciencemag.org/content/124/3212/103.

[21] F. Reines et al. “Detection of the free anti-neutrino”. In: *Phys. Rev.* 117 (1960), pp. 159–173. DOI: 10.1103/PhysRev.117.159.

[22] C. S. Wu et al. “Experimental Test of Parity Conservation in Beta Decay”. In: *Physical Review* 105.4 (Feb. 1957), pp. 1413–1415. ISSN: 0031-899X. DOI: 10.1103/PhysRev.105.1413. URL: https://link.aps.org/doi/10.1103/PhysRev.105.1413.

[23] M. Goldhaber, L. Grodzins, and A. W. Sunyar. “Helicity of Neutrinos”. In: *Phys. Rev.* 109 (1958), pp. 1015–1017. DOI: 10.1103/PhysRev.109.1015.

[24] G. Danby et al. “Observation of High-Energy Neutrino Reactions and the Existence of Two Kinds of Neutrinos”. In: *Physical Review Letters* 9.1 (July 1962), pp. 36–44. ISSN: 0031-9007. DOI: 10.1103/PhysRevLett.9.36. URL: https://link.aps.org/doi/10.1103/PhysRevLett.9.36.

[25] R. Davis, D. S. Harmer, and K. C. Hoffman. “Search for Neutrinos from the Sun”. In: *Physical Review Letters* 20.21 (May 1968), pp. 1205–1209. ISSN: 0031-9007. DOI: 10.1103/PhysRevLett.20.1205. URL: https://link.aps.org/doi/10.1103/PhysRevLett.20.1205.

[26] J. Bahcall et al. “Solar neutrino flux”. In: *Astrophys. J.* 137 (1963), pp. 344–346. DOI: 10.1086/147513.

[27] J. Bahcall. “The solar neutrino problem”. In: *Comments Nucl. Part. Phys.* 5.2 (1972), pp. 59–64.

[28] J. N. Bahcall and R. Davis. “Solar Neutrinos - a Scientific Puzzle”. In: *Science* 191 (1976), pp. 264–267. DOI: 10.1126/science.191.4224.264.

[29] B. Pontecorvo. “Neutrino experiments and the problem of conservation of leptonic charge”. In: *Sov. Phys. JETP* 26.984-988 (1968), p. 165.

[30] K. Hirata et al. “Experimental study of the atmospheric neutrino flux”. In: *Physics Letters B* 205.2-3 (1988), pp. 416–420.

[31] D. Casper et al. “Measurement of atmospheric neutrino composition with the IMB-3 detector”. In: *Phys. Rev. Lett.* 66 (20 May 1991), pp. 2561–2564. DOI: 10.1103/PhysRevLett.66.2561. URL: https://link.aps.org/doi/10.1103/PhysRevLett.66.2561.

[32] P. A. Cherenkov. “Visible emission of clean liquids by action of gamma radiation”. In: *Dokl. Akad. Nauk SSSR*. Vol. 2. 8. 1934, pp. 451–454.

[33] Y. Fukuda et al. “Measurement of a small atmospheric $\nu\mu/\nu$e ratio”. In: *Physics Letters, Section B: Nuclear, Elementary Particle and High-Energy Physics* 433.1-2 (Aug. 1998), pp. 9–18. ISSN: 03702693. DOI: 10.1016/S0370-2693(98)00476-6.

[34] M. L. Perl et al. “Properties of the proposed τ charged lepton”. In: *Physics Letters B* 70.4 (1977), pp. 487–490.

[35] B. Adeva et al. “Measurement of Z0 decays to hadrons, and a precise determination of the number of neutrino species”. In: *Physics Letters B* 237.1 (1990), pp. 136–146.

[36] K. Kodama et al. “Observation of tau neutrino interactions”. In: *Physics Letters, Section B: Nuclear, Elementary Particle and High-Energy Physics* 504.3 (Apr. 2001), pp. 218–224. ISSN: 03702693. DOI: 10.1016/S0370-2693(01)00307-0.

[37] K. Kodama et al. “Final tau-neutrino results from the DONuT experiment”. In: *Phys. Rev. D* 78 (2008), p. 052002. DOI: 10.1103/PhysRevD.78.052002. arXiv: 0711.0728 [hep-ex].

[38] M. B. Gavela et al. “Standard model CP violation and baryon asymmetry”. In: *Mod. Phys. Lett. A* 9 (1994), pp. 795–810. DOI: 10.1142/S0217732394000629. arXiv: hep-ph/9312215.

[39] K. Abe et al. “Indication of Electron Neutrino Appearance from an Accelerator-produced Off-axis Muon Neutrino Beam”. In: *Phys. Rev. Lett.* 107 (2011), p. 041801. DOI: 10.1103/PhysRevLett.107.041801. arXiv: 1106.2822 [hep-ex].

[40] P. Adamson et al. “Improved search for muon-neutrino to electron-neutrino oscillations in MINOS”. In: *Phys. Rev. Lett.* 107 (2011), p. 181802. DOI: 10.1103/PhysRevLett.107.181802. arXiv: 1108.0015 [hep-ex].

[41] F. P. An et al. “Observation of electron-antineutrino disappearance at Daya Bay”. In: *Phys. Rev. Lett.* 108 (2012), p. 171803. DOI: 10.1103/PhysRevLett.108.171803. arXiv: 1203.1669 [hep-ex].

[42] A. Bettini. *Introduction to Elementary Particle Physics*. Cambridge University Press, 2008. ISBN: 9781139472555.

[43] Z. Maki, M. Nakagawa, and S. Sakata. *Remarks on the Unified Model · of Elementary Particles*. Tech. rep. 5. 1962. URL: https://academic.oup.com/ptp/article/28/5/870/1858382.

[44] P. A. Zyla et al. “Review of particle physics”. In: *Progress of Theoretical and Experimental Physics* 2020.8 (2020), pp. 1–2093. ISSN: 20503911. DOI: 10.1093/ptep/ptaa104. URL: https://doi.org/10.1093/ptep/ptaa104.

[45] L. Wolfenstein. “Neutrino oscillations in matter”. In: *Physical Review D* 17.9 (May 1978), pp. 2369–2374. ISSN: 0556-2821. DOI: 10.1103/PhysRevD.17.2369. URL: https://link.aps.org/doi/10.1103/PhysRevD.17.2369.

[46] I. Esteban et al. “NuFit-6.0: updated global analysis of three-flavor neutrino oscillations”. In: *JHEP* 12 (2024), p. 216. DOI: 10.1007/JHEP12(2024)216. arXiv: 2410.05380 [hep-ph].

[47] K. Sutton. “Results from the NOvA-T2K Joint Analysis”. In: *Neutrino 2024*. Milano, Italy, June 2024. URL: https://agenda.infn.it/event/37867/contributions/227857/.

[48] K. Abe et al. *Hyper-Kamiokande Design Report*. May 2018. arXiv: 1805.04163 [physics.ins-det].

[49] K. Seiya et al. “RF system upgrade for 1.3 MW operation of J-PARC main ring”. In: *JACoW* IPAC2024 (2024), TUPC10. DOI: 10.18429/JACoW-IPAC2024-TUPC10.

[50] K. Abe et al. “T2K ND280 Upgrade - Technical Design Report”. In: (Jan. 2019). arXiv: 1901.03750 [physics.ins-det].

[51] K. Abe et al. "T2K neutrino flux prediction". In: *Phys. Rev. D* 87.1 (2013). [Addendum: Phys.Rev.D 87, 019902 (2013)], p. 012001. DOI: 10.1103/PhysRevD.87.012001. arXiv: 1211.0469 [hep-ex].

[52] D. S. Ayres et al. "The NOvA Technical Design Report". In: (Oct. 2007). DOI: 10.2172/935497.

[53] P. A. Machado, O. Palamara, and D. W. Schmitz. "The Short-Baseline Neutrino Program at Fermilab". In: *Ann. Rev. Nucl. Part. Sci.* 69 (2019), pp. 363–387. DOI: 10.1146/annurev-nucl-101917-020949. arXiv: 1903.04608 [hep-ex].

[54] B. Russell. "The 2x2 Demonstrator - A demonstrator for the DUNE ND-LAr Near Detector based on the ArgonCube Design". In: *PoS* TAUP2023 (2024), p. 221. DOI: 10.22323/1.441.0221.

[55] B. Abi et al. "Long-baseline neutrino oscillation physics potential of the DUNE experiment: DUNE Collaboration". In: *European Physical Journal C* 80.10 (Oct. 2020). ISSN: 14346052. DOI: 10.1140/epjc/s10052-020-08456-z.

[56] S. Amerio et al. "Design, construction and tests of the ICARUS T600 detector". In: *Nucl. Instrum. Meth. A* 527 (2004), pp. 329–410. DOI: 10.1016/j.nima.2004.02.044.

[57] R. Acciarri et al. "Design and Construction of the MicroBooNE Detector". In: *JINST* 12.02 (2017), P02017. DOI: 10.1088/1748-0221/12/02/P02017. arXiv: 1612.05824 [physics.ins-det].

[58] A. Abed Abud et al. "The DUNE Far Detector Vertical Drift Technology. Technical Design Report". In: *JINST* 19.08 (2024), T08004. DOI: 10.1088/1748-0221/19/08/T08004. arXiv: 2312.03130 [hep-ex].

[59] B. Abi et al. "First results on ProtoDUNE-SP liquid argon time projection chamber performance from a beam test at the CERN Neutrino Platform". In: *JINST* 15.12 (2020), P12004. DOI: 10.1088/1748-0221/15/12/P12004. arXiv: 2007.06722 [physics.ins-det].

[60] D. collaboration. "Deep Underground Neutrino Experiment (DUNE) Near Detector Preliminary Design Report - TMS chapter". In: (2025). Publication in preparation.

[61] K. D. Smith et al. "Progress in the design and manufacture of the KLOE solenoid for the DAPHNE ring at Frascati". In: *IEEE Trans. Appl. Supercond.* 7.2 (1997). Ed. by M. Adams, pp. 630–632. DOI: 10.1109/77.614583.

[62] V. Pia. "Reconstruction of neutrino interactions in SAND with an innovative liquid Argon imaging detector". In: *JINST* 19.02 (2024), p. C02073. DOI: 10.1088/1748-0221/19/02/C02073.

[63] D. Goeldi. "A Novel Liquid Argon Time Projection Chamber Detector: The ArgonCube Concept". PhD thesis. University of Bern, 2018. URL: https://jinst.sissa.it/jinst/theses/2018_JINST_TH_002.pdf.

[64] D. E. Groom, N. V. Mokhov, and S. I. Striganov. "Muon stopping power and range tables 10-MeV to 100-TeV". In: *Atom. Data Nucl. Data Tabl.* 78 (2001), pp. 183–356. DOI: 10.1006/adnd.2001.0861.

[65] C. Amsler et al. “Review of Particle Physics”. In: *Phys. Lett. B* 667 (2008), pp. 1–1340. DOI: 10.1016/j.physletb.2008.07.018.

[66] N. F. V. Duarte. “Proportional counters equipped with thin B4C conversion layers for the detection of slow neutrons”. PhD thesis. Universidade de Coimbra (Portugal), 2021.

[67] C. W. Fabjan and T. Ludlam. “Calorimetry in High-energy Physics”. In: *Ann. Rev. Nucl. Part. Sci.* 32 (1982), pp. 335–389. DOI: 10.1146/annurev.ns.32.120182.002003.

[68] S. Masciocchi. *Uni-heidelberg.* [Accessed 22-03-2025]. URL: https://www.physi.uni-heidelberg.de/~sma/teaching/ParticleDetectors2/sma_HadronicCalorimeters.pdf.

[69] G. Charpak, D. Rahm, and H. Steiner. “Some developments in the operation of multiwire proportional chambers”. In: *Nucl. Instrum. Meth.* 80 (1970), pp. 13–34. DOI: 10.1016/0029-554X(70)90293-4.

[70] D. R. Nygren. “The time projection chamber: A new 4 pi detector for charged particles, eConf”. In: *C740805* 58 (1974).

[71] W. Willis and V. Radeka. “Liquid-argon ionization chambers as total-absorption detectors”. In: *Nuclear Instruments and Methods* 120.2 (1974), pp. 221–236.

[72] C. Allen and C. Allen. *Astrophysical Quantities.* Springer series in electrophysics. Athlone Press, 1973. ISBN: 9780485111507.

[73] C. Tegeler, R. Span, and W. Wagner. “A new equation of state for argon covering the fluid region for temperatures from the melting line to 700 K at pressures up to 1000 MPa”. In: *Journal of Physical and Chemical Reference Data* 28.3 (1999), pp. 779–850.

[74] E. Shibamura et al. “Drift velocities of electrons, saturation characteristics of ionization and W-values for conversion electrons in liquid argon, liquid argon-gas mixtures and liquid xenon”. In: *Nucl. Instrum. Meth.* 131 (1975), pp. 249–258. DOI: 10.1016/0029-554X(75)90327-4.

[75] M. Miyajima et al. “Average energy expended per ion pair in liquid argon”. In: *Phys. Rev. A* 9 (1974), pp. 1438–1443. DOI: 10.1103/PhysRevA.9.1438.

[76] T. Doke et al. “Estimation of Fano factors in liquid argon, krypton, xenon and xenon-doped liquid argon”. In: *Nucl. Instrum. Meth.* 134 (1976), pp. 353–357. DOI: 10.1016/0029-554X(76)90292-5.

[77] A. Gonidec et al. *Temperature and Electric Field Strength Dependence of Electron Drift Velocity in Liquid Argon.* Tech. rep. ATL-LARG-96-058. ATL-A-PN-58. Geneva: CERN, Dec. 1996. URL: https://cds.cern.ch/record/682073.

[78] W. Walkowiak. “Drift velocity of free electrons in liquid argon”. In: *Nucl. Instrum. Meth. A* 449 (2000), pp. 288–294. DOI: 10.1016/S0168-9002(99)01301-7.

[79] S. Amoruso et al. “Analysis of the liquid argon purity in the ICARUS T600 TPC”. In: *Nucl. Instrum. Meth. A* 516 (2004), pp. 68–79. DOI: 10.1016/j.nima.2003.07.043.

[80] E. Aprile, K. Giboni, and C. Rubbia. “A Study of Ionization Electrons Drifting Large Distances in Liquid and Solid Argon”. In: *Nucl. Instrum. Meth. A* 241 (1985), pp. 62–71. DOI: 10.1016/0168-9002(85)90516-9.

[81] M. Boulay and A. Hime. “Technique for direct detection of weakly interacting massive particles using scintillation time discrimination in liquid argon”. In: *Astropart. Phys.* 25 (2006), pp. 179–182. DOI: 10.1016/j.astropartphys.2005.12.009.

[82] T. Doke et al. “Absolute Scintillation Yields in Liquid Argon and Xenon for Various Particles”. In: *Japanese Journal of Applied Physics* 41.Part 1, No. 3A (Mar. 2002), pp. 1538–1545. ISSN: 0021-4922. DOI: 10.1143/JJAP.41.1538. URL: https://iopscience.iop.org/article/10.1143/JJAP.41.1538.

[83] E. Grace and J. A. Nikkel. “Index of refraction, Rayleigh scattering length, and Sellmeier coefficients in solid and liquid argon and xenon”. In: *Nucl. Instrum. Meth. A* 867 (2017), pp. 204–208. DOI: 10.1016/j.nima.2017.06.031. arXiv: 1502.04213 [physics.ins-det].

[84] G. Seidel, R. Lanou, and W. Yao. “Rayleigh scattering in rare gas liquids”. In: *Nucl. Instrum. Meth. A* 489 (2002), pp. 189–194. DOI: 10.1016/S0168-9002(02)00890-2. arXiv: hep-ex/0111054.

[85] N. Ishida et al. “Attenuation length measurements of scintillation light in liquid rare gases and their mixtures using an improved reflection suppresser”. In: *Nuclear Instruments and Methods in Physics Research Section A: Accelerators, Spectrometers, Detectors and Associated Equipment* 384.2-3 (1997), pp. 380–386.

[86] M. Sneep and W. Ubachs. “Direct measurement of the Rayleigh scattering cross section in various gases”. In: *Journal of Quantitative Spectroscopy and Radiative Transfer* 92.3 (2005), pp. 293–310.

[87] P. Cennini et al. “Performance of a three-ton liquid argon time projection chamber”. In: *Nuclear Instruments and Methods in Physics Research Section A: Accelerators, Spectrometers, Detectors and Associated Equipment* 345.2 (1994), pp. 230–243.

[88] V. Atrazhev and I. Timoshkin. “Transport of electrons in atomic liquids in high electric fields”. In: *IEEE transactions on dielectrics and electrical insulation* 5.3 (1998), pp. 450–457.

[89] E. Shibamura et al. “Ratio of diffusion coefficient to mobility for electrons in liquid argon”. In: *Phys. Rev. A* 20.6 (1979), p. 2547. DOI: 10.1103/PhysRevA.20.2547.

[90] R. Acciarri et al. “A Study of Electron Recombination Using Highly Ionizing Particles in the ArgoNeuT Liquid Argon TPC”. In: *JINST* 8 (2013), P08005. DOI: 10.1088/1748-0221/8/08/P08005. arXiv: 1306.1712 [physics.ins-det].

[91] P. Sorensen. “Anisotropic diffusion of electrons in liquid xenon with application to improving the sensitivity of direct dark matter searches”. In: *Nucl. Instrum. Meth. A* 635 (2011), pp. 41–43. DOI: 10.1016/j.nima.2011.01.089. arXiv: 1102.2865 [astro-ph.IM].

[92] A. Hitachi et al. *Effect of ionization density on the time dependence of luminescence from liquid argon and xenon.* 1983.

[93] S. Kubota, M. Hishida, and M. Suzuki. "Dynamical behavior of free electrons in the recombination process in liquid argon, krypton, and xenon". In: *Phys. Rev. B* 20.8 (1979), p. 3486. DOI: 10.1103/PhysRevB.20.3486.

[94] A. Wright. *Optical Attenuation in Liquid Argon.* Tech. rep. 2011.

[95] R. Acciarri et al. "Effects of Nitrogen contamination in liquid Argon". In: *JINST* 5 (2010), P06003. DOI: 10.1088/1748-0221/5/06/P06003. arXiv: 0804.1217 [nucl-ex].

[96] O. Palamara. "Event reconstruction in LAr-TPC". In: *AIP Conference Proceedings.* Vol. 1222. 2010, pp. 122–126. ISBN: 9780735407633. DOI: 10.1063/1.3399272. URL: https://doi.org/10.1063/1.3399272.

[97] C. Rubbia et al. "Underground operation of the ICARUS T600 LAr-TPC: first results". In: *JINST* 6 (2011), P07011. DOI: 10.1088/1748-0221/6/07/P07011. arXiv: 1106.0975 [hep-ex].

[98] R. Acciarri et al. "A Proposal for a Three Detector Short-Baseline Neutrino Oscillation Program in the Fermilab Booster Neutrino Beam". In: (Mar. 2015). arXiv: 1503.01520 [physics.ins-det].

[99] B. Ali-Mohammadzadeh et al. "Design and implementation of the new scintillation light detection system of ICARUS T600". In: *JINST* 15.10 (2020), T10007. DOI: 10.1088/1748-0221/15/10/T10007. arXiv: 2006.05261 [physics.ins-det].

[100] A. Heggestuen. "Light detection and cosmic rejection in the ICARUS LArTPC at Fermilab". In: *JINST* 19.05 (2024), p. C05038. DOI: 10.1088/1748-0221/19/05/C05038. arXiv: 2312.05684 [hep-ex].

[101] C. Anderson et al. "The ArgoNeuT Detector in the NuMI Low-Energy Beam Line at Fermilab". In: *JINST* 7 (2012), P10019. DOI: 10.1088/1748-0221/7/10/P10019. arXiv: 1205.6747 [physics.ins-det].

[102] A. Ereditato et al. "Design and operation of ARGONTUBE: a 5 m long drift liquid argon TPC". In: *JINST* 8 (2013), P07002. DOI: 10.1088/1748-0221/8/07/P07002. arXiv: 1304.6961 [physics.ins-det].

[103] A. Ereditato et al. "Measurement of the drift field in the ARGONTUBE LAr TPC with 266 nm pulsed laser beams". In: *JINST* 9.11 (2014), P11010. DOI: 10.1088/1748-0221/9/11/P11010. arXiv: 1408.6635 [physics.ins-det].

[104] A. A. Aguilar-Arevalo et al. "Significant Excess of ElectronLike Events in the MiniBooNE Short-Baseline Neutrino Experiment". In: *Phys. Rev. Lett.* 121.22 (2018), p. 221801. DOI: 10.1103/PhysRevLett.121.221801. arXiv: 1805.12028 [hep-ex].

[105] G. De Geronimo et al. "Front-end ASIC for a Liquid Argon TPC". In: *IEEE Trans. Nucl. Sci.* 58 (2011), pp. 1376–1385. DOI: 10.1109/TNS.2011.2127487.

[106] R. Acciarri et al. "Noise Characterization and Filtering in the MicroBooNE Liquid Argon TPC". In: *JINST* 12.08 (2017), P08003. DOI: 10.1088/1748-0221/12/08/P08003. arXiv: 1705.07341 [physics.ins-det].

[107] P. Abratenko et al. “Demonstration of new MeV-scale capabilities in large neutrino LArTPCs using ambient radiogenic and cosmogenic activity in MicroBooNE”. In: *Phys. Rev. D* 111.3 (2025), p. 032005. DOI: 10.1103/PhysRevD.111.032005. arXiv: 2410.18419 [hep-ex].

[108] L. Bugel et al. “Demonstration of a Lightguide Detector for Liquid Argon TPCs”. In: *Nucl. Instrum. Meth. A* 640 (2011), pp. 69–75. DOI: 10.1016/j.nima.2011.03.003. arXiv: 1101.3013 [physics.ins-det].

[109] C. Adams et al. “Design and construction of the MicroBooNE Cosmic Ray Tagger system”. In: *JINST* 14.04 (2019), P04004. DOI: 10.1088/1748-0221/14/04/P04004. arXiv: 1901.02862 [physics.ins-det].

[110] C. Adams et al. “A method to determine the electric field of liquid argon time projection chambers using a UV laser system and its application in MicroBooNE”. In: *JINST* 15.07 (2020), P07010. DOI: 10.1088/1748-0221/15/07/P07010. arXiv: 1910.01430 [physics.ins-det].

[111] P. Abratenko et al. “Measurement of space charge effects in the MicroBooNE LArTPC using cosmic muons”. In: *JINST* 15.12 (2020), P12037. DOI: 10.1088/1748-0221/15/12/P12037. arXiv: 2008.09765 [physics.ins-det].

[112] R. Acciarri et al. “The Pandora multi-algorithm approach to automated pattern recognition of cosmic-ray muon and neutrino events in the MicroBooNE detector”. In: *Eur. Phys. J. C* 78.1 (2018), p. 82. DOI: 10.1140/epjc/s10052-017-5481-6. arXiv: 1708.03135 [hep-ex].

[113] P. Abratenko et al. “Search for an anomalous excess of inclusive charged-current ν_e interactions in the MicroBooNE experiment using Wire-Cell reconstruction”. In: *Phys. Rev. D* 105.11 (2022), p. 112005. DOI: 10.1103/PhysRevD.105.112005. arXiv: 2110.13978 [hep-ex].

[114] P. Abratenko et al. “Search for an anomalous excess of charged-current quasielastic νe interactions with the MicroBooNE experiment using Deep-Learning-based reconstruction”. In: *Phys. Rev. D* 105.11 (2022), p. 112003. DOI: 10.1103/PhysRevD.105.112003. arXiv: 2110.14080 [hep-ex].

[115] B. Abi et al. *The Single-Phase ProtoDUNE Technical Design Report.* June 2017. arXiv: 1706.07081 [physics.ins-det].

[116] L. Manzanillas Velez. “Status of ProtoDUNE-II”. In: *PoS* ICHEP2024 (2025), p. 219. DOI: 10.22323/1.476.0219.

[117] A. A. Machado et al. “The X-ARAPUCA: An improvement of the ARAPUCA device”. In: Apr. 2018. DOI: 10.1088/1748-0221/13/04/C04026. arXiv: 1804.01407 [physics.ins-det].

[118] R. Álvarez-Garrote et al. “Measurement of the absolute efficiency of the X-ARAPUCA photon detector for the DUNE Far Detector 1”. In: *Eur. Phys. J. C* 84.10 (2024), p. 1004. DOI: 10.1140/epjc/s10052-024-13393-2. arXiv: 2405.12014 [physics.ins-det].

[119] D. S. Akerib et al. “The Large Underground Xenon (LUX) Experiment”. In: *Nucl. Instrum. Meth. A* 704 (2013), pp. 111–126. DOI: 10.1016/j.nima.2012.11.135. arXiv: 1211.3788 [physics.ins-det].

[120] D. S. Akerib et al. "LUX-ZEPLIN (LZ) Conceptual Design Report". In: (Sept. 2015). arXiv: 1509.02910 [physics.ins-det].

[121] C. Cuesta. "Status of ProtoDUNE Dual Phase". In: *PoS* EPS-HEP2019 (2020), p. 381. DOI: 10.22323/1.364.0381. arXiv: 1910.10115 [physics.ins-det].

[122] J. Asaadi et al. "First Demonstration of a Pixelated Charge Readout for Single-Phase Liquid Argon Time Projection Chambers". In: *Instruments* 4.1 (2020), p. 9. DOI: 10.3390/instruments4010009. arXiv: 1801.08884 [physics.ins-det].

[123] D. Nygren and Y. Mei. *Q-Pix: Pixel-scale Signal Capture for Kiloton Liquid Argon TPC Detectors: Time-to-Charge Waveform Capture, Local Clocks, Dynamic Networks*. Sept. 2018. arXiv: 1809.10213 [physics.ins-det].

[124] R. Acciarri et al. *Long-Baseline Neutrino Facility (LBNF) and Deep Underground Neutrino Experiment (DUNE) Conceptual Design Report Volume 2: The Physics Program for DUNE at LBNF*. Dec. 2015. URL: http://arxiv.org/abs/1512.06148.

[125] J. Bürgi et al. "Improvement and Characterisation of the ArCLight Large-Area Dielectric Light Detector for Liquid-Argon Time Projection Chambers". In: *Instruments* 8 (2024), p. 48. DOI: 10.3390/instruments8040048. arXiv: 2409.13613 [physics.ins-det].

[126] N. Anfimov et al. "Development of the Light Collection Module for the Liquid Argon Time Projection Chamber (LArTPC)". In: *Journal of Instrumentation*. Vol. 15. 7. 2020. DOI: 10.1088/1748-0221/15/07/C07022. URL: https://doi.org/10.1088/1748-0221/15/07/C07022.

[127] P. Koller. "A Method to Improve the Neutrino Energy Reconstruction in LArTPCs". Available at https://boristheses.unibe.ch/3222/. PhD thesis. University of Bern, 2021.

[128] A. Machado and E. Segreto. "ARAPUCA a new device for liquid argon scintillation light detection". In: *Journal of Instrumentation* 11.02 (Feb. 2016), pp. C02004–C02004. ISSN: 1748-0221. DOI: 10.1088/1748-0221/11/02/C02004. URL: https://iopscience.iop.org/article/10.1088/1748-0221/11/02/C02004.

[129] V. M. Gehman et al. "Fluorescence Efficiency and Visible Re-emission Spectrum of Tetraphenyl Butadiene Films at Extreme Ultraviolet Wavelengths". In: *Nucl. Instrum. Meth. A* 654 (2011), pp. 116–121. DOI: 10.1016/j.nima.2011.06.088. arXiv: 1104.3259 [astro-ph.IM].

[130] C. Benson, G. D. O. Gann, and V. Gehman. "Measurements of the intrinsic quantum efficiency and absorption length of tetraphenyl butadiene thin films in the vacuum ultraviolet regime". In: *Eur. Phys. J. C* 78 (2018), p. 329. DOI: 10.1140/epjc/s10052-018-5807-z. URL: https://doi.org/10.1140/epjc/s10052-018-5807-z.

[131] E. Segreto. "Evidence of delayed light emission of TetraPhenyl Butadiene excited by liquid Argon scintillation light". In: *Phys. Rev. C* 91.3 (2015), p. 035503. DOI: 10.1103/PhysRevC.91.035503. arXiv: 1411.4524 [physics.ins-det].

[132] L. Calivers. "Development and Characterisation of a Novel Light Detector: ArCLight". Available online: https://cds.cern.ch/record/2886536. MA thesis. University of Bern, 2021.

[133] M. Kuźniak and A. M. Szelc. "Wavelength Shifters for Applications in Liquid Argon Detectors". In: *Instruments* 5.1 (2020), p. 4. DOI: 10.3390/instruments5010004. arXiv: 2012.15626 [physics.ins-det].

[134] S. Piatek. *What is an SiPM and how does it work? — Hamamatsu Photonics — hub.hamamatsu.com.* https://hub.hamamatsu.com/us/en/technical-notes/mppc-sipms/what-is-an-SiPM-and-how-does-it-work.html. [Accessed 18-12-2024].

[135] P. P. M. Jansweijer, H. Z. Peek, and E. De Wolf. "White Rabbit: Sub-nanosecond timing over Ethernet". In: *Nucl. Instrum. Meth. A* 725 (2013). Ed. by G. Anton et al., pp. 187–190. DOI: 10.1016/j.nima.2012.12.096.

[136] V. Chmill et al. "On the characterisation of SiPMs from pulse-height spectra". In: *Nucl. Instrum. Meth. A* 854 (2017), pp. 70–81. DOI: 10.1016/j.nima.2017.02.049. arXiv: 1609.01181 [physics.ins-det].

[137] C. Andreopoulos et al. "The GENIE Neutrino Monte Carlo Generator". In: *Nucl. Instrum. Meth.* A614 (2010), pp. 87–104. DOI: 10.1016/j.nima.2009.12.009. arXiv: 0905.2517 [hep-ph].

[138] D. Heck et al. *CORSIKA: A Monte Carlo code to simulate extensive air showers.* Feb. 1998.

[139] M. C. et al. *An Enegry Deposition Simulation.* URL: https://github.com/ClarkMcGrew/edep-sim/.

[140] S. Agostinelli et al. "GEANT4 - A Simulation Toolkit". In: *Nucl. Instrum. Meth. A* 506 (2003), pp. 250–303. DOI: 10.1016/S0168-9002(03)01368-8.

[141] A. Abed Abud et al. "Highly-parallelized simulation of a pixelated LArTPC on a GPU". In: *JINST* 18.04 (2023), P04034. DOI: 10.1088/1748-0221/18/04/P04034. arXiv: 2212.09807 [physics.comp-ph].

[142] P. Madigan. "Measurement of Muon Capture on Argon with a Pixelated Liquid Argon Time Projection Chamber". Available at https://escholarship.org/uc/item/7k13v4b0. PhD thesis. UC, Berkeley (main), UC, Berkeley (main), 2023.

[143] E. L. Snider and G. Petrillo. "LArSoft: Toolkit for Simulation, Reconstruction and Analysis of Liquid Argon TPC Neutrino Detectors". In: *J. Phys. Conf. Ser.* 898.4 (2017). Ed. by R. Mount and C. Tull, p. 042057. DOI: 10.1088/1742-6596/898/4/042057.

[144] S. Vinogradov. "Analytical models of probability distribution and excess noise factor of Solid State Photomultiplier signals with crosstalk". In: *Nucl. Instrum. Meth. A* 695 (2012). Ed. by P. Bourgeois et al., pp. 247–251. DOI: 10.1016/j.nima.2011.11.086. arXiv: 1109.2014 [physics.ins-det].

[145] J. S. Marshall and M. A. Thomson. "The Pandora Software Development Kit for Pattern Recognition". In: *Eur. Phys. J. C* 75.9 (2015), p. 439. DOI: 10.1140/epjc/s10052-015-3659-3. arXiv: 1506.05348 [physics.data-an].

[146] F. Drielsma et al. “Scalable, End-to-End, Deep-Learning-Based Data Reconstruction Chain for Particle Imaging Detectors”. In: *34th Conference on Neural Information Processing Systems*. Feb. 2021. arXiv: 2102.01033 [hep-ex].

[147] P. Abratenko et al. “First demonstration of O(1 ns) timing resolution in the MicroBooNE liquid argon time projection chamber”. In: *Phys. Rev. D* 108.5 (2023), p. 052010. DOI: 10.1103/PhysRevD.108.052010. arXiv: 2304.02076 [hep-ex].

[148] J. Asaadi et al. “Emanation and bulk fluorescence in liquid argon from tetraphenyl butadiene wavelength shifting coatings”. In: *JINST* 14.02 (2019), P02021. DOI: 10.1088/1748-0221/14/02/P02021. arXiv: 1804.00011 [physics.ins-det].

[149] J. Asaadi et al. “A New Concept for Kilotonne Scale Liquid Argon Time Projection Chambers”. In: *Instruments* 4.1 (2020), p. 6. DOI: 10.3390/instruments4010006. arXiv: 1908.10956 [physics.ins-det].

[150] P. Adamson et al. “Measurement of the underground atmospheric muon charge ratio using the MINOS Near Detector”. In: *Phys. Rev. D* 83 (2011), p. 032011. DOI: 10.1103/PhysRevD.83.032011. arXiv: 1012.3391 [hep-ex].

[151] D. Mei and A. Hime. “Muon-induced background study for underground laboratories”. In: *Phys. Rev. D* 73 (2006). [Erratum: Phys.Rev.D 109, 019901 (2024)], p. 053004. DOI: 10.1103/PhysRevD.73.053004. arXiv: astro-ph/0512125.

[152] P. Benetti et al. “Measurement of the specific activity of 39Ar in natural argon”. In: *Nuclear Instruments and Methods in Physics Research Section A: Accelerators, Spectrometers, Detectors and Associated Equipment* 574.1 (2007), pp. 83–88.

[153] X. Mougeot. “Reliability of usual assumptions in the calculation of β and ν spectra”. In: *Phys. Rev. C* 91.5 (2015). [Erratum: Phys.Rev.C 92, 059902 (2015)], p. 055504. DOI: 10.1103/PhysRevC.91.055504.

[154] P. Adamson et al. “The NuMI Neutrino Beam”. In: *Nucl. Instrum. Meth. A* 806 (2016), pp. 279–306. DOI: 10.1016/j.nima.2015.08.063. arXiv: 1507.06690 [physics.acc-ph].

[155] D. Day et al. “Study of νd charged-current two-pion production in the threshold region”. In: *Phys. Rev. D* 28 (11 Dec. 1983), pp. 2714–2720. DOI: 10.1103/PhysRevD.28.2714. URL: https://link.aps.org/doi/10.1103/PhysRevD.28.2714.

[156] T. Kitagaki et al. “Charged-current exclusive pion production in neutrino-deuterium interactions”. In: *Phys. Rev. D* 34 (9 Nov. 1986), pp. 2554–2565. DOI: 10.1103/PhysRevD.34.2554. URL: https://link.aps.org/doi/10.1103/PhysRevD.34.2554.

[157] A. Ereditato et al. “Study of ionization signals in a liquid Argon TPC doped with Nitrogen”. In: *JINST* 3 (2008), P10002. DOI: 10.1088/1748-0221/3/10/P10002. arXiv: 0808.3939 [physics.ins-det].

[158] L. Aliaga et al. “Design, Calibration, and Performance of the MINERvA Detector”. In: *Nucl. Instrum. Meth. A* 743 (2014), pp. 130–159. DOI: 10.1016/j.nima.2013.12.053. arXiv: 1305.5199 [physics.ins-det].

[159] A. Abed Abud et al. “Performance of a Modular Ton-Scale Pixel-Readout Liquid Argon Time Projection Chamber”. In: *Instruments* 8.3 (2024), p. 41. DOI: 10.3390/instruments8030041. arXiv: 2403.03212 [physics.ins-det].

[160] J. Asaadi, D. A. Dwyer, and B. Russell. “Novel Liquid Argon Time-Projection Chamber Readouts”. In: *Annual Review of Nuclear and Particle Science* 74 (2024).

[161] T. Włostowski et al. “Trigger and RF Distribution Using White Rabbit”. In: *15th International Conference on Accelerator and Large Experimental Physics Control Systems.* 2015, WEC3O01. DOI: 10.18429/JACoW-ICALEPCS2015-WEC3O01.

[162] S. Gundacker and A. Heering. “The silicon-photomultiplier: fundamentals and applications of a modern solid-state photon detector”. In: *Phys. Med. Biol.* 65.17 (2020), 17TR01. DOI: 10.1088/1361-6560/ab7b2d.

[163] P. Adamson et al. “Precision Measurement of the Speed of Propagation of Neutrinos using the MINOS Detectors”. In: *Phys. Rev. D* 92.5 (2015), p. 052005. DOI: 10.1103/PhysRevD.92.052005. arXiv: 1507.04328 [hep-ex].

[164] M. Torti et al. “Results from Cryo-PoF: Power over fiber for fundamental and applied physics at cryogenic temperature”. In: *Nucl. Instrum. Meth. A* 1068 (2024), p. 169753. DOI: 10.1016/j.nima.2024.169753.

[165] OpenAI. *ChatGPT: Language Model for Text Refinement.* https://openai.com/chatgpt. Accessed: February 18, 2025. 2025.

Erklärung

gemäss Art. 18 PromR Phil.-nat. 2019

Name/Vorname: Calivers Livio Jonas

Matrikelnummer: 14-916-795

Studiengang: Physik

Bachelor ☐ Master ☐ Dissertation ☑

Titel der Arbeit: Demonstration of a Novel Modular Neutrino Detector

LeiterIn der Arbeit: Michele Weber
Igor Kreslo (Co-Leitung)

Ich erkläre hiermit, dass ich diese Arbeit selbständig verfasst und keine anderen als die angegebenen Quellen benutzt habe. Alle Stellen, die wörtlich oder sinngemäss aus Quellen entnommen wurden, habe ich als solche gekennzeichnet. Mir ist bekannt, dass andernfalls der Senat gemäss Artikel 36 Absatz 1 Buchstabe r des Gesetzes über die Universität vom 5. September 1996 und Artikel 69 des Universitätsstatuts vom 7. Juni 2011 zum Entzug des Doktortitels berechtigt ist. Für die Zwecke der Begutachtung und der Überprüfung der Einhaltung der Selbständigkeitserklärung bzw. der Reglemente betreffend Plagiate erteile ich der Universität Bern das Recht, die dazu erforderlichen Personendaten zu bearbeiten und Nutzungshandlungen vorzunehmen, insbesondere die Doktorarbeit zu vervielfältigen und dauerhaft in einer Datenbank zu speichern sowie diese zur Überprüfung von Arbeiten Dritter zu verwenden oder hierzu zur Verfügung zu stellen.

Bern, 13.04.2025

Ort/Datum

Unterschrift